UNIVERSITY OF CALIFORNIA

Santa Barbara

Development of Versatile Synthetic Methods for Silicone Materials

A dissertation submitted in partial satisfaction of the

requirements for the degree Doctor of Philosophy

in Materials

by

Colton Allen D'Ambra

Committee in charge:

Professor Christopher M. Bates, Co-Chair

Professor Craig J. Hawker, Co-Chair

Professor Rachel Segalman

Professor Glenn Fredrickson

March 2024

The dissertation of Colton Allen D'Ambra is approved.

_____
Glenn Fredrickson

_____
Rachel Segalman

_____
Craig Hawker, Committee Co-Chair

_____
Christopher Bates, Committee Co-Chair

March 2024

ACKNOWLEDGEMENTS

First off, I want to thank my advisors, Chris Bates and Craig Hawker, for giving me the opportunity to work in their research groups. They have been incredibly helpful and patient throughout this journey. Working in their groups has taught me an incredible amount about how to learn effectively and apply what I have learned to do groundbreaking research. In addition to learning academically, I have also learned a lot about myself and have grown significantly as a person throughout my time here. They have fostered an inclusive and collaborative environment that I have fit into quite nicely.

I wouldn't be where I am today without the support and training from numerous graduate students, post-docs, staff scientists, and instrument managers. Learning from such knowledgeable people has been a privilege. I want to specifically thank Rachel Behrens for maintaining the polymer characterization facilities. Her dedication to the department and her positive attitude has resulted in world-class characterization facilities, and without her, my research results wouldn't be the same.

I also want to thank my industry collaborators at Dow. Through this collaboration, I have learned a significant amount about what research looks like industrially. Additionally, the time spent on the Dow collaboration has molded me into an excellent communicator and refined my collaboration skills. Importantly, this collaboration gave me the opportunity to work with excellent graduate students and post-docs who have taught me an incredible amount about science, collaboration, communication, and myself. Thank you to Allison Abdilla, Zhishuai Geng, David Goldfeld, Michael Czuczola, and Elizabeth Murphy for working with me on this project and sharing your knowledge with me. Pat Getty deserves

special acknowledgement for being my partner on much of the work that I have presented in this dissertation. His dedication to the projects has been very motivating for me, and his contributions have been incredibly helpful. This dissertation wouldn't be the same without him.

I'd also like to thank my family for always believing in me. They've never doubted that I was capable of achieving the goals that I set for myself, and their unwavering support has given me confidence and helped me believe in myself.

The friends that I have made along the way have been some of the best that I have ever had and have shown me what it means to be a good friend. They support me in all things and have given me necessary outlets to escape from work and have fun. They introduced me to climbing, which rapidly became one of my favorite hobbies. Climbing trips and weekly outings to the climbing gym have been a fun way for me to get away from work and get out of my apartment.

My dog, Suzy, also deserves a special shoutout. She has been my best friend throughout this entire journey. Taking care of her has helped me take care of myself. My experience during Covid would have been much different if I didn't have her to motivate me to get outside and take care of each other.

Finally, I'd like to thank my partner, Tiffani, for supporting me throughout the last year and a half. Her unwavering support has been incredibly reassuring and has helped me grow into a more confident person. She has helped me learn to set boundaries and to take care of myself, all of which has been incredibly important during such a rigorous program. I cherish the time we've spent together and the adventures we have been on and am excited to see where the future takes us.

CURRICULUM VITAE OF COLTON ALLEN D'AMBRA

March 2024

Education

2018 – 2024 University of California, Santa Barbara
Doctor of Philosophy in Department of Materials

2014 – 2018 University of Texas, Austin
Bachelor of Science in Chemical Engineering
Bachelor of Science and Arts in Chemistry

Professional Employment

2018 – Present, Graduate Student Researcher, University of California, Santa Barbara
Advisors: Professor Christopher Bates and Professor Craig Hawker
- Developed synthetic platform for the synthesis of siloxane-containing graft copolymers
- Investigated structure-property relationships of dynamic silicone networks
- Coordinated team of graduate students in a University Partnership Initiative with Dow
- Selective deposition of polymeric thin films on patterned silicon substrates

2016 – 2018, Undergraduate Student Researcher and Mentor, University of Texas, Austin
Advisor: Professor Lauren DePue
- Synthesized Schiff-base ligands for novel lanthanide metal complexes
- Characterization of crystal structure and luminescent properties
- Trained new students in laboratory fundamentals
- Maintained good laboratory practices

2016 – 2017, Undergraduate Student Researcher, University of Texas, Austin
Advisor: Professor Benny Freeman
- Created polymer solutions and cast them into 20 μm thick membranes
- Tested mechanical and chemical properties of polymer membranes
- Designed and constructed systems to test properties of polymer membranes

2015 – 2017, Student Associate, Perry–Castañeda Library
Supervisor: Kenneth McFarland
- Retrieved and organized requested books in a timely and efficient manner
- Checked out books and answered general questions
- Helped patrons choose and find books

Publications

- **D'Ambra, C. A.**, Getty, P. T., Czuczola, M., Murphy E. A., Abdilla, A., Biswas, S., Mecca, J. M., Bekemeier, T. D., Swier, S., Hawker, C. J., Bates, C. M. Facile preparation of tunable polyborosiloxane networks via hydrosilylation. *Submitted.*
- **D'Ambra, C. A.**, Getty, P. T., Czuczola, M., Murphy E. A., Abdilla, A., Biswas, S., Mecca, J. M., Bekemeier, T. D., Swier, S., Hawker, C. J., Bates, C. M. Versatile synthesis

of siloxane-based graft copolymers with tunable grafting density. *J. Polym. Sci*. **2024**, 62, 1, 92–101.

- Abdilla, A., **D'Ambra, C. A.**, Geng, Z., Shin, J. J., Czuczola M., Goldfeld, D. J., Biswas, S., Mecca, J. M., Swier, S., Bekemeier, T. D., Laitar, D. S., Bates, M. W., Bates, C. M., Hawker, C. J. Silicone-based polymer blends: Enhancing properties through compatibilization. *J. Polym. Sci.* **2021**, 59, 19, 2114–2128.
- Scheuermann, A. M., Wakidi, H., Lill, A. T., Oh, S., Llanes, L. C., D'Ambra, C. A., Antoine, S., Wang M., Chabinyc, M. L., Nguyen, T. Q., Read de Alaniz, J., Bates, C. M. Multiwavelength Photodetectors Based on an Azobenzene Polymeric Ionic Liquid. *ACS Appl. Polym. Mater.* **2021**, 3, 10, 5125–5133.
- Moon, J. D.; Bridge, A. T.; **D'Ambra, C**.; Freeman, B. D.; Paul, D. R. Gas separation properties of polybenzimidazole/thermally-rearranged polymer blends. *J. Membrane Sci.* **2019**, 582, 182–193.
- Zhang, Y.; **D'Ambra, C**. A.; Katsumata, R.; Burns, R. L.; Somervell, M.; Segalman, R. A.; Hawker, C. J.; Bates, C. M. Rapid and Selective Deposition of Patterned Thin Films on Heterogeneous Substrates via Spin Coating. *ACS Appl. Mater. and Interfaces.* **2019**, 11, 21177–21183.
- Narang, G. S., Moon J. D., Zhang, W., Miller G. C., Choudhury, S. R., Shaver, A., Vondrasek, B., Lesko, J. J., Fallon, J. J., Bortner, M., **D'Ambra, C. D**., Freeman, B. D., Riffle J. S. *Polym.* **2018**, 138, 156-168.

Awards

May 2023, Heeger Travel Fellowship, UC Santa Barbara
August 2023, Heeger Travel Fellowship, UC Santa Barbara
September 2018, UCSB Graduate Division Fellowship, UC Santa Barbara

Fields of Study

Major Field: Materials Chemistry

Studies in Development of Novel Methods for the Synthesis of Polymeric Materials with Professors Christopher M. Bates and Craig J. Hawker

ABSTRACT

Development of Versatile Synthetic Methods for Silicone Materials

by

Colton Allen D'Ambra

Polymers containing a backbone of repeated Si–O bonds, referred to as siloxanes or silicones, are a ubiquitous class of materials due to their collection of unique properties. The exceptionally wide Si–O bond angle and high deformability of the backbone bonds results in a low glass transition temperature of –120 °C and a crystallization temperature below room temperature. Additionally, the high bond dissociation energy gives rise to decomposition temperatures above 300 °C and results in a chemically inert polymer. The combination of these features result in a massive temperature window while maintaining inert. With a market size of over $4 billion, polydimethylsiloxane (PDMS) is the most common siloxane and has been the subject of decades of research. These research and development efforts have led to the material being used in numerous environments ranging from cosmetics to aerospace.

The utility of PDMS arises from the sophisticated methods used to tune the polymer chemistry, which result in a range of properties appropriate for numerous different applications. Robust chemical reactions, like hydrosilylation, have led to an extremely broad scope of functional groups that can be synthetically bonded to the siloxane backbone. This same strategy has been used to attach polymers, polymerization initiators, or polymerizable moieties to the siloxane chain, leading to a broad scope of possible siloxane-based copolymer architectures. One architecture that is lacking in synthetic versatility, however, is graft copolymers with a siloxane backbone and polymeric grafts based on vinyl monomers. Chapter

2 of this dissertation outlines a methodology to synthesize graft copolymers with siloxane backbones using a combination of thiol–ene click chemistry and atom-transfer radical polymerization. Optimization of polymerization conditions enabled the synthesis of graft copolymers with a range of grafting densities and molecular weights > 5 MDa. Degradation of the siloxane backbone enabled characterization of the polymerized grafts, showcasing dispersities around 1.2 and molecular weights close to the targeted values.

In order to form a freestanding polymeric material, the siloxane must be crosslinked. The network architecture is an important parameter that can be manipulated to control the properties of the material. Additionally, novel functionality can be incorporated through the usage of a dynamic crosslinker. An example of such a material is Silly Putty, which is PDMS crosslinked through borosiloxane bonds. The method of synthesizing this material, however, has remained largely unchanged since the 1940s and remains a time and energy intensive process with limited tunabilty. In Chapter, 3 we demonstrate a novel methodology to synthesize polyborosiloxane networks using hydrosilylation in minutes. While the current state-of-the-art is limited to end-functionalized PDMS chains, our developed method gives access to backbone-functionalized PDMS starting materials, which drastically increases the degree of tunability over the final network properties.

In Chapter 4, we expand upon this method by synthesizing boronate esters containing varying functional groups to investigate the impact of the crosslinker chemical environment on the stress relaxation dynamics. We demonstrate an unprecedented level of control over the rate of stress relaxation for polyborosiloxane materials while maintaining a facile and robust crosslinking method.

The newly developed methodologies for graft copolymers and functional polymeric networks will enable future investigations into the properties of these materials and their incorporation into complex composite systems to expand upon the current availability of silicone materials.

TABLE OF CONTENTS

LIST OF FIGURES

Chapter 1. An Introduction to Silicones

1.1 A Brief History of Silicones

Polymers containing repeating Si–O bonds, commonly referred to as silicones or siloxanes, are a ubiquitous class of polymer with numerous uses academically and industrially. The widespread use of silicones started in the 1930s when Corning Glass commercialized a silicone fluid used in aircrafts.[1] Shortly after, the company commercialized a crosslinked silicone elastomer, leading to a rapid expansion of silicone technology. With an estimated market size of $4.5 billion in 2022, polydimethylsiloxane (PDMS) is by far the most commercially relevant siloxane.[2] Characteristic properties of PDMS includes flexibility, chemical resistance, thermal stability, hydrophobicity, and water vapor permeability, leading to applications including lubricants,[3–5] surfactants,[6,7] coatings,[8–11] medical implants,[12,13] household appliances,[14] cosmetics,[15] sealants,[16–18] flexible electronics,[19–21] electrical insulation,[22,23] and microfluidic devices.[24,25]

1.2 Origin of Anomalous Properties

The siloxane backbone has numerous distinguishing features compared to C–C and C–O bonds that give rise to unique properties. The key difference is the siloxane bond itself. The bond lengths of Si–O and Si–C (1.63 Å and 1.90 Å, respectively) are longer than C–O and C–C (1.426 Å and 1.53 Å, respectively).[26] Si–O–Si bonds have a wider bond angle than that of carbon-based bonds (143° compared to 110°) and a higher deformability, being able to stretch to form a 180° bond along the Si–O–Si path.[27,28] The combination of these features results in a highly flexible backbone that leads to an exceptionally low glass transition temperature (T_g)

for PDMS of –125 °C with a crystallization temperature of –50 °C. Furthermore, the Si–O bond is exceptionally strong with a bond dissociation energy of 450 kJ/mol, which is significantly higher than the value of 350 kJ/mol for C–C and C–O bonds. The higher bond dissociation energy results in exceptional thermal and chemical stability. Consequently, the combination of low T_g and high thermal stability results in a large temperature range that silicone materials can be used.[29]

1.3 Industrial Scale Synthesis of Siloxanes

Industrial scale synthesis of siloxane-based materials started in the 1940s with the establishment of the direct process by Eugene Rochow, depicted in Figure 1.1.[1] This method effectively turns sand into siloxane.[30] Elemental silicon is synthesized using SiO_2 and carbon in an arc furnace then crushed and packed into a fluidized bed reactor. With a host of metals being added as promoters, chloromethane is fed through the reactor, producing predominantly dichlorodimethylsilane. Subsequent hydrolysis produces an 8 membered ring consisting of 4 dimethylsiloxane units, commonly referred to as D_4. A ring opening polymerization can then be performed using D_4 and an end-capping siloxane dimer to produce a polymeric species.

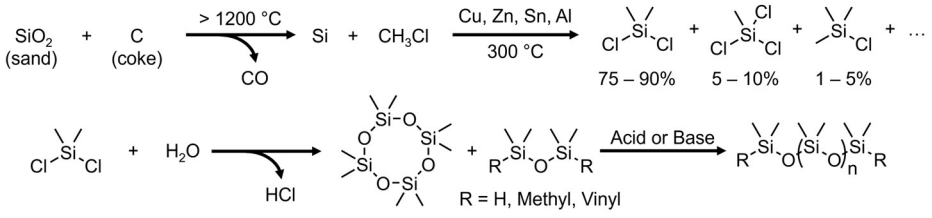

Figure 1.1. Rochow-Muller direct method to produce polymeric silicones industrially.

1.4 Tunability in Properties of Silicones

Controlled variations in properties for silicones can be achieved through several different methods including the incorporation of functional groups, the synthesis of PDMS-based copolymers, and the variation in network properties. These three complementary methods enable precise control over the chemical, physical, and mechanical properties of siloxane-based materials.

1.4.1 Functional Groups

While the most common siloxane, PDMS, contains methyl groups bonded to the silicon atoms, changes in this substituent can have drastic effects on the material properties. Since PDMS is chemically inert, functionalization of a methyl-terminated PDMS molecule is difficult. Figure 1.1 above introduces one method to incorporate a reactive handle onto a siloxane polymer: using a functionalized siloxane dimer as a chain-transfer agent leading to targeted functional groups on the chain-end of the polymer.[31] Additionally, the aforementioned direct method to synthesize PDMS enables copolymerization by using cyclic monomers analogous to D_4 to produce PDMS copolymers with the desired functional group, including phenyl, ethyl, vinyl, and hydride. Importantly, the PDMS chain undergoes rapid scrambling during the acid or base mediated polymerization, so despite being incorporated 4 repeat units at a time, these functional groups are randomly distributed throughout the polymer chain.[32,33] Addition of these comonomers have significant effects on the bulk and interfacial properties of the resulting siloxane material. For example, phenylmethylsiloxane repeat units can be incorporated to increase the viscosity, density, and index of refraction. The T_g also varies from –125 to –30 °C depending on the ratio of dimethylsiloxane to phenylmethylsiloxane monomers.[34]

Post-functionalization of siloxane copolymers is an additional strategy that enables the synthetic attachment of numerous functional groups.[35–37] The development of hydrosilylation has been one of the most enabling technologies in the silicone industry. First reported in 1947 by Leo Sommer,[38] hydrosilylation is an addition reaction between an alkene and a hydridosilane. Development of the highly efficient Speier's catalyst in 1957 prompted significant interest academically and industrially. The reaction enabled the facile functionalization of siloxane polymers with an incredibly broad chemical scope. As an example, the addition of fluorinated groups imparts enhanced anti-wetting, anti-icing, and solvent resistance leading to many automotive and aerospace applications.[29]

1.4.2 Copolymers

The covalent attachment of two polymers is a sophisticated strategy to overcome their innate immiscibility to achieve properties inaccessible to the individual homopolymers. There are three predominant strategies used to synthesize complex macromolecular structures composed of PDMS and a separate polymer.[39] The first strategy involves using PDMS as a polymeric substrate for attaching a separate macromolecule. The starting polymers involved in this method must have complementary chemical functionalities that enable efficient coupling reactions such as azide–alkyne click, thiol–ene click, and hydrosilylation. Hundreds of manuscripts have been devoted to hydrophilic PDMS copolymers synthesized through hydrosilylation of alkene-terminated poly(ethylene glycol) with applications as surface modifiers,[40–44] surfactants,[45,46] and in gas separation membranes.[47]

Advancements in organic chemistry and polymerization techniques have enabled the synthesis of polymers directly from siloxanes with near limitless control over the monomer scope and resulting polymer architecture. Both uncontrolled and controlled radical

polymerization methods have been used to synthesize copolymers from vinyl monomers, and an excellent review from the Boutevin group in 2010 captured the breadth of techniques used to make these materials and their properties.[48] In addition to radical polymerization methods, ring-opening polymerization techniques have been performed starting from PDMS macroinitiators to synthesize block copolymers with polyesters and polypeptides.[49–51]

Functionalization of PDMS with a polymerizable end-group enables PDMS to act as a macromonomer to generate branched structures. Control over the degree of branching has significant effects on the rheological properties of the final material, so precise control over this feature is of utmost importance for tuning the material properties.[52] Copolymerization of vinyl monomers with PDMS macromonomers has been successfully demonstrated to achieve good control over the composition of the resulting graft copolymer, achieving tunability in grafting density with comonomers of ethylene,[53] styrene,[54] vinyl alcohol,[55] acrylates,[56] and methacrylates.[57]

Despite the numerous methods to synthesize PDMS-based block copolymers, one architecture that is severely lacking in synthetic versatility is graft copolymers with a PDMS backbone. While a few methods exist showcasing the synthesis of such polymers, the methods lack the ability to achieve high molecular weight grafts and high grafting densities. The three strategies described above are limited in the scope of synthesizable graft copolymers. Methods to attach polymers to a PDMS backbone struggle to reach high conversion at high grafting density due to steric hindrance. Additionally, polymerizing vinyl monomers using PDMS as a macroinitiator through radical polymerization methods is similarly limited. Radical coupling of propagating polymer chains is a difficult termination event to avoid, and the high number of polymer chains per backbone leads to gelation at a low degree of bimolecular termination.

Optimization of polymerization conditions to synthesize graft copolymers with very little bimolecular termination is necessary to impart versatility in the synthesis of such polymers.

1.4.3 **Network Parameters**

To prepare a freestanding silicone material, it must first be crosslinked. The two most common methods of crosslinking silicones industrially are hydrosilylation and condensation, though the number of methods reported academically is constantly increasing.[58–62] Changes in the silicone network architecture have dramatic consequences on the resulting material properties, and control over this network architecture is critical for developing a material formulation appropriate for a particular application.[63] Numerous interdependent parameters affect the properties of the final material including crosslink density, molecular weight between crosslinks, crosslinker functionality, stoichiometric ratio between complementary reactive functional groups, and network defects.[64–66]

Novel properties can also be introduced to silicone networks through functional crosslinkers. Incorporation of dynamic motifs into a crosslinked network imparts self-healing and reprocessablity.[67,68] One dynamic motif of particular importance for this dissertation is the exchange of borosiloxane bonds. Networks crosslinked with such bonds can experience rapid self-healing due to the exchange of B–O–Si bonds across an interface. This dynamic motif experiences numerous other modes of bond exchange in addition to the exchange of covalent bonds that give rise to novel frequency dependent properties where the material is viscous at low frequencies and is elastic at high frequencies. An excellent representation of a material with such a dynamic motif is Silly Putty. While the material started as a children's toy, numerous manuscripts have reported the incorporation of polyborosiloxanes into composite

systems to develop self-healing double networks,[69] remarkably sensitive pressure sensors,[70] and impact-resistant thermoplastic elastomers.[71]

Despite being initially developed in the 1940's, the synthesis of polyborosiloxane networks has remained largely unchanged and remains a time consuming and energy intensive process.[72,73] Such networks are formed through the condensation of boric acid with hydroxy-terminated PDMS, forming water as a byproduct, which must then be removed to prevent hydrolysis. A robust method to rapidly form polyborosiloxane networks at moderate temperatures would be a significant development that would greatly benefit the field.

1.5 Outline of Dissertation

Chapter 2 develops a methodology to synthesize graft copolymers with a PDMS backbone using a combination of two robust and versatile reactions: thiol–ene click and atom-transfer radical polymerization. Quantitative functionalization of commercially available, vinyl-functionalized PDMS precursors with a tertiary bromide ATRP initiator was achieved for PDMS backbones containing 1 – 50 mol% vinyl-containing comonomers. Optimization of polymerization conditions to reduce bimolecular termination events enabled the synthesis of PDMS graft copolymers with high grafting density and molecular weights over 5 MDa. Subsequent degradation of the PDMS backbone with tetrabutylammonium fluoride enabled the isolation and characterization of the synthesized grafts, showcasing dispersity values around 1.2 and measured molecular weights similar to the target value. The developed synthetic platform will enable important future studies to investigate the influence of the flexible PDMS backbone on the rheological properties of the resulting graft copolymer. Additionally, the technique is applicable to other polymeric backbones and showcases the

ability to suppress gelation during the synthesis of graft copolymers with high grafting densities and targetable molecular weights through controlled radical polymerization methods.

Chapter 3 establishes a novel synthetic protocol to synthesize polyborosiloxane networks through hydrosilylation. The strategy takes advantage of a commercially available crosslinker that contains vinyldimethylsiloxane moieties covalently bonded to a boron core. The borosiloxane-containing crosslinker enables network formation in 10 minutes at 90 °C, which is a remarkable improvement over condensation methods that take hours to days to fully crosslink. Step-strain rheological experiments capture the stress relaxation behavior of the network and confirmed that the materials closely reproduce the properties of previously reported polyborosiloxane materials. The versatility of hydrosilylation enables network formation through backbone-functionalized PDMS, whereas condensation is limited to end-functionalized PDMS. Importantly, a decrease in sample-to-sample variation was observed for networks prepared with backbone-functionalized PDMS. A combination of static and dynamic crosslinkers was used to demonstrate control over the timescale of stress relaxation and imparted resistance to solvents. This synthetic procedure will enable the development of new polyborosiloxane-based crosslinked networks with unprecedented control over the properties and increased reproducibility while drastically reducing the time required to prepare the materials.

Chapter 4 extends on the work in Chapter 3 by synthesizing novel borosiloxane crosslinkers based on boronic acids to increase the control over the rate of stress relaxation. Boronate ester crosslinkers with aliphatic and aromatic substituents were synthesized through the esterification of the appropriate boronic acid with dimethylvinylchlorosilane. Subsequent characterization of the crosslinkers confirmed the successful synthesis and purification of the

crosslinkers. Preliminary results showcase significantly increased tunability in the rate of stress relaxation depending on the functionality of the boronate ester crosslinker.

1.6 References

(1) Rochow, E. G.; Gilliam, W. F. Polymeric Methyl Silicon Oxides. *J Am Chem Soc* **1941**, *63* (3), 798–800.

(2) *Global Polydimethylsiloxane (PDMS) Industry*; 2024. https://www.reportlinker.com/p06032564/Global-Polydimethylsiloxane-PDMS-Industry.html?utm_source=GNW (accessed 2024-02-04).

(3) Wang, Y.; Zhang, L.; Liu, A.; Wu, C.; Li, W. Tribological Performance of Silicone Oil Based Al2O3 Nano Lubricant for an Mg Alloy Subjected to Sliding at Elevated Temperatures. *Tribol Int* **2022**, *175*.

(4) Brown, E. D. Methyl Alkyl Silicones. A New Class of Lubricants. *A S L E Transactions* **1966**, *9* (1), 31–35.

(5) Lonsky, P. Some Characteristics of Silicones Developed as Lubricants. *Journal of Synthetic Lubrication* **1985**, *1* (4), 302–313.

(6) Han, F.; Deng, Y. Y.; Zhou, Y. W.; Xu, B. C. Carbohydrate-Modified Silicone Surfactants. *J Surfactants Deterg* **2012**, *15* (2), 123–129.

(7) Zhu, S.; Miller, W. G.; Scriven, L. E.; Davis, H. T. Superspreading of Water-Silicone Surfactant on Hydrophobic Surfaces. *Colloids Surf A Physicochem Eng Asp* **1994**, *90*, 63–78.

(8) Li, G. J.; Wei, Y. Bin; Ren, R. M. Preparation of High-Temperature-Resistance Silicone Paints. *Adv Mat Res* **2012**, *602–604*, 1676–1679.

(9) Hinder, S. J.; Lowe, C.; Maxted, J. T.; Watts, J. F. Migration and Segregation Phenomena of a Silicone Additive in a Multilayer Organic Coating. *Prog Org Coat* **2005**, *54* (2), 104–112.

(10) Bubat, A.; Scholz, W. Silicone Additives for Paints and Coatings. *Chimia* **2002**, *56* (5), 203.

(11) Hu, P.; Xie, Q.; Ma, C.; Zhang, G. Silicone-Based Fouling-Release Coatings for Marine Antifouling. *Langmuir* **2020**, *36* (9), 2170–2183.

(12) Son, J.; Kim, C. S.; Yang, J. Comparison of Experimental Porous Silicone Implants and Porous Silicone Implants. *Graefe's Archive for Clinical and Experimental Ophthalmology* **2012**, *250* (6), 879–885.

(13) Chao, A. H.; Garza, R.; Povoski, S. P. A Review of the Use of Silicone Implants in Breast Surgery. *Expert Rev Med Devices* **2016**, *13* (2), 143–156.

(14) Wang, D.; Klein, J.; Mejía, E. Catalytic Systems for the Cross-Linking of Organosilicon Polymers. *Chem Asian J* **2017**, *12* (11), 1180–1197.

(15) *Principles of Polymer Science and Technology in Cosmetics and Personal Care*; Goddard, E. D., Gruber, J. V., Eds.; 1999.

(16) Lu, Z.; Xu, L.; He, Y.; Zhou, J. One-Step Facile Route to Fabricate Functionalized Nano-Silica and Silicone Sealant Based Transparent Superhydrophobic Coating. *Thin Solid Films* **2019**, *692*, 137560.

(17) Storozhenko, P. A.; Minas'yan, R. M.; Polivanov, A. N.; Nikitushkin, I. V.; Minas'yan, O. I. New Thermally Conductive Silicone Adhesive Sealants. *Polymer Science, Series D* **2017**, *10* (3), 221–224.

(18) de Buyl, F. Silicone Sealants and Structural Adhesives. *Int J Adhes Adhes* **2001**, *21* (5), 411–422.

(19) Blackburn, S. C.; O'Sullivan, O. T.; Hinkens, D.; Tapsak, M. Synthesis of High Refractive Index Silicone Materials Incorporating Aromatic Moieties with Adjacent Linkage Groups for Flexible Electronic Displays. *Silicon* **2016**, *8* (4), 541–552.

(20) Kamino, B. A.; Bender, T. P. The Use of Siloxanes, Silsesquioxanes, and Silicones in Organic Semiconducting Materials. *Chem Soc Rev* **2013**, *42* (12), 5119.

(21) Zhang, X.; Li, N.; Wang, G.; Zhang, C.; Zhang, Y.; Zeng, F.; Liu, H.; Yi, G.; Wang, Z. Research Status of Polysiloxane-Based Piezoresistive Flexible Human Electronic Sensors. *RSC Adv* **2023**, *13* (24), 16693–16711.

(22) Ansorge, S.; Schmuck, F.; Papailiou, K. Impact of Different Fillers and Filler Treatments on the Erosion Suppression Mechanism of Silicone Rubber for Use as Outdoor Insulation Material. *IEEE Transactions on Dielectrics and Electrical Insulation* **2015**, *22* (2), 979–988.

(23) Chen, W. J.; Zeng, X.; Lai, X.; Li, H.; Fang, W. Z.; Hou, F. Suppression Effect and Mechanism of Platinum and Nitrogen-Containing Silane on the Tracking and Erosion of Silicone Rubber for High-Voltage Insulation. *ACS Appl Mater Interfaces* **2016**, *8* (32), 21039–21045.

(24) McDonald, J. C.; Duffy, D. C.; Anderson, J. R.; Chiu, D. T.; Wu, H.; Schueller, O. J. A.; Whitesides, G. M. Fabrication of Microfluidic Systems in Poly(Dimethylsiloxane). *Electrophoresis* **2000**, *21* (1), 27–40.

(25) Niculescu, A.-G.; Chircov, C.; Bîrcă, A. C.; Grumezescu, A. M. Fabrication and Applications of Microfluidic Devices: A Review. *Int J Mol Sci* **2021**, *22* (4), 2011.

(26) Krumpfer, J. W.; McCarthy, T. J. Rediscovering Silicones: “Unreactive” Silicones React with Inorganic Surfaces. *Langmuir* **2011**, *27* (18), 11514–11519.

(27) Mark, J. E. Some Interesting Things about Polysiloxanes. *Acc Chem Res* **2004**, *37* (12), 946–953.

(28) Mark, J. E. Overview of Siloxane Polymers. In *Silicones and Silicone-Modified Materials*; Clarson, S. J., Fitzgerald, J. J., Owen, M. J., Smith, S. D., Eds.; American Chemical Society: Washington D.C., 2000.

(29) Liu, J.; Yao, Y.; Li, X.; Zhang, Z. Fabrication of Advanced Polydimethylsiloxane-Based Functional Materials: Bulk Modifications and Surface Functionalizations. *Chemical Engineering Journal* **2021**, *408*, 127262.

(30) Lewis, L. N. From Sand to Silicones: An Overview of the Chemistry of Silicones. In *Silicones and Silicone-Modified Materials*; Clarson, S. J., Fitzgerald John J., Owen, M. J., Smith, S. D., Eds.; American Chemical Society: Washington D.C., 2000.

(31) Pang, Y.; Koh, J. J.; Li, Z.; He, C. Reactive Functionally Terminated Polyorganosiloxanes. In *Silicon Containing Hybrid Copolymers*; Wiley, 2020; pp 23–61.

(32) Zheng, P.; McCarthy, T. J. A Surprise from 1954: Siloxane Equilibration Is a Simple, Robust, and Obvious Polymer Self-Healing Mechanism. *J Am Chem Soc* **2012**, *134* (4), 2024–2027.

(33) Kantor, S. W.; Grubb, W. T.; Osthoff, R. C. The Mechanism of the Acid- and Base-Catalyzed Equilibration of Siloxanes. *J Am Chem Soc* **1954**, *76* (20), 5190–5197.

(34) Yilgör, E.; Yilgör, I. Silicone Containing Copolymers: Synthesis, Properties and Applications. *Progress in Polymer Science*. Elsevier Ltd 2014, pp 1165–1195.

(35) Marciniec, B. Functionalisation and Cross-Linking of Organosilicon Polymers. In *Hydrosilylation*; Marciniec, B., Ed.; Springer Netherlands: Dordrecht, 2009; pp 159–189.

(36) Sample, C. S.; Lee, S.-H.; Bates, M. W.; Ren, J. M.; Lawrence, J.; Lensch, V.; Gerbec, J. A.; Bates, C. M.; Li, S.; Hawker, C. J. Metal-Free Synthesis of Poly(Silyl Ether)s under Ambient Conditions. *Macromolecules* **2019**, *52* (5), 1993–1999.

(37) Brook, M. A. New Control Over Silicone Synthesis Using SiH Chemistry: The Piers–Rubinsztajn Reaction. *Chemistry – A European Journal* **2018**, *24* (34), 8458–8469.

(38) Sommer, L. H.; Pietrusza, E. W.; Whitmore, F. C. PEROXIDE-CATALYZED ADDITION OF TRICHLOROSILANE TO 1-OCTENE. *J Am Chem Soc* **1947**, *69* (1), 188–188.

(39) Zaman, Q.; Zia, K. M.; Zuber, M.; Mabkhot, Y. N.; Almalki, F.; Hadda, T. Ben. A Comprehensive Review on Synthesis, Characterization, and Applications of Polydimethylsiloxane and Copolymers. *International Journal of Plastics Technology* **2019**, *23* (2), 261–282.

(40) Yao, M.; Fang, J. Hydrophilic PEO-PDMS for Microfluidic Applications. *Journal of Micromechanics and Microengineering* **2012**, *22* (2), 025012.

(41) Hartmann, S.; Elsaesser, M. S.; Hüsing, N. Polysiloxane-Based Block Copolymers as Structure-Directing Agents in the Synthesis of Hierarchically Organized Silica Monoliths. *Z Anorg Allg Chem* **2014**, *640* (3–4), 641–648.

(42) Wong, I.; Ho, C.-M. Surface Molecular Property Modifications for Poly(Dimethylsiloxane) (PDMS) Based Microfluidic Devices. *Microfluid Nanofluidics* **2009**, *7* (3), 291.

(43) Gökaltun, A.; Kang, Y. B.; Yarmush, M. L.; Usta, O. B.; Asatekin, A. Simple Surface Modification of Poly(Dimethylsiloxane) via Surface Segregating Smart Polymers for Biomicrofluidics. *Sci Rep* **2019**, *9* (1), 7377.

(44) Trantidou, T.; Elani, Y.; Parsons, E.; Ces, O. Hydrophilic Surface Modification of PDMS for Droplet Microfluidics Using a Simple, Quick, and Robust Method via PVA Deposition. *Microsyst Nanoeng* **2017**, *3* (1), 16091.

(45) Yang, J.; Wegner, G.; Koningsveld, R. Phase Behavior of Ethylene Oxide-Dimethylsiloxane PEO-PDMS-PEO Triblock Copolymers with Water. *Colloid Polym Sci* **1992**, *270* (11), 1080–1084.

(46) Kunieda, H.; Uddin, Md. H.; Horii, M.; Furukawa, H.; Harashima, A. Effect of Hydrophilic- and Hydrophobic-Chain Lengths on the Phase Behavior of A−B-Type Silicone Surfactants in Water. *J Phys Chem B* **2001**, *105* (23), 5419–5426.

(47) Reijerkerk, S. R.; Knoef, M. H.; Nijmeijer, K.; Wessling, M. Poly(Ethylene Glycol) and Poly(Dimethyl Siloxane): Combining Their Advantages into Efficient CO2 Gas Separation Membranes. *J Memb Sci* **2010**, *352* (1–2), 126–135.

(48) Pouget, E.; Tonnar, J.; Lucas, P.; Lacroix-Desmazes, P.; Ganachaud, F.; Boutevin, B. Well-Architectured Poly(Dimethylsiloxane)-Containing Copolymers Obtained by Radical Chemistry. *Chem Rev* **2010**, *110* (3), 1233–1277.

(49) Lee, W. K. Synthesis of Polyester/Poly(Dimethylsiloxane)/Polyester Triblock Copolymers and Their Rearrangement under Water: Rearrangement of PDMS-Containing Copolymers. *Compos Interfaces* **2006**, *13* (2–3), 159–171.

(50) Johnson, J. C.; Korley, L. T. J.; Tsige, M. Coarse-Grained Modeling of Peptidic/PDMS Triblock Morphology. *J Phys Chem B* **2014**, *118* (47), 13718–13728.

(51) Papadopoulos, P.; Floudas, G.; Schnell, I.; Lieberwirth, I.; Nguyen, T. Q.; Klok, H.-A. Thermodynamic Confinement and α-Helix Persistence Length in Poly(γ-Benzyl-l-Glutamate)-b-Poly(Dimethyl Siloxane)-b-Poly(γ-Benzyl-l-Glutamate) Triblock Copolymers. *Biomacromolecules* **2006**, *7* (2), 618–626.

(52) Haugan, I. N.; Maher, M. J.; Chang, A. B.; Lin, T. P.; Grubbs, R. H.; Hillmyer, M. A.; Bates, F. S. Consequences of Grafting Density on the Linear Viscoelastic Behavior of Graft Polymers. *ACS Macro Lett* **2018**, *7* (5), 525–530.

(53) Tian, B.; Zhang, X.; Fan, H. Synthesis of Polyethylene-g-Polydimethylsiloxane Graft Copolymers by Copolymerization of Ethylene with Polydimethylsiloxane Macromonomer. *Eur Polym J* **2019**, *118*, 578–585.

(54) Wu, N.; Huang, L.; Zheng, A.; Xiao, H. Surface Properties of Block and Graft Polystyrene–Polydimethylsiloxane Copolymers. *J Appl Polym Sci* **2006**, *99* (6), 2936–2942.

(55) Tezuka, Y.; Fukushima, A.; Matsui, S.; Imai, K. Surface Studies on Poly(Vinyl Alcohol)—Poly(Dimethylsiloxane) Graft Copolymers. *J Colloid Interface Sci* **1986**, *114* (1), 16–25.

(56) Jin, L.; Tian, J.; Li, J.; Yan, X.; Qi, D. Investigation of the Water Barrier Properties of Graft Copolymer Latex Films of Acrylate and Poly(Dimethylsiloxane) Macromonomers Synthesized by RAFT Miniemulsion Polymerization. *Eur Polym J* **2022**, *168*, 111107.

(57) Shinoda, H.; Miller, P. J.; Matyjaszewski, K. Improving the Structural Control of Graft Copolymers by Combining ATRP with the Macromonomer Method. *Macromolecules* **2001**, *34* (10), 3186–3194.

(58) Mukherjee, S.; Xie, R.; Reynolds, V. G.; Uchiyama, T.; Levi, A. E.; Valois, E.; Wang, H.; Chabinyc, M. L.; Bates, C. M. Universal Approach to Photo-Crosslink Bottlebrush Polymers. *Macromolecules* **2020**, *53* (3), 1090–1097.

(59) Choi, C.; Self, J. L.; Okayama, Y.; Levi, A. E.; Gerst, M.; Speros, J. C.; Hawker, C. J.; Read de Alaniz, J.; Bates, C. M. Light-Mediated Synthesis and Reprocessing of Dynamic Bottlebrush Elastomers under Ambient Conditions. *J Am Chem Soc* **2021**, *143* (26), 9866–9871.

(60) Ye, J.; Jin, H.; Zu, Z.; Yu, B.; Xiang, H.; Zhang, M. Dynamic Crosslinked Silicones and Their Composites: A Review. *Engineered Science* **2023**.

(61) Li, S.; Zhang, J.; He, J.; Liu, W.; Wang, Y.; Huang, Z.; Pang, H.; Chen, Y. Functional PDMS Elastomers: Bulk Composites, Surface Engineering, and Precision Fabrication. *Advanced Science* **2023**, *10* (34).

(62) Hu, P.; Madsen, J.; Skov, A. L. One Reaction to Make Highly Stretchable or Extremely Soft Silicone Elastomers from Easily Available Materials. *Nat Commun* **2022**, *13* (1), 370.

(63) Mazurek, P.; Vudayagiri, S.; Skov, A. L. How to Tailor Flexible Silicone Elastomers with Mechanical Integrity: A Tutorial Review. *Chem Soc Rev* **2019**, *48* (6), 1448–1464.

(64) Beech, H. K.; Lin, T.-S.; Mochigase, H.; Olsen, B. D. Kinetic Model for Off-Stoichiometric Cross-Linking Reactions of End-Linked Polymer Networks. *Macromolecules* **2023**, *56* (23), 9410–9418.

(65) Rebello, N. J.; Beech, H. K.; Olsen, B. D. Adding the Effect of Topological Defects to the Flory–Rehner and Bray–Merrill Swelling Theories. *ACS Macro Lett* **2021**, *10* (5), 531–537.

(66) Danielsen, S. P. O.; Beech, H. K.; Wang, S.; El-Zaatari, B. M.; Wang, X.; Sapir, L.; Ouchi, T.; Wang, Z.; Johnson, P. N.; Hu, Y.; Lundberg, D. J.; Stoychev, G.; Craig, S. L.; Johnson, J. A.; Kalow, J. A.; Olsen, B. D.; Rubinstein, M. Molecular Characterization of Polymer Networks. *Chem Rev* **2021**, *121* (8), 5042–5092.

(67) Ye, J.; Jin, H.; Zu, Z.; Yu, B.; Xiang, H.; Zhang, M. Dynamic Crosslinked Silicones and Their Composites: A Review. *Engineered Science* **2023**.

(68) Deriabin, K. V.; Filippova, S. S.; Islamova, R. M. Self-Healing Silicone Materials: Looking Back and Moving Forward. *Biomimetics* **2023**, *8* (3), 286.

(69) Chen, C.; Fei, H.-F.; Watkins, J. J.; Crosby, A. J. Soft Double-Network Polydimethylsiloxane: Fast Healing of Fracture Toughness. *J Mater Chem A Mater* **2022**, *10* (21), 11667–11675.

(70) Boland, C. S.; Khan, U.; Ryan, G.; Barwich, S.; Charifou, R.; Harvey, A.; Backes, C.; Li, Z.; Ferreira, M. S.; Möbius, M. E.; Young, R. J.; Coleman, J. N. Sensitive Electromechanical Sensors Using Viscoelastic Graphene-Polymer Nanocomposites. *Science (1979)* **2016**, *354* (6317), 1257–1260.

(71) Zhao, Z.; Liu, F.; Yang, X.; Zhang, D.; Luan, S.; Xu, D.; Shi, T. Structure and Impact Properties of a Thermoplastic Elastomer/Silly Putty Blend. *Polym Int* **2022**, *71* (3), 328–337.

(72) Liu, Z.; Picken, S. J.; Besseling, N. A. M. Polyborosiloxanes (PBSs), Synthetic Kinetics, and Characterization. *Macromolecules* **2014**, *47* (14), 4531–4537.

(73) McGregor, R. R.; Warrick, E. Treating Dimethyl Silicone Polymer with Boric Oxide, 1947.

Chapter 2. Versatile synthesis of siloxane-based graft copolymers with tunable grafting density[1]

2.1 Introduction

Graft copolymers are a useful class of advanced materials with properties that can be precisely tuned by modifying the backbone and side chains.[1–5] Numerous experimental and computational studies have yielded insights into how these design parameters influence material properties,[6–11] leading to applications in viscosity modification,[12,13] thermoplastic elastomers,[14–19] photonics,[20–22] pressure sensors,[23] 3D printing,[24,25] and polymer composites.[26–28]

The development of this diverse range of graft-copolymer-based materials has been enabled by controlled polymerization techniques along with grafting-to,[29–36] grafting-through,[37–40] or grafting-from[41–50] methodologies to attach the requisite side chains. The grafting-from method, in combination with atom-transfer radical polymerization (ATRP), is of particular interest due to the broad range of vinyl-based side chains that can be synthesized from a single initiator-functionalized backbone. Key to this versatility is the compatibility and stability of the ATRP process towards siloxanes.[51–55] The resulting graft copolymers with siloxane backbones are broadly desirable because of the unique properties imparted by flexible and thermally stable Si–O–Si bonds.[56–58]

Several research groups have reported the synthesis of graft copolymers with siloxane backbones using controlled radical polymerization.[59–61] However, these studies are limited to

[1] This chapter was originally published in *Journal of Polymer Science*. Reproduced with permission from *Journal of Polymer Science* 2024, 62, 1, 92-101. Copyright 2024, John Wiley and Sons.

low grafting densities and modest backbone molecular weights due to the prevalence of radical-coupling that leads to crosslinked gels.[62] Despite these limitations, researchers have developed unique applications for graft copolymers with siloxane backbones including water-repellant pigment dispersants and thermally stable liquid-crystalline polymers.[63,64] A more versatile synthetic platform that provides access to a diverse range of PDMS graft copolymers with high molecular weights and tunable grafting densities would therefore provide unique access to libraries of PDMS-based materials for structure–property relationship studies, bridging the gap between linear block copolymers and polymeric bottlebrushes.

Herein, we report the development of a versatile methodology for preparing PDMS-based graft copolymer libraries with tunable molecular weights and grafting densities (Figure 1). This strategy leverages robust thiol–ene click chemistry to quantitatively functionalize commercially available polydimethylsiloxane-*co*-polyvinylmethylsiloxane (PDMS-*co*-PVMS) with thiol-containing ATRP initiators. Subsequent chain growth of methyl methacrylate (MMA) and styrene (S) was performed using copper(I)-catalyzed ATRP, yielding graft copolymers with tunable molecular weights and grafting densities as evidenced by selective degradation experiments. Numerous polyacrylate grafts were prepared using copper(II)-catalyzed, UV-light-induced ATRP to demonstrate the broad applicability of this approach to a wide variety of graft copolymers and polymerization conditions. This synthetic strategy enables the preparation of high molecular weight materials (>1 MDa) with versatility further illustrated through the co-incorporation of thiol mixtures during PDMS backbone functionalization. In summary, the methodology described herein provides access to an expanded library of PDMS-based graft copolymers and highlights the potential to readily manipulate material properties like solid state fluorescence.

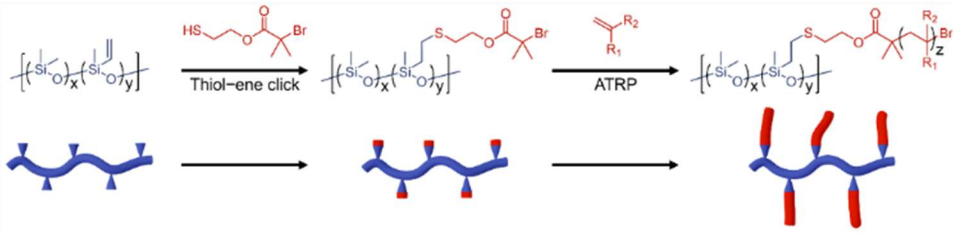

Figure 2.1. General synthetic strategy for preparing siloxane-based macroinitiators and corresponding graft copolymers.

2.2 Results and Discussion

In designing a versatile synthetic strategy, PDMS-*co*-PVMS copolymers were selected as starting materials given the wide range of molecular weights and levels of backbone functionalization that are commercially available. PVMS content was determined using ^{1}H NMR by comparing the integration values of the unique methyl resonances for dimethylsiloxane repeat units at $\delta = 0 - 0.3$ ppm to the integration values for the distinct vinyl protons from vinylmethylsiloxane at $\delta = 5.7 - 6.1$ ppm. For thiol–ene coupling, 2-mercaptoethyl α-bromoisobutyrate (HS–EBiB) was synthesized by acylation of bis(2-hydroxyethyl)disulfide followed by reduction of the disulfide to give the desired thiol group (Figures 2.9–2.13). Quantitative functionalization was achieved for PDMS-*co*-PVMS copolymers ranging from 17 to 225 kDa and a wide range of grafting densities (1 – 50 mol% PVMS incorporation, Figure 2.13). For the initial library of PMMA graft copolymers, polymeric side chains were grown from the siloxane backbone through copper(I) ATRP using CuBr as the catalyst and *N*,*N*,*N*′,*N*″,*N*″-pentamethyldiethylenetriamine (PMDETA) as ligand in chlorobenzene. This reaction sequence afforded a range of samples denoted PDMS$_x$-g_y-PMMA$_z$ where x refers to the PDMS backbone molecular weight (in Da), y represents the

number of grafts, and *z* corresponds to the average PMMA molecular weight per graft (in Da). Figure 2.2 demonstrates the successful synthesis of PDMS macroinitiator and subsequent MMA polymerization to produce $PDMS_{28k}$-g_{35}-$PMMA_{20k}$.

Because highly branched macromolecules like $PDMS_{28k}$-g_{35}-$PMMA_{20k}$ have a significantly smaller hydrodynamic radius compared to linear analogues, ^{1}H NMR spectroscopy proved to be more reliable than size-exclusion chromatography (conventional calibration) for estimating molecular weights. The introduction of PMMA-grafted arms was confirmed using ^{1}H NMR spectroscopy (Figure 2.2) with diagnostic resonance of the methyl ester protons on MMA observed at δ = 3.6 ppm. Furthermore, the H atoms corresponding to $-CH_2$ and $-CH_3$ units along the PMMA backbone are present at δ = 1.7 – 2.1 ppm and δ = 0.7 – 1.1 ppm, respectively (Figure 2.14). To calculate the total PMMA molecular weight, the ratio of ^{1}H NMR integration values for the methyl ester group from PMMA to the methyl groups along the siloxane backbone was calculated with the assumption that the molecular weight of the siloxane backbone remained constant. For the graft copolymer $PDMS_{28k}$-g_{35}-$PMMA_{20k}$, the ratio of MMA to DMS protons was 8.5:1 which leads to a total calculated molecular weight of ~700 kDa. The side-chain molecular weight was determined assuming equivalent reactivity of each ATRP initiating unit, resulting in an average 20 kDa per PMMA grafted arm.

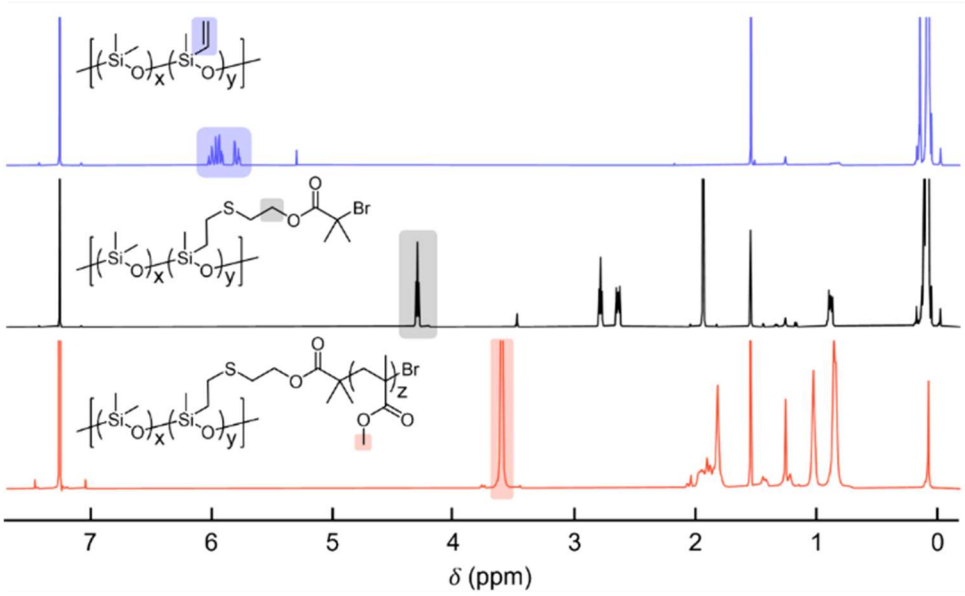

Figure 2.2. Representative ^{1}H NMR characterization of $PDMS_{28k}$-g_{35}-$PMMA_{20k}$ synthesized from PDMS-*co*-PVMS with diagnostic protons highlighted.

Size-exclusion-chromatography (SEC) with a differential refractive index (dRI) detector was used to investigate changes in nominal molecular weight and molar mass distribution upon functionalization of PDMS-*co*-PVMS with HS–EBiB and subsequent polymerization of MMA (Figure 2.3). After attaching the ATRP initiator, the peak shifts slightly to a higher elution time due to the addition of sterically bulky, polar substituents along the siloxane backbone that lead to a minor reduction in hydrodynamic volume. Upon polymerizing MMA, the SEC peak for the grafted product was observed at significantly lower retention time, confirming the successful grafting-from polymerization of MMA with minimal to no formation of linear chains (Figures 2.3 and 2.29 – 2.36).

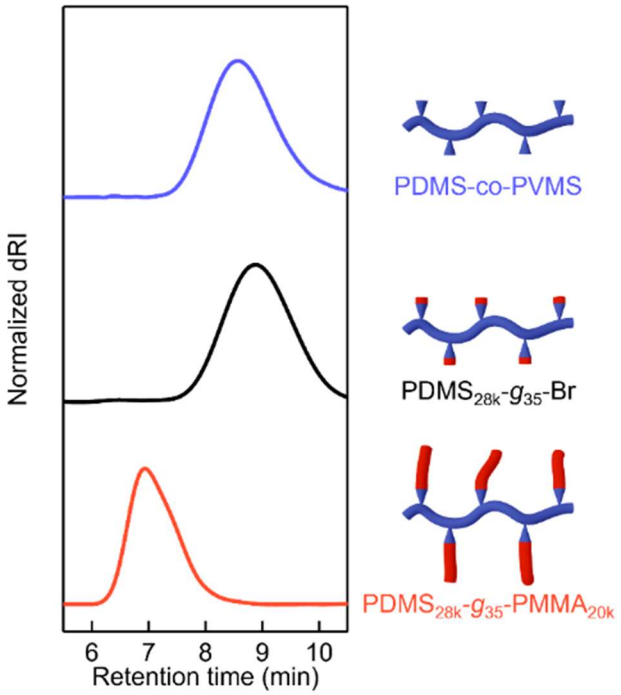

Figure 2.3. SEC traces of PDMS-*co*-PVMS (28 kDa, 35 vinyl units) starting polymer, macroinitiator $PDMS_{28k}$-g_{35}-Br, and graft copolymer $PDMS_{28k}$-g_{35}-$PMMA_{20k}$. The dRI signal for PDMS-*co*-PVMS and $PDMS_{28k}$-g_{35}-Br are inverted for better comparison.

Radical–radical coupling that leads to crosslinking is a known challenge in grafting-from strategies, frequently resulting in insoluble gels due to bimolecular termination of propagating polymer chains.[65] This is especially significant for graft copolymers with a high number of initiation sites along the backbone where even minimal radical–radical coupling can form a network. For example, conditions based off previous work were only successful for low molecular weight copolymers with up to 35 grafts,[66] and insoluble gels were obtained for samples having higher levels of backbone functionalization at conversions as low as 15%. To address this issue, polymerization conditions were optimized to minimize radical–radical coupling reactions at high grafting densities and molecular weights. Here, by lowering the

catalyst and monomer concentrations while increasing reaction temperature, higher conversions were achieved while avoiding gelation allowing for the synthesis of graft copolymers based on a wide variety of PDMS-*co*-PVMS starting polymers featuring both high molecular weights and degrees of backbone functionalization (Table 2.1).

To further demonstrate the synthetic versatility of this strategy, styrene and acrylic monomers were also polymerized from the $PDMS_{28k}$-g_{35}-Br macroinitiator. As expected for styrene polymerization at 110 °C, a minor amount of autopolymerization leads to a small peak in the SEC chromatogram that corresponds with polystyrene homopolymer (Figure 2.37). Acrylates are readily polymerized via photoinitiated ATRP using copper(II) bromide as catalyst and an aliphatic tertiary amine (Me_6Tren) ligand under 365 nm irradiation (Figure 2.14). These conditions efficiently polymerize numerous acrylates[67–69] with poly(methyl acrylate) (PMA), poly(oligoethyleneglycol acrylate) (POEGA), poly(isobornyl acrylate) (PiBA), and poly(tetrafluoroethyl acrylate) (PTFEA) successfully grown from the same PDMS macroinitiator, highlighting the ability to incorporate hydrophilic, hydrophobic, and fluorinated repeat units into PDMS-based graft copolymers (Figures 2.15 – 2.19). Notably, in contrast to MMA, acrylates can be polymerized to higher conversions ~70% without gelation, though the SEC traces showed increased homopolymerization (Figures 2.37 – 2.42).

Table 2.1. Summary of synthesized grafts copolymers.

Sample	Siloxane M_n(kDa)	Number of grafts[a]	Graft M_n[a] (kDa per graft)	Total M_n[a] (kDa)
$PDMS_{17k}$-$g_{2.3}$-$PMMA_{20k}$	17	2.3	20	63
$PDMS_{17k}$-$g_{2.3}$-$PMMA_{41k}$	17	2.3	41	112
$PDMS_{23k}$-$g_{3.3}$-$PMMA_{15k}$	23	3.3	15	73
$PDMS_{28k}$-g_{35}-$PMMA_{20k}$	28	35	20	690

$PDMS_{50k}$-g_{300}-$PMMA_{4k}$	50	300	4	1300
$PDMS_{50k}$-g_{300}-$PMMA_{14k}$	50	300	14	4000
$PDMS_{225k}$-g_{350}-$PMMA_{1k}$	225	350	1	680
$PDMS_{225k}$-g_{350}-$PMMA_{5k}$	225	350	5	2000
$PDMS_{225k}$-g_{350}-$PMMA_{17k}$	225	350	17	>5000
$PDMS_{225k}$-g_{350}-$PMMA_{68k}$	225	350	68	>5000
$PDMS_{28k}$-g_{35}-PS_{23k}	28	35	23	310
$PDMS_{28k}$-g_{35}-PMA_{17k}	28	35	17	600
$PDMS_{225k}$-g_{350}-PMA_{22k}	225	350	22	>5000
$PDMS_{225k}$-g_{350}-PMA_{65k}	225	350	65	>5000
$PDMS_{28k}$-g_{35}-$PiBA_{40k}$	28	35	40	1400
$PDMS_{28k}$-g_{35}-$PTFEA_{18k}$	28	35	18	630
$PDMS_{28k}$-g_{35}-$POEGA_{20k}$	28	35	20	720

[a] Calculated based on ^{1}H NMR.

After demonstrating the versatility of preparing grafted macromolecules from ATRP-functionalized PDMS backbones, thermal properties of the resulting copolymers were characterized via differential-scanning calorimetry (DSC) and thermal gravimetric analysis (TGA). In all cases, the DSC and TGA profiles were dominated by the vinyl grafts because they constitute most of the mass fraction for each material.[70–72] For example, the DSC trace of macroinitiator $PDMS_{28k}$-g_{35}-Br shows a sharp decrease in heat flow around –110 °C corresponding to the glass-transition temperature (T_g) of PDMS (Figure 2.43). Following grafting, each copolymer displayed a T_g value corresponding to that expected for a homopolymer of the side chain with values ranging from ~110 °C for PMMA to –70 °C for POEGA. Note that these materials conceivably could still contain a T_g corresponding to PDMS that is just much weaker, broader, and difficult to detect due to the high weight percent of

acrylate. Additionally, POEGA grafted systems exhibited a cold crystallization at –45 °C and a melting peak at –5 °C (Figure 2.44).

To verify the controlled nature of grafting-from polymerizations, graft copolymers were treated with tetrabutylammonium fluoride (TBAF) to selectively degrade the PDMS backbone. The resulting homopolymer side-chains were isolated by precipitation (for high molecular weights) or by washing with water for low-molecular-weight materials. Figure 2.4 highlights degradation results for $PDMS_{28k}$-g_{35}-$PMMA_{20k}$ which illustrate minimal chain–chain coupling during the ATRP process. The symmetrical SEC trace measured after degradation corresponds to a molecular weight of 24 kDa with a molar-mass dispersity of $Đ$ = 1.18 relative to poly(methyl methacrylate) standards. This compares favorably with the theoretical molecular weight of 20 kDa based on the original grafted copolymer and PDMS backbone. Likewise, most graft copolymers in this study contain side chains with actual molecular weights agreeing with theoretical values. Notably, these observations suggest that the bimodal character of some SEC traces after graft growth (e.g., Figures 2.29 – 2.30) originates from a confluence of dispersity in the number of arms per molecule and molar mass, not an uncontrolled graft polymerization process. Only at very high grafting density was deviation between the observed grafted and theoretical molecular weights detected, which may be due to incomplete initiation, although low dispersities were again observed (Figures 2.45 – 2.57). These selective degradation studies support the well-controlled nature of the graft polymerization process with minimal radical–radical coupling even at high molecular weights and grafting densities.

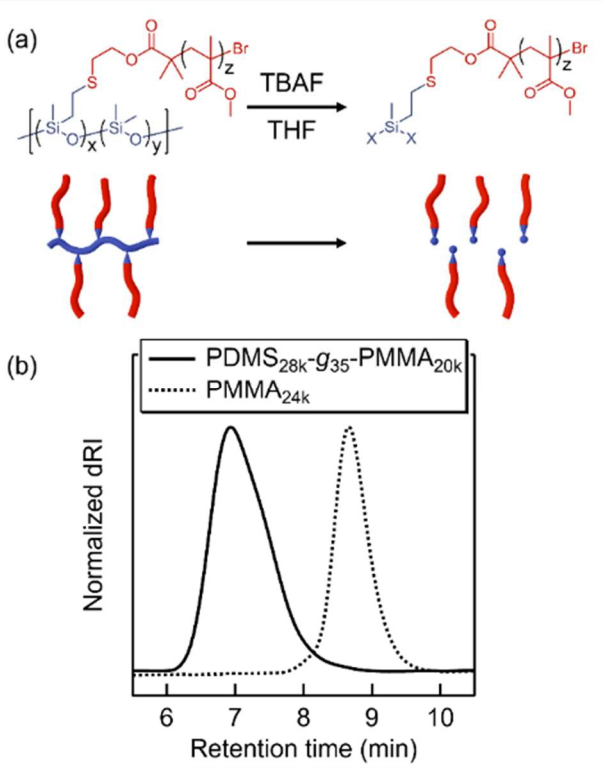

Figure 2.4. (a) Selective backbone degradation of PDMS-based graft copolymers with TBAF permits characterization of the side chains after grafting-from polymerization. (b) SEC traces corresponding to $PDMS_{28k}$-g_{35}-$PMMA_{20k}$ and recovered $PMMA_{24k}$ with a measured number-average molecular weight of 24 kDa (PMMA standards).

Table 2.2. Molecular weight and dispersity of isolated grafted side-chains following degradation of the PDMS backbone with TBAF.

Sample	Calculated side-chain M_n (kDa)[a]	Homopolymer M_n (kDa)[b]	$Đ$
$PDMS_{17k}$-$g_{2.3}$-$PMMA_{21k}$	21	33	1.31
$PDMS_{28k}$-g_{35}-$PMMA_{20k}$	20	24	1.18
$PDMS_{50k}$-g_{300}-$PMMA_{4k}$	4	4	1.30
$PDMS_{50k}$-g_{300}-$PMMA_{14k}$	14	26	1.32

$PDMS_{225k}$-g_{350}-$PMMA_{1k}$	1	3	1.31
$PDMS_{225k}$-g_{350}-$PMMA_{5k}$	5	8	1.39
$PDMS_{225k}$-g_{350}-$PMMA_{17k}$	17	21	1.17
$PDMS_{225k}$-g_{350}-$PMMA_{68k}$	68	67	1.36
$PDMS_{28k}$-g_{35}-PS_{23k}	23	25	1.20
$PDMS_{28k}$-g_{35}-PMA_{17k}	17	16	1.19
$PDMS_{225k}$-g_{350}-PMA_{22k}	22	20	1.15
$PDMS_{225k}$-g_{350}-PMA_{65k}	65	43	1.36
$PDMS_{28k}$-g_{35}-$PiBA_{40k}$	40	23	1.10

[a] Calculated based on ^{1}H NMR.
[b] SEC molecular weights compared to linear PMMA standards for PMMA and to linear PS samples for PS, PMA, and PiBA.

An advantage of this synthetic platform is the ability to introduce a mixture of functionalized and unfunctionalized thiols along the PDMS backbone. For example, grafting density was tuned by functionalizing a single parent PDMS-*co*-PVMS copolymer with mixtures of the thiol-functionalized ATRP initiator (HS–EBiB) and 1-dodecanethiol (DDSH) as a non-functional diluent. As illustrated in Figure 2.5, a library of materials with different grafting densities was achieved by changing the molar ratio of HS–EBiB to DDSH from 1:9 to 1:4 and 2:3 during the thiol–ene coupling step. In this case, the starting PDMS-*co*-PVMS copolymer had a molecular weight of 225 kDa with an average of 350 vinyl functional groups along the backbone.

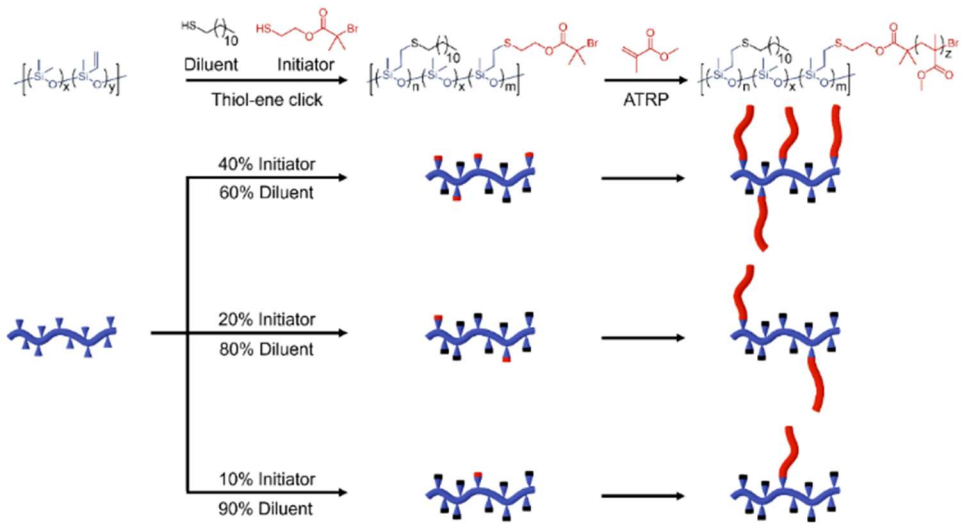

Figure 2.5. Synthesis of PDMS macroinitiator with a tunable number of ATRP initiation sites by varying the ratio of HS–EBiB to DDSH using the same starting PDMS-*co*-PVMS copolymer.

For this library of materials, the ratio of substituents along the backbone was determined by ^{1}H NMR spectroscopy (Figures 2.58 – 2.60) with the incorporation of functionalized and unfunctionalized thiols quantified by integrating the unique resonances at δ = 2.7 ppm and δ = 2.5 ppm corresponding to the two S–CH_2 units of the ATRP initiator fragment and the two S–CH_2 units of the dodecyl substituent, respectively (Figure 2.6). In all cases, the product composition corresponded closely with the feed ratio. Additionally, unique resonances at 4.3 ppm corresponding to the ATRP initiator are present and integrate to the expected values. By simply varying the relative ratio of EBiB and DDSH, three macroinitiators were synthesized from the same commercially available 225 kDa PDMS-*co*-PVMS polymer to produce macroinitiators with approximately 35, 80, and 140 ATRP initiation sites per chain (out of a possible 350 vinyl groups). As shown in Figure 2.61, the SEC traces of these macroinitiators exhibit a monotonic increase in retention time with increasing EBiB functionalization that is fully consistent with the shift described above for $PDMS_{28k}$-g_{35}-Br.

PMMA side chains with a target molecular weight of 20 kDa were grafted from each of the PDMS macroinitiators in this sequence using optimized ATRP conditions: 0.25:1 molar ratio of CuBr to PMDETA and a 4:1 volume ratio of chlorobenzene to monomer at 70 °C. After purification of the graft copolymers, ^{1}H NMR spectroscopy was used to determine overall copolymer composition with molecular weights measured to be ~3 MDa, 1.6 MDa, and 840 kDa based on 140, 80, and 35 grafted arms, respectively. As expected, the SEC traces in Figure 2.7a show a decrease in retention time as the number of grafts increases due to the increase in overall molecular weight. The siloxane backbone was then selectively degraded using TBAF with the isolated grafted arms being analyzed by SEC (Figure 2.7b). Significantly, the grafted arms from the three different starting copolymers were shown to have monomodal molecular weight distributions with low dispersities of ~1.2 and similar molecular weights based on PMMA standards (~20 kDa). The similarity in growth profiles for the grafting process illustrates the ability to tune molecular weight and grafting density with vinyl-based grafts based on a commercially available, high molecular weight PDMS starting polymer.

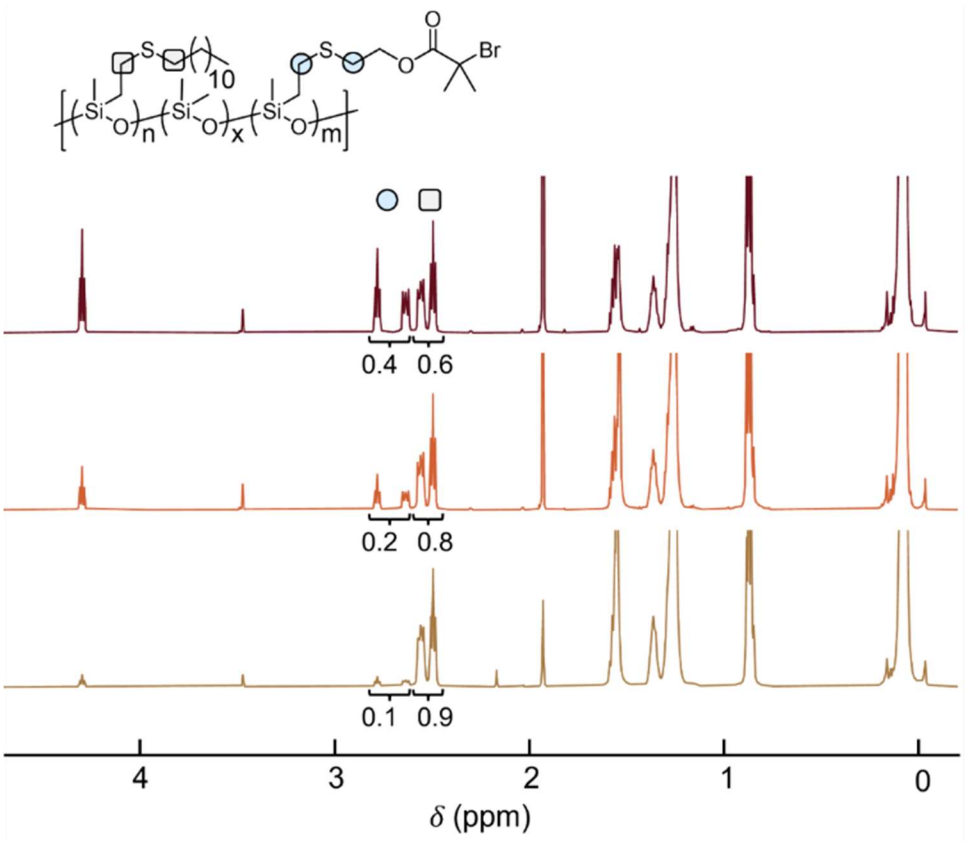

Figure 2.6. ^{1}H NMR spectra for PDMS macroinitiators with the thioether peaks of each substituent labeled and quantified to show the ratio of functional EBiB units to non-functional DDSH groups. The resulting macroinitiators have 140, 80, and 35 ATRP initiation groups along the backbone and were synthesized from the same starting materials by varying the ratio of thiols.

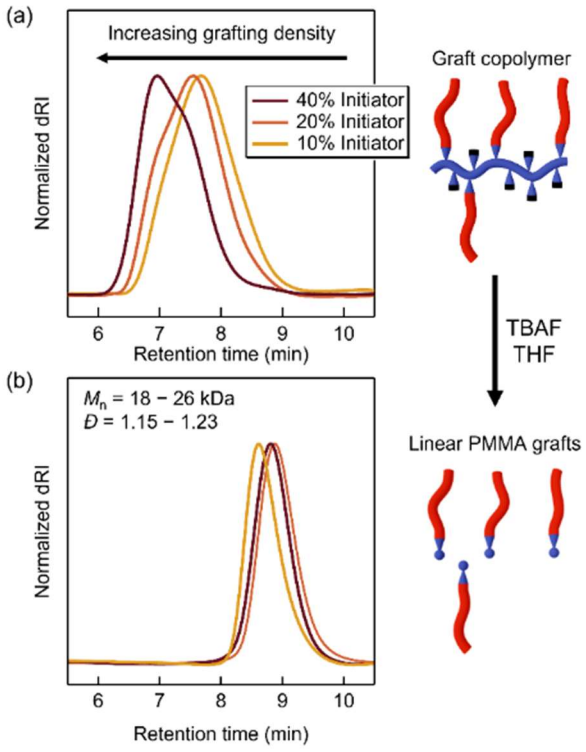

Figure 2.7. (a) SEC traces of graft copolymers with tunable grafting density and controlled molecular weights starting from the same commercially available vinyl siloxane. (b) Recovered linear PMMA grafts after selective degradation of the graft copolymer with TBAF.

To further highlight the ability to introduce different thiols, a mixture of EBiB and a thiol-containing fluorophore was attached to a PDMS backbone (Figure 2.8a). Due to the overlapping absorbance of 2,2-dimethoxy-2-phenylacetophenone (DMPA) and the fluorophore, the thiol–ene click reaction was performed under thermal conditions using azoisobutyronitrile (AIBN). A molar ratio of 95:5 HS–EBiB:7-mercapto-4-methylcoumain was employed during thiol–ene coupling with ^{1}H NMR spectroscopy again confirming the incorporation of 4-methylcoumarin units (Figure 2.65). In this system, unique resonances of the methylcoumarin unit were observed for the thioether peak (δ = 3.1 ppm) as well as the

methyl unit (δ = 2.3 ppm) and aromatic group (δ = 6.2, 7.1, and 7.4 ppm). Based on the integration of these resonances and those from EBIB, the molar incorporation of fluorophore was calculated to be 4%, which compares favorably with the 5% feed ratio (Figure 2.66). Further verification of fluorophore incorporation was obtained by SEC analysis using a combination of photodiode array (PDA) and dRI detection (Figure 2.67), illustrating the consistent level of chromophore incorporation across the molecular weight distribution of the PDMS backbone (Figure 2.68).

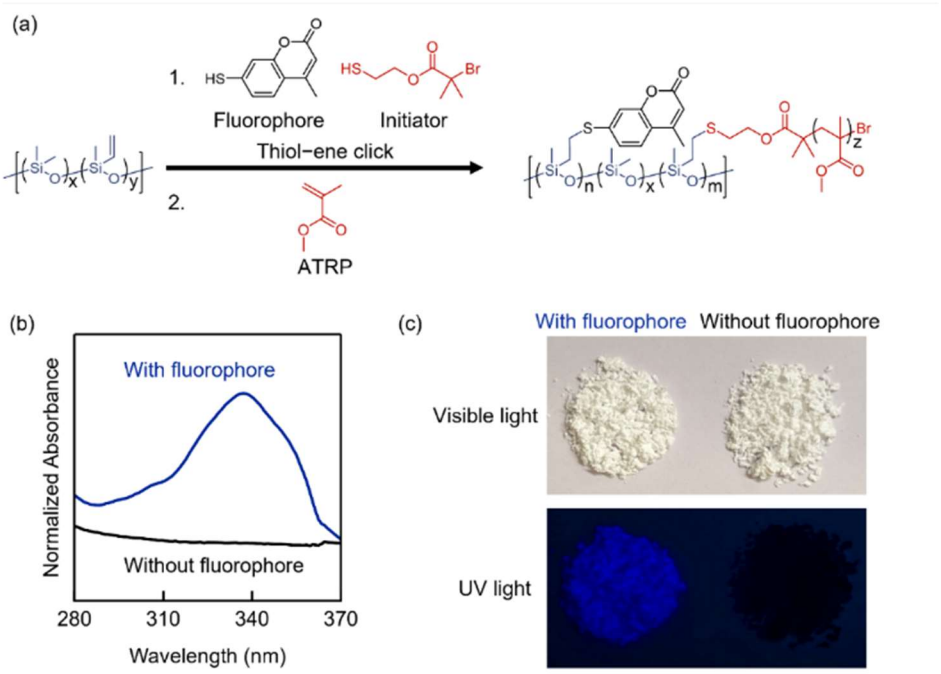

Figure 2.8. (a) Synthetic scheme for a graft copolymer with a siloxane backbone and an attached fluorophore with PMMA graft arms. (b) Light absorbance at 330 nm measured with an in-line PDA detector at the retention time corresponding to the peak dRI signal for a PDMS-*g*-PMMA copolymer with and without a fluorophore. (c) Images of graft copolymers with and without a covalently attached fluorophore under visible light (top) and 254 nm light (bottom).

Growth of PMMA chains from the coumarin functionalized PDMS backbone was accomplished using a ratio of 0.25:1 CuBr to ATRP initiator and a 4:1 volume ratio of solvent to monomer at 70 °C. By ^{1}H NMR analysis, the grafted copolymer was shown to have a total molecular weight of ~300 kDa with ~8 kDa PMMA grafted arms. Both PDA and dRI detectors attached to an SEC show a shift to lower retention time, corresponding to an increase in molecular weight (Figures 2.68 – 2.70). As expected, the graft PMMA-PDMS copolymer with covalently bound fluorescent coumarin along its backbone exhibits a strong absorbance at 330 nm while the corresponding graft copolymer with no fluorophore incorporation shows no absorbance (Figure 2.8b) and a significant difference in solid-state fluorescence (Figure 2.8c).

2.3 Conclusions

In summary, a tunable synthetic platform was presented for the preparation of high molecular weight PDMS-*g*-PMMA graft copolymers from commercially available PDMS-*co*-PVMS backbones. Numerous vinyl groups along the backbone were quantitatively functionalized with HS–EBiB using thiol–ene click chemistry followed by the polymerization of a wide range of vinyl monomers using ATRP. This allows grafted arms with good control over molecular weight and low dispersities to be prepared. Importantly, selective backbone degradation enabled the isolation and characterization of linear grafted arms, further highlighting the degree of control over the ATRP process and minimal radical–radical chain coupling even at high molecular weights and degrees of backbone functionalization. The versatility of this strategy was further exemplified using mixtures of thiols during the initial thiol–ene functionalization step. A combination of EBiB and dodecane thiol (DDSH) as a non-functional thiol allowed for accurate control over the number of ATRP initiation sites per siloxane backbone and resulting grafting density from a common starting PDMS derivative.

Alternatively, a mixture of EBiB and thiol-functionalized fluorophore was used for the synthesis of multifunctional graft copolymers exhibiting solid-state fluorescence due to labeling of the PDMS backbone. Based on commercially available starting materials, the versatility and scalability of this synthetic strategy will enable future studies on graft copolymer systems with vinyl side-chains and flexible siloxane-based backbones.

2.4 Materials and Methods

2.4.1 Materials

Methyl methacrylate (MMA, 99%, stabilized, Acros Organics), polystyrene (PS, 99%, stabilized, Acros Organics), methyl acrylate (MA, 99%, stabilized, Acros Organics), isobornyl acrylate (iBA, 99%, stabilized, Acros Organics), trifluoroethyl acrylate (TFEA, 99%, stabilized, TCI), oligoethyleneglycol acrylate (OEGA, M_n = 480 Da, 99%, stabilized, Acros Organics) were filtered through basic alumina to remove any inhibitor prior to use. Copper(I) bromide (CuBr, 98%, Sigma-Aldrich) was purified by washing in glacial acetic acid and rinsed with ethanol and diethyl ether then dried under vacuum prior to use. Azobisisobutyronitrile (AIBN, Sigma-Aldrich) was recrystallized from methanol, vacuum filtered, and dried under vacuum prior to use. N,N,N′,N″,N″-Pentamethyldiethylenetriamine (PMDETA, TCI), α-bromoisobuytryl bromide (BiBB, 98%, Sigma-Aldrich), 2-hydroxyethyl disulfide (technical grade, Sigma-Aldrich), 1-dodecanethiol (DDSH, 97%, Alfa Aesar), 7-mercapto-4-methylcoumarin (97%, Sigma-Aldrich) tris(2-carboxyethyl)phosphine hydrochloride (TCEP•HCl, Sigma-Aldrich), tetrabutylammonium fluoride solution (TBAF, 1 M in THF, Sigma-Aldrich), triethylamine (TEA, reagent grade, Fisher Scientific), chlorobenzene, methanol, dichloromethane (DCM), tetrahydrofuran (THF), ethanol, ethyl acetate, dimethyl sulfoxide (DMSO), and diethyl ether were used as received.

2.4.2 Characterization Methods

Size-exclusion chromatography (SEC) was performed on a Waters Alliance HPLC system using two Tosoh TSKgel SuperHZM-N columns containing 3 μm crosslinked polystyrene beads and a Waters 2410 Differential Refractometer with chloroform with 0.25% triethylamine as the mobile phase at a 0.35 mL/min flow rate. Number and weight average molecular weights (M_n and M_w respectively) were calculated based on polystyrene standards to calculate dispersity ($Đ$), unless otherwise specified. ^{1}H nuclear magnetic resonance (NMR) spectroscopy was performed on a Varian 600 MHz using a relaxation delay (d_1) of 4.8 seconds. ^{13}C NMR spectroscopy was performed on a Bruker 500 MHz with a d_1 of 10 seconds.

2.4.3 Synthetic Methods

Synthesis of bis[2-(2'-bromoisobutyryloxy)ethyl]disulfide following modified literature procedure[73]

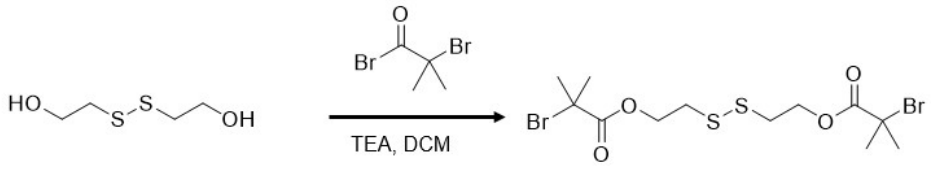

2-hydroxyethyl disulfide (3.8 g, 24.5 mmol, 1 eq) was dissolved into 30 mL DCM in a 100 mL round bottom flask with a stir bar. Triethylamine (6.95 g, 68.7 mmol, 2.8 eq) was added to the solution. The solution was placed into an ice water bath and allowed to cool. 20 mL DCM was mixed separately with BiBB (14.1 g, 61.3 mmol, 2.5 eq) and added dropwise via addition funnel (the addition funnel was capped with a rubber septum and pierced with a needle). The solution was kept at 0 °C until the BiBB was completely added and 30 minutes thereafter before removing the flask from the ice bath and allowing it to warm to room temperature while stirring overnight. The product was purified by gravity filtering off the salt

using a cotton ball placed in a funnel followed by a series of washes (50 mL of: water, 1 M HCl, saturated $NaHCO_3$, water, brine). The organic layer was dried with $MgSO_4$ and passed through a silica column with DCM as the mobile phase ($R_f = 0.9$). The solvent was removed *in vacuo* to recover a slightly yellow and hazy oil (6.45 g, 55% yield).

^{1}H NMR (600 MHz, $CDCl_3$): δ. 4.42 (t, J = 6.6 Hz, 4H), 2.96 (t, J = 6.6 Hz, 4H), 1.92 (s, 12H).

^{13}C NMR (126 MHz, $CDCl_3$): δ. 171.49, 63.54, 55.51, 36.77, 30.73.

Indexed NMR spectra are shown in Figure 2.9 and Figure 2.10.

Synthesis of mercaptoethyl α-bromoisobutyrate

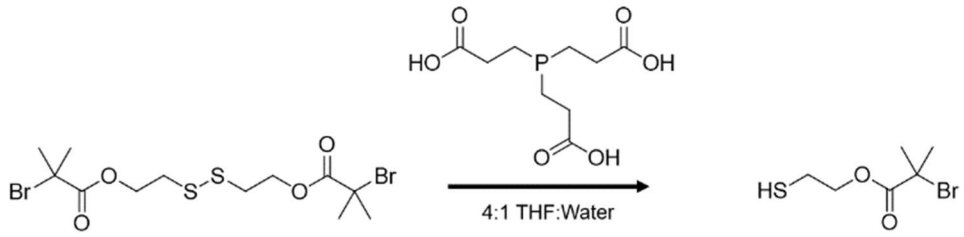

TCEP•HCl (2.4 g, 8.3 mmol, 1.5 eq) was dissolved in 70 mL of a 4:1 THF and water mixture in a 100 mL round bottom flask with a stir bar. Next bis[2-(2′-bromoisobutyryloxy)ethyl]disulfide (2.5 g, 5.5 mmol, 1 eq) was added and the solution was sealed with a rubber septum and left to stir overnight. The THF was removed *in vacuo*. 20 mL of DI water was added, and the product was washed 4 times with 50 mL of DCM to extract the product. The DCM layers were combined and dried with $MgSO_4$, and the solvent was removed under vacuum, resulting in a faintly yellow clear oil (2.2 grams, 82% yield).

^{1}H NMR (600 MHz, $CDCl_3$): δ. 4.30 (t, J = 6.5 Hz, 4H), 2.79 (t, J = 8.6 Hz, 4H), 1.94 (s, 12H), 1.57 (t, J = 8.6 1H).

^{13}C NMR (126 MHz, CDCl3): δ. 171.33, 67.00, 55.64, 30.72, 23.06.

Indexed NMR spectra are shown in Figure 2.11 and Figure 2.12.

General procedure for ATRP initiator functionalization of PDMS-co-PVMS

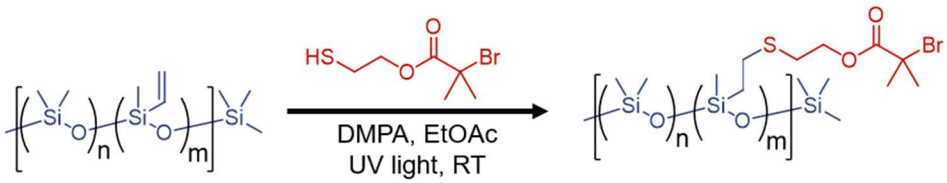

The siloxane (VDT-731, 0.5 g, 18 µmmol polymer, 0.63 mmol vinyl groups) was dissolved into 8 mL of ethyl acetate in a 20 mL vial charged with a stir bar. HS–EBiB (0.28 g, 1.25 mmol, 2 eq per vinyl) and DMPA (16 mg, 63 µmol, 0.1 eq per vinyl) were added. The solution was irradiated with 365 nm light for 2 hours, and then precipitated directly into 40 mL of room temperature methanol, centrifuged, and isolated, then dried under vacuum to recover a clear viscous oil (0.9 g, 70% yield).

^{1}H NMR (600 MHz, $CDCl_3$): δ. 4.30 (t, 2H), 2.57 (dd, 2H), 2.50 (dd, 2H), 1.93 (s, 6H), 0.9 (m, 2H), 0.05 – 0.12 (m, 63H).

Indexed NMR spectrum is shown in Figure 2.11.

General procedure for ATRP initiator and dodecane functionalization of PDMS-co-PVMS. Specific example corresponds to the synthesis of 10 mol% initiator and 90% diluent from VDT-954 (225 kDa, 10 mol% vinyl, 350 vinyl groups)

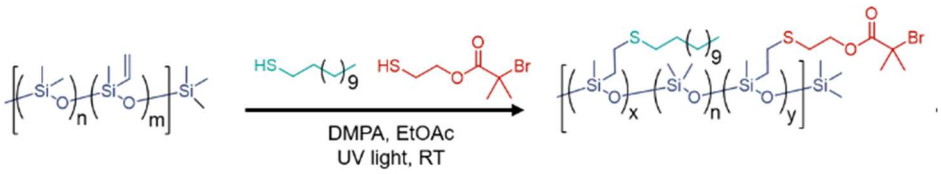

The siloxane (1 g, 350 eq vinyl per 1 eq polymer, 4.4 µmol polymer, 1.5 mmol vinyl) was dissolved into 8 mL of ethyl acetate in a 20 mL vial charged with a stir bar. HS–EBiB (100 mg, 0.2 eq per vinyl, 0.44 mmol), DDSH (570 mg, 1.8 eq per vinyl, 2.8 mmol) and DMPA (80 mg, 0.2 eq per vinyl 0.31 mmol) were added. The solution was irradiated with 365 nm light for 2 hours and then precipitated into 40 mL of cold methanol. Subsequently, the recovered polymer was dissolved into 3 mL DCM and precipitated into 40 mL of a 1:1 mixture of room temperature acetone and methanol to remove DDSH since it has poor solubility in methanol. The material was then centrifuged, isolated, and dried under vacuum to recover a clear viscous oil (0.2 g, 20% yield). Low yield was due to partial solubility of polymer in the precipitation mixture.

^{1}H NMR (600 MHz, $CDCl_3$): δ. 4.30 (t, 0.2 H), 2.78 (dd, 0.2 H), 2.66 (dd, 0.2 H), 2.57 (dd, 1.8 H), 2.50 (dd, 1.8 H), 1.93 (s, 0.6 H), 1.55 (m, 0.6 H), 0.9 (m, 2H), 0.05 – 0.12 (m, 63H). Indexed NMR spectrum is shown in Figure 2.58.

General procedure for ATRP reaction: Synthesis of $PDMS_{28k}$-g_{35}-$PMMA_{20k}$

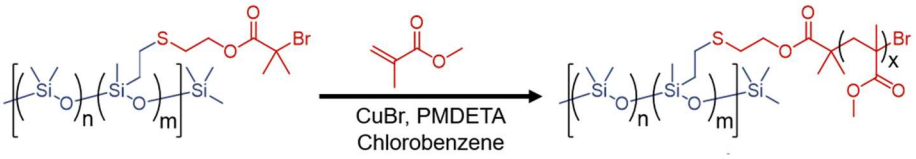

To a 100 mL three neck flask charged with a stir bar was added ATRP macroinitiator (100 mg, 3.57 µmol polymer, 125 µmol total initiator, 1 eq), 6.6 mL chlorobenzene (1:1 volume ratio to MMA), MMA (6.26 g, 62.5 mmol, 17500 eq, 500 eq per initiator), and PMDETA (22 mg, 125 µmol, 35 eq, 1 eq per initiator). The three neck flask was sealed with three rubber septa and degassed with nitrogen for 10 minutes followed by the rapid addition of

CuBr (18 mg, 125 μmol, 35 eq, 1 eq per initiator) (added by quickly removing the septum while maintaining a flow of nitrogen and quickly replacing the septum after addition). The solution was degassed for an additional 2 minutes then placed in an oil bath at 50 °C and reacted for two hours. The septum was removed to quench the reaction and the conversion was calculated to be 36% by comparing the ^{1}H NMR integration values of the methoxy peaks of the MMA monomer and PMMA. The reaction was filtered through basic alumina to remove the catalyst and ligand then precipitated into methanol, and a white powder was collected and dried under vacuum.

^{1}H NMR (600 MHz, $CDCl_3$): δ. 3.65 (s, 3 H), 1.74 – 2.07 (m, 2 H), 0.7 – 1.1 (m, 3 H), 0.05 – 0.12 (m, 0.46H). Figure 2.14 shows the full spectrum ^{1}H NMR spectrum.

*If the above procedure resulted in a gel or significant high molecular weight shouldering via SEC, a 4:1 ratio of chlorobenzene to MMA was used along with 0.25 eq CuBr compared to 1 eq initiator. In Table 2.1, samples synthesized from 225 kDa and 50 kDa macroinitors used these conditions.

Styrene was polymerized with the same procedure as above with a 1:1 ratio of monomer:solvent and a 1:1 ratio of catalyst:initiator at 110 °C. The NMR spectrum for the product is shown in Figure 2.15.

General procedure for ATRP reaction to polymerize acrylates: Synthesis of PDMS$_{28k}$-g$_{35}$-PMA$_{17k}$

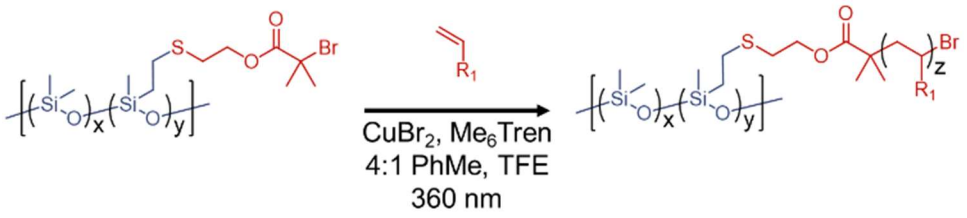

A stock solution was initially prepared to better control the addition of ligand and catalyst. A new stock solution was prepared the day that the reaction took place. To a 20 mL vial was added 2.4 mL TFE, 2.7 mg $CuBr_2$, and 16.8 mg Me_6Tren. The vial was sonicated for 30 minutes to dissolve the $CuBr_2$. To a separate 20 mL vial charged with a stir bar was added toluene (1.6 g), TFE (300 mg), MMA (2.3 g, 26.5 mmol, 15000 eq, 420 eq per initiator), and macroinitiator (50 mg, 1.8 µmol, 62.5 µmol initiator, 1 eq). Subsequently, 244 µL of the stock solution was added to the reaction vessel. The overall solution had a 1:1 volume ratio of monomer:solvent and 0.2 eq $CuBr_2$ per initiator, 0.12 eq Me_6Tren per initiator. The 20 mL vial reaction vessel was sealed with a septum and degassed with nitrogen for 15 minutes. Then, the reaction solution as placed under a UV light source and stirred for two hours, resulting in a final conversion of 44%. The reaction solution was precipitated directly into cold methanol (2 centrifuge tubes with 40 mL each) then centrifuged and dried.

The NMR spectra for each polymerized acrylate graft copolymer are shown in Figures 2.16 – 2.19.

General procedure for degrafting of PMMA from graft copolymer

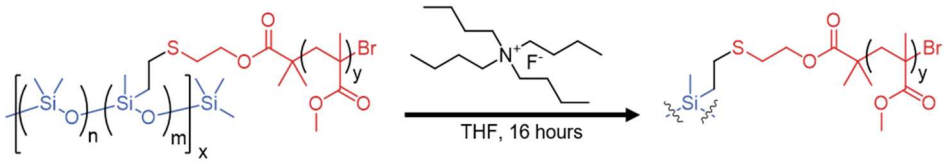

Approximately 100 mg copolymer was dissolved into 3 mL THF followed by the addition of TBAF solution (2 eq per siloxane repeat unit). The solution was left to stir overnight at room temperature then precipitated into 20 mL of cold methanol. If the polymer was too low of a molecular weight (>5 kDa), it couldn't be recovered via precipitation, so the solvent of the reaction solution as reduced under vacuum and redissolved in 3 mL ethyl acetate followed by a basic alumina plug, washed with 30 mL of 1 M NaOH, dried in $MgSO_4$, and then the solvent was removed under vacuum.

For the copolymers with dodecane chains, a different washing procedure was used to purify the PMMA. The THF from the crude solution was removed *in vacuo* and the polymer was dissolved into 30 mL DMSO. This solution was washed 3 times with 50 mL of diethyl ether. The DMSO and ether layer would form a miscible solution in the separatory funnel when shaken but would separate into layers when poured into a beaker. The DMSO layer could then be separated from the ether layer. Next, the DMSO solution was diluted with 100 mL of ethyl acetate and washed with 30 mL of brine around 5 times to remove the DMSO. The ethyl acetate layer was dried with $MgSO_4$. The volume was reduced to roughly 1 mL *in vacuo* before precipitation into 20 mL hexanes where the product was recovered as a white powder.
^{1}H NMR spectra for recovered homopolymers are shown in Figures 2.20 – 2.23.

Procedure for synthesis of ATRP macroinitiator with covalently bound methylcoumarin moieties starting from PDMS-*co*-PVMS (VDT-731, 28 kDa, 35 grafts).

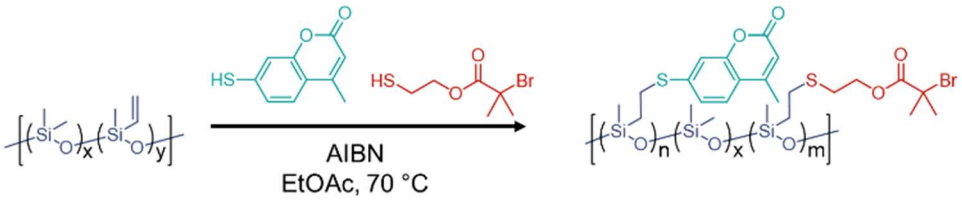

The siloxane (500 mg, 35 eq vinyl per 1 eq polymer, 18 µmol polymer, 630 µmol vinyl) was dissolved into 3 mL of ethyl acetate in a 20 mL vial charged with a stir bar. HS–EBiB (380 mg, 2.85 eq per vinyl, 1.8 mmol), 7-mercapto-4-methylcoumarin (18 mg, 0.15 eq per vinyl, 94 µmol) and AIBN (28 mg, 0.8 eq per vinyl, 500 µmol) were added. The solution was degassed with nitrogen for 10 minutes and then placed into an oil bath at 70 °C. Subsequently, the reaction solution was allowed to cool to room temperature, then was precipitated into 35 mL cold methanol in a centrifuge tube. The supernatant was decanted, and the polymer was dissolved with 3 mL ethyl acetate then precipitated again into 35 mL cold methanol. This process was repeated once more for a total of three precipitations. The polymer solution was dissolved into 3 mL ethyl acetate to transfer to a vial and dried under vacuum. 220 mg polymer was recovered corresponding to a 33% yield.

^{1}H NMR (600 MHz, $CDCl_3$): δ. 7.45 (d, 0.04 H), 7.08 – 7.16 (m, 0.08 H), 6.20 (s, 0.04 H), 4.30 (t, 1.92 H), 3.04 (dd, 0.08 H), 2.57 (dd, 1.92 H), 2.50 (dd, 1.92 H), 2.38 (s, 0.12 H), 1.93 (s, 5.76 H), 0.9 (m, 2H), 0.05 – 0.12 (m, 63H).

Indexed NMR spectra are shown in Figure 2.65 and Figure 2.66.

2.5 Characterization Data

2.5.1 ^{1}H and ^{13}C NMR spectra of small molecules and polymers

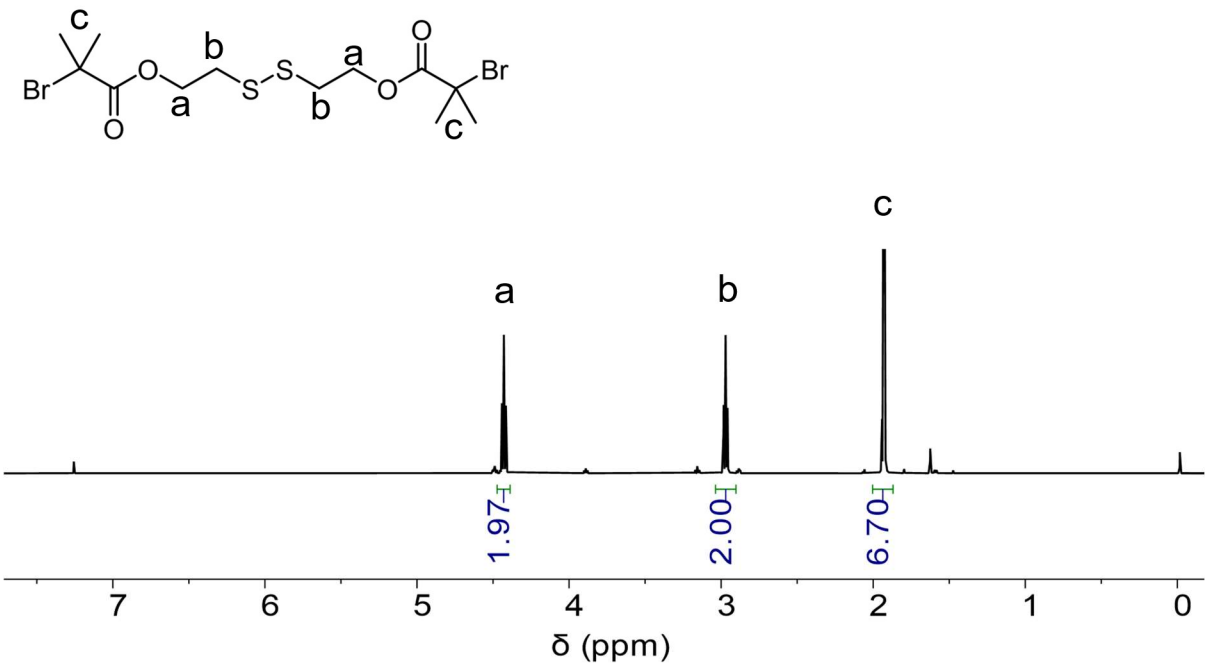

Figure 2.9. ^{1}H NMR spectrum of bis[2-(2′-bromoisobutyryloxy)ethyl]disulfide ($CDCl_3$, 600 MHz).

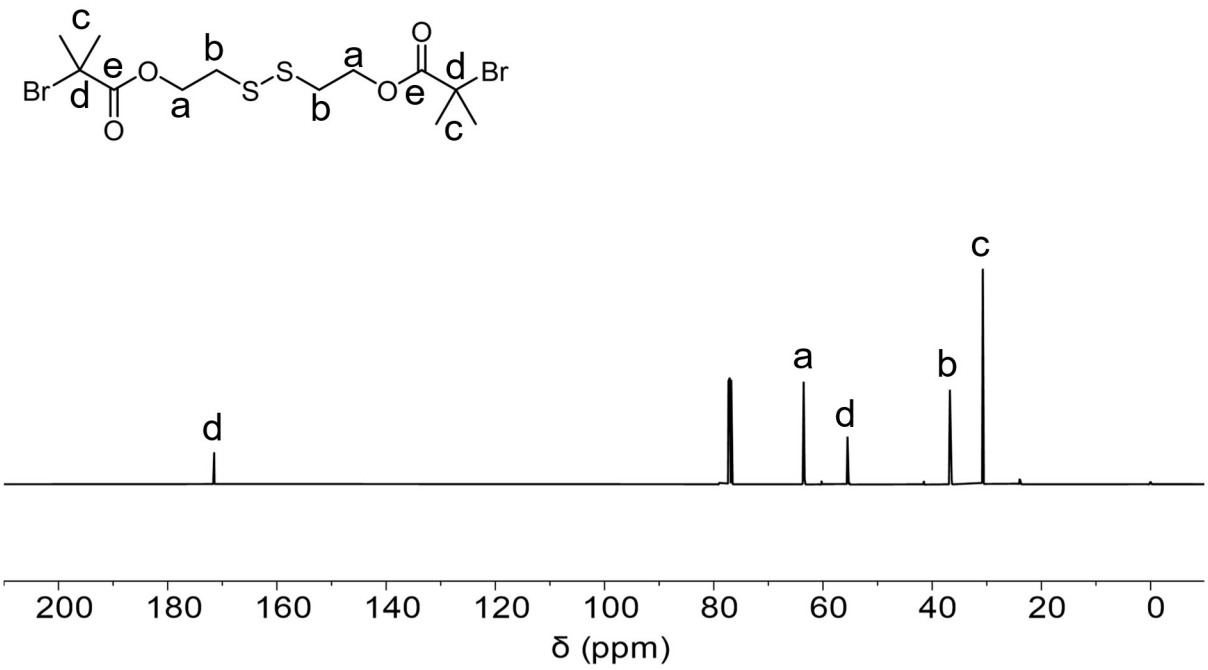

Figure 2.10. ^{13}C NMR spectrum of bis[2-(2′-bromoisobutyryloxy)ethyl]disulfide ($CDCl_3$, 126 MHz).

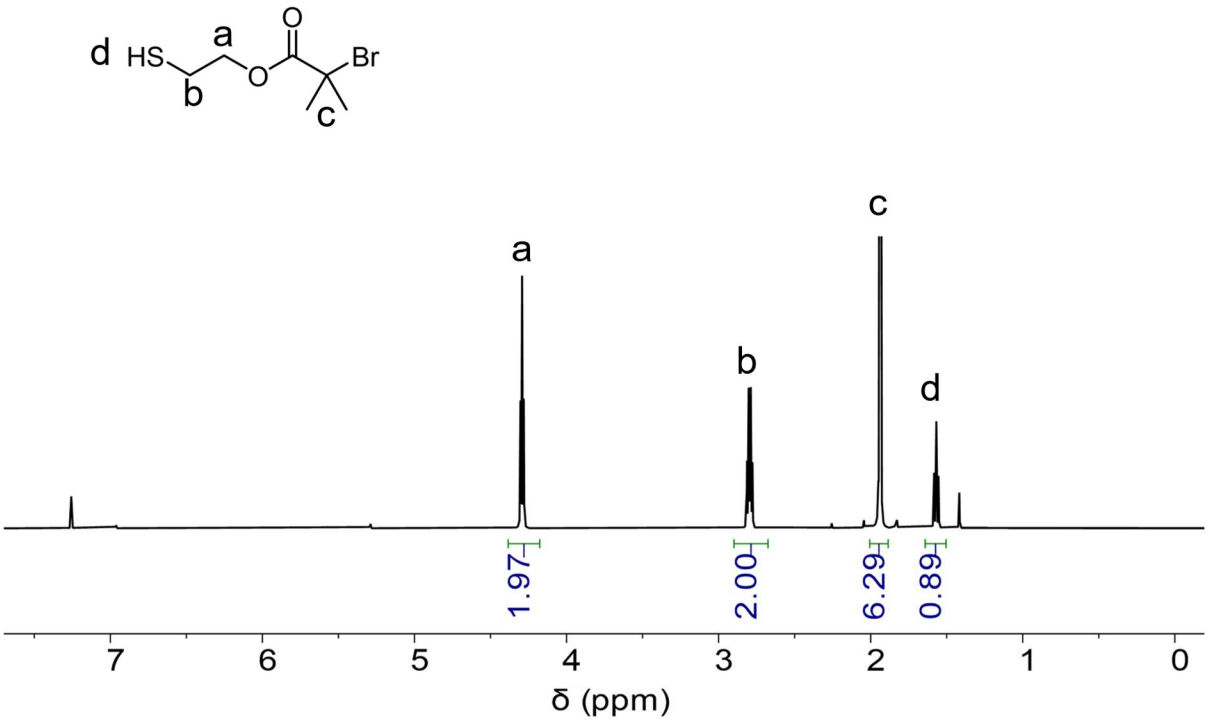

Figure 2.11. ^{1}H NMR spectrum of mercaptoethyl α-bromoisobutyrate ($CDCl_3$, 600 MHz).

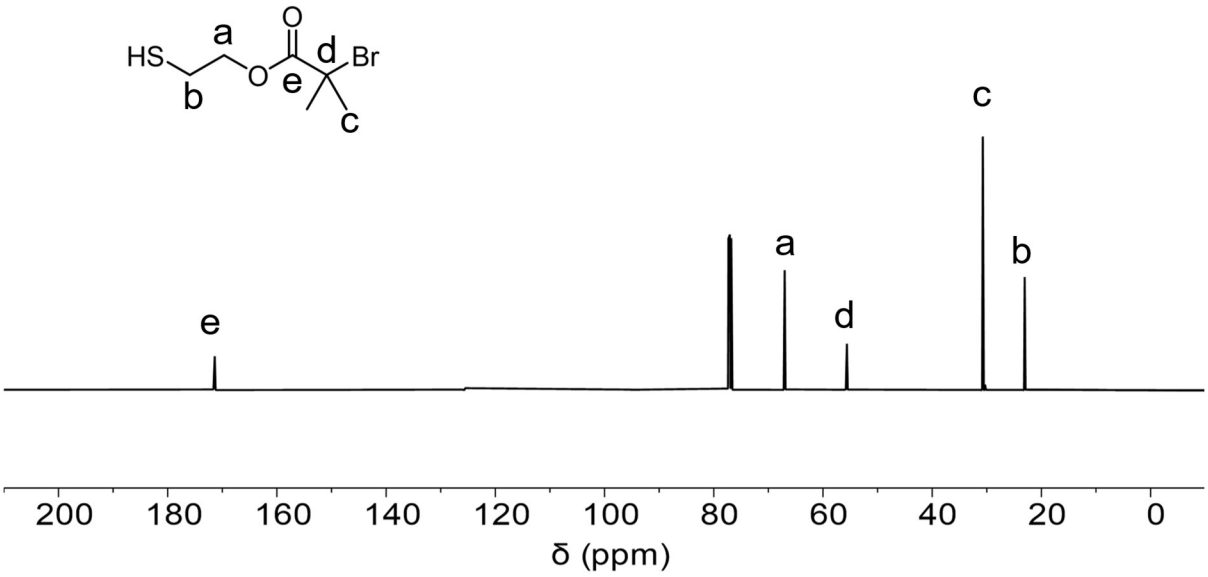

Figure 2.12. ^{13}C NMR spectrum of mercaptoethyl α-bromoisobutyrate disulfide ($CDCl_3$, 126 MHz).

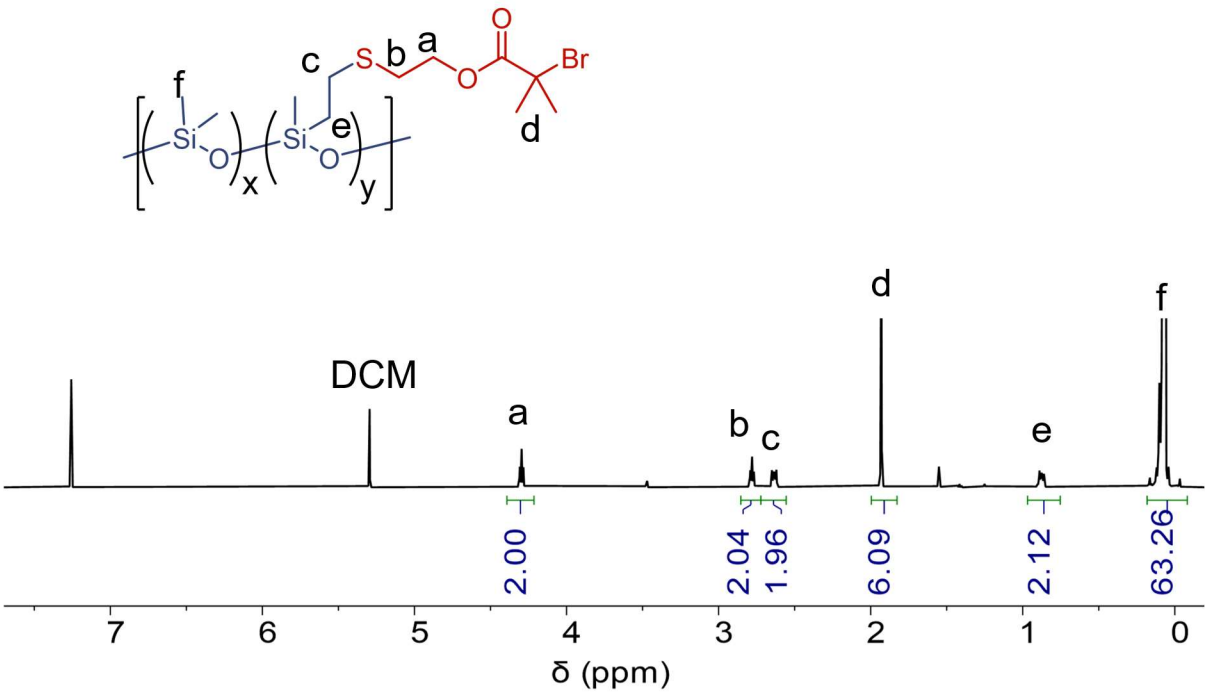

Figure 2.13. ^{1}H NMR of a representative PDMS-g-Br macroinitiator, corresponding to $PDMS_{28k}$-g_{35}-Br ($CDCl_3$, 600 MHz).

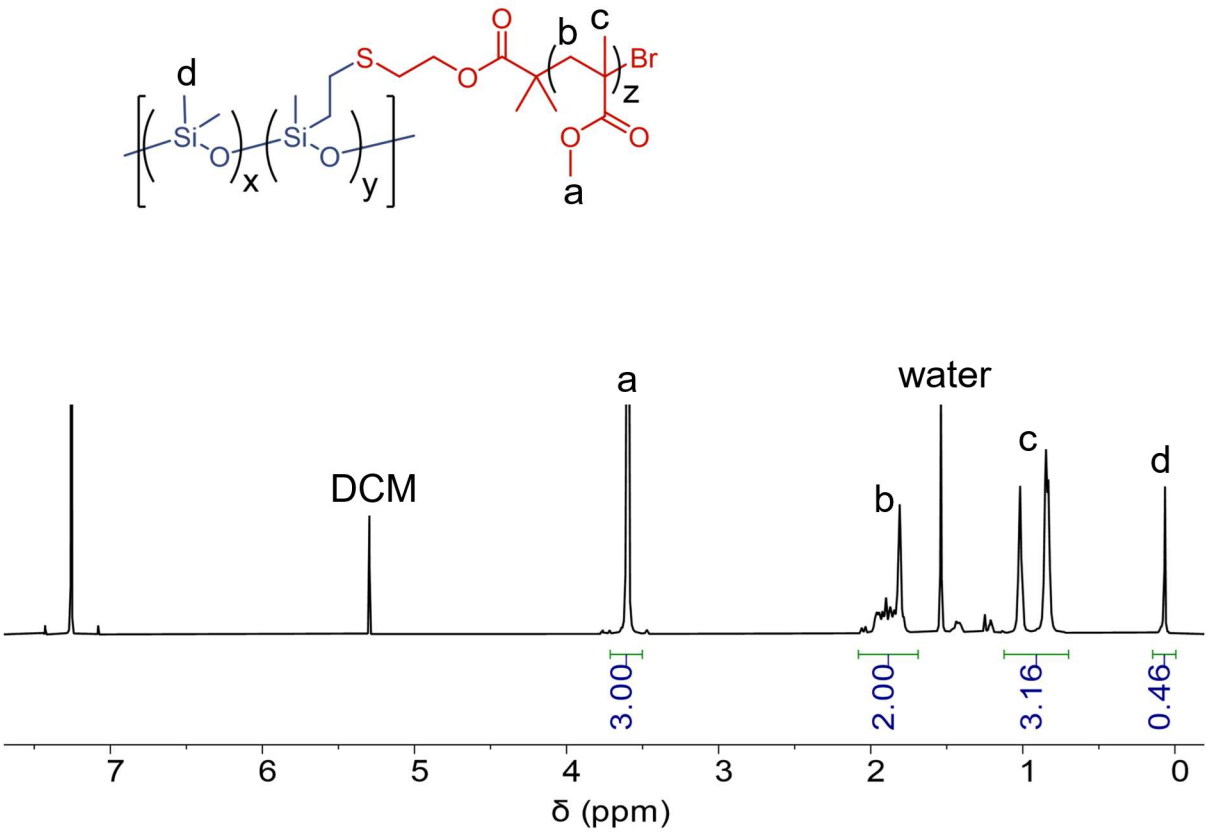

Figure 2.14. ^{1}H NMR of a representative PDMS-g-PMMA copolymer, corresponding to $PDMS_{28k}$-g_{35}-$PMMA_{20k}$ ($CDCl_3$, 600 MHz).

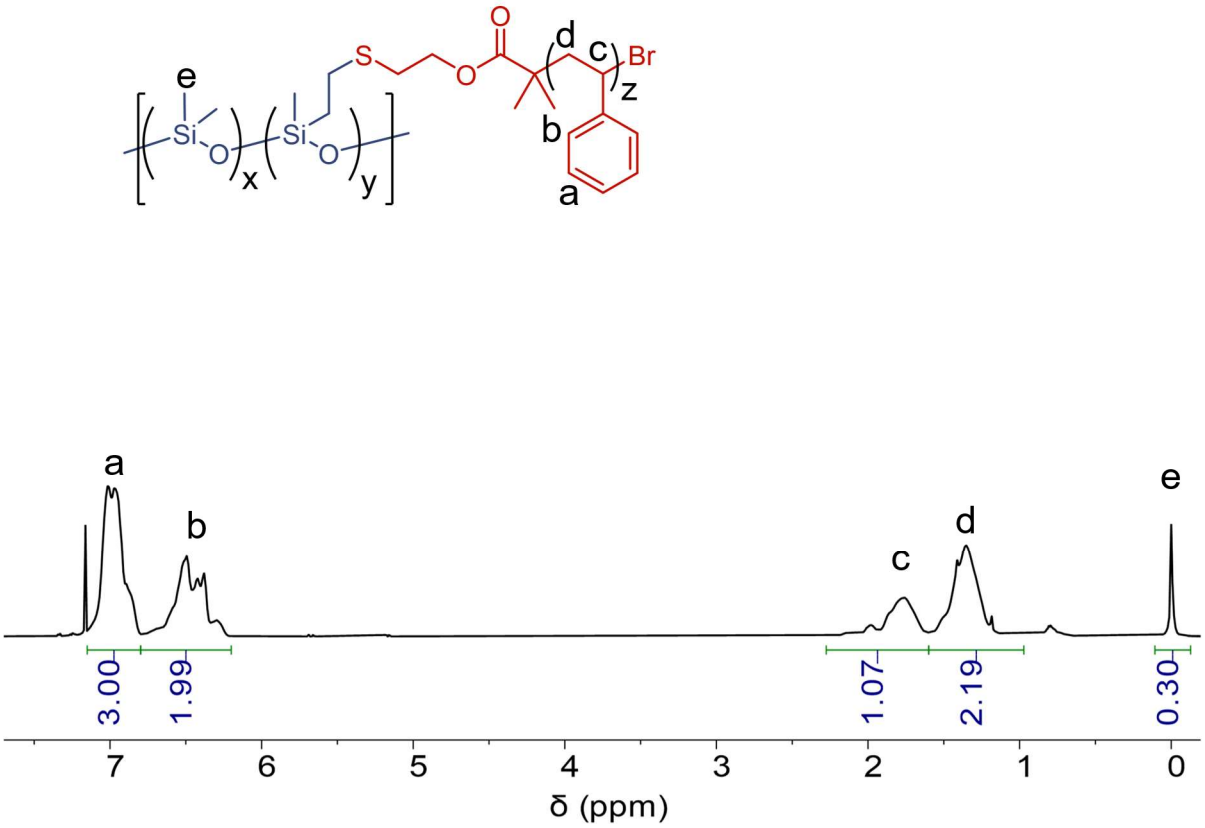

Figure 2.15. ^{1}H NMR of a representative PDMS-g-PS copolymer, corresponding to $PDMS_{28k}$-g_{35}-PS_{23k} ($CDCl_3$, 600 MHz).

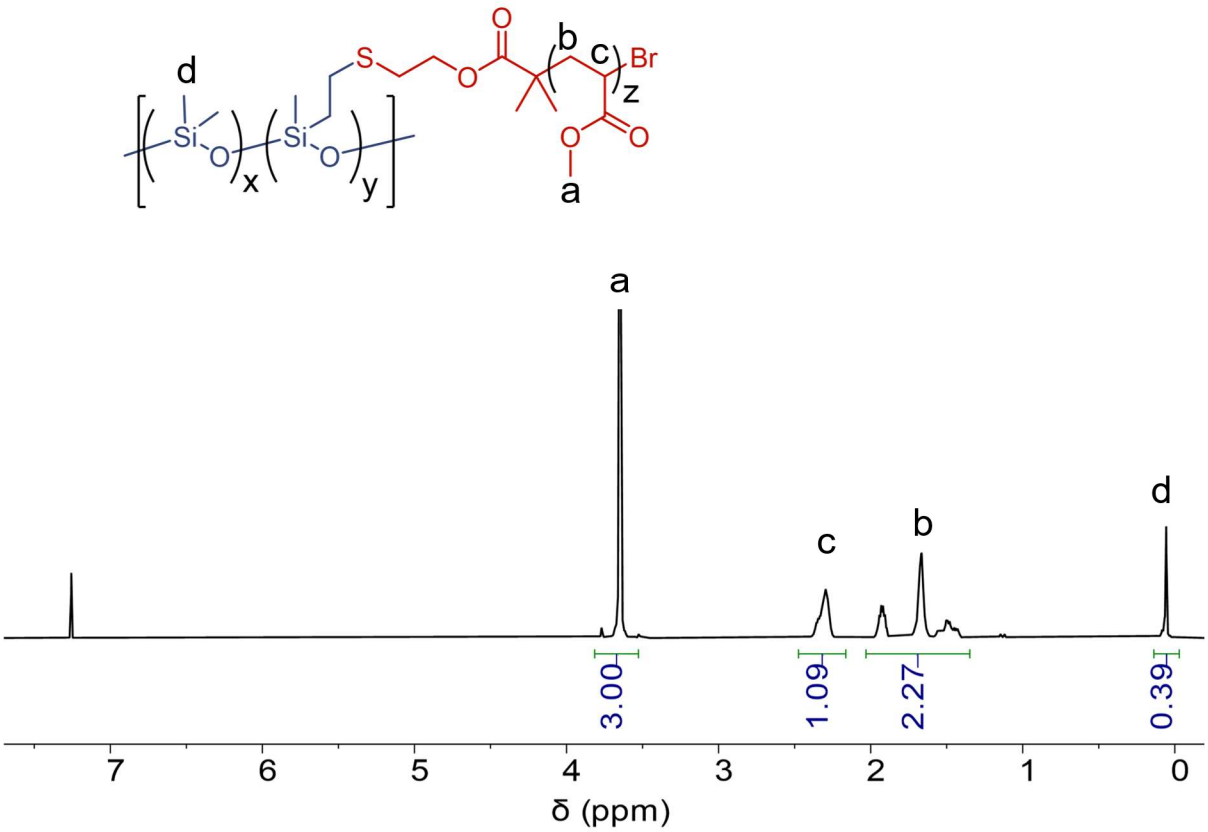

Figure 2.16. ^{1}H NMR of a representative PDMS-g-PMA copolymer, corresponding to $PDMS_{28k}$-g_{35}-PMA_{17k} ($CDCl_3$, 600 MHz).

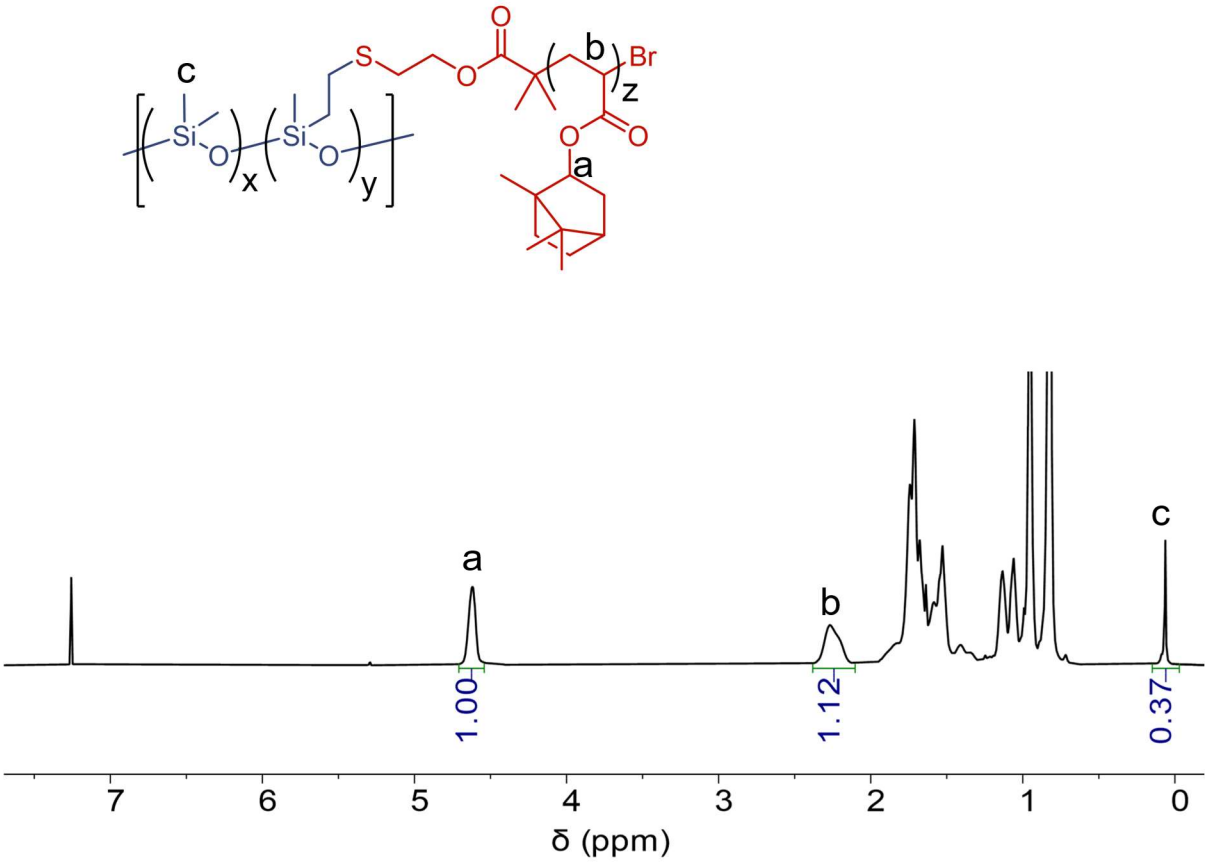

Figure 2.17. ^{1}H NMR of a representative PDMS-g-PiBA copolymer, corresponding to $PDMS_{28k}$-g_{35}-$PiBA_{40k}$ ($CDCl_3$, 600 MHz).

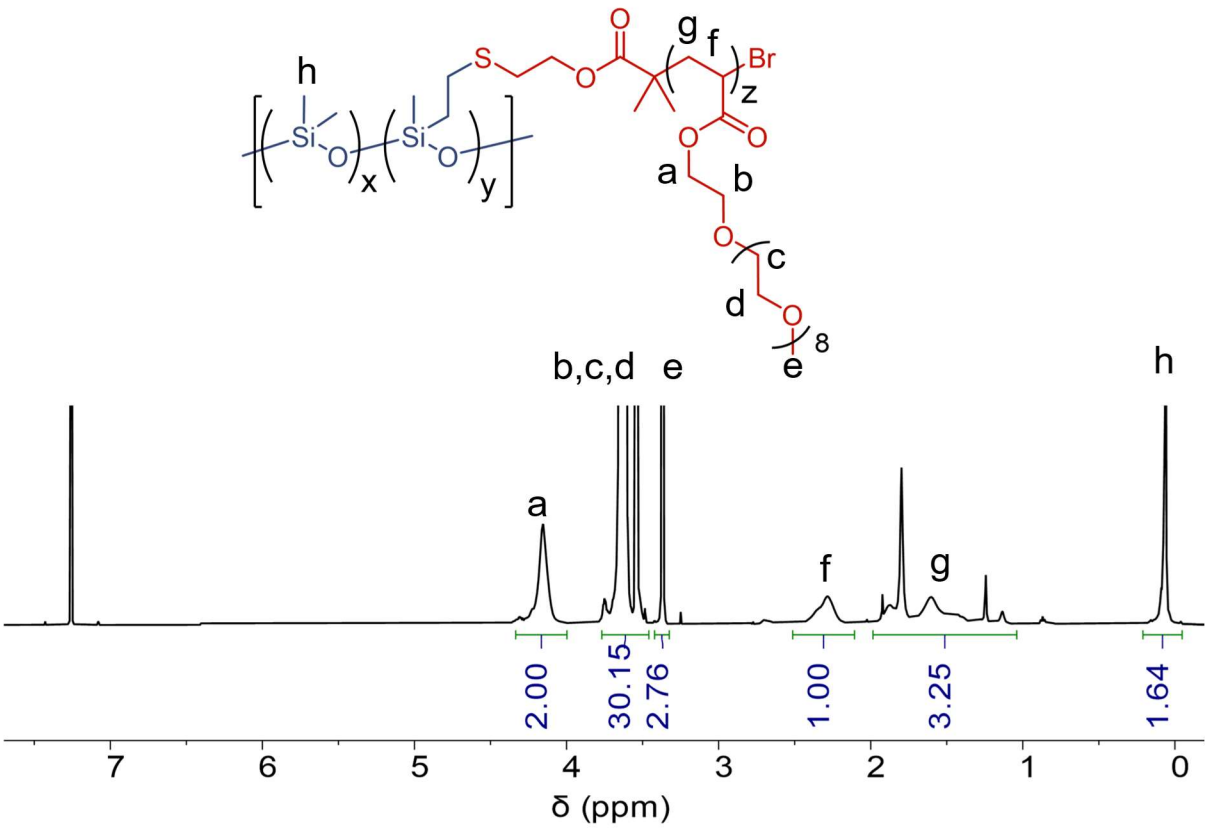

Figure 2.18. ^{1}H NMR of a representative PDMS-g-POEGA copolymer, corresponding to $PDMS_{28k}$-g_{35}-$POEGA_{20k}$ ($CDCl_3$, 600 MHz).

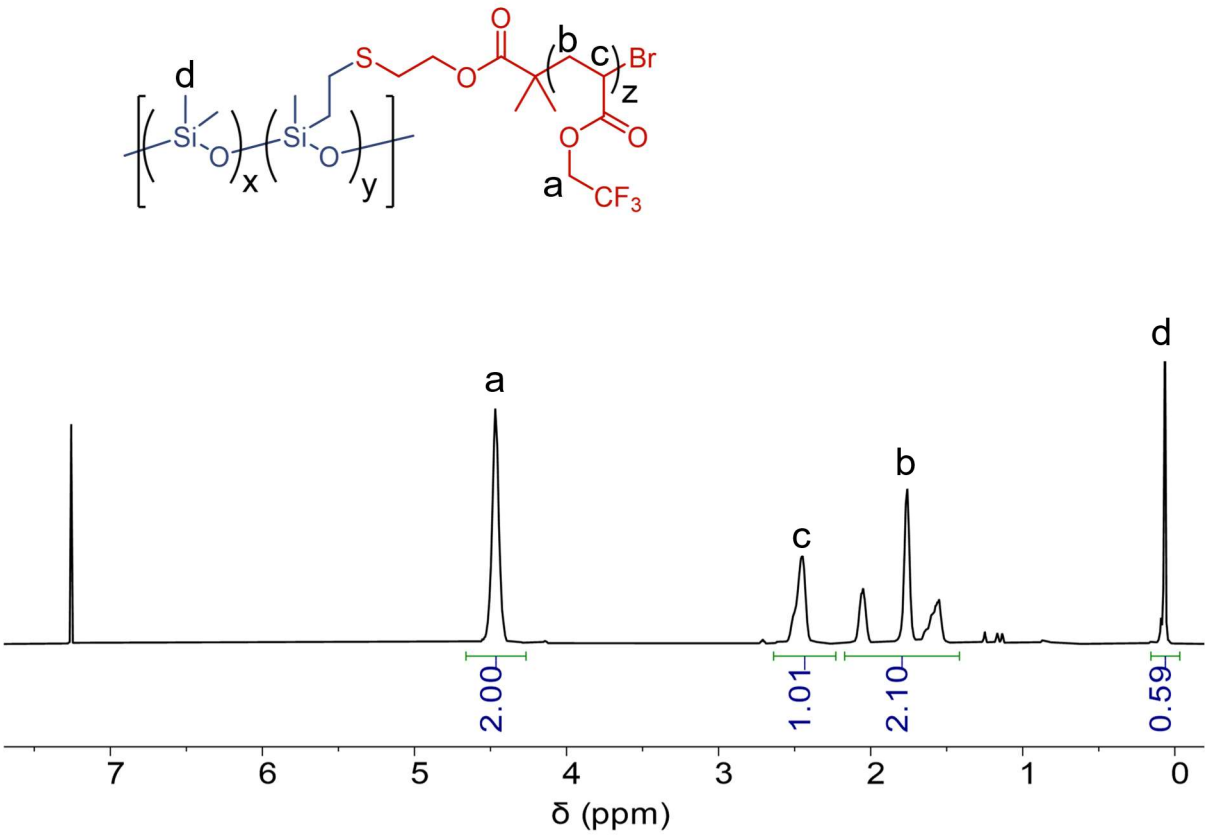

Figure 2.19. ^{1}H NMR of a representative PDMS-g-PTFEA copolymer, corresponding to $PDMS_{28k}$-g_{35}-$PTFEA_{18k}$ ($CDCl_3$, 600 MHz).

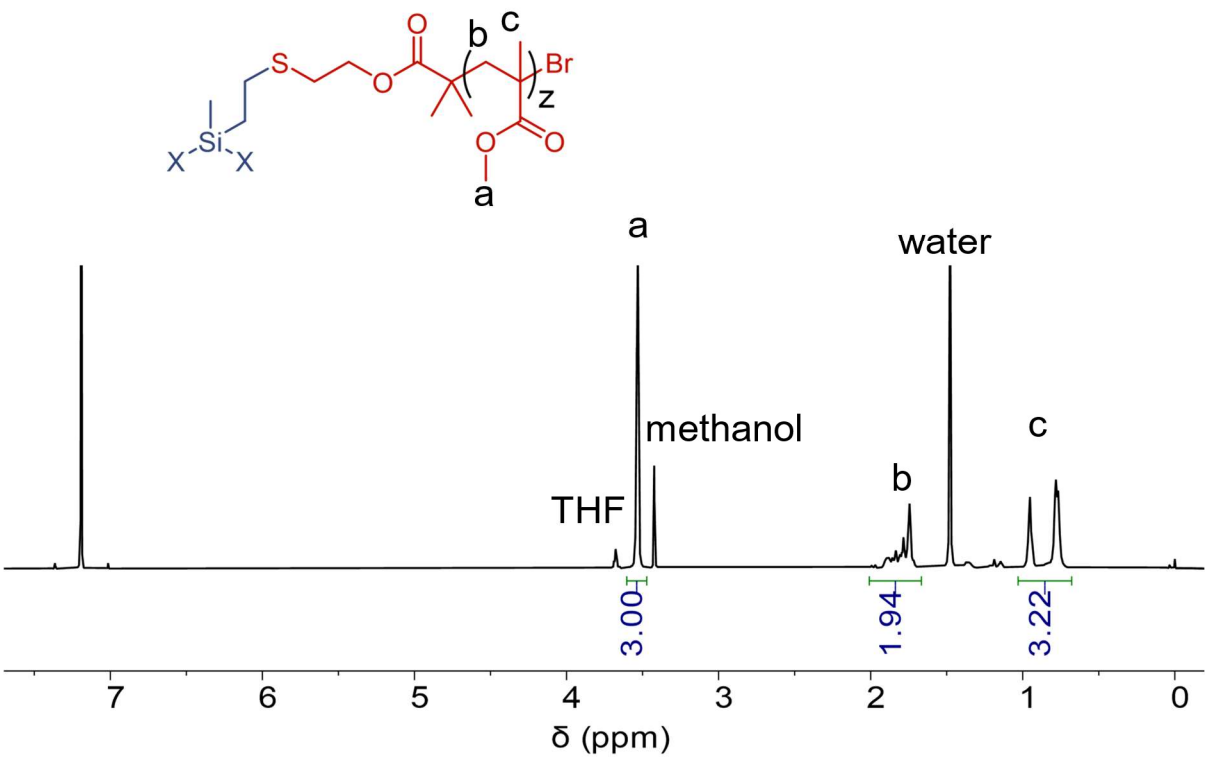

Figure 2.20. Typical ^{1}H NMR of PMMA recovered from TBAF degradation of PDMS-g-PMMA copolymer. This sample is the product of degradation of $PDMS_{28k}$-g_{35}-$PMMA_{20k}$ ($CDCl_3$, 600 MHz).

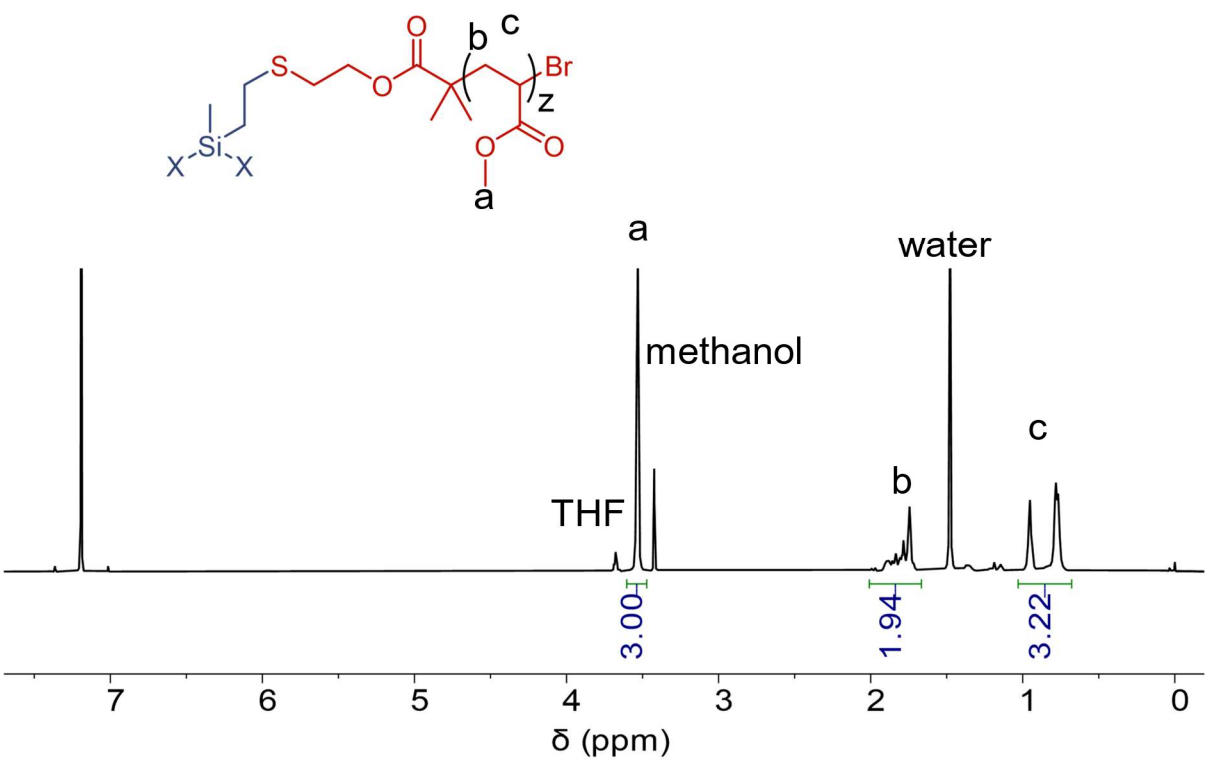

Figure 2.21. Typical ^{1}H NMR of PMA recovered from TBAF degradation of PDMS-g-PMA copolymer. This sample is the product of degradation of $PDMS_{28k}$-g_{35}-PMA_{17k} ($CDCl_3$, 600 MHz).

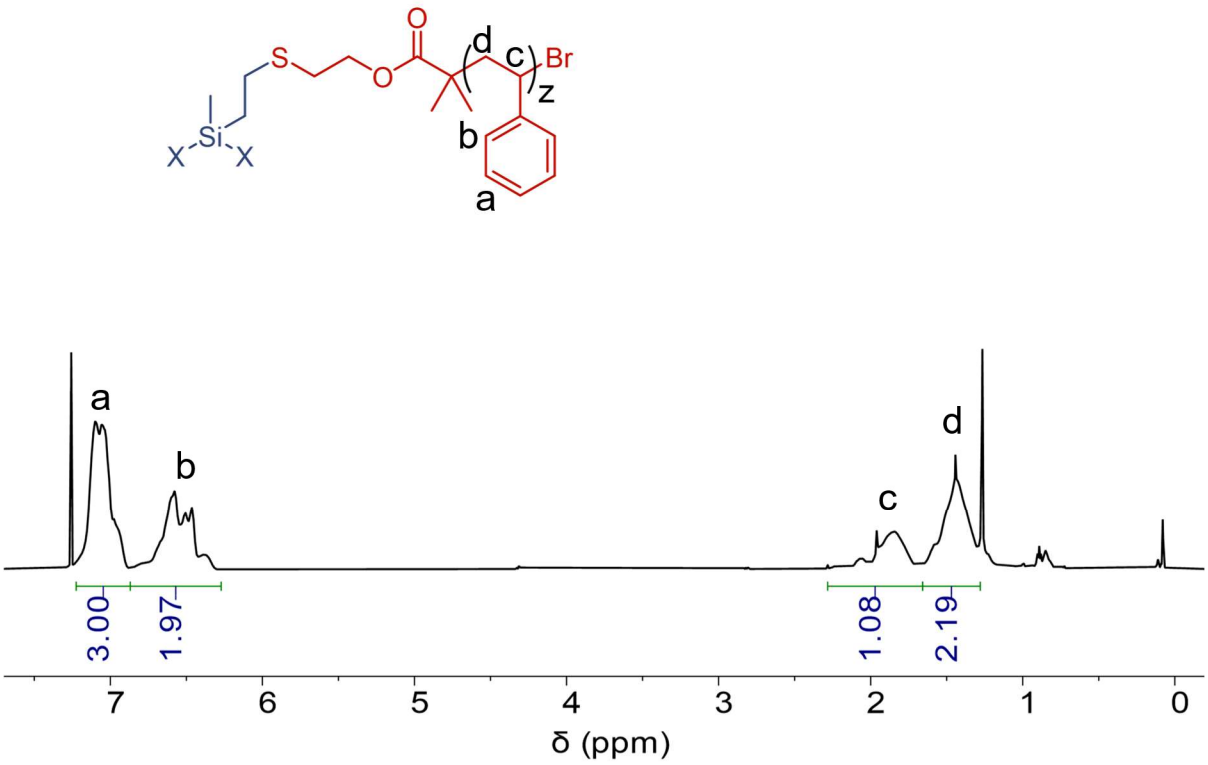

Figure 2.22. Typical ^{1}H NMR of PS recovered from TBAF degradation of PDMS-g-PS copolymer. This sample is the product of degradation of $PDMS_{28k}$-g_{35}-PS_{23k} ($CDCl_3$, 600 MHz).

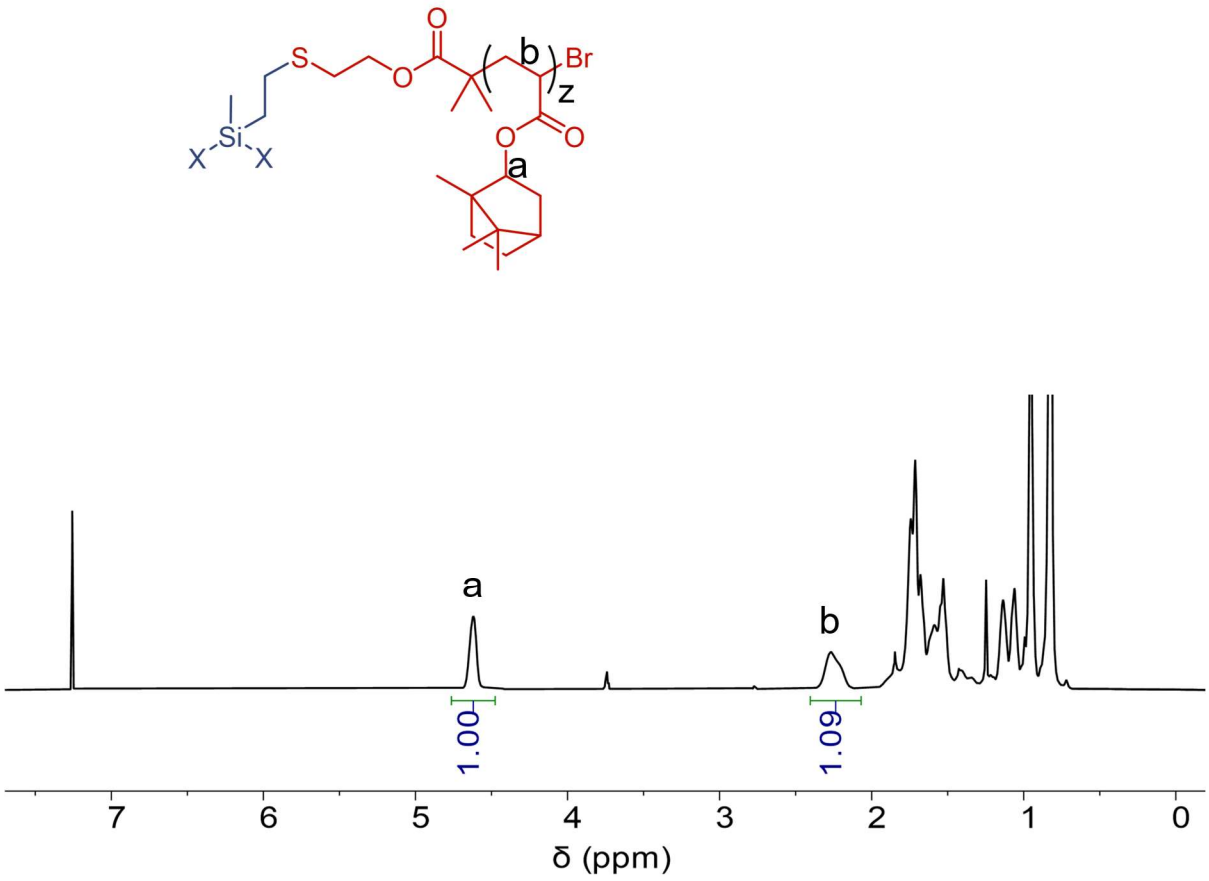

Figure 2.23. Typical ^{1}H NMR of PiBA recovered from TBAF degradation of PDMS-g-PiBA copolymer. This sample is the product of degradation of $PDMS_{28k}$-g_{35}-$PiBA_{40k}$ ($CDCl_3$, 600 MHz).

2.5.2 SEC traces of the synthesized macroinitiators and graft copolymers listed in Table 2.1

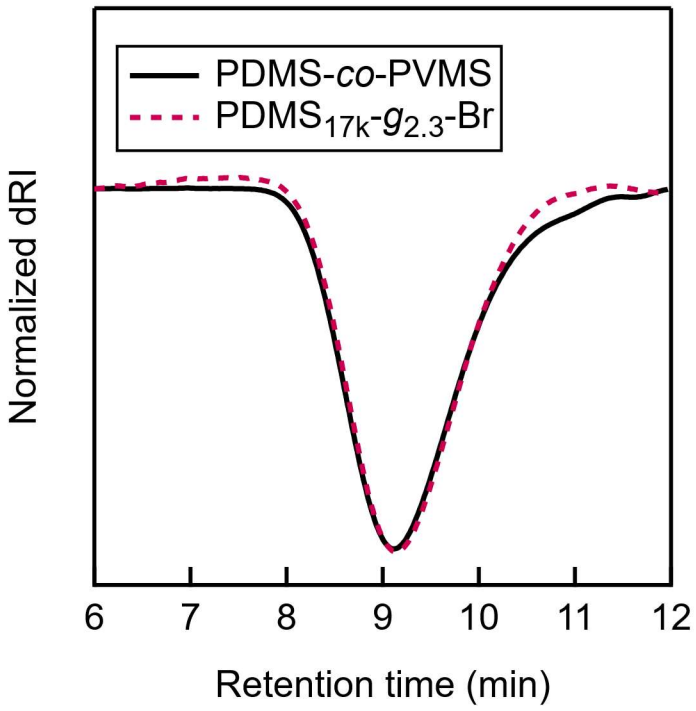

Figure 2.24. SEC trace of $PDMS_{17k}$-$g_{2.3}$-Br macroinitiator and commercial PDMS starting material (VDT-123).

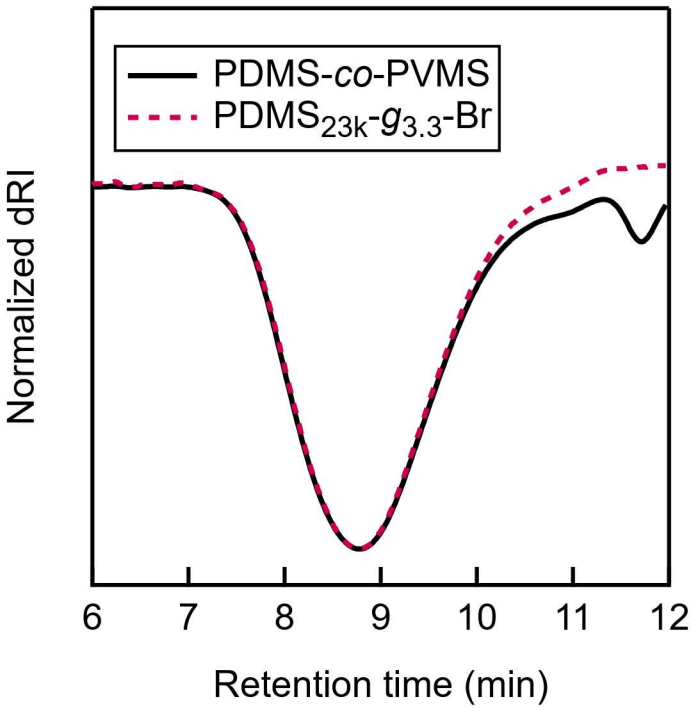

Figure 2.25. SEC trace of $PDMS_{23k}$-$g_{3.3}$-Br macroinitiator and commercial PDMS starting material (VDT-127).

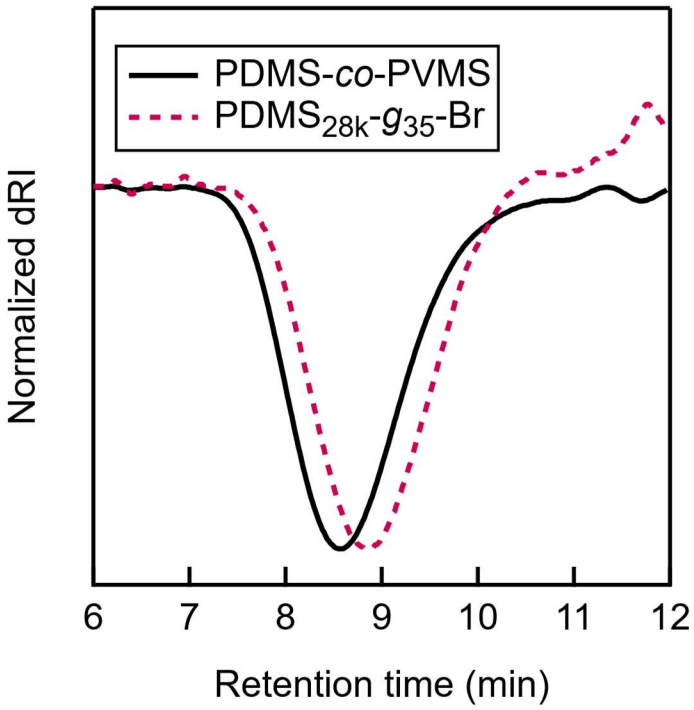

Figure 2.26. SEC trace of $PDMS_{28k}$-g_{35}-Br macroinitiator and commercial PDMS starting material (VDT-731).

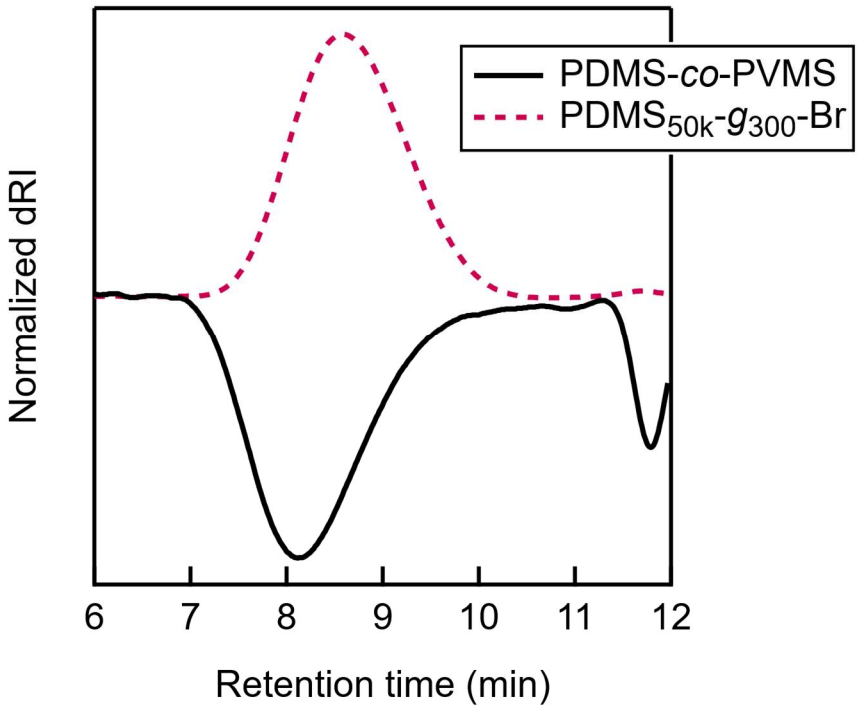

Figure 2.27. SEC trace of $PDMS_{50k}$-g_{300}-Br macroinitiator and commercial PDMS starting material (VDT-5035).

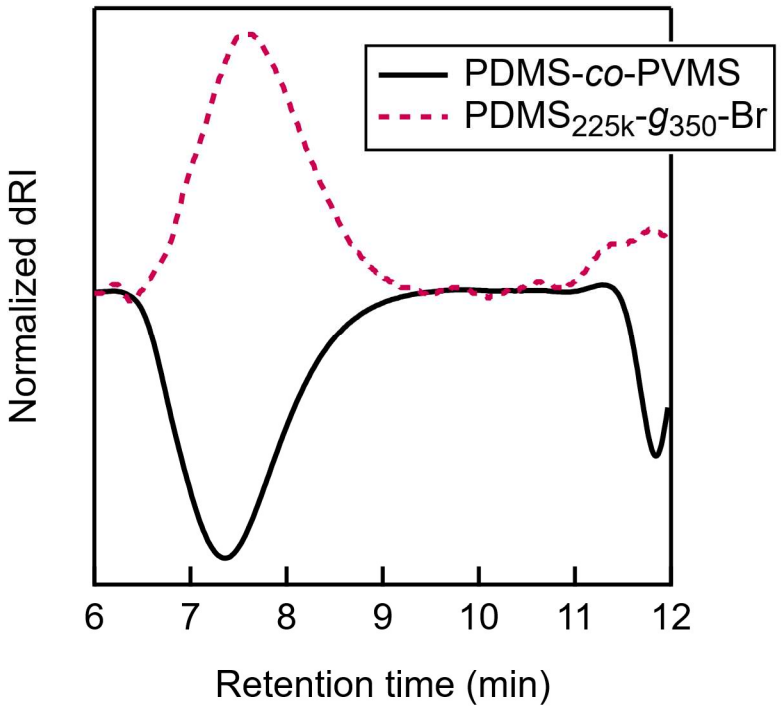

Figure 2.28. SEC trace of $PDMS_{225k}$-g_{350}-Br macroinitiator and commercial PDMS starting material (VDT-954).

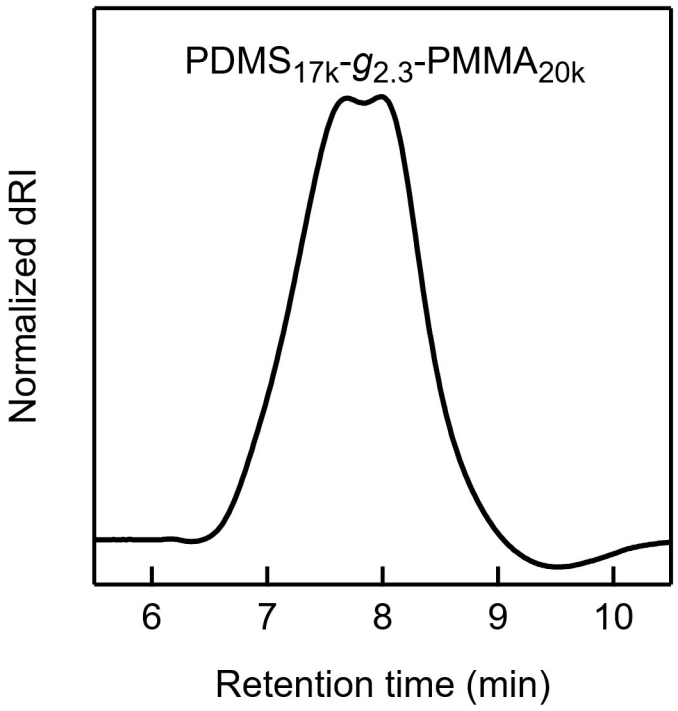

Figure 2.29. SEC trace of $PDMS_{17k}$-$g_{2.3}$-$PMMA_{20k}$ graft copolymer.

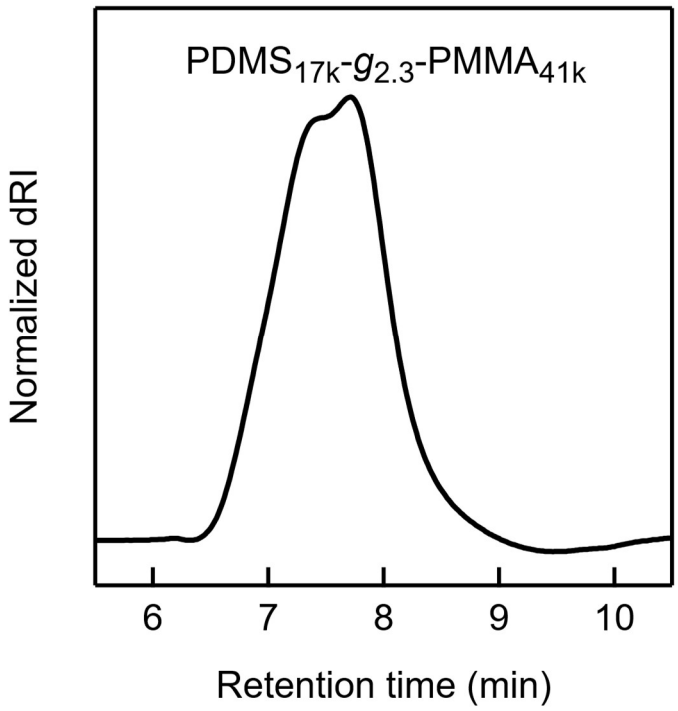

Figure 2.30. SEC trace of $PDMS_{17k}$-$g_{2.3}$-$PMMA_{41k}$ graft copolymer.

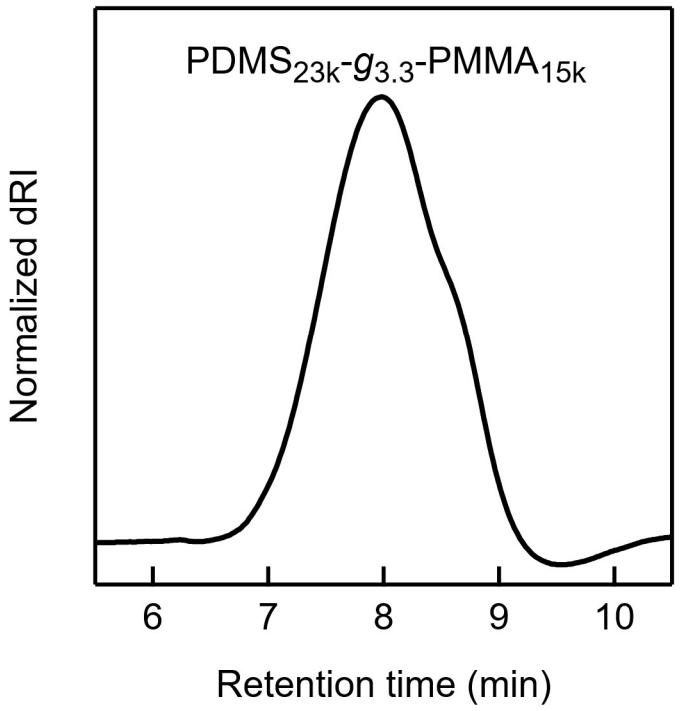

Figure 2.31. SEC trace of $PDMS_{23k}$-$g_{3.3}$-$PMMA_{15k}$ graft copolymer.

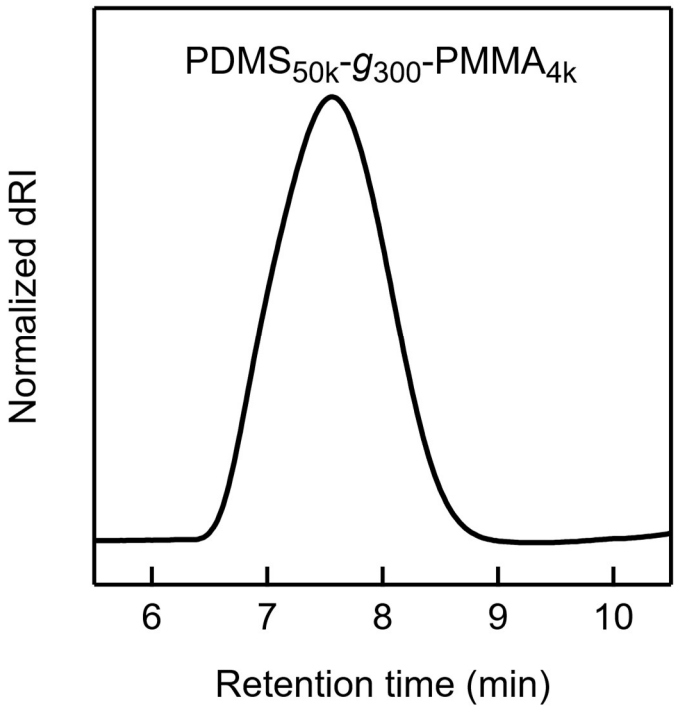

Figure 2.32. SEC trace of $PDMS_{50k}$-g_{300}-$PMMA_{4k}$ graft copolymer.

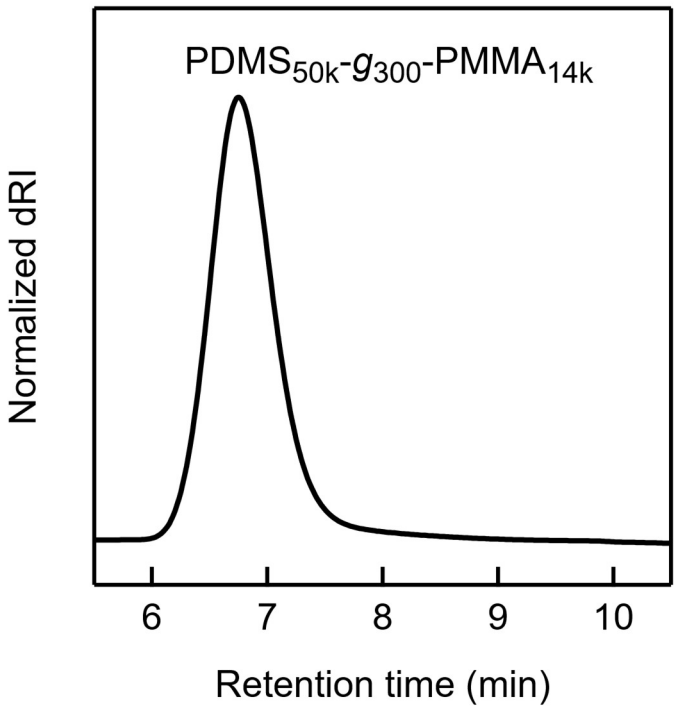

Figure 2.33. SEC trace of $PDMS_{50k}$-g_{300}-$PMMA_{14k}$ graft copolymer.

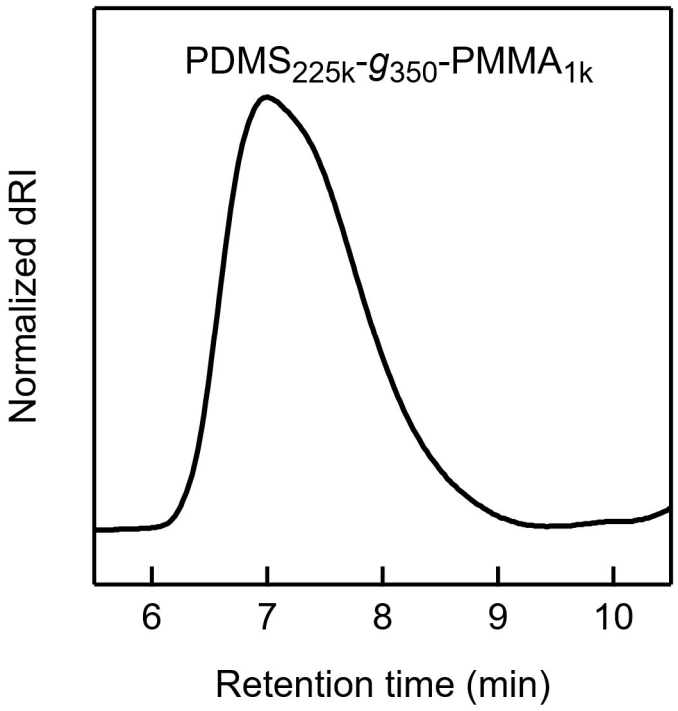

Figure 2.34. SEC trace of $PDMS_{225k}$-g_{350}-$PMMA_{1k}$ graft copolymer.

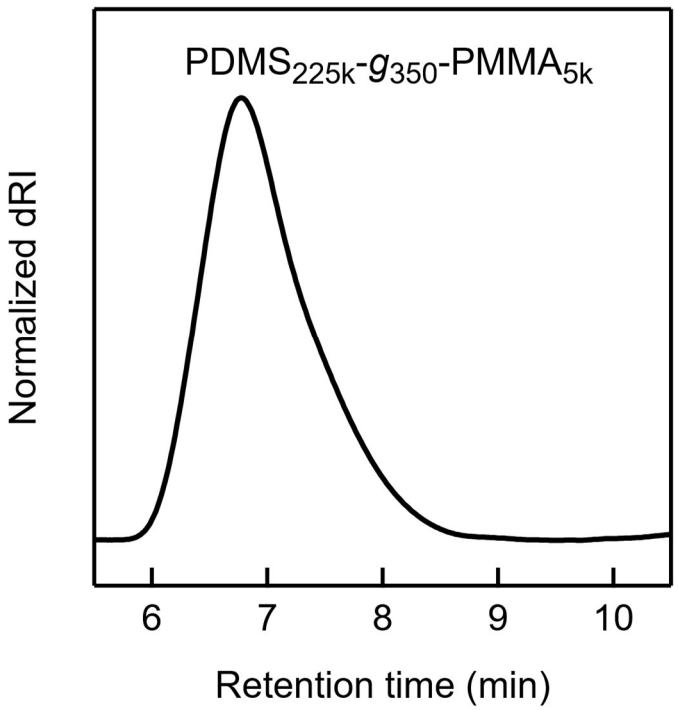

Figure 2.35. SEC trace of $PDMS_{225k}$-g_{350}-$PMMA_{5k}$ graft copolymer.

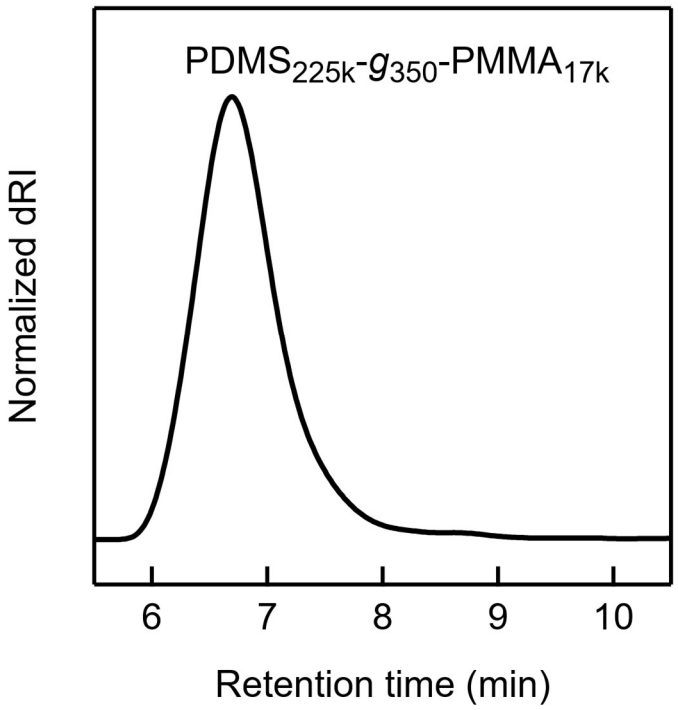

Figure 2.36. SEC trace of $PDMS_{225k}$-g_{350}-$PMMA_{17k}$ graft copolymer.

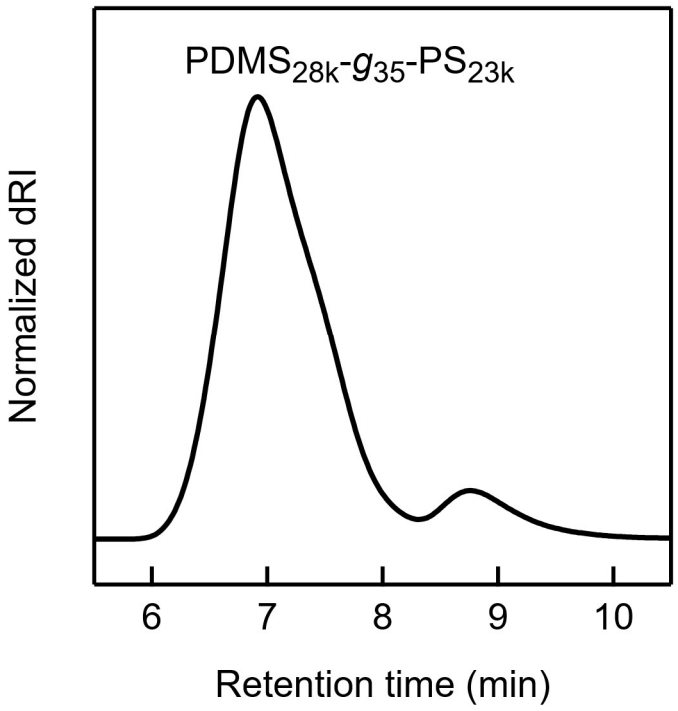

Figure 2.37. SEC trace of $PDMS_{28k}$-g_{35}-PS_{23k} graft copolymer.

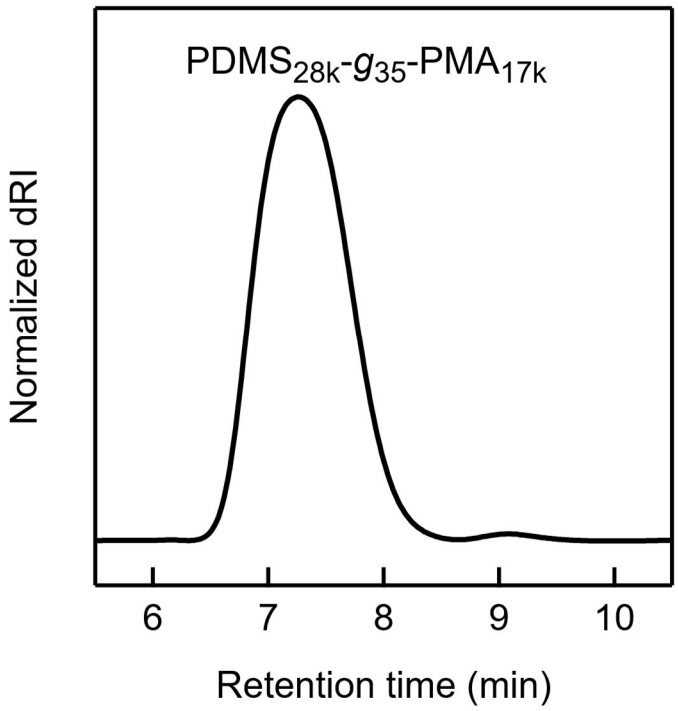

Figure 2.38. SEC trace of $PDMS_{28k}$-g_{35}-PMA_{17k} graft copolymer.

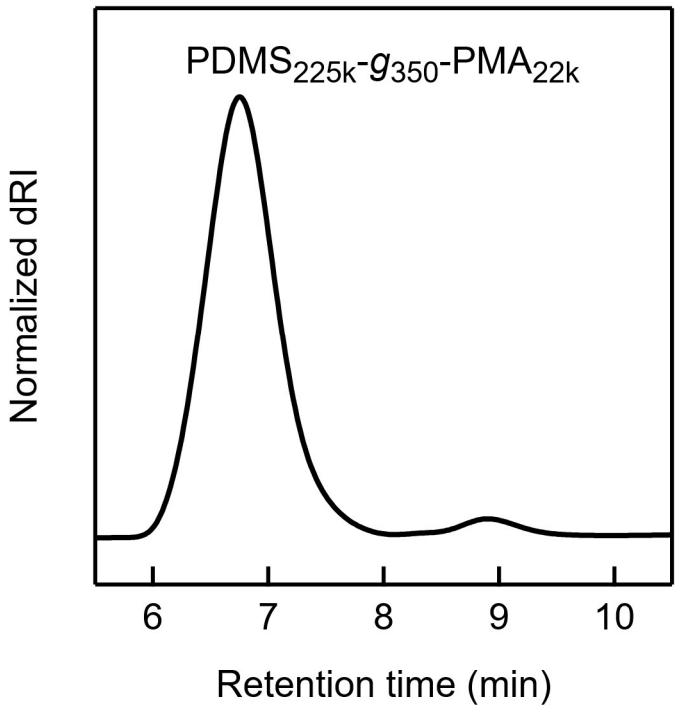

Figure 2.39. SEC trace of $PDMS_{225k}$-g_{350}-PMA_{22k} graft copolymer.

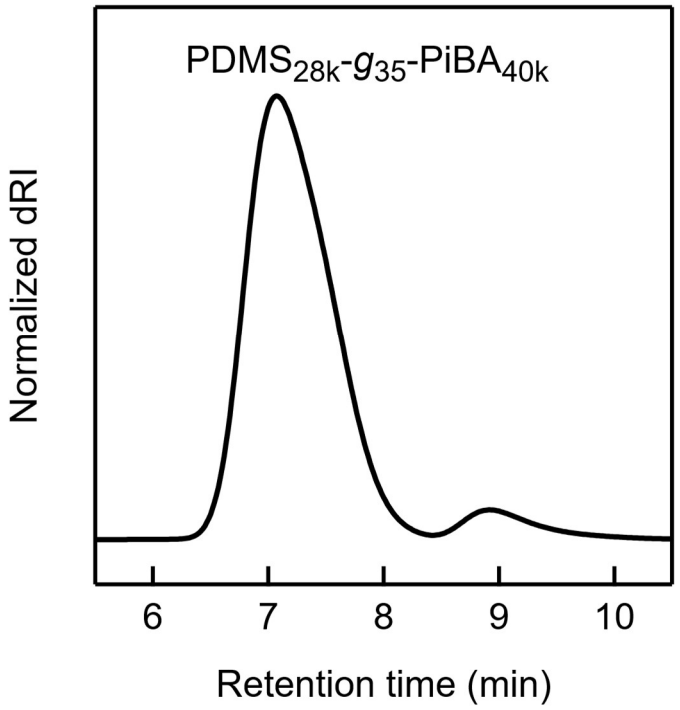

Figure 2.40. SEC trace of $PDMS_{28k}$-g_{35}-$PiBA_{40k}$ graft copolymer.

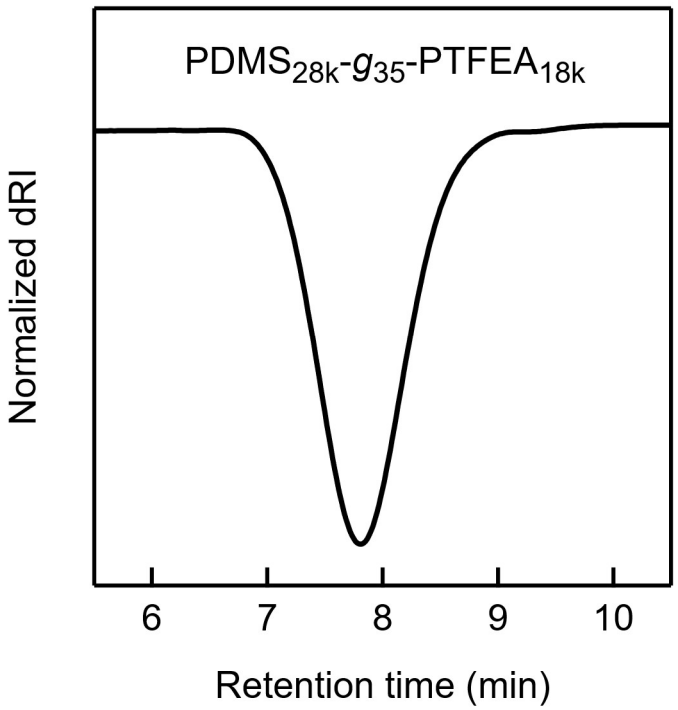

Figure 2.41. SEC trace of $PDMS_{28k}$-g_{35}-$PTFEA_{18k}$ graft copolymer.

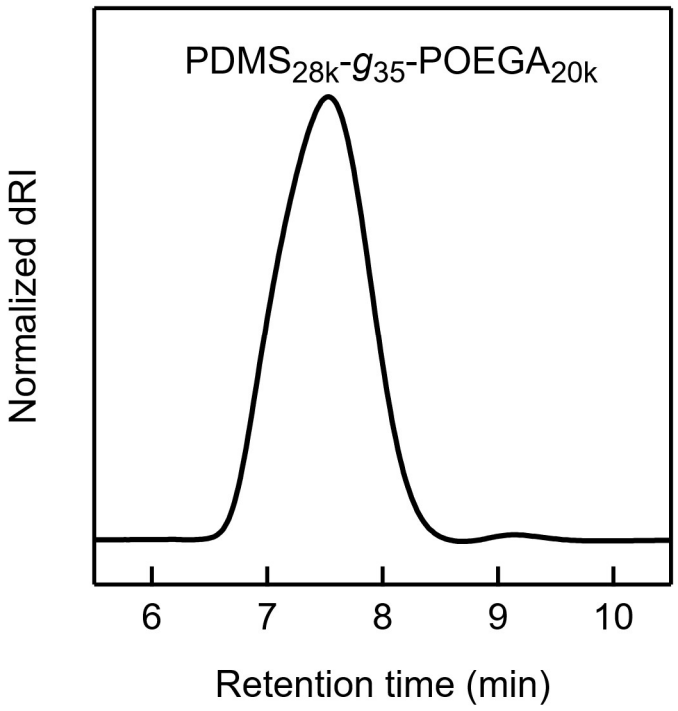

Figure 2.42. SEC trace of $PDMS_{28k}$-g_{35}-$POEGA_{20k}$ graft copolymer.

2.5.3 Thermal characterization of graft copolymers

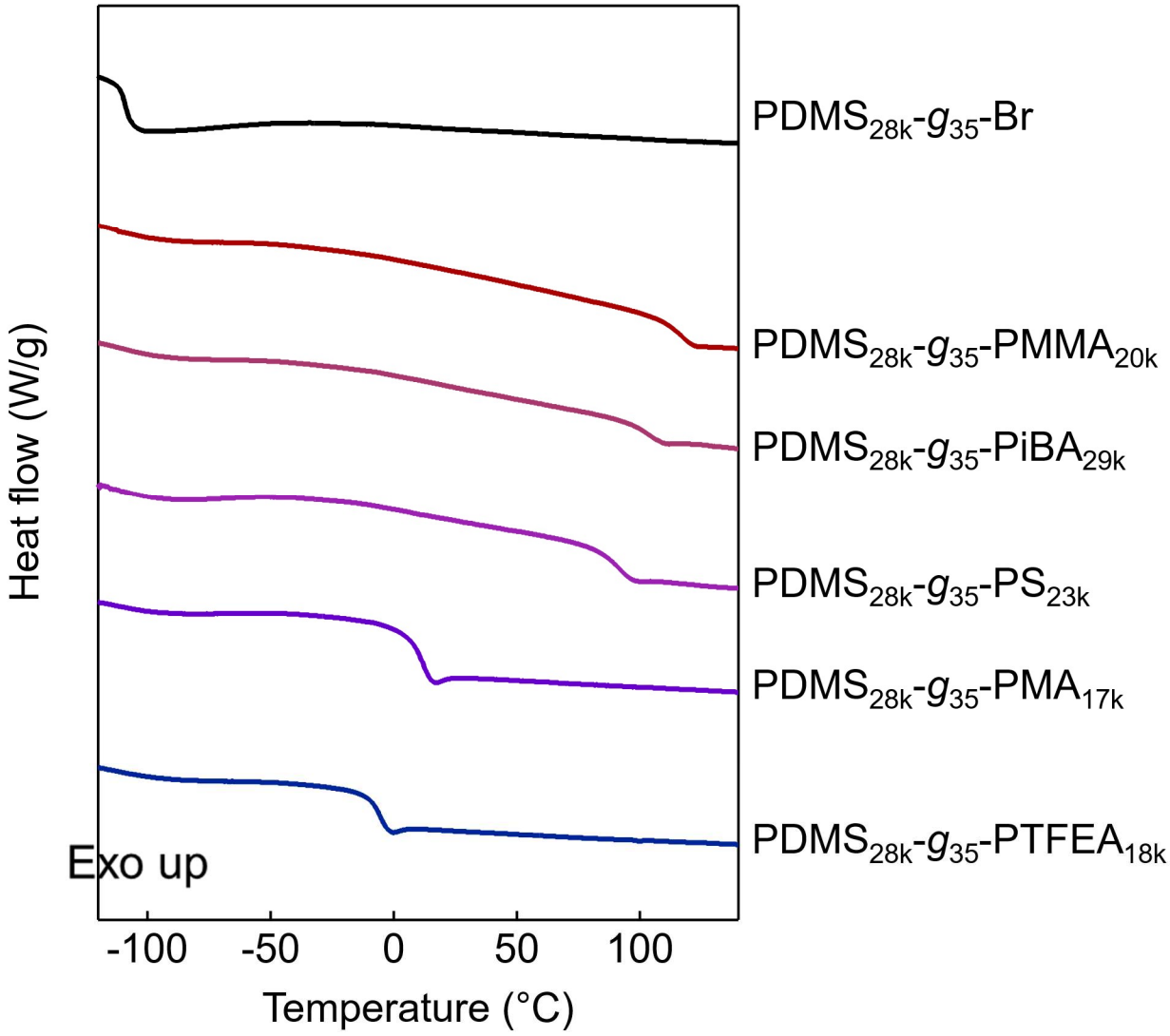

Figure 2.43. DSC traces for the listed macroinitiator and graft copolymers with the labeled PDMS molecular weight, number of grafts, and molecular weight per graft calculated with NMR. Traces shown are the on the second heating cycle, heated at 10 °C per minute.

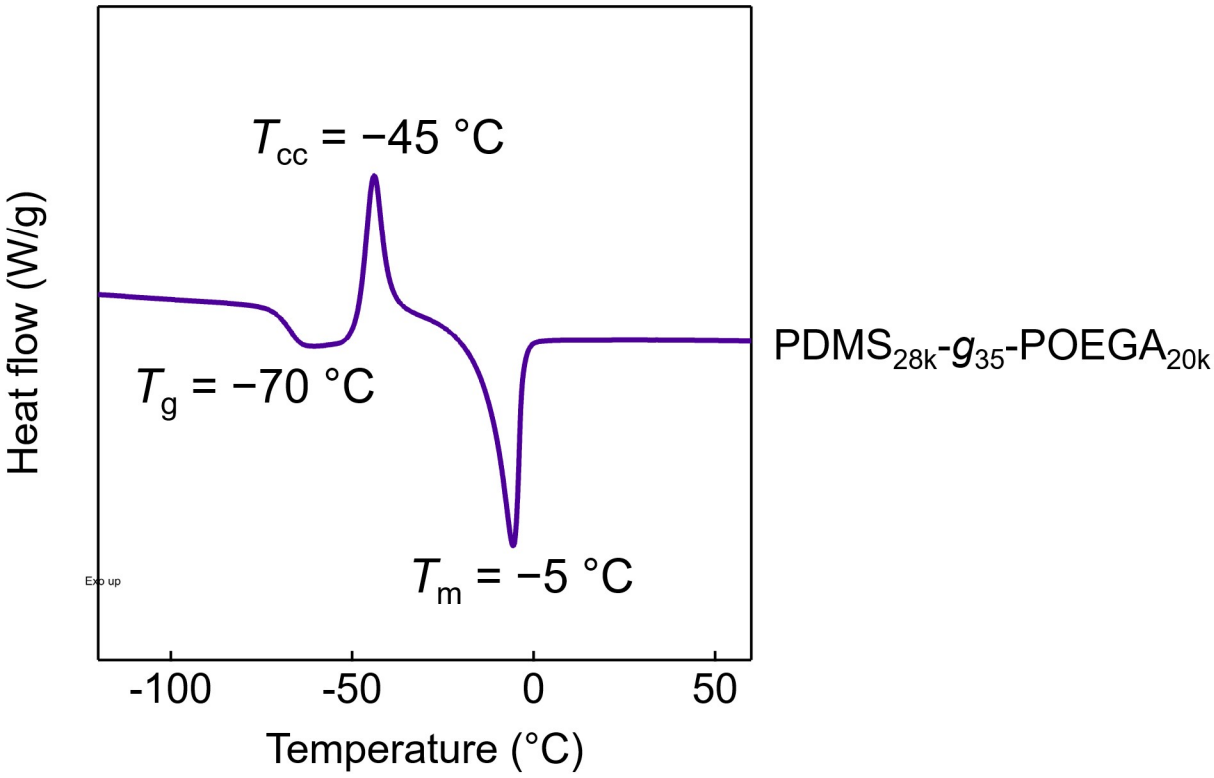

Figure 2.44. DSC trace for the listed graft copolymer with the labeled PDMS molecular weight, number of grafts, and molecular weight per graft calculated with NMR. Trace shown is the second heating cycle, heated at 10 °C per minute with the glass transition (T_g), cold crystallization exotherm (T_{cc}), and melting endotherm (T_m) labeled.

Table 2.3. Glass transition values (T_g) for selected macroinitiator and synthesized copolymers.

Sample	T_g (°C)
PDMS$_{28k}$-g_{35}-Br	–110
PDMS$_{28k}$-g_{35}-PMMA$_{20k}$	115
PDMS$_{28k}$-g_{35}-PS$_{23k}$	100

$PDMS_{28k}$-g_{35}-$PiBA_{29k}$	90
$PDMS_{28k}$-g_{35}-PMA_{17k}	10
$PDMS_{28k}$-g_{35}-$PTFEA_{18k}$	–10
$PDMS_{28k}$-g_{35}-$POEGA_{20k}$	–70

2.5.4 SEC traces of the copolymers before and after treatment with TBAF corresponding to entries in Table 2.2

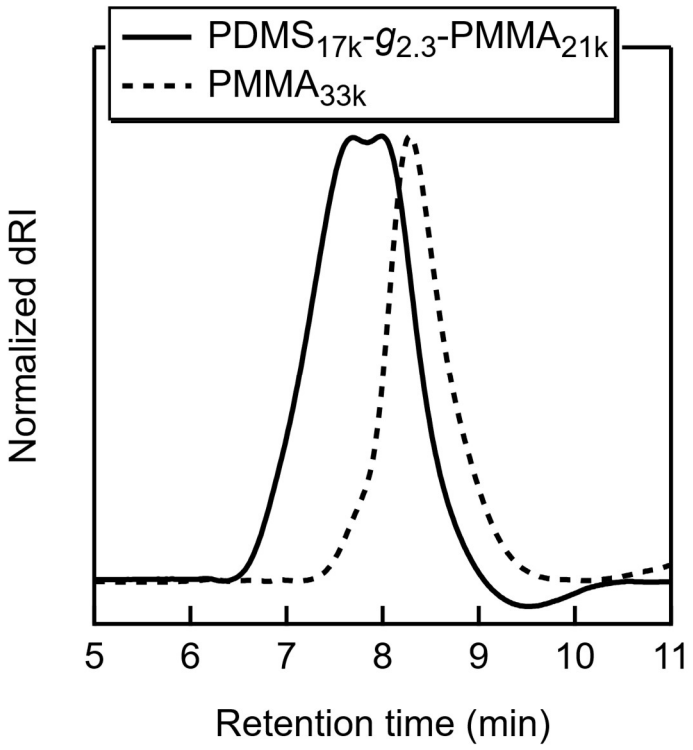

Figure 2.45. SEC trace of $PDMS_{17k}$-$g_{2.3}$-$PMMA_{21k}$ and the recovered linear PMMA after TBAF degradation of the graft copolymer.

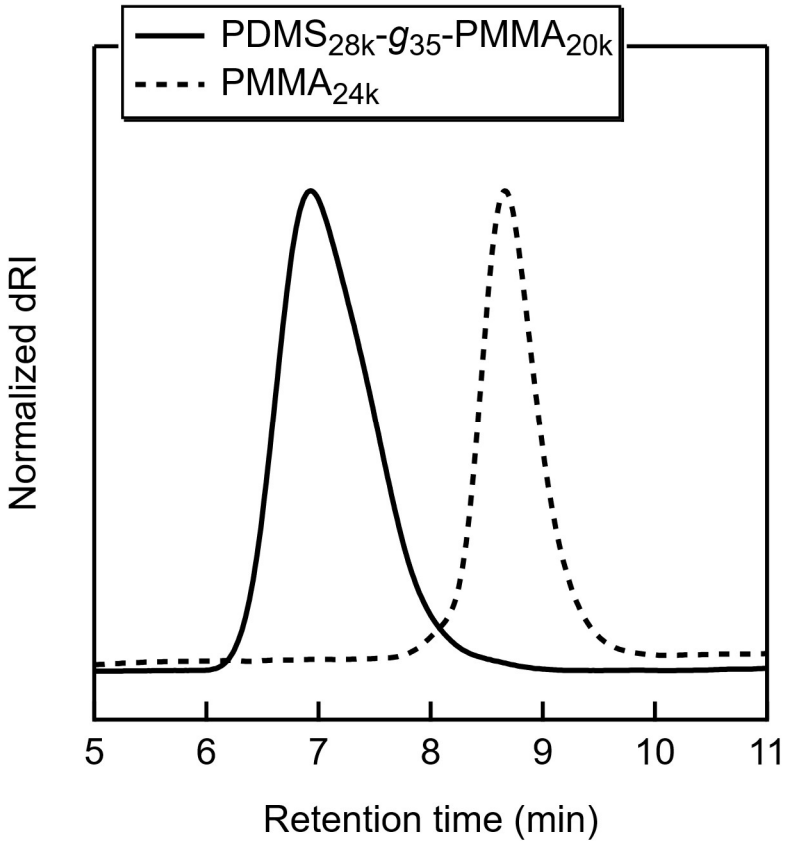

Figure 2.46. SEC trace of $PDMS_{28k}$-g_{35}-$PMMA_{20k}$ and the recovered linear PMMA after TBAF degradation of the graft copolymer.

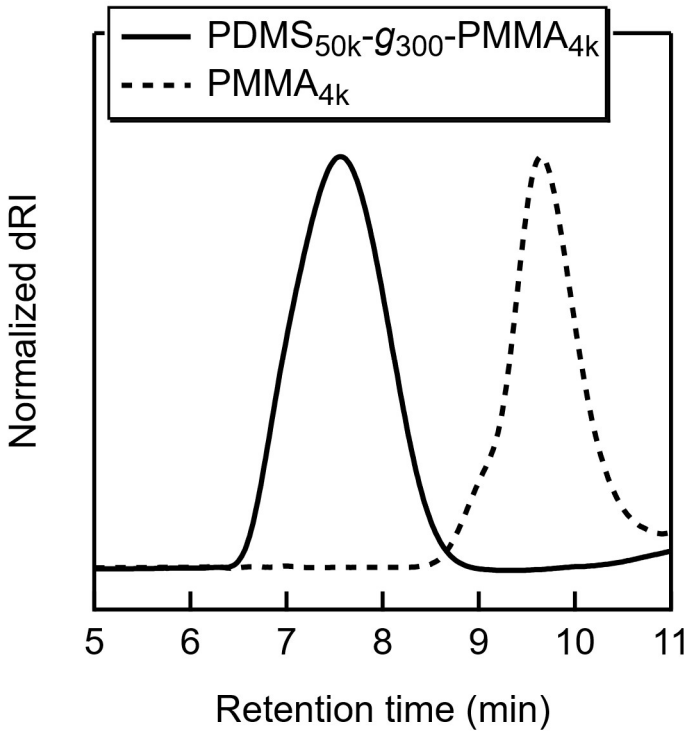

Figure 2.47. SEC trace of $PDMS_{50k}$-g_{300}-$PMMA_{3k}$ and the recovered linear PMMA after TBAF degradation of the graft copolymer.

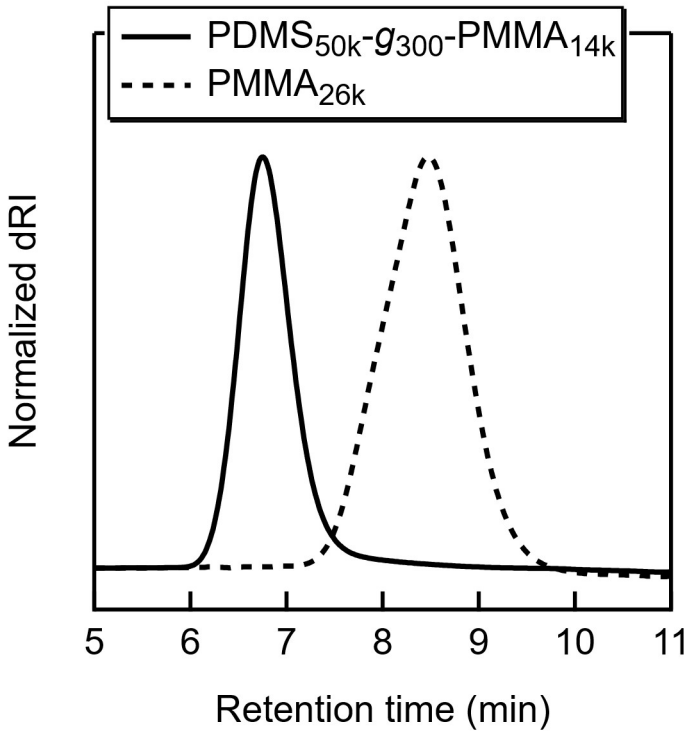

Figure 2.48. SEC trace of $PDMS_{50k}$-g_{300}-$PMMA_{14k}$ and the recovered linear PMMA after TBAF degradation of the graft copolymer.

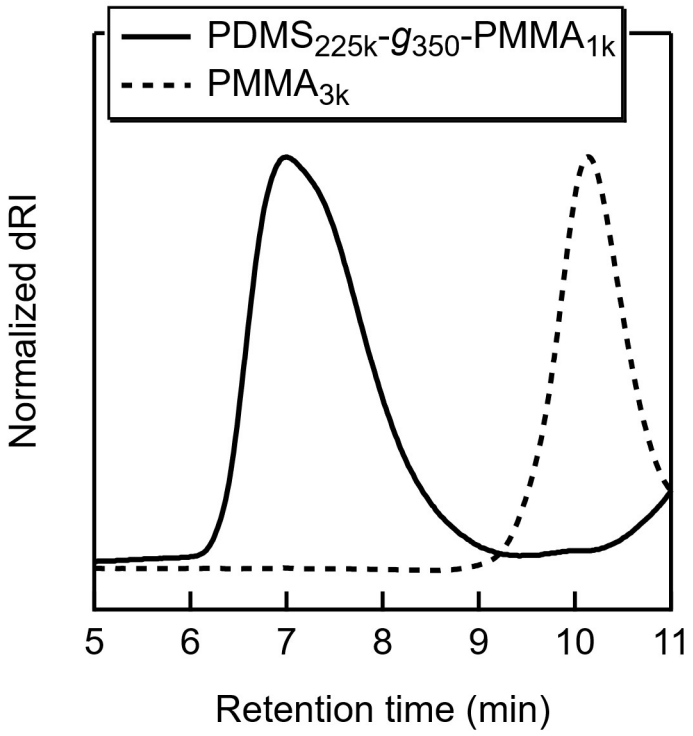

Figure 2.49. SEC trace of $PDMS_{225k}$-g_{350}-$PMMA_{1k}$ and the recovered linear PMMA after TBAF degradation of the graft copolymer.

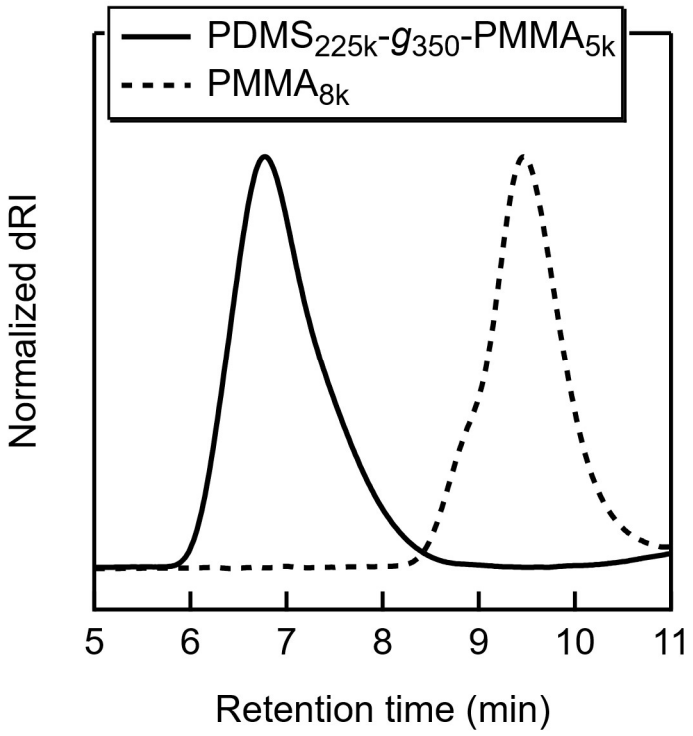

Figure 2.50. SEC trace of $PDMS_{225k}$-g_{350}-$PMMA_{5k}$ and the recovered linear PMMA after TBAF degradation of the graft copolymer.

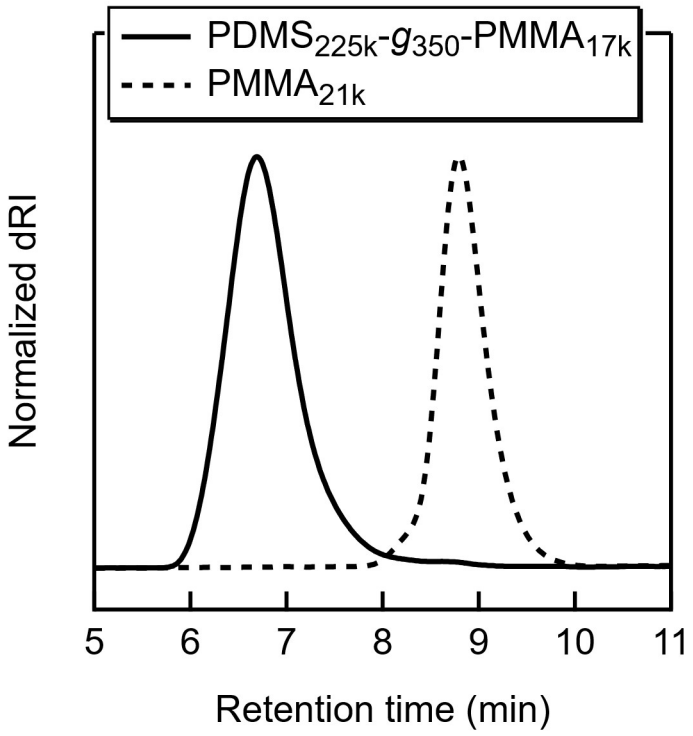

Figure 2.51. SEC trace of $PDMS_{225k}$-g_{350}-$PMMA_{17k}$ and the recovered linear PMMA after TBAF degradation of the graft copolymer.

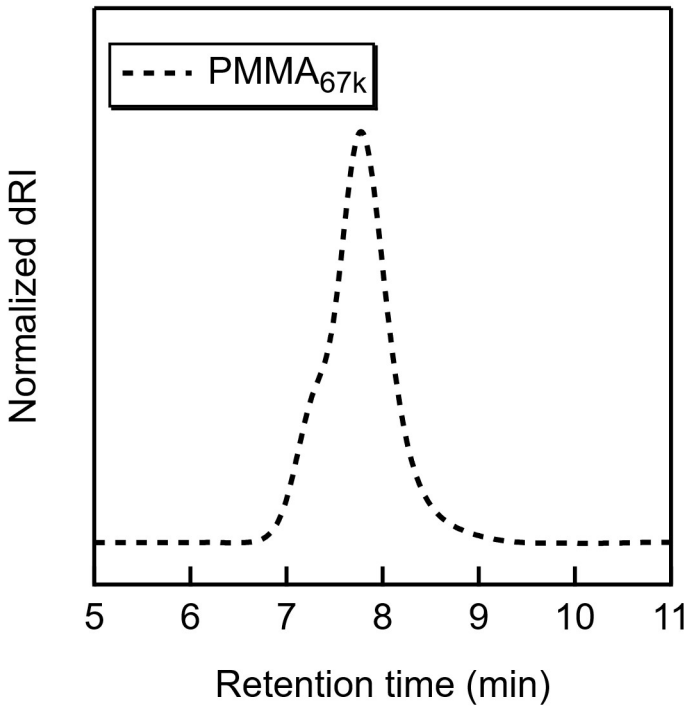

Figure 2.52. SEC trace of recovered linear PMMA from degradation of the polymer $PDMS_{225k}$-g_{350}-$PMMA_{68k}$. Graft copolymer trace is not shown because the polymer was too high molecular weight.

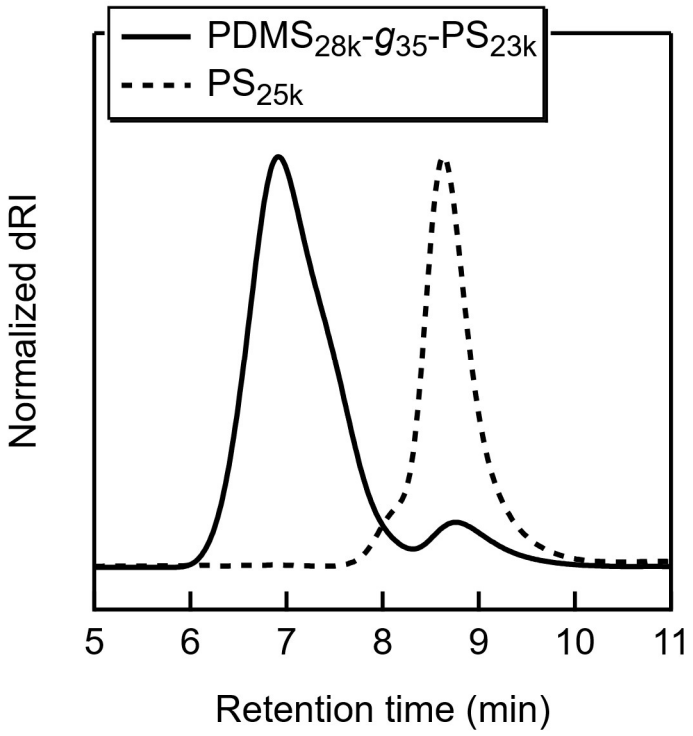

Figure 2.53. SEC trace of $PDMS_{28k}$-g_{35}-PS_{23k} and the recovered linear PS after TBAF degradation of the graft copolymer.

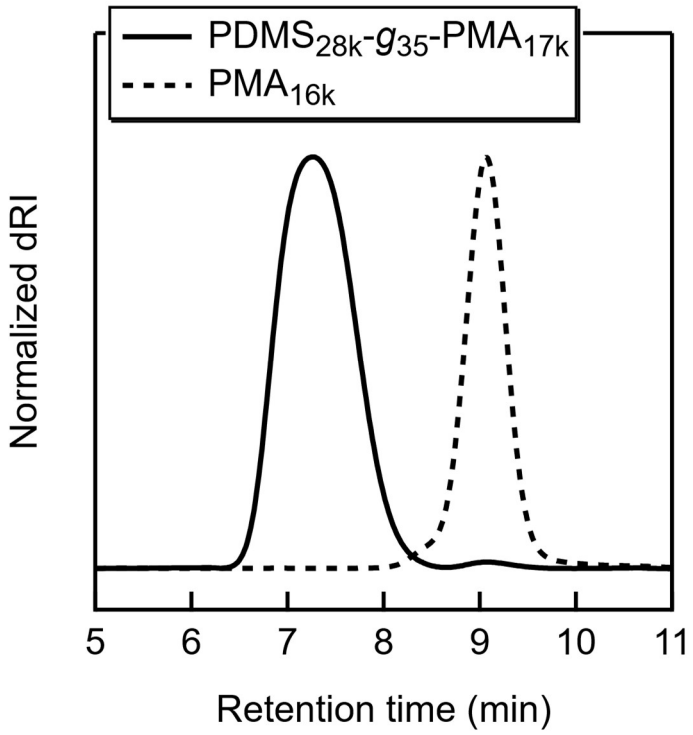

Figure 2.54. SEC trace of $PDMS_{28k}$-g_{35}-PMA_{17k} and the recovered linear PMA after TBAF degradation of the graft copolymer.

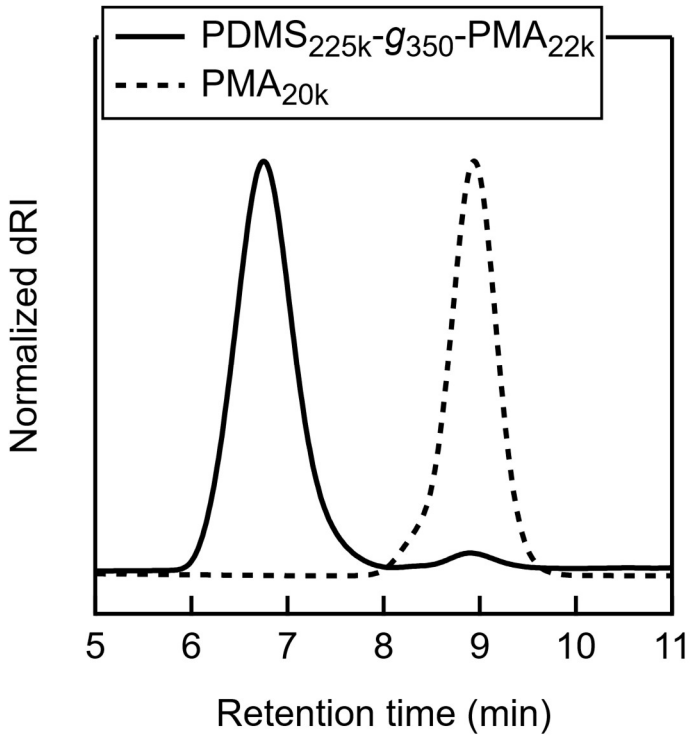

Figure 2.55. SEC trace of $PDMS_{225k}$-g_{350}-PMA_{22k} and the recovered linear PMA after TBAF degradation of the graft copolymer.

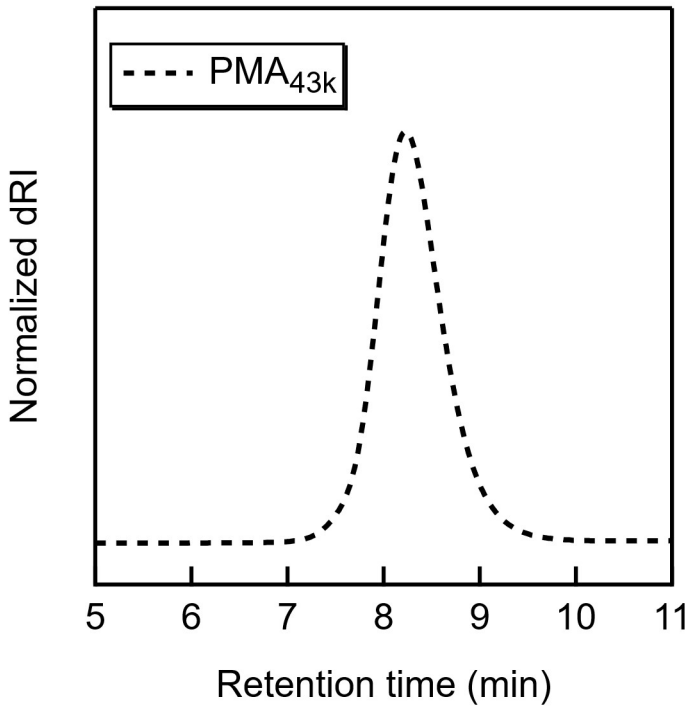

Figure 2.56. SEC trace of recovered linear PMA from degradation of the polymer $PDMS_{225k}$-g_{350}-PMA_{65k}. Graft copolymer trace is not shown because the polymer was too high molecular weight.

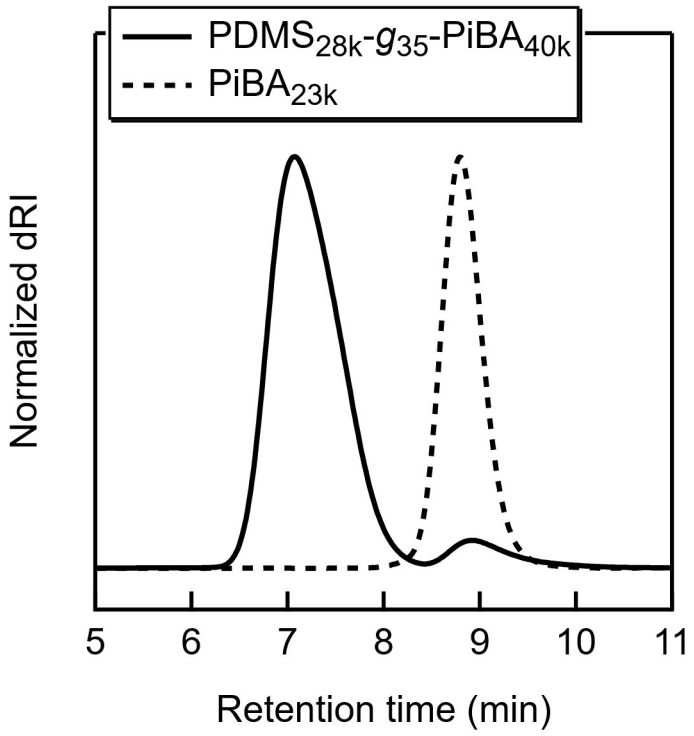

Figure 2.57. SEC trace of $PDMS_{28k}$-g_{35}-$PiBA_{40k}$ and the recovered linear PiBA after TBAF degradation of the graft copolymer.

2.5.5 Characterization of materials used to make copolymers with tunable grafting densities

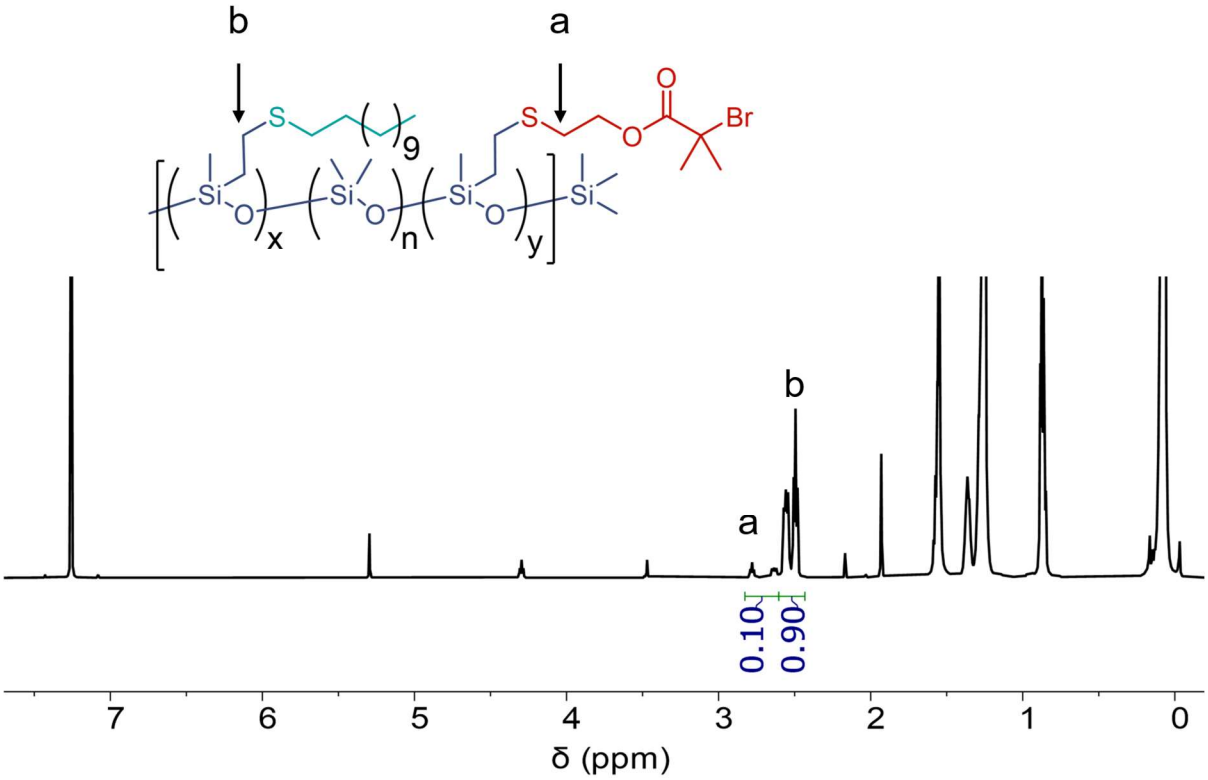

Figure 2.58. ^{1}H NMR spectrum of PDMS$_{225k}$-*g*$_{35}$-Br with peaks used to calculate the ratio of incorporated initiator and diluent labeled.

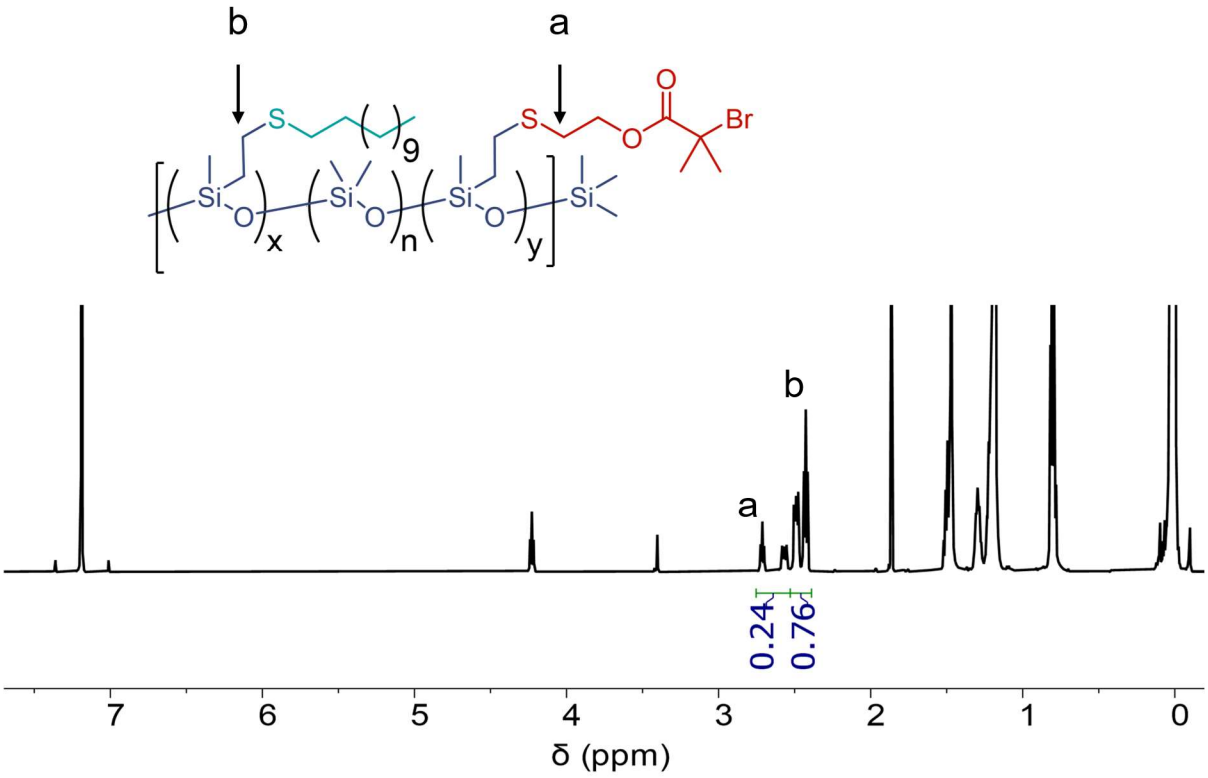

Figure 2.59. ^{1}H NMR spectrum of $PDMS_{225k}$-g_{80}-Br with peaks used to calculate the ratio of incorporated initiator and diluent labeled.

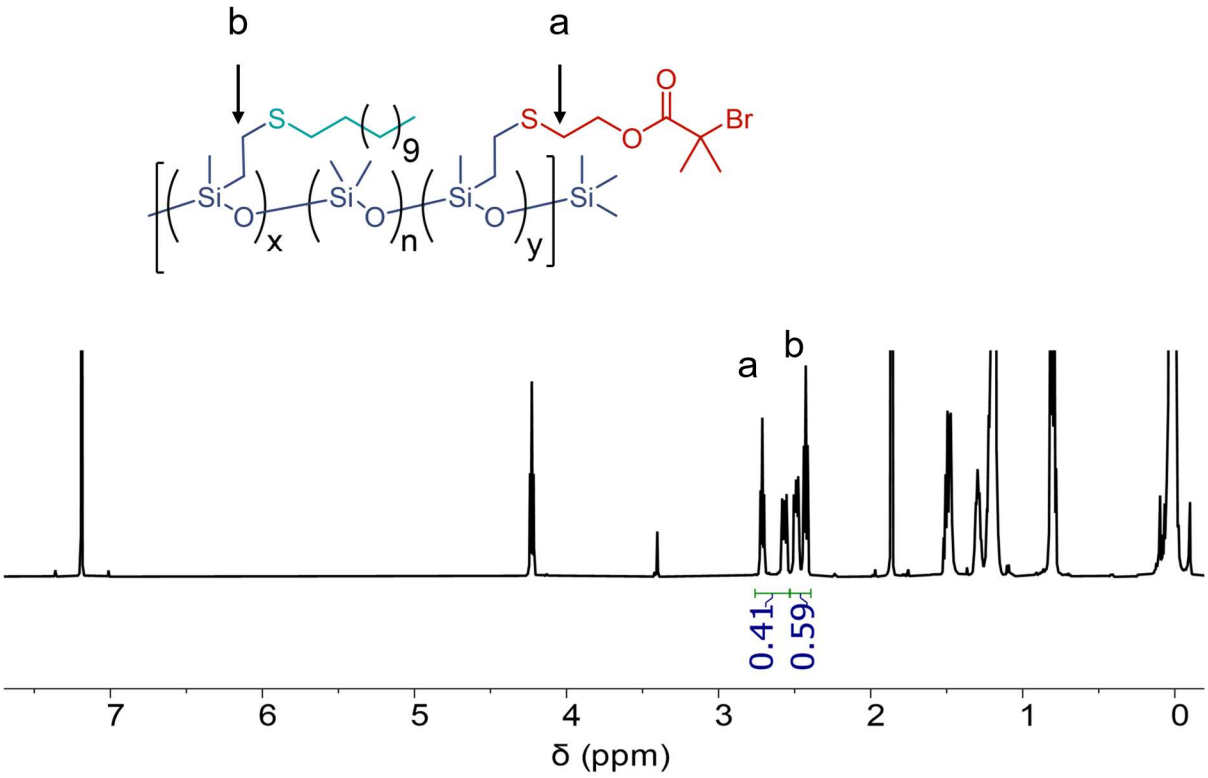

Figure 2.60. ^{1}H NMR spectrum of PDMS$_{225k}$-g_{140}-Br with peaks used to calculate the ratio of incorporated initiator and diluent labeled.

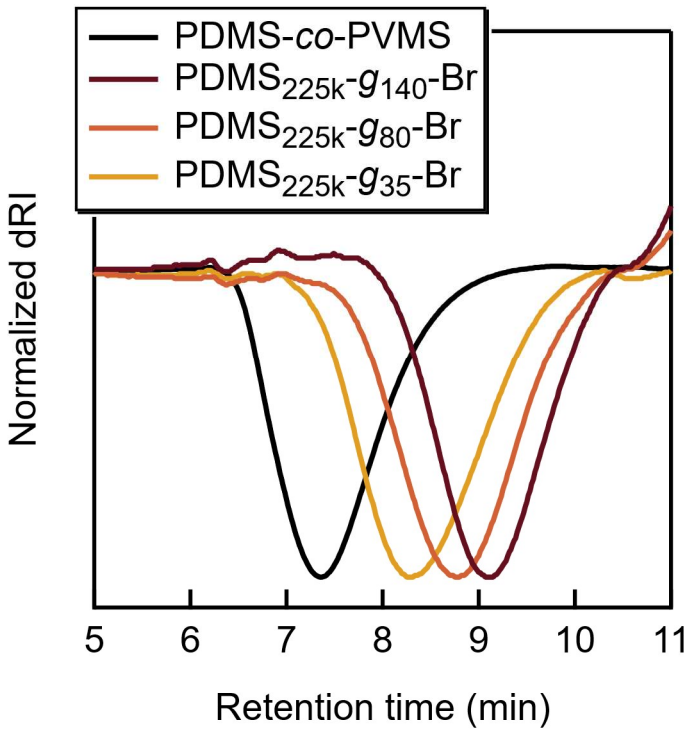

Figure 2.61. SEC traces of PDMS-*co*-PVMS (VDT-954) and the resulting macroinitiators after attaching DDSH and HS–EBiB through thiol–ene click chemistry with varying ratios to achieve the targeted amount of initiation sites.

Table 2.4. Dispersity and molecular weight of the graft copolymers synthesized with variable grafting density and the dispersity and molecular weight of the recovered linear PMMA. Copolymer molecular weights were calculated through ^{1}H NMR, and homopolymer molecular weight were measured via SEC compared to PMMA standards.

Sample	Copolymer M_n (kDa)	PMMA M_n (kDa)	PMMA $Đ$

$PDMS_{225k}$-g_{35}-$PMMA_{17k}$	2900	21	1.24
$PDMS_{225k}$-g_{80}-$PMMA_{16k}$	1600	23	1.23
$PDMS_{225k}$-g_{140}-$PMMA_{18k}$	840	26	1.15

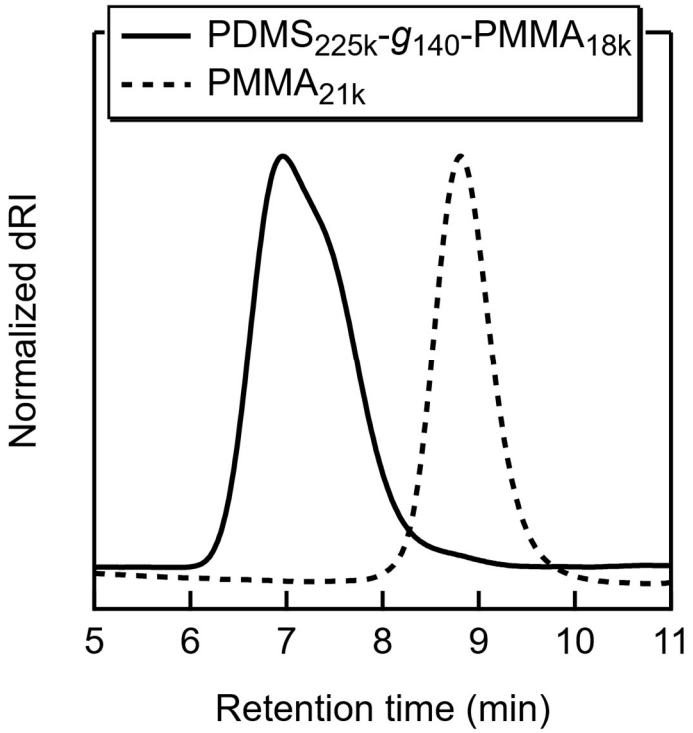

Figure 2.62. SEC trace of $PDMS_{225k}$-g_{140}-$PMMA_{18k}$ and the recovered linear PMMA after TBAF degradation of the graft copolymer.

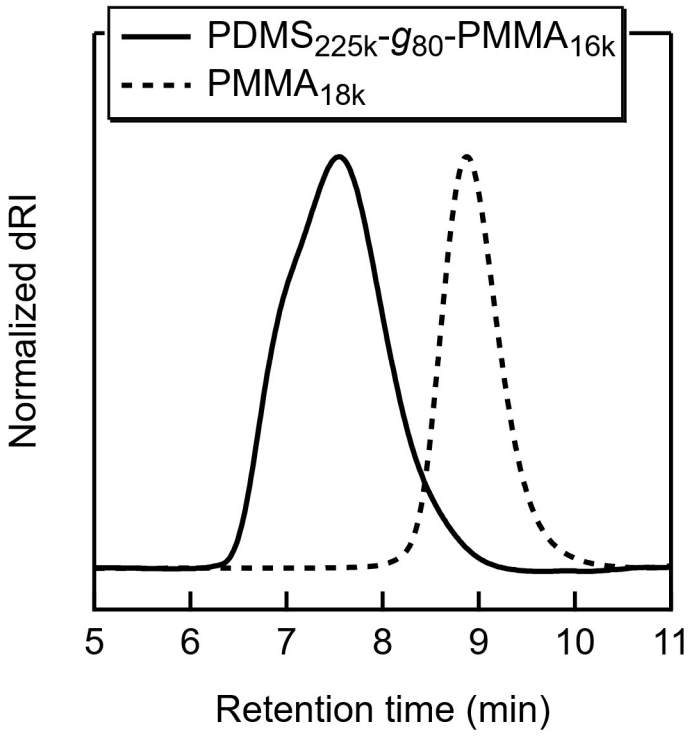

Figure 2.63. SEC trace of $PDMS_{225k}$-g_{80}-$PMMA_{16k}$ and the recovered linear PMMA after TBAF degradation of the graft copolymer.

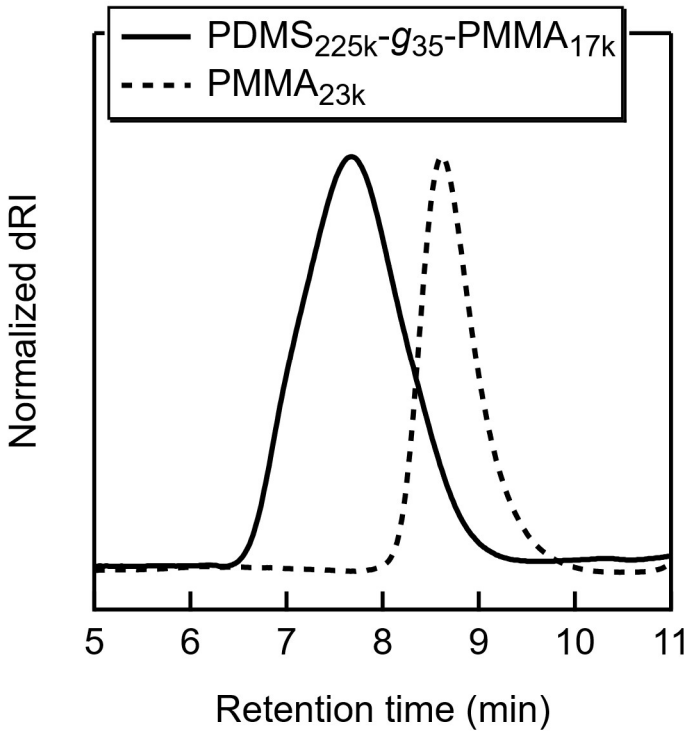

Figure 2.64. SEC trace of $PDMS_{225k}$-g_{35}-$PMMA_{17k}$ and the recovered linear PMMA after TBAF degradation of the graft copolymer

2.5.6 Characterization of macroinitiator and graft copolymer with covalently attached fluorophore

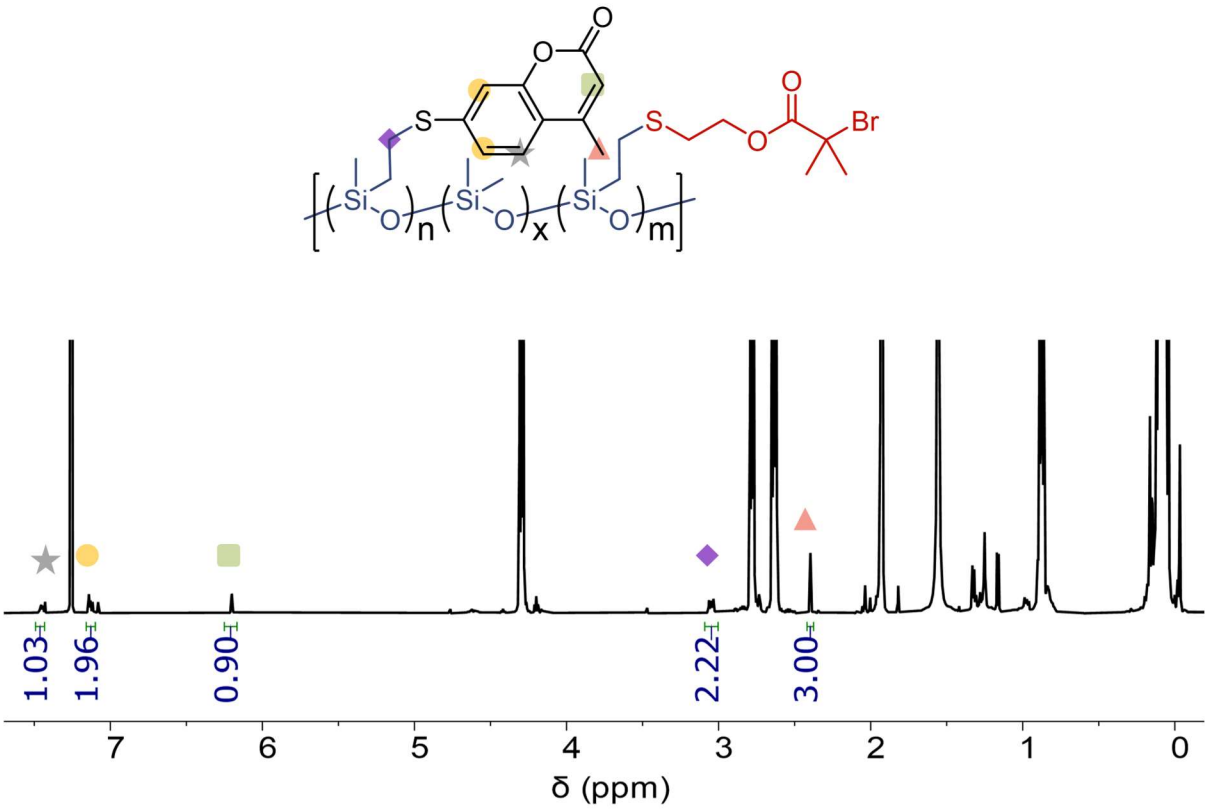

Figure 2.65. NMR spectrum corresponding to $PDMS_{28k}$-g_{35}-Br with covalently bound methylcoumarin units. Diagnostic protons corresponding to methylcoumarin are highlighted.

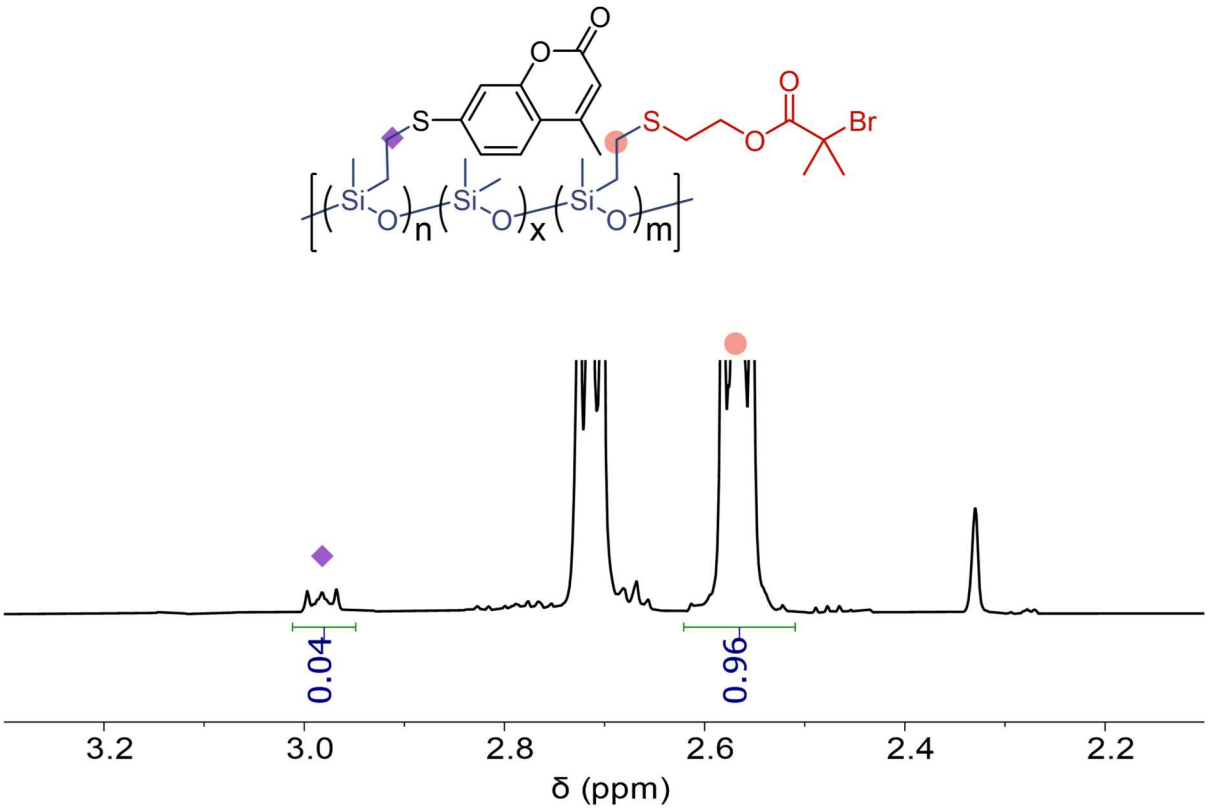

Figure 2.66. Zoomed in ^{1}H NMR spectrum corresponding to Figure S57. Highlighted peaks correspond to the signals used to quantify the incorporation of methylcoumarin.

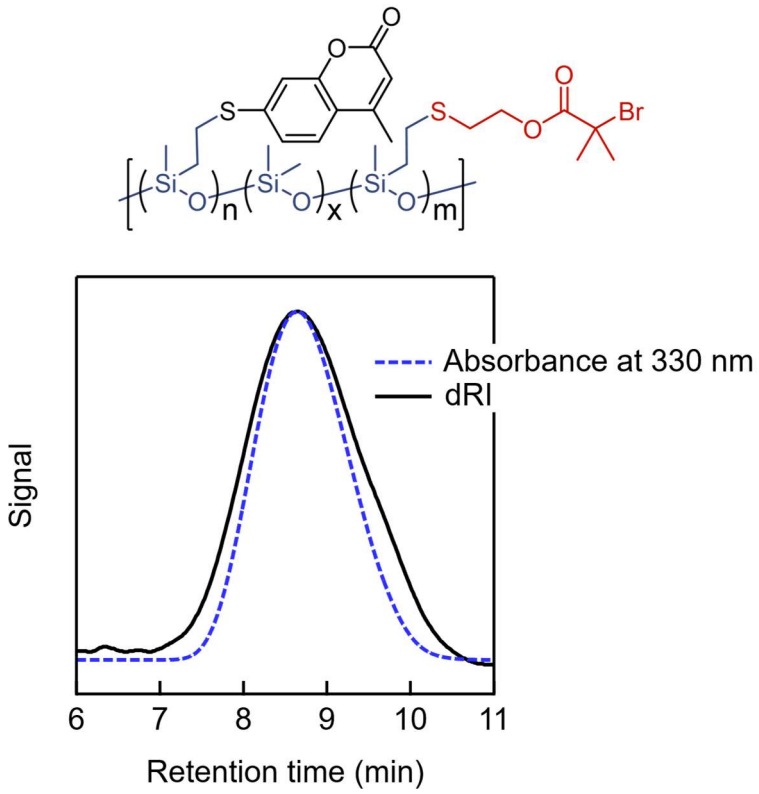

Figure 2.67. SEC trace of macroinitiator with attached fluorophore with dRI (solid) signal and light absorbance at 330 nm from photodiode array detector (dashed).

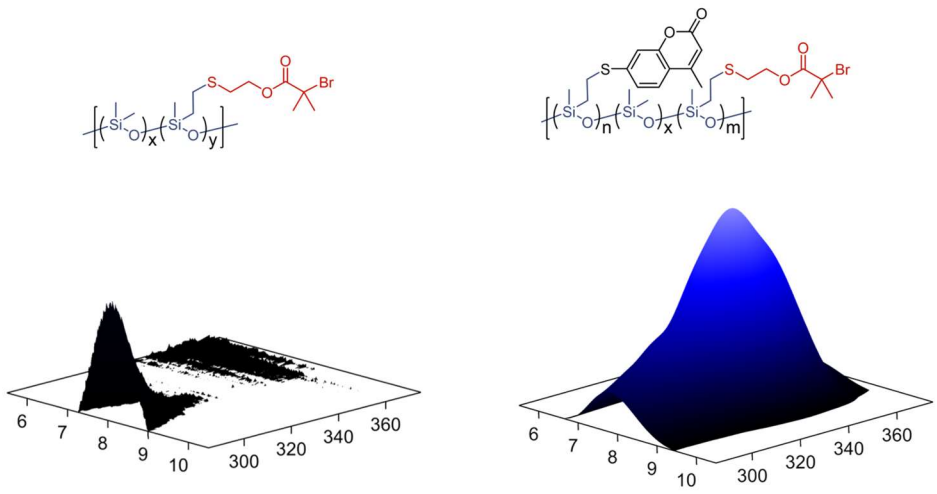

Figure 2.68. 3D SEC light absorbance plots showing light absorbance versus retention time and wavelength for macroinitiator without fluorophore (left) and with fluorophore (right).

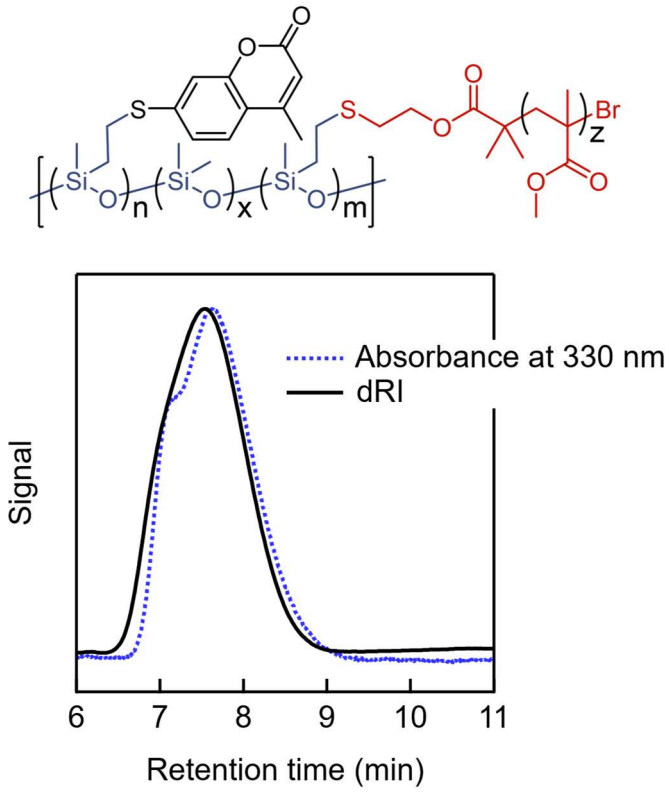

Figure 2.69. SEC trace of graft copolymer, $PDMS_{28k}$-g_{35}-$PMMA_{8k}$ with attached fluorophore with dRI (solid) signal and light absorbance at 330 nm from photodiode array detector (dashed).

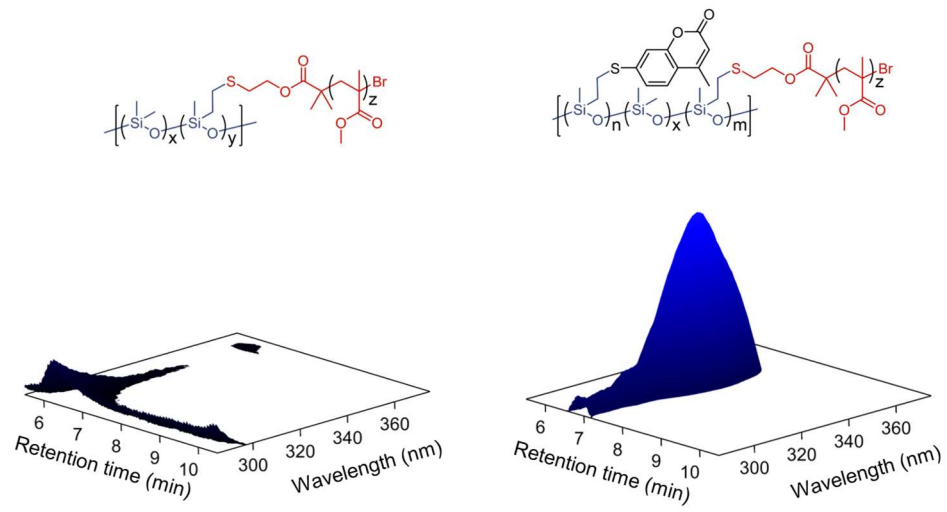

Figure 2.70. 3D SEC light absorbance plots showing light absorbance versus retention time and wavelength for graft copolymer without fluorophore (left) and with fluorophore (right).

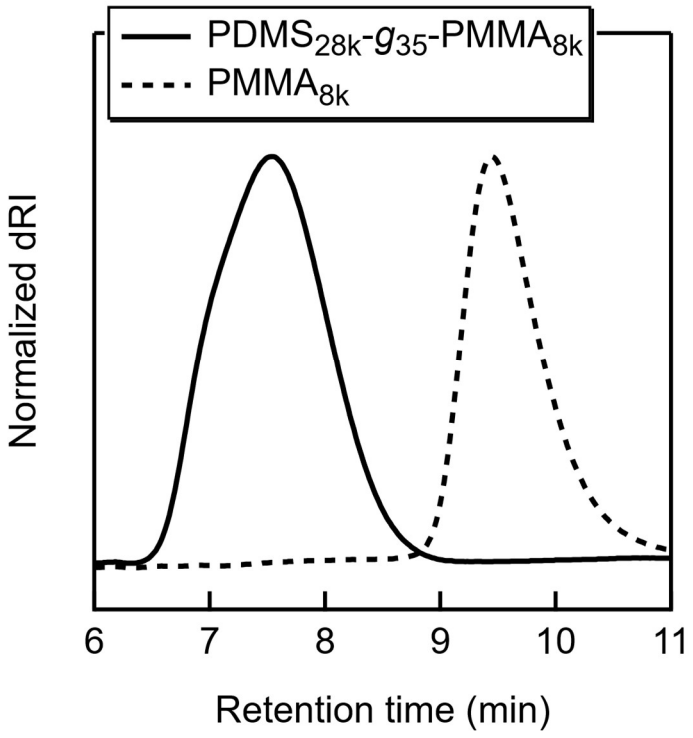

Figure 2.71. SEC trace of fluorescent graft copolymer $PDMS_{28k}$-g_{35}-$PMMA_{8k}$ and the recovered linear $PMMA_{8k}$ after TBAF degradation of the graft copolymer.

2.6 References

(1) Matsen, M. W. Effect of Architecture on the Phase Behavior of AB-Type Block Copolymer Melts. *Macromolecules* **2012**, *45* (4), 2161–2165.

(2) Levi, A. E.; Lequieu, J.; Horne, J. D.; Bates, M. W.; Ren, J. M.; Delaney, K. T.; Fredrickson, G. H.; Bates, C. M. Miktoarm Stars via Grafting-Through Copolymerization: Self-Assembly and the Star-to-Bottlebrush Transition. *Macromolecules* **2019**, *52* (4), 1794–1802.

(3) Allen, M. J.; Wangkanont, K.; Raines, R. T.; Kiessling, L. L. ROMP from ROMP: A New Approach to Graft Copolymer Synthesis. *Macromolecules* **2009**, *42* (12), 4023–4027.

(4) Chang, A. B.; Lin, T. P.; Thompson, N. B.; Luo, S. X.; Liberman-Martin, A. L.; Chen, H. Y.; Lee, B.; Grubbs, R. H. Design, Synthesis, and Self-Assembly of Polymers with Tailored Graft Distributions. *J Am Chem Soc* **2017**, *139* (48), 17683–17693.

(5) Zografos, A.; Lynd, N. A.; Bates, F. S.; Hillmyer, M. A. Impact of Macromonomer Molar Mass and Feed Composition on Branch Distributions in Model Graft Copolymerizations. *ACS Macro Lett* **2021**, *10* (12), 1622–1628.

(6) Hadjichristidis, N.; Iatrou, H.; Pitsikalis, M.; Mays, J. Macromolecular Architectures by Living and Controlled/Living Polymerizations. *Prog Polym Sci* **2006**, *31* (12), 1068–1132.

(7) Ohno, S.; Matyjaszewski, K. Controlling Grafting Density and Side Chain Length in Poly(n-Butyl Acrylate) by ATRP Copolymerization of Macromonomers. *J Polym Sci A Polym Chem* **2006**, *44* (19), 5454–5467.

(8) Jeong, S. H.; Kim, J. M.; Baig, C. Rheological Influence of Short-Chain Branching for Polymeric Materials under Shear with Variable Branch Density and Branching Architecture. *Macromolecules* **2017**, *50* (11), 4491–4500.

(9) Paturej, J.; Sheiko, S. S.; Panyukov, S.; Rubinstein, M. Molecular Structure of Bottlebrush Polymers in Melts. *Sci Adv* **2016**, *2* (11), e1601478.

(10) Liang, H.; Cao, Z.; Wang, Z.; Sheiko, S. S.; Dobrynin, A. V. Combs and Bottlebrushes in a Melt. *Macromolecules* **2017**, *50* (8), 3430–3437.

(11) Abadi, M.; Serag, M. F.; Habuchi, S. Entangled Polymer Dynamics beyond Reptation. *Nat Commun* **2018**, *9*, 5098.

(12) Savoji, M. T.; Zhao, D.; Muisener, R. J.; Schimossek, K.; Schoeller, K.; Lodge, T. P.; Hillmyer, M. A. Poly(Alkyl Methacrylate)-Grafted Polyolefins as Viscosity Modifiers for Engine Oil: A New Mechanism for Improved Performance. *Ind Eng Chem Res* **2018**, *57* (6), 1840–1850.

(13) Brant, P.; Lu, J.; Shivokhin, M.; Yakovlev, S.; Kang, S.; Welke, B.; Raney, M.; Throckmorton, J.; Rapp, J.; Wang, H.; Yablon, D. Strategy for Scalable Comb Block Polyolefin Synthesis. Efficient Graft of Isotactic Polypropylene to a Commercial Broad Molecular Weight Distribution, Hyperbranched, Ethylene Methylacrylate Copolymer. *Macromolecules* **2020**, *53* (15), 6353–6368.

(14) Wang, W.; Lu, W.; Goodwin, A.; Wang, H.; Yin, P.; Kang, N. G.; Hong, K.; Mays, J. W. Recent Advances in Thermoplastic Elastomers from Living Polymerizations:

Macromolecular Architectures and Supramolecular Chemistry. *Prog Polym Sci* **2019**, *95*, 1–31.

(15) Lynd, N. A.; Oyerokun, F. T.; O'Donoghue, D. L.; Handlin, D. L.; Fredrickson, G. H. Design of Soft and Strong Thermoplastic Elastomers Based on Nonlinear Block Copolymer Architectures Using Self-Consistent-Field Theory. *Macromolecules* **2010**, *43* (7), 3479–3486.

(16) Zhang, J.; Schneiderman, D. K.; Li, T.; Hillmyer, M. A.; Bates, F. S. Design of Graft Block Polymer Thermoplastics. *Macromolecules* **2016**, *49* (23), 9108–9118.

(17) Zhang, J.; Li, T.; Mannion, A. M.; Schneiderman, D. K.; Hillmyer, M. A.; Bates, F. S. Tough and Sustainable Graft Block Copolymer Thermoplastics. *ACS Macro Lett* **2016**, *5* (3), 407–412.

(18) Lu, C.; Yu, J.; Wang, C.; Wang, J.; Chu, F. Fabrication of UV-Absorbent Cellulose-Rosin Based Thermoplastic Elastomer via "Graft from" ATRP. *Carbohydr Polym* **2018**, *188*, 128–135.

(19) Jiang, F.; Wang, Z.; Qiao, Y.; Wang, Z.; Tang, C. A Novel Architecture toward Third-Generation Thermoplastic Elastomers by a Grafting Strategy. *Macromolecules* **2013**, *46* (12), 4772–4780.

(20) Liberman-Martin, A. L.; Chu, C. K.; Grubbs, R. H. Application of Bottlebrush Block Copolymers as Photonic Crystals. *Macromol Rapid Commun* **2017**, *38* (13), 1700058.

(21) Wang, Z.; Chan, C. L. C.; Zhao, T. H.; Parker, R. M.; Vignolini, S. Recent Advances in Block Copolymer Self-Assembly for the Fabrication of Photonic Films and Pigments. *Adv Opt Mater* **2021**, *9* (21), 2100519.

(22) Kerr-Phillips, T.; Damavandi, M.; Pilkington, L. I.; Whitehead, K. A.; Travas-Sejdic, J.; Barker, D. Effects of Neutral, Anionic and Cationic Polymer Brushes Grafted from Poly(Para-Phenylene Vinylene) and Poly(Para-Phenylene Ethynylene) on the Polymer's Photoluminescent Properties. *Polymers* **2022**, *14* (14).

(23) Reynolds, V. G.; Mukherjee, S.; Xie, R.; Levi, A. E.; Atassi, A.; Uchiyama, T.; Wang, H.; Chabinyc, M. L.; Bates, C. M. Super-Soft Solvent-Free Bottlebrush Elastomers for Touch Sensing. *Mater Horiz* **2020**, *7* (1), 181–187.

(24) Nian, S.; Zhu, J.; Zhang, H.; Gong, Z.; Freychet, G.; Zhernenkov, M.; Xu, B.; Cai, L. H. Three-Dimensional Printable, Extremely Soft, Stretchable, and Reversible Elastomers from Molecular Architecture-Directed Assembly. *Chemistry of Materials* **2021**, *33* (7), 2436–2445.

(25) Xie, R.; Mukherjee, S.; Levi, A. E.; Reynolds, V. G.; Wang, H.; Chabinyc, M. L.; Bates, C. M. Room Temperature 3D Printing of Super-Soft and Solvent-Free Elastomers. *Sci Adv* **2020**, *6* (46), eabc6900.

(26) Self, J. L.; Zervoudakis, A. J.; Peng, X.; Lenart, W. R.; Macosko, C. W.; Ellison, C. J. Linear, Graft, and Beyond: Multiblock Copolymers as Next-Generation Compatibilizers. *JACS Au* **2022**, *2* (2), 310–321.

(27) Fortelný, I.; Jůza, J. The Effects of Copolymer Compatibilizers on the Phase Structure Evolution in Polymer Blends—a Review. *Materials* **2021**, *14* (24), 7786.

(28) Klimovica, K.; Pan, S.; Lin, T. W.; Peng, X.; Ellison, C. J.; Lapointe, A. M.; Bates, F. S.; Coates, G. W. Compatibilization of IPP/HDPE Blends with PE-g-IPP Graft Copolymers. *ACS Macro Lett* **2020**, *9* (8), 1161–1166.

(29) Sarkar, R.; Gowd, E. B.; Ramakrishnan, S. Precise Control of Grafting Density in Periodically Grafted Amphiphilic Copolymers: An Alternate Strategy to Fine-Tune the Lamellar Spacing in the Sub-10 Nm Regime. *Polym Chem* **2020**, *11* (25), 4143–4154.

(30) Hadjichristidis, N.; Pitsikalis, M.; Pispas, S.; Iatrou, H. Polymers with Complex Architecture by Living Anionic Polymerization. *Chem Rev* **2001**, *101* (12), 3747–3792.

(31) Riva, R.; Schmeits, S.; Jérôme, C.; Jérôme, R.; Lecomte, P. Combination of Ring-Opening Polymerization and "Click Chemistry": Toward Functionalization and Grafting of Poly(ε-Caprolactone). *Macromolecules* **2007**, *40* (4), 796–803.

(32) Huang, J.; Xiao, Z.; Liang, H.; Lu, J. Star Graft Copolymer via Grafting-onto Strategy Using a Combination of Reversible Addition-Fragmentation Chain Transfer Arm-First Technique and Aldehyde-Aminooxy Click Reaction. *Polym Int* **2014**, *63* (6), 1122–1128.

(33) Turowec, B. A.; Gillies, E. R. Synthesis, Properties and Degradation of Polyisobutylene–Polyester Graft Copolymers. *Polym Int* **2017**, *66* (1), 42–51.

(34) Karamdoust, S.; Crewdson, P.; Ingratta, M.; Gillies, E. R. Synthesis and Properties of Arborescent Polyisobutylene-Poly(Ethylene Oxide) Graft Copolymers: A Comparison of Linear and Arborescent Graft Copolymer Architectures. *Polym Int* **2015**, *64* (5), 611–620.

(35) Karamdoust, S.; Bonduelle, C. V.; Amos, R. C.; Turowec, B. A.; Guo, S.; Ferrari, L.; Gillies, E. R. Synthesis and Properties of Butyl Rubber-Poly(Ethylene Oxide) Graft Copolymers with High PEO Content. *J Polym Sci A Polym Chem* **2013**, *51* (16), 3383–3394.

(36) Soleimani, A.; Moustafa, M. M. A. R.; Borecki, A.; Gillies, E. R. A Comparison of Covalent and Noncovalent Strategies for Paclitaxel Release Using Poly(Ester Amide) Graft Copolymer Micelles. *Can J Chem* **2015**, *93* (4), 399–405. https://doi.org/10.1139/cjc-2014-0349.

(37) Higuchi, M.; Kanazawa, A.; Aoshima, S. Design of Graft Architectures via Simultaneous Kinetic Control of Cationic Vinyl-Addition Polymerization of Vinyl Ethers, Coordination Ring-Opening Polymerization of Cyclic Esters, and Merging at the Propagating Chain End. *Macromolecules* **2020**, *53* (10), 3822–3831.

(38) Lin, T. P.; Chang, A. B.; Chen, H. Y.; Liberman-Martin, A. L.; Bates, C. M.; Voegtle, M. J.; Bauer, C. A.; Grubbs, R. H. Control of Grafting Density and Distribution in Graft Polymers by Living Ring-Opening Metathesis Copolymerization. *J Am Chem Soc* **2017**, *139* (10), 3896–3903.

(39) Wang, W.; Wang, W.; Lu, X.; Bobade, S.; Chen, J.; Kang, N. G.; Zhang, Q.; Mays, J. Synthesis and Characterization of Comb and Centipede Multigraft Copolymers PnBA-g-PS with High Molecular Weight Using Miniemulsion Polymerization. *Macromolecules* **2014**, *47* (21), 7284–7295.

(40) Wang, Z.; Yuan, L.; Tang, C. Sustainable Elastomers from Renewable Biomass. *Acc Chem Res* **2017**, *50* (7), 1762–1773.

(41) Dadashi-Silab, S.; Doran, S.; Yagci, Y. Photoinduced Electron Transfer Reactions for Macromolecular Syntheses. *Chem Rev* **2016**, *116* (17), 10212–10275.

(42) Matyjaszewski, K. Advanced Materials by Atom Transfer Radical Polymerization. *Advanced Materials* **2018**, *30* (23), 1706441.

(43) Maharana, T.; Pattanaik, S.; Routaray, A.; Nath, N.; Sutar, A. K. Synthesis and Characterization of Poly(Lactic Acid) Based Graft Copolymers. *React Funct Polym* **2015**, *93*, 47–67.

(44) Thakur, M. K.; Thakur, V. K.; Gupta, R. K.; Pappu, A. Synthesis and Applications of Biodegradable Soy Based Graft Copolymers: A Review. *ACS Sustain Chem Eng* **2016**, *4* (1), 1–17.

(45) Baek, P.; Voorhaar, L.; Barker, D.; Travas-Sejdic, J. Molecular Approach to Conjugated Polymers with Biomimetic Properties. *Acc Chem Res* **2018**, *51* (7), 1581–1589.

(46) Guo, X.; Choi, B.; Feng, A.; Thang, S. H. Polymer Synthesis with More Than One Form of Living Polymerization Method. *Macromol Rapid Commun* **2018**, *39* (20), 1800479.

(47) Sumerlin, B. S.; Neugebauer, D.; Matyjaszewski, K. Initiation Efficiency in the Synthesis of Molecular Brushes by Grafting from via Atom Transfer Radical Polymerization. *Macromolecules* **2005**, *38* (3), 702–708.

(48) Wang, Z.; Wang, Z.; Zhang, Y.; Jiang, F.; Fang, H. Synthesis and Characterization of Designed Cellulose-Graft-Polyisoprene Copolymers. *Polym Chem* **2014**, *5* (10), 3379–3388.

(49) Wang, M.; Kee, S.; Baek, P.; Ting, M. S.; Zujovic, Z.; Barker, D.; Travas-Sejdic, J. Photo-Patternable, Stretchable and Electrically Conductive Graft Copolymers of Poly(3-Hexylthiophene). *Polym Chem* **2019**, *10* (46), 6278–6289.

(50) Damavandi, M.; Baek, P.; Pilkington, L. I.; Javed Chaudhary, O.; Burn, P.; Travas-Sejdic, J.; Barker, D. Synthesis of Grafted Poly(p-Phenyleneethynylene) via ARGET ATRP: Towards Nonaggregating and Photoluminescence Materials. *Eur Polym J* **2017**, *89*, 263–271.

(51) Wang, Z.; Yuan, L.; Tang, C. Sustainable Elastomers from Renewable Biomass. *Acc Chem Res* **2017**, *50* (7), 1762–1773.

(52) Polymeropoulos, G.; Zapsas, G.; Ntetsikas, K.; Bilalis, P.; Gnanou, Y.; Hadjichristidis, N. 50th Anniversary Perspective: Polymers with Complex Architectures. *Macromolecules* **2017**, *50* (4), 1253–1290.

(53) Strover, L. T.; Malmström, J.; Travas-Sejdic, J. Graft Copolymers with Conducting Polymer Backbones: A Versatile Route to Functional Materials. *The Chemical Record* **2016**, *16* (1), 393–418.

(54) Coudane, J.; Van Den Berghe, H.; Mouton, J.; Garric, X.; Nottelet, B. Poly(Lactic Acid)-Based Graft Copolymers: Syntheses Strategies and Improvement of Properties for Biomedical and Environmentally Friendly Applications: A Review. *Molecules* **2022**, *27* (13), 4135.

(55) Feng, C.; Li, Y.; Yang, D.; Hu, J.; Zhang, X.; Huang, X. Well-Defined Graft Copolymers: From Controlled Synthesis to Multipurpose Applications. *Chem Soc Rev* **2011**, *40* (3), 1282–1295.

(56) Weinhold, F.; West, R. The Nature of the Silicon-Oxygen Bond. *Organometallics* **2011**, *30* (21), 5815–5824.

(57) *Silicones and Silicone-Modified Materials*, 1st ed.; Clarson, S. J., Fitzgerald, J. J., Owen, M. J., Smith, S. D., Eds.; American Chemical Society: Washington, DC, 2000.

(58) Berthier, E.; Young, E. W. K.; Beebe, D. Engineers Are from PDMS-Land, Biologists Are from Polystyrenia. *Lab Chip* **2012**, *12* (7), 1224–1237.

(59) Pouget, E.; Tonnar, J.; Lucas, P.; Lacroix-Desmazes, P.; Ganachaud, F.; Boutevin, B. Well-Architectured Poly(Dimethylsiloxane)-Containing Copolymers Obtained by Radical Chemistry. *Chem Rev* **2010**, *110* (3), 1233–1277.

(60) Nakagawa, Y.; Miller, P. J.; Matyjaszewski, K. Development of Novel Attachable Initiators for Atom Transfer Radical Polymerization, Synthesis of Block and Graft Copolymers from Poly(Dimethylsiloxane) Macroinitiators. *Polymer* **1998**, *39* (21), 5163–5170.

(61) Taran, E.; Donose, B.; Higashitani, K.; Asandei, A. D.; Scutaru, D.; Hurduc, N. ATRP Grafting of Styrene from Benzyl Chloride Functionalized Polysiloxanes: An AFM and TGA Study of the Cu(0)/Bpy Catalyst. *Eur Polym J* **2006**, *42* (1), 119–125.

(62) Seidi, F.; Salimi, H.; Shamsabadi, A. A.; Shabanian, M. Synthesis of Hybrid Materials Using Graft Copolymerization on Non-Cellulosic Polysaccharides via Homogenous ATRP. *Prog Polym Sci* **2018**, *76*, 1–39.

(63) Huang, C.; Yi, L.; Yuan, H.; Chen, C. A Route to Modify Polymeric Pigment Dispersants with Polysiloxanes by Atom Transfer Radical Polymerization. *Adv Mat Res* **2012**, *441*, 478–483.

(64) Wang, G.; Xiong, Y.; Tang, H. Synthesis and Characterization of a Graft Side-Chain Liquid Crystalline Polysiloxane. *J Organomet Chem* **2015**, *775*, 50–54.

(65) Hong, S. C.; Pakula, T.; Matyjaszewski, K. Preparation of Polyisobutene-Graft-Poly(Methyl Methacrylate) and Polyisobutene-Graft-Polystyrene with Different Compositions and Side Chain Architectures through Atom Transfer Radical Polymerization (ATRP). *Macromol Chem Phys* **2001**, *202* (17), 3392–3402.

(66) Shi, L. Y.; Zhou, Y.; Shen, Z.; Fan, X. H. Hierarchical Structures in Thin Films of Macrophase- and Microphase-Separated AB/AC Diblock Copolymer Blends. *Macromolecules* **2012**, *45* (13), 5530–5537.

(67) Levi, A. E.; Fu, L.; Lequieu, J.; Horne, J. D.; Blankenship, J.; Mukherjee, S.; Zhang, T.; Fredrickson, G. H.; Gutekunst, W. R.; Bates, C. M. Efficient Synthesis of Asymmetric Miktoarm Star Polymers. *Macromolecules* **2020**, *53* (2), 702–710.

(68) Murphy, E. A.; Chen, Y. Q.; Albanese, K.; Blankenship, J. R.; Abdilla, A.; Bates, M. W.; Zhang, C.; Bates, C. M.; Hawker, C. J. Efficient Creation and Morphological Analysis of ABC Triblock Terpolymer Libraries. *Macromolecules* **2022**, *55* (19), 8875–8882.

(69) Anastasaki, A.; Nikolaou, V.; Zhang, Q.; Burns, J.; Samanta, S. R.; Waldron, C.; Haddleton, A. J.; McHale, R.; Fox, D.; Percec, V.; Wilson, P.; Haddleton, D. M. Copper(II)/Tertiary Amine Synergy in Photoinduced Living Radical Polymerization: Accelerated Synthesis of ω-Functional and α,ω-Heterofunctional Poly(Acrylates). *J Am Chem Soc* **2014**, *136* (3), 1141–1149.

(70) Lin, H.; Wagner, E. Van; Swinnea, J. S.; Freeman, B. D.; Pas, S. J.; Hill, A. J.; Kalakkunnath, S.; Kalika, D. S. Transport and Structural Characteristics of Crosslinked Poly(Ethylene Oxide) Rubbers. *J Memb Sci* **2006**, *276* (1–2), 145–161.

(71) Granville, A. M.; Boyes, S. G.; Akgun, B.; Foster, M. D.; Brittain, W. J. Thermoresponsive Behavior of Semifluorinated Polymer Brushes. *Macromolecules* **2005**, *38* (8), 3263–3270.

(72) Jakubowski, W.; Juhari, A.; Best, A.; Koynov, K.; Pakula, T.; Matyjaszewski, K. Comparison of Thermomechanical Properties of Statistical, Gradient and Block

Copolymers of Isobornyl Acrylate and n-Butyl Acrylate with Various Acrylate Homopolymers. *Polymer* **2008**, *49* (6), 1567–1578.

(73) Ge, X.; Fu, Q.; Su, L.; Li, Z.; Zhang, W.; Chen, T.; Yang, H.; Song, J. Light-Activated Gold Nanorod Vesicles with NIR-II Fluorescence and Photoacoustic Imaging Performances for Cancer Theranostics. *Theranostics* **2020**, *10* (11), 4809–4821. https://doi.org/10.7150/thno.44376.

Chapter 3. Facile preparation of tunable polyborosiloxane networks via hydrosilylation

3.1 Introduction

Polyborosiloxane networks are a class of crosslinked polymers containing Si–O–B bonds. Since their discovery in the 1940s, the unique combination of dynamic material properties and thermal stability has generated significant industrial and academic interest, including the commercialization of a polyborosiloxane system as Silly Putty.[1,2] The useful viscoelasticity of polyborosiloxane networks arises from the dynamic character of borate ester (B–O) groups and the various mechanisms of exchange they undergo on different time scales, leading to frequency-dependent properties with control over a material flowing, bouncing, or breaking at different strain rates.[3] Specifically, B–O covalent bonds can undergo rearrangement, which may occur through an associative or dissociative mechanism depending on the presence of water.[4–10] In addition to covalent bond exchange, weaker intramolecular interactions also act as dynamic crosslinks in polyborosiloxane networks. Dative bonds form between the empty p orbital of boron atoms and the lone pair electrons of oxygen atoms along

the siloxane backbone. Residual water also results in partial hydrolysis of the B–O–Si bonds into B–OH groups that can then participate in additional hydrogen bonding.[11,12] A combination of these numerous dynamic crosslinks and the chemical/thermal stability of the parent polydimethylsiloxane building blocks explains the potential for polyborosiloxane-based materials to find applications in shock-wave dissipators,[13,14] impact-resistant composites,[15,16] insulation,[17] fireproofing,[18,19] coatings,[20,21] flexible conductors,[22–24] and magnetic gels,[25] among other areas of contemporary importance.

Despite such widespread use, the synthesis of polyborosiloxane networks has remained largely unchanged since the 1940s. The first reports of polyborosiloxane synthesis involved treating methyl-terminated PDMS with boric acid at elevated temperatures to produce a viscoelastic material.[1,2] Since then, most reported methods rely on the condensation of boric acid and telechelic, silanol-terminated PDMS.[3,26–31] There remain significant challenges with this approach. Notably, the condensation reaction of Si–OH and B–OH generates byproducts including water that are deleterious to network integrity and, therefore, must be removed. Furthermore, boric acid is insoluble in PDMS, requiring high temperatures (>150 °C) to promote modest solubility. Alternatively, alcohol-based solvents may be used to dissolve boric acid into PDMS, but the solvent must then be removed through heat treatment. Both approaches require high temperature and long reaction times that cause chain-scission of the siloxane backbone, altering the final network structure and producing networks that are highly sensitive to preparation conditions.[27]

A recently published, novel method for fabricating polyborosiloxane networks addresses these solubility problems and improves control over the resulting polymer network.[32] Inspired by Rubinsztajn's 2014 report showcasing the dehydrocarbon condensation of

trimethyl borate and diphenylsilane in the presence of tris(pentafluorophenylborane) to form a borosiloxane bond and the corresponding alkane hydrocarbon,[33] the Muzafarov group synthesized polyborosiloxane networks by reacting alkyl borates with hydride-terminated PDMS and copolymers containing hydromethylsiloxane repeat units via hydrogen elimination.[32] In doing so, they demonstrated unprecedented control over network architecture. However, this chemistry is intolerant to oxygen and produces flammable gaseous byproducts, limiting its viability in the development of new materials.

Inspired by the aforementioned challenges, we developed a robust synthetic platform for synthesizing polyborosiloxane networks that is simple, scalable, and tunable (Figure 3.1). The key ingredient in this method is the use of tris(dimethylvinylsilyl)borate as a crosslinker.This commercially available building block features both Si–O–B bonds and reactive alkene moieties that are amenable to hydrosilylation—a highly efficient addition reaction that proceeds rapidly in air.[34] An additional benefit of crosslinking via hydrosilylation chemistry rather than condensation reactions is that unwanted byproducts are avoided and the initial solubility of the crosslinker in PDMS is significantly improved (*vide infra*). As shown below, this approach is amenable to a wide variety of PDMS starting materials having different molecular weights and architectures (Figure 3.1), as well as the co-incorporation of different crosslinkers to yield mixed dynamic–static networks. In summary, this versatile and simple synthetic strategy unlocks access to a diverse range of dynamic PDMS-based materials.

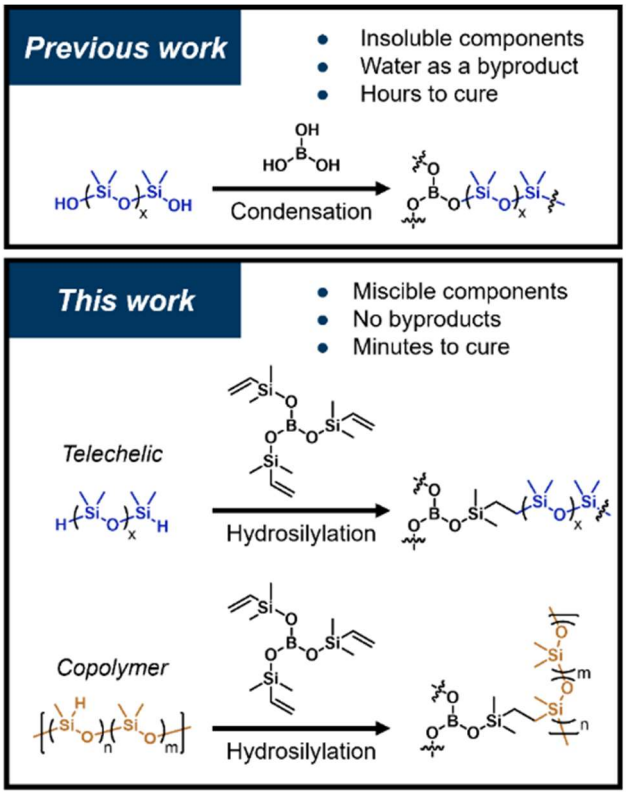

Figure 3.1. This work describes the efficient synthesis of polyborosiloxane networks by hydrosilylation chemistry, which is simple, efficient, and highly tunable in contrast to traditional condensation chemistry.

3.2 Sample Preparation Procedure

After degassing the Si–H functional PDMS precursor under vacuum to remove any dissolved oxygen, tris(dimethylvinylsilyl)borate was added in a 1:1 ratio of Si–H:alkene units. Then, a solution of Karstedt's catalyst inhibited with dimethyl fumarate was added such that the resulting reaction mixture contained 20 ppm Pt and 60 ppm dimethyl fumarate by mass (Figure 3.2). The mixture was poured into a container and heated at 90 °C for 10 minutes to form roughly 1.5 mm thick elastomers. Rheology discs with diameters of 25 mm were punched out at 140 °C and rapidly transferred to a rheometer. The temperature was chosen to minimize the impact of thermal expansion on the sample geometry during characterization.

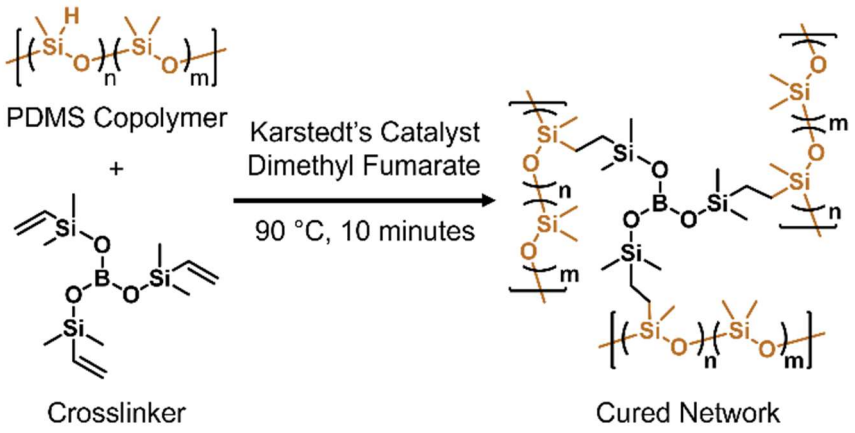

Figure 3.2. Synthesis of a polyborosiloxane network using Si–H containing PDMS copolymer and tris(dimethylvinylsilyl)borate through hydrosilylation catalyzed by 20 ppm of platinum introduced through Karstedt's catalyst inhibited with 60 ppm dimethyl fumarate with no added solvent.

3.3 Rapid Mixing and Efficient Curing

The efficient mixing and curing of polyborosiloxane networks synthesized by hydrosilylation is evident visually (Figure 3.3a) and quantitatively as measured by rheometry (Figure 3.3b). As an initial demonstration, silyl-hydride–terminated PDMS (5 kDa), tris(dimethylvinylsilyl)borate, Karstedt's catalyst, and inhibitor (dimethyl fumarate) were mixed at room temperature, resulting in a transparent solution (Figure 3.3a, *left*).[35] As expected, after loading this solution onto a 25 mm rheometer plate, the mixture is a flowable liquid, as evidenced by the storage modulus being less than the loss modulus ($G' < G''$). Subsequent heating of the solution to 90 °C at a rate of approximately 30 °C/min yielded an immediate increase in G' and solidification ($G' > G''$) followed by a plateau in G' and G'' within ~2 minutes (Figure 3.3b). Such rapid and complete curing at a moderate temperature with hydrosilylation is a significant advantage over traditional condensation, which typically takes

hours to days at higher temperatures and may require the removal of solvent. As shown in Figure 3.3a (*right*), the resulting sample is transparent. Similar results were obtained for a variety of Si–H functional PDMS starting materials with varying molecular weights and Si–H groups either at the chain ends or distributed along the polymer backbone (Figure 3.9).

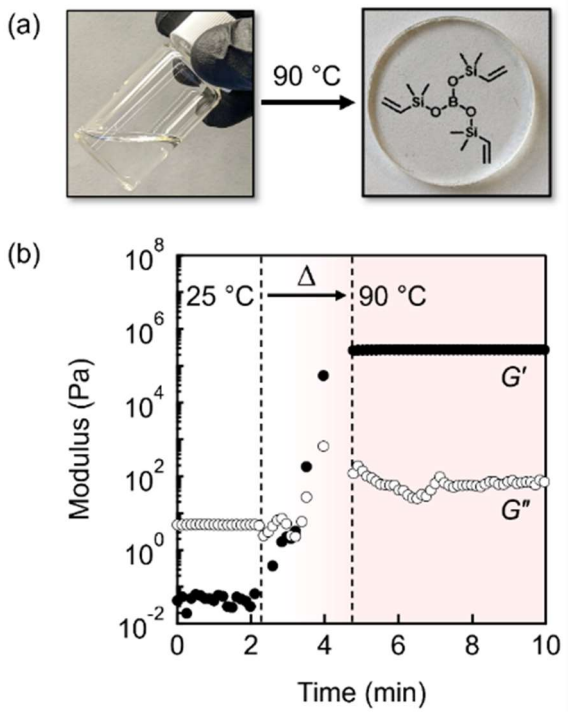

Figure 3.3. Rapid and efficient curing of polyborosiloxane networks via hydrosilylation. (a) Photograph of 5 kDa telechelic Si–H functional PDMS mixed with tris(dimethylvinylsilyl)borate, Karstedt's catalyst, and inhibitor (dimethyl fumarate) at room temperature followed by curing at 90 °C. (b) Oscillatory rheometry indicates fast and complete curing within minutes when heated from 25 °C to 90 °C at a rate of 60 °C/min.

A key advantage of polyborosiloxane networks synthesized via hydrosilylation with tris(dimethylvinylsilyl)borate is synthetic choice. Other commercially available PDMS

prepolymers can be used to form dynamic networks. For example, fast and efficient curing analogous to Figure 3.3 was also observed with various copolymers consisting of monomers of dimethylsiloxane and hydromethylsiloxane, where multiple Si–H groups are statistically distributed along the polymer chain (summarized in Table 3.1). Significantly, tris(dimethylvinylsilyl)borate was miscible at all tested concentrations for every PDMS prepolymer tested. In all cases, transparent networks were formed with a 1:1 stoichiometry of Si–H groups to vinyl groups (Figure 3.9).

Network formation was further confirmed through infrared and nuclear magnetic resonance spectroscopy as shown in Figure 3.4; note that these data are shown for formulations containing PDMS copolymer as a representative example. Infrared spectra (Figure 3.4a) highlight the disappearance of Si–H bond vibrations at 2250 cm^{-1}, suggesting the hydrosilylation reaction reaches high conversion. Furthermore, both the crosslinker and the cured networks show vibrations at 1350 cm^{-1} as expected for Si–O–B bonds.[36] These data further reinforced by ^{29}Si NMR (Figure 3.4b): a distinct peak at $\delta = 0.8$ ppm in the crosslinker shifts to $\delta = 13$ ppm after the addition of PDMS Si–H units to the vinyl groups of the crosslinker. Peaks corresponding to Si–H bonds in the PDMS prepolymer that are present between $\delta = 35 – 39$ ppm also disappear upon coupling. Small peaks in the vicinity of $\delta = 6.6$ ppm corresponding to the trimethylsilyl end groups are also visible in both the starting material and the product.

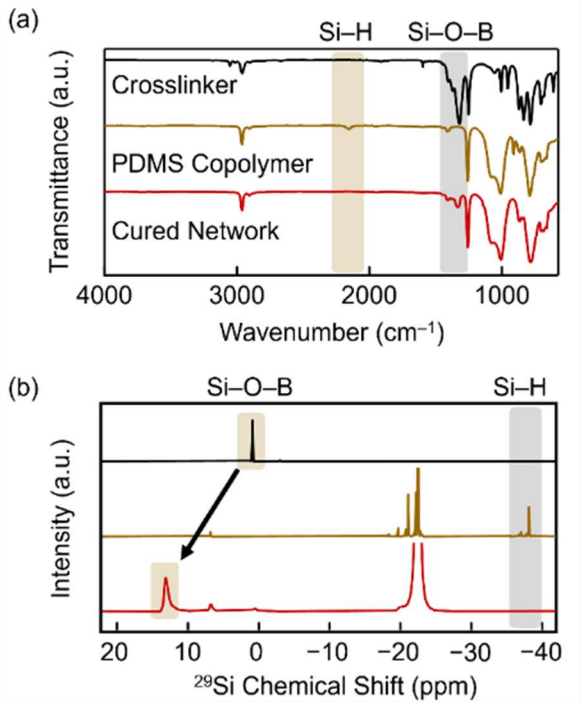

Figure 3.4. Efficient formation of polyborosiloxane networks containing a 20 kDa siloxane copolymer with 20 Si–H units as a representative example. (a) Fourier-transform infrared spectroscopy showing consumption of Si–H units from hydrosilylation and retention of Si–O–B bonds in the cured network. (b) ^{29}Si nuclear magnetic resonance spectroscopy showing shift in the Si–O–B moiety from hydrosilylation and consumption of Si–H units. Note that the crosslinker and copolymer NMR were collected in $CDCl_3$, while the spectrum of the cured network was necessarily acquired in the solid state.

3.4 Tunable Stress Relaxation

To compare the viscoelastic properties of polyborosiloxane networks prepared via our novel synthetic method (hydrosilylation) and previous approaches (condensation), stress-relaxation experiments were performed in triplicate on hydrosilylation samples prepared from: (i) a 5 kDa telechelic Si–functional PDMS, and (ii) a 6 kDa Si–functional PDMS copolymer with an average of 6 Si–H units.[5,37] Step–strain measurements were collected over a range of

temperatures to capture the temperature-dependent stress-relaxation behavior (Figure 3.5a, 3.5b). Note that the temperature range shown for the copolymer is higher than that of the telechelic material due to slower dynamics of the former. Experimental characteristic relaxation times ($\tau_{1/e}$) were determined as the time required for the relaxation modulus (G) to reach 0.37 of its original value.[38] Our polyborosiloxane networks show an Arrhenius relationship between the rate of stress relaxation and temperature (T) as expected for dynamic covalent networks (Figure 3.5c).[39] The average activation energy (E_a) of networks obtained from telechelic (48 ± 2 kJ/mol) and copolymer (41 ± 1 kJ/mol) precursors falls within the range previously reported for similar dynamic motifs (34 – 77 kJ/mol),[5,28,37,40] indicating that our polyborosiloxanes have similar material properties to traditional systems with greatly enhanced synthetic availability.

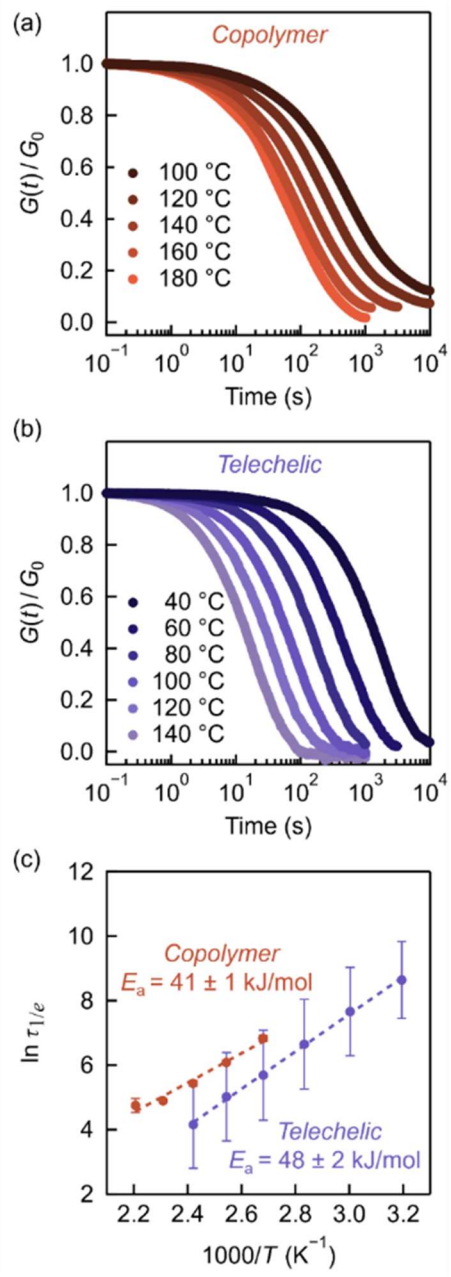

Figure 3.5. Polyborosiloxanes synthesized via hydrosilylation are dynamic and undergo tunable stress relaxation based on the network architecture resulting from the use of different precursors (telechelic vs. copolymer). Decay of normalized modulus over time after applying a 1% step strain at varying temperatures for networks prepared from (a) 6 kDa Si–H functional PDMS copolymer with an average of 6 Si–H units per polymer chain and (b) 5 kDa telechelic

Si–H functional PDMS. (c) Arrhenius temperature dependence of the relaxation time measured via stress relaxation for both networks. Error bars represent standard deviations calculated from triplicate measurements samples.

Comparing the error bars in Figure 3.5c, networks prepared from copolymer precursors showed significantly better reproducibility relative to those synthesized with telechelic PDMS. While the error in activation energy is small for both networks, variation in the Arrhenius prefactor for the telechelic systems is observed. This sample-to-sample variation may be due to chain end fidelity and differences in the number of Si–H bonds per molecule for the different PDMS precursors. The network connectivity, is significantly impacted by lower than ideal chain end fidelity (n = 2) resulting in network defects and potentially dramatic variability in mechanical properties with small changes in formulation or curing conditions. Conversely, the copolymer precursor has an average of 6 Si–H bonds per chain. Variation in the number of Si–H bonds, therefore, have less of an effect on overall network connectivity, leading to improved reproducibility. We emphasize that the ability to use Si-H–containing PDMS copolymers as a starting material in the synthesis of polyborosiloxane networks is another distinguishing advantage of the hydrosilylation synthetic route, as analogous precursors with silanols distributed along the backbone (for traditional condensation networks) are not commercially available.

Single and stretched exponential fits applied to the stress-relaxation data further suggest more homogeneous networks are generated from hydrosilylation compared to traditional condensation polymerization. Representative fits are shown in Figure 3.14. The data (Tables 3.2 and 3.3) display good agreement between three different time constants—$\tau_{1/e}$, τ_{exp}, τ_{KWW}—calculated via three different methods—experimental, single exponential fit, and stretched

exponential fit, respectively. For the networks prepared from a telechelic precursor, the stretched exponential model provides the best fit and β values near 1 (0.84 – 0.89), suggesting modest heterogeneity in the relaxation environment. In contrast, recent work from Porath and Evans[37] on similar polyborosiloxane networks synthesized via condensation inferred β = 0.64 – 0.83. The higher values of β and tighter range suggest PBS networks prepared via hydrosilylation are more homogeneous, likely due to the high conversion of the hydrosilylation reaction and the lack of deleterious water produced by condensation. Polyborosiloxane networks prepared from PDMS precursors of different molecular weights all yielded similar qualitative results, with differences in relaxation times related to architecture, the concentration of crosslinks, and network defectivity (Figure 3.15).

3.5 Mixed Crosslinkers

An additional advantage of hydrosilylation is the ability to introduce multiple, different crosslinking groups into the starting formation. This provides a simple mechanism to tune dynamics and mechanical properties through formulation analogous to other types of dynamic chemistry.[4,41–44] As an illustrative example, tetraallylsilane was selected as a co-crosslinker to improve the dimensional stability of polyborosiloxane networks by introducing static crosslinks in addition to dynamic crosslinks derived from tris(dimethylvinylsilyl)borate (Figure 3.6).

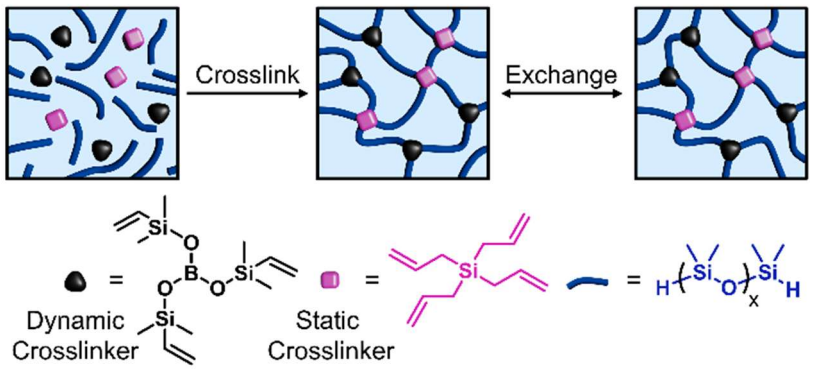

Figure 3.6. Hydrosilylation chemistry unlocks the ability to mix dynamic and static crosslinkers to produce mixed polyborosiloxane systems; tetraallylsilane is shown as a representative example of a static crosslinker.

The rate of stress relaxation in polyborosiloxanes containing mixed crosslinkers was found to be readily tunable based on the stoichiometric ratio between dynamic and static crosslinks (Figure 3.7). As the incorporation of static crosslinks increases, the rate of stress relaxation decreases due to a reduction in the number of exchangeable bonds. To visually showcase the different stress-relaxation dynamics, bear-shaped samples were created from different formulations and monitored over time under ambient conditions (Figure 3.7a). The incorporation of static crosslinks significantly slowed stress relaxation at room temperature. A fully dynamic material (0% static crosslinks) showed significant deformation after 6 days while the three samples with static crosslinks exhibited no such change. After 16 days, the sample with 30% static crosslinks started to show slight deformation that became more pronounced after 30 days. Even after this extended amount of time, samples with a higher loading of static crosslinker (70% and 100%) retained their original dimensions. The rheometry data in Figure 3.7b quantifies this behavior and highlights the pronounced effect static crosslinker has on the rate of stress relaxation, as depicted, at 140 °C; samples can be readily designed to fully relax (0% static) or undergo no relaxation (100% static) with intermediate behavior readily achieved by simply tuning the starting formulation, *i.e.* the relative ratio of static to dynamic crosslinker.

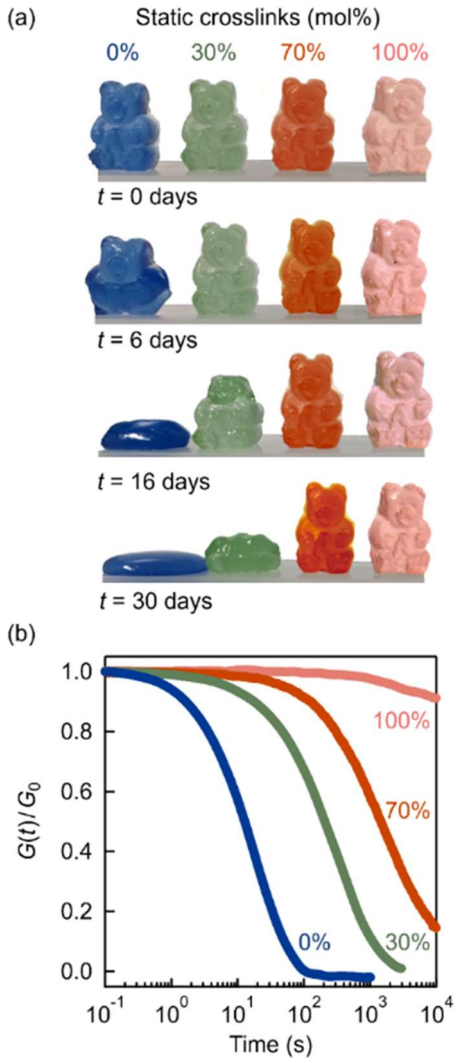

Figure 3.7. Mixtures of static and dynamic crosslinkers provide fine control over relaxation dynamics in polyborosiloxane networks. (a) Visual representation of changes in shape over time for networks prepared from 5 kDa telechelic PDMS with varied amounts of tris(dimethylvinylsilyl)borate as the dynamic crosslinker and tetraallylsilane as the static crosslinker. The listed composition corresponds to the percentage of crosslinks from tetraallylsilane relative to the total number of crosslinks. (b) Corresponding stress relaxation measurements performed at 140 °C.

Typical polyborosiloxane networks are susceptible to hydrolysis and alcoholysis of Si–O–B bonds, which can limit the applicability of these materials. For example, a common method to remove Silly Putty from clothing is the use of rubbing alcohol (isopropanol) to degrade the network. We postulated that introducing static crosslinks would also impart alcohol-based solvent resistance by stabilizing the network. To test this hypothesis, fish-shaped samples were prepared with different ratios of static and dynamic crosslinks (Figure 3.17), followed by soaking in methanol for four days (Figure 3.8). Significantly, the introduction of static crosslinks in both the telechelic- and copolymer-derived networks provides structural integrity that prevents complete dissolution after methanolysis of the borate ester bonds. Interestingly, networks prepared from telechelic PDMS materials required circa 60% of static crosslinks to remain intact, while analogous copolymer networks showed stability starting at 20%. These findings are in qualitative agreement with a recent publication that developed theory to predict the changes in properties of dynamic networks as static crosslinks are incorporated. Specifically, Ramis *et al.* calculated the minimum fraction of static crosslinks required to form a fully percolating static network, finding that value depends on the functionality of the static crosslinker and starting polymer.[45] For our materials, the functionality of the starting polymer increases from 2 for the telechelic network to ≈6 for the copolymer network, resulting in a drastic decrease in the fraction of static crosslinks required to stabilize the network.

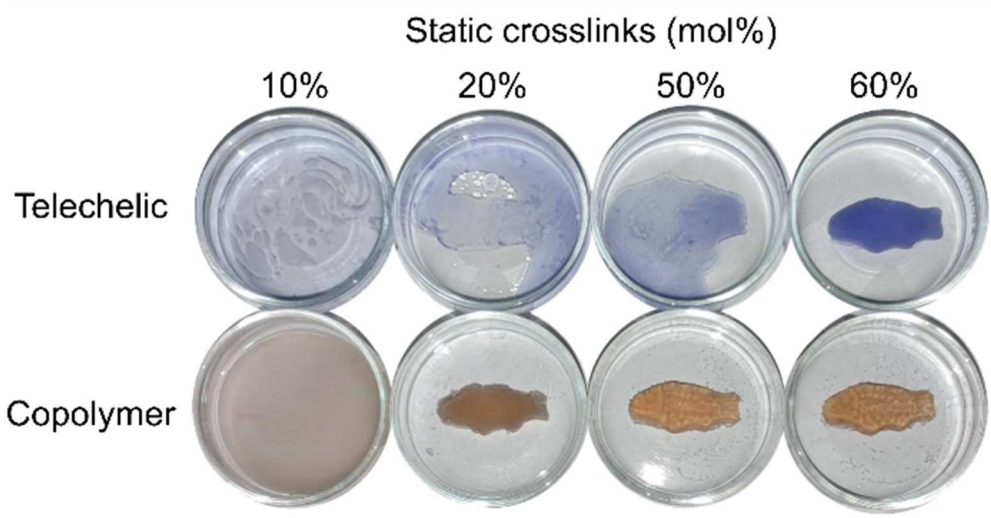

Figure 3.8. Introduction of static crosslinker in the hydrosilylation formulation imparts structural stability in the presence of reactive solvent (as depicted: methanol) that disrupts borate ester crosslinks. Images show polyborosiloxane networks prepared from 5 kDa telechelic PDMS (*top*, blue) with 2 Si–H units per polymer chain or 6 kDa PDMS copolymer (*bottom*,orange) containing an average of 6 Si–H units per polymer chain. Crosslinkers used were tris(dimethylvinylsilyl)borate (dynamic) and tetraallylsilane (static). The listed composition corresponds to the percentage of crosslinks from tetraallylsilane relative to the total number of crosslinks. The dishes were covered during evaluation to limit evaporation of methanol.

3.6 Conclusions

A novel method for preparing polyborosiloxane networks was developed to take advantage of commercially available starting materials and robust hydrosilylation chemistry. Key to this approach is the use of tris(dimethylvinylsilyl)borate as an efficient crosslinker for PDMS precursors that contain Si–H bonds. The placement of Si–H groups at either the chain ends or

throughout a copolymer backbone leads to significantly different network structures and performace. The efficient nature of crosslinking via hydrosilylation was confirmed with rheometry, infrared spectroscopy, and ^{29}Si nuclear magnetic resonance spectroscopy. Complete curing can be achieved in minutes at 90 °C, yielding dynamic networks that undergo tunable stress relaxation as a function of formulation and temperature. Importantly, the relaxation time and Arrhenius temperature dependence are consistent with literature polyborosiloxane-based materials that were synthesized by traditional condensation chemistry. In addition to efficient, low-temperature curing, an additional advantage of hydrosilylation is the ability to readily incorporate a mixture of static and dynamic crosslinks via formulation modifications to control relaxation dynamics and solvent resistance. In summary, hydrosilylation is a simple, powerful, and accessible synthetic platform for creating dynamic siloxane-based materials that we anticipate will be broadly useful throughout the materials community and beyond.

3.7 Materials and Methods

All materials were used as received unless specified. Tris(dimethylvinylsilyl)borate and siloxane samples were purchased from Gelest Inc. unless otherwise specified. Tris(dimethylvinylsilyl)borate was stored over molecular sieves in a sealed vial with a nitrogen atmosphere. Acetonitrile, toluene, calcium hydride, lithium bis(trimethylsilyl)amide (LiHMDS, 1 M solution in hexnanes), chlorodimethylsilane, tetraallylsilane, Karstedt's catalyst (2 wt% Pt in xylenes), dimethyl fumarate, and telechelic Si–H functional PDMS of 14 kDa and 25 kDa were purchased from Millipore Sigma. Hexamethylcyclotrisiloxane (D_3) was purchased from TCI and stirred in a suspension of calcium hydride overnight at 80 °C followed by sublimation and storage in dried THF under an argon atmosphere. Telechelic Si–H

functional PDMS of 2 kDa and 8 kDa were synthesized following a previously reported method, detailed below.[46] An inhibited catalyst solution was prepared by prepared by mixing 1 mL Karstedt's catalyst solution, 1 mL toluene, and 40 mg dimethyl fumarate (4 molar equivalents compared to Pt).

Representative synthesis of H–PDMS–H

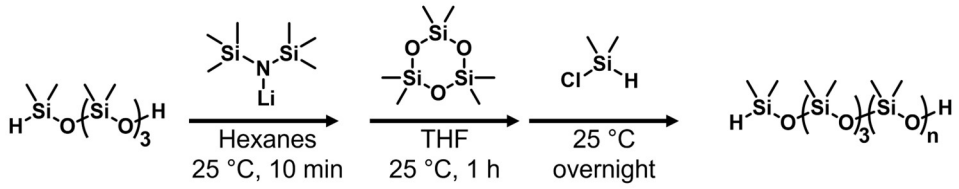

An Si–H and Si–OH functional initiator was synthesized following a previously reported method.[47] A 250 mL two neck round bottom flask equipped with a stir bar was flame dried and purged with argon. A 50 wt% solution of the initiator in hexanes (3.87 mL, 5 mmol) and 1 M LiHMDS in hexanes (5 mL, 5 mmol) were added and stirred under argon for 10 min at room temperature. Then, D_3 in THF (1.9 M, 45.1 mL, 85 mmol) was added to initiate the polymerization. The reaction mixture was stirred at room temperature for 1 h followed by adding chlorodimethylsilane (1.6 mL, 15 mmol) to quench the polymerization. After stirring the quenched solution overnight, the organic solvent was removed under low pressure. Subsequently, hexanes was added to the crude reaction mixture. The mixture was washed with water, saturated $NaHCO_3$, and brine. The combined organic layer was dried over $MgSO_4$ and the organic solvent was removed under reduced pressure. The washed product was precipitated into acetonitrile three times then dried under vacuum to obtain a colorless oil.

3.7.1 Representative example of curing networks

To a 20 mL glass vial, 3 grams (0.6 mmol) of 5 kDa telechelic Si–H functional PDMS were added and degassed at 90 °C for at least 15 minutes. Next, 125 mg (0.4 mmol) of tris(dimethylvinylsilyl)borate, and 6 μL inhibited Karstedt's catalyst solution were added to achieve a 1:1 stoichiometric ratio of Si–H to alkene functional groups and 20 ppm Pt. This mixture was vortexed for 1 minute and briefly degassed at room temperature to remove any air bubbles. The solution was poured into a polystyrene dish and heated at 90 °C for 10 minutes to obtain a solid and flexible elastomer.

3.7.2 Representative example of curing shaped networks with dual crosslinkers

To prepare a 70 mol% static crosslinker sample, 3 grams (0.6 mmol) of degassed 5 kDa telechelic Si–functional PDMS, 38 mg (0.12 mmol) of tris(dimethylvinylsilyl)borate, 40 mg (0.21 mmol) of tetraallylsilane, and 6 μL inhibited Karstedt's catalyst solution were added to achieve a 1:1 stoichiometric ratio of Si–H to alkene functional groups and 20 ppm Pt. This mixture was vortexed for 1 minute and briefly degassed at room temperature to remove any air bubbles. The solution was poured into a polystyrene dish and heated at 90 °C for 10 minutes to obtain a solid and flexible elastomer. Alternatively, the solution was poured into an Ecoflex mold and heated at 90 °C for 20 minutes to obtain a solid material. Molded samples were left on the benchtop to track their stress relaxation in an ambient atmosphere at room temperature.

3.7.3 Methanolysis of polyborosiloxane networks

Elastomers prepared in molded shapes were placed in a petri dish filled with methanol. The dishes were left on the benchtop, covered to limit solvent evaporation, and refilled when necessary. Images were taken to track the changes over time.

3.7.4 Swelling ratio and gel fraction measurements

After curing the polyborosiloxane solution into elastomers, three ≈200 mg samples were prepared, weighed, and placed in separate, sealed vials containing n-heptane at room temperature. After 24 hours, the samples were removed from the vials, blotted dry, and the mass was measured. The swelling ratio was defined as the ratio between the swollen mass and the initial mass. Subsequently, the n-heptane was removed *in vacuo* from the vials, and the remaining mass corresponded to the sol portion of the elastomer. Additionally, the swollen elastomer samples were dried under vacuum to collect the gel portion of the elastomer. To minimize measurement error, the gel fraction was calculated based on both portions, resulting in two values per individual sample. Error bars represent standard deviations for each measurement.

Table 3.1. Summary of Si–H-containing PDMS copolymers utilized during the study. Molar mass was provided by the supplier (Gelest), and the average number of Si–H units was measured via ^{1}H NMR.

Product Code	Molecular weight (kDa)	Average number of Si–H units
HMS-071	2	2
HMS-082	6	6
HMS-053	20	20
HMS-064	50	31

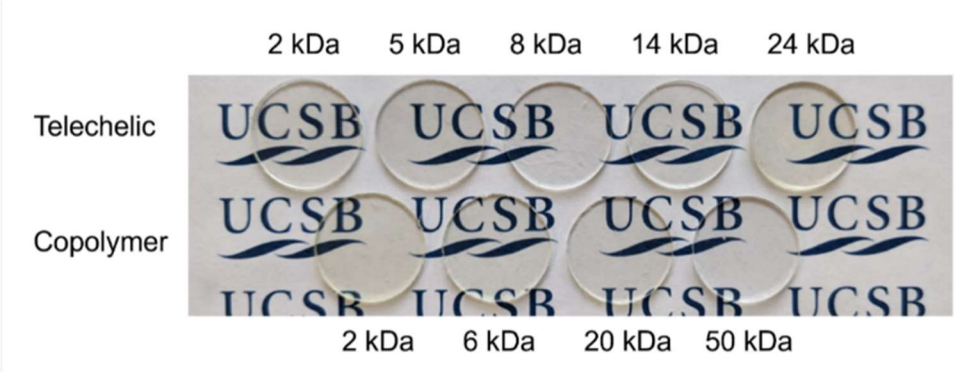

Figure 3.9. Representative image of rheology discs made from the listed starting polymer and tris(dimethylvinylsilyl) borate. Yellow tinge is due to Pt clusters precipitating from Karstedt's catalyst during curing.

3.8 **Chemical Characterization**

Attenuated total reflectance Fourier transform infrared spectroscopy (ATR-FTIR) spectra were collected on a Nicolet is10 spectrometer with a diamond ATR accessory. All spectra were collected with 64 scans and a resolution of 4 cm^{-1} in absorbance mode, baseline corrected, and displayed in transmittance mode. Proton nuclear magnetic resonance (NMR) spectra were taken on a Varian Unity Inova AS600 600MHz at 25 °C with 16 scans and a relaxation delay (d_1) of 15 seconds. Solution state ^{11}B, ^{13}C, and ^{29}Si NMR spectra were taken on a Bruker Avance NEO 500 MHz at 25 °C. ^{11}B spectra used a d_1 value of 2 seconds and 64 scans. ^{13}C used a d_1 value of 2 seconds and 256 scans. ^{29}Si used a d_1 value of 60 seconds and 32 scans. Solid-state NMR (ssNMR) spectra were taken on a Bruker AVANCE500 WB with magic-angle spinning (MAS) of 14 kHz at 30° pulses. Samples were ground and placed into a 4 mm Bruker zirconia rotor. ^{29}Si ssNMR spectra were captured with a d_1 of 30 seconds and 4856 scans. ^{11}B ssNMR spectra were captured with a d_1 of 6 seconds and 12248 scans and background corrected.

3.9 Rheology

In order to limit hydrolysis and oxygen permeation, rheology experiments were performed immediately after network fabrication. 25 mm discs were punched out of cured networks at 140 °C and immediately transferred onto the 25 mm stainless steel parallel plate within the environmental chamber of the rheometer and held at the same temperature. Rheology experiments were performed on a strain-controlled TA Instruments ARES-G2 rheometer affixed with a forced convection oven in a nitrogen atmosphere.

Stress relaxation experiments were performed by rapidly applying a 1% strain and monitoring the decay in measured stress over time. Three samples were measured to ensure consistency (Figures 3.10, 3.11, and 3.12). The applied strain was confirmed to be in the linear viscoelastic regime of each sample (Figure 3.13). For sample series requiring multiple temperatures, rheology experiments were performed from high to low temperature. Single (Equation 1) and stretched (Equation 2) exponential fits were applied to stress relaxation data measurements for a polyborosiloxane network prepared from a 5 kDa telechelic Si–H functional PDMS precursor. Representative fits are shown in Figure 3.14, and averaged values with standard deviations are shown in Tables 3.2 and 3.3.

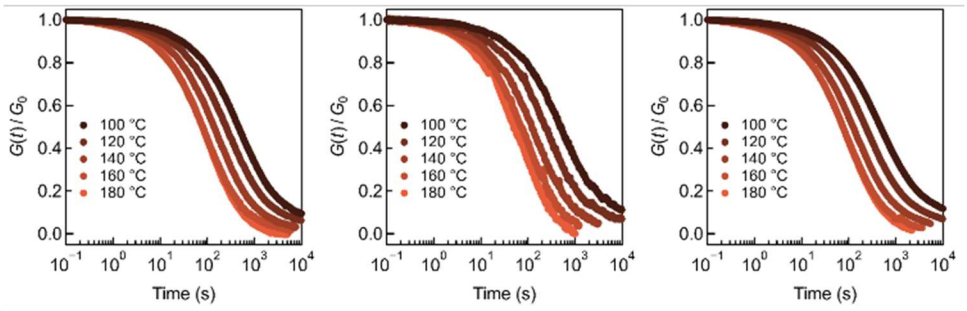

Figure 3.10. Triplicate stress relaxation measurements for a polyborosiloxane network prepared from a 6 kDa Si–H functional PDMS copolymer with an average of 6 Si–H moieties per polymer chain.

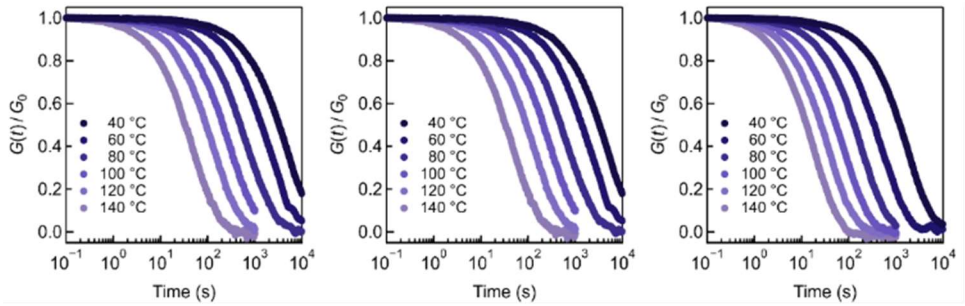

Figure 3.11. Triplicate stress relaxation measurements for a polyborosiloxane network prepared from a 5 kDa telechelic Si–H functional PDMS precursor.

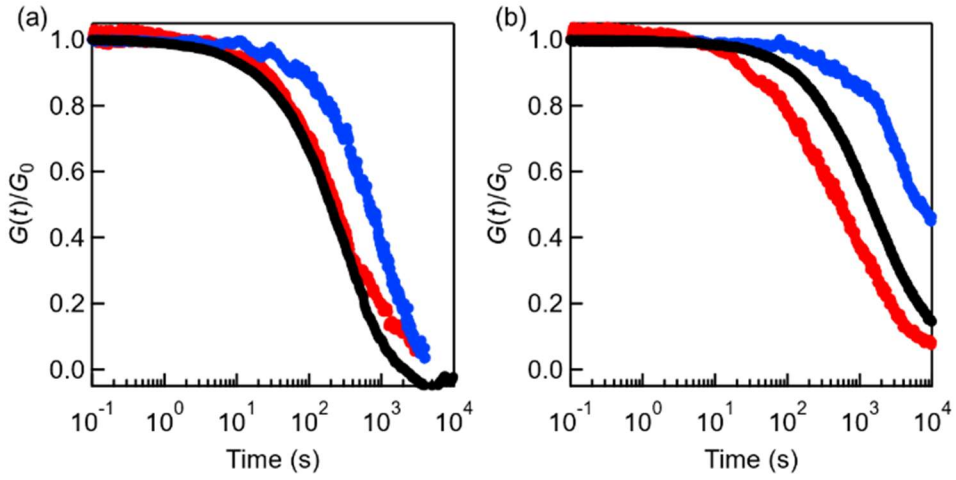

Figure 3.12. Triplicate stress relaxation measurements for a polyborosiloxane network prepared from a 5 kDa telechelic Si–H functional PDMS precursor with (a) 30% static crosslinks and (b) 70% static crosslinks.

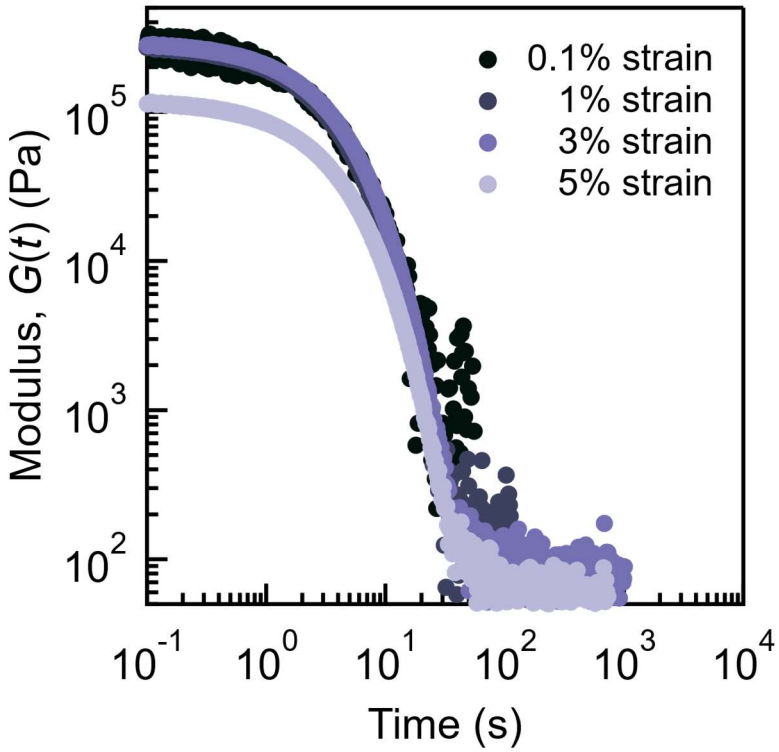

Figure 3.13. Representative example of determining appropriate strain for stress relaxation experiments. 1% strain was used for all stress relaxation experiments.

$$\frac{G(t)}{G_0} = \left(1 - \frac{G_{res}}{G_0}\right) e^{\left\{-(t-t_0)/\tau_{exp}\right\}} + \frac{G_{res}}{G_0}$$

Equation 3.1. Single exponential fitting equation.

$$\frac{G(t)}{G_0} = \left(1 - \frac{G_{res}}{G_0}\right) e^{\left\{-\left((t-t_0)/\tau_{KWW}\right)^{\beta}\right\}} + \frac{G_{res}}{G_0}$$

Equation 3.2. Stretched exponential fitting equation, also known as the Kohlrausch–Williams–Watts (KWW) equation.

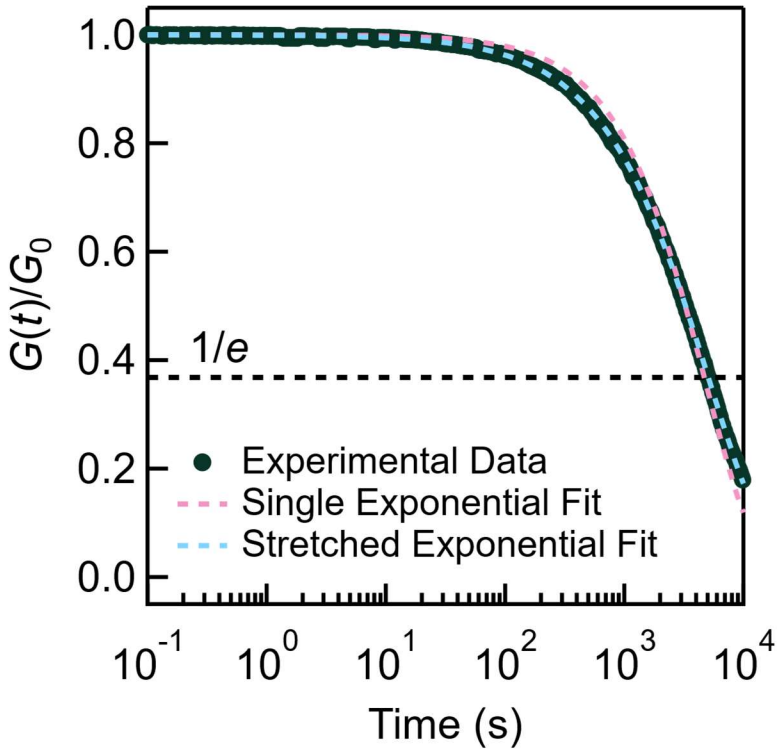

Figure 3.14. Representative single and stretched exponential fits for stress relaxation measurements for a polyborosiloxane network prepared from a 5 kDa Si–H functional telechelic PDMS precursor.

Table 3.32. Average stress relaxation times determined via experiment ($\tau_{1/e}$) and single (τ_{exp}) and stretched (τ_{KWW}) exponential fits for a polyborosiloxane network prepared from a 5 kDa Si–H functional telechelic PDMS precursor.

T (°C)	Replicate	$\tau_{1/e}$ (s)	τ_{exp} (s)	τ_{KWW} (s)	β
140	Replicate 1	51	50	53	0.86
	Replicate 2	280	270	270	0.94
	Replicate 3	19	19	19	0.89
120	Replicate 1	150	140	150	0.84
	Replicate 2	630	600	620	0.89
	Replicate 3	40	38	40	0.86
100	Replicate 1	330	320	340	0.84
	Replicate 2	1300	1300	1300	0.83

	Replicate 3	85	80	85	0.84
80	Replicate 1	770	750	810	0.81
	Replicate 2	3200	3100	3200	0.87
	Replicate 3	200	200	210	0.84
60	Replicate 1	2200	2100	2200	0.83
	Replicate 2	8300	7900	8200	0.90
	Replicate 3	540	520	550	0.83
40	Replicate 1	5100	4700	5100	0.83
	Replicate 2	20000	19000	20000	0.88
	Replicate 3	1900	1800	1900	0.84

Table 3.3. Average stress relaxation times determined via experiment ($\tau_{1/e}$) and single (τ_{exp}) and stretched (τ_{KWW}) exponential fits for a polyborosiloxane network prepared from a 6 kDa Si–H functional PDMS copolymer with an average of 6 Si–H moieties per polymer chain.

T (°C)	Replicate	$\tau_{1/e}$ (s)	τ_{exp} (s)	τ_{KWW} (s)	β
180	Replicate 1	90	80	91	0.69
	Replicate 2	130	110	130	0.67
	Replicate 3	130	120	140	0.68
160	Replicate 1	130	100	120	0.69
	Replicate 2	130	110	130	0.65
	Replicate 3	140	120	140	0.65
140	Replicate 1	210	170	190	0.66
	Replicate 2	230	170	210	0.64
	Replicate 3	250	200	240	0.65
120	Replicate 1	420	320	380	0.65
	Replicate 2	430	310	380	0.63
	Replicate 3	470	340	410	0.64
100	Replicate 1	920	590	700	0.66
	Replicate 2	910	600	740	0.62
	Replicate 3	860	610	740	0.64

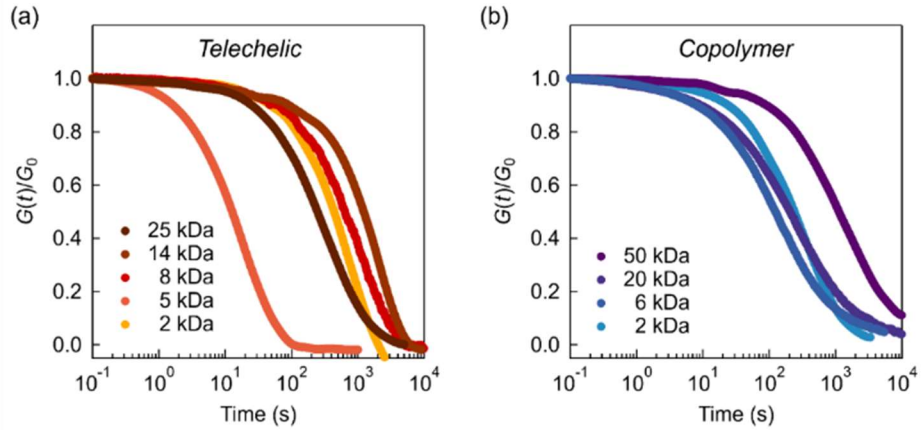

Figure 3.15. (a) Comparison of stress relaxation dynamics for polyborosiloxane networks made from telechelic Si–H functional PDMS at varying molecular weights. (b) Comparison of stress relaxation dynamics for polyborosiloxane networks made from Si–H functional PDMS copolymers of varying molecular weight and similar crosslink density.

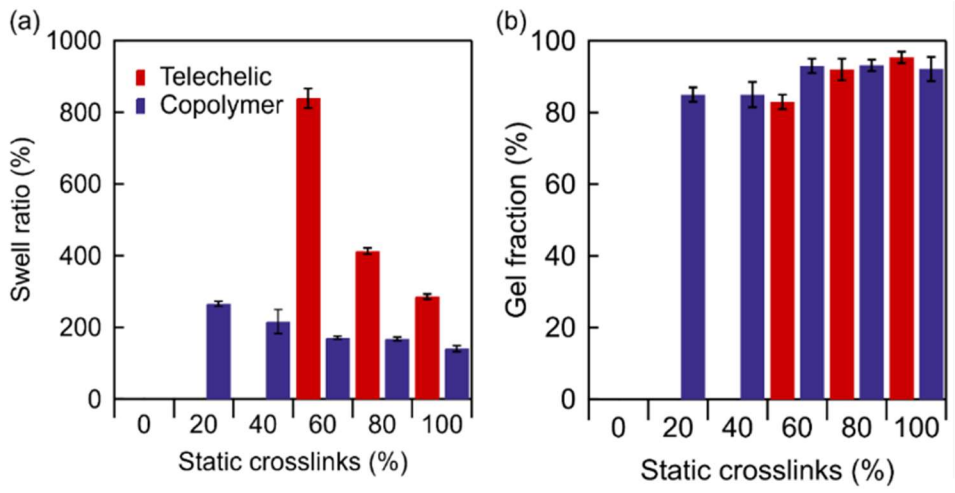

Figure 3.16. (a) Swelling ratio of polyborosiloxane networks prepared from 5 kDa telechelic Si–H functional PDMS precursor and 6 kDa Si–H functional PDMS copolymer precursor with an average of 6 Si–H moieties with the corresponding ratio of static crosslinks produced by tuning the ratio of tris(dimethylvinylsilyl)borate to tetraallylsilane. Swelling ratio is defined as

the swollen mass divided by the original mass after soaking in n-heptane for 24 hours. (b) Corresponding gel fractions. Samples with no measured value of swelling ratio and gel fraction completely dissolved.

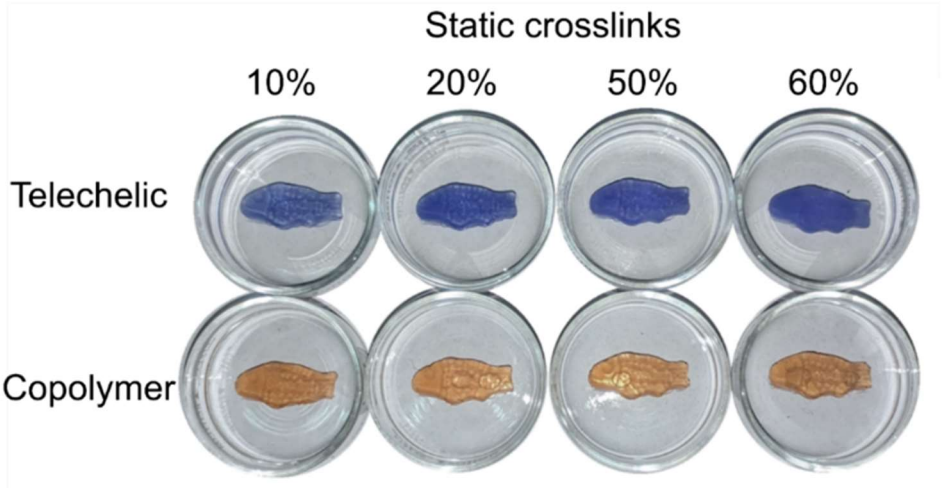

Figure 3.17. Fish-shaped crosslinked networks prepared from 5 kDa Si–H functional telechelic PDMS (*top*, blue) or 6 kDa Si–H functional PDMS copolymer (*bottom*,orange) containing an average of 6 Si–H moieties per polymer chain. Crosslinkers used were tris(dimethylvinylsilyl)borate (dynamic) and tetraallylsilane (static) with the listed compositions corresponding to the mole percentage of crosslinks coming from tetraallylsilane.

3.10 References

(1) Wright, J. G. E. Process for Making Puttylike Elastic Plastic, Siloxane Derivative Composition Containing Zinc Hydroxide, 1951.

(2) McGregor, R. R.; Warrick, E. Treating Dimethyl Silicone Polymer with Boric Oxide, 1947.

(3) Tang, M.; Wang, W.; Xu, D.; Wang, Z. Synthesis of Structure-Controlled Polyborosiloxanes and Investigation on Their Viscoelastic Response to Molecular Mass of Polydimethylsiloxane Triggered by Both Chemical and Physical Interactions. *Ind Eng Chem Res* **2016**, *55* (49), 12582–12589.

(4) Cash, J. J.; Kubo, T.; Dobbins, D. J.; Sumerlin, B. S. Maximizing the Symbiosis of Static and Dynamic Bonds in Self-Healing Boronic Ester Networks. *Polym Chem* **2018**, *9* (15), 2011–2020.

(5) Röttger, M.; Domenech, T.; Van Der Weegen, R.; Breuillac, A.; Nicolaÿ, R.; Leibler, L. High-Performance Vitrimers from Commodity Thermoplastics through Dioxaborolane Metathesis. *Science (1979)* **2017**, *356*, 62–65.

(6) Cash, J. J.; Kubo, T.; Bapat, A. P.; Sumerlin, B. S. Room-Temperature Self-Healing Polymers Based on Dynamic-Covalent Boronic Esters. *Macromolecules* **2015**, *48* (7), 2098–2106.

(7) Yang, Y.; Du, F. S.; Li, Z. C. Thermally Healable and Reprocessable Polymethacrylate Networks Based on Diol-Mediated Metathesis of 6-Membered Boronic Esters. *Polym Chem* **2020**, *11* (11), 1860–1870.

(8) Cho, S.; Hwang, S. Y.; Oh, D. X.; Park, J. Recent Progress in Self-Healing Polymers and Hydrogels Based on Reversible Dynamic B-O Bonds: Boronic/Boronate Esters, Borax, and Benzoxaborole. *J Mater Chem A Mater* **2021**, *9* (26), 14630–14655.

(9) Zhang, X.; Zhao, Y.; Wang, S.; Jing, X. Cross-Linked Polymers Based on B-O Bonds: Synthesis, Structure and Properties. *Mater Chem Front* **2021**, *5* (15), 5534–5548.

(10) Bapat, A. P.; Sumerlin, B. S.; Sutti, A. Bulk Network Polymers with Dynamic B-O Bonds: Healable and Reprocessable Materials. *Mater Horiz* **2020**, *7* (3), 694–714. https://doi.org/10.1039/c9mh01223k.

(11) Tang, M.; Zheng, P.; Wang, K.; Qin, Y.; Jiang, Y.; Cheng, Y.; Li, Z.; Wu, L. Autonomous Self-Healing, Self-Adhesive, Highly Conductive Composites Based on a Silver-Filled Polyborosiloxane/Polydimethylsiloxane Double-Network Elastomer. *J Mater Chem A Mater* **2019**, *7* (48), 27278–27288.

(12) Liu, F.; Lin, Y.; Yang, X.; Zhang, D.; Xu, D.; Luan, S. Study of Hydrolysis Behaviour of Polyborosiloxane. *Polymer* **2023**, *278*, 126005.

(13) Lee, J.; Jing, B. B.; Porath, L. E.; Sottos, N. R.; Evans, C. M. Shock Wave Energy Dissipation in Catalyst-Free Poly(Dimethylsiloxane) Vitrimers. *Macromolecules* **2020**, *53* (12), 4741–4747.

(14) Zhao, J.; Jiang, N.; Zhang, D.; He, B.; Chen, X. Study on Optimization of Damping Performance and Damping Temperature Range of Silicone Rubber by Polyborosiloxane Gel. *Polymers* **2020**, *12* (5), 1196.

(15) Xu, C.; Wang, Y.; Wu, J.; Song, S.; Cao, S.; Xuan, S.; Jiang, W.; Gong, X. Anti-Impact Response of Kevlar Sandwich Structure with Silly Putty Core. *Compos Sci Technol* **2017**, *153*, 168–177.

(16) Myronidis, K.; Thielke, M.; Kopeć, M.; Meo, M.; Pinto, F. Polyborosiloxane-Based, Dynamic Shear Stiffening Multilayer Coating for the Protection of Composite Laminates under Low Velocity Impact. *Compos Sci Technol* **2022**, *222*, 109395.

(17) Yue, C.; Zhao, L.; Guan, L.; Zhang, X.; Qu, C.; Wang, D.; Weng, L. Vitrimeric Silicone Composite with High Thermal Conductivity and High Repairing Efficiency as Thermal Interface Materials. *J Colloid Interface Sci* **2022**, *620*, 273–283.

(18) Qiu, J.; Lai, X.; Li, H.; Gao, J.; Zeng, X.; Liao, X. Facile Fabrication of a Novel Polyborosiloxane-Decorated Layered Double Hydroxide for Remarkably Reducing Fire Hazard of Silicone Rubber. *Compos B Eng* **2019**, *175*, 107068.

(19) Dong, Y.; Chen, W.; Zhou, X. Synthesis and Characterization of Amino-Terminated Phosphorous Polyborosiloxane and Its Effect on Flame Retardancy of Polymethacrylimide. *Mater Today Chem* **2021**, *20*, 100437.

(20) Ma, J.; Porath, L. E.; Haque, M. F.; Sett, S.; Rabbi, K. F.; Nam, S. W.; Miljkovic, N.; Evans, C. M. Ultra-Thin Self-Healing Vitrimer Coatings for Durable Hydrophobicity. *Nat Commun* **2021**, *12* (1), 5210.

(21) Liu, K.; Pei, A.; Lee, H. R.; Kong, B.; Liu, N.; Lin, D.; Liu, Y.; Liu, C.; Hsu, P. C.; Bao, Z.; Cui, Y. Lithium Metal Anodes with an Adaptive "Solid-Liquid" Interfacial Protective Layer. *J Am Chem Soc* **2017**, *139* (13), 4815–4820.

(22) Wu, Q.; Xiong, H.; Peng, Y.; Yang, Y.; Kang, J.; Huang, G.; Ren, X.; Wu, J. Highly Stretchable and Self-Healing "Solid-Liquid" Elastomer with Strain-Rate Sensing Capability. *ACS Appl Mater Interfaces* **2019**, *11* (21), 19534–19540.

(23) Wu, T.; Chen, B. Synthesis of Multiwalled Carbon Nanotube-Reinforced Polyborosiloxane Nanocomposites with Mechanically Adaptive and Self-Healing Capabilities for Flexible Conductors. *ACS Appl Mater Interfaces* **2016**, *8* (36), 24071–24078.

(24) Zhao, C.; Wang, Y.; Gao, L.; Xu, Y.; Fan, Z.; Liu, X.; Ni, Y.; Xuan, S.; Deng, H.; Gong, X. High-Performance Liquid Metal/Polyborosiloxane Elastomer toward Thermally Conductive Applications. *ACS Appl Mater Interfaces* **2022**, *14* (18), 21564.

(25) Wang, Y.; Wang, S.; Xu, C.; Xuan, S.; Jiang, W.; Gong, X. Dynamic Behavior of Magnetically Responsive Shear-Stiffening Gel under High Strain Rate. *Compos Sci Technol* **2016**, *127*, 169–176. https://doi.org/10.1016/j.compscitech.2016.03.009.

(26) Liu, Z.; Picken, S. J.; Besseling, N. A. M. Polyborosiloxanes (PBSs), Synthetic Kinetics, and Characterization. *Macromolecules* **2014**, *47* (14), 4531–4537.

(27) Kurkin, A.; Lipik, V.; Tan, K. B. L.; Seah, G. L.; Zhang, X.; Tok, A. I. Y. Correlations Between Precursor Molecular Weight and Dynamic Mechanical Properties of Polyborosiloxane (PBS). *Macromol Mater Eng* **2021**, *306* (11), 2100360.

(28) Porath, L.; Huang, J.; Ramlawi, N.; Derkaloustian, M.; Ewoldt, R. H.; Evans, C. M. Relaxation of Vitrimers with Kinetically Distinct Mixed Dynamic Bonds. *Macromolecules* **2022**, *55* (11), 4450–4458.

(29) Drozdov, F. V.; Manokhina, E. A.; Vu, T. D.; Muzafarov, A. M. Polyborosiloxanes (PBS): Evolution of Approaches to the Synthesis and the Prospects of Their Application. *Polymers* **2022**, *14* (22), 4824.

(30) Zhao, Y.; Qin, T.; Jiang, C.; Li, J.; Xiong, Y.; Liu, S.; Qin, J.; Shi, X.; Zhang, G. Boronic Ester-Based Vitrimeric Methylvinyl Silicone Elastomer with "Solid-Liquid" Feature and Rate-Dependent Mechanical Performance. *Polymer* **2023**, *265*, 125545.

(31) Seetapan, N.; Fuongfuchat, A.; Sirikittikul, D.; Limparyoon, N. Unimodal and Bimodal Networks of Physically Crosslinked Polyborodimethylsiloxane: Viscoelastic and Equibiaxial Extension Behaviors. *Journal of Polymer Research* **2013**, *20*, 183.

(32) Drozdov, F. V.; Milenin, S. A.; Gorodov, V. V.; Demchenko, N. V.; Buzin, M. I.; Muzafarov, A. M. Crosslinked Polymers Based on Polyborosiloxanes: Synthesis and Properties. *J Organomet Chem* **2019**, *891*, 72–77.

(33) Rubinsztajn, S. New Facile Process for Synthesis of Borosiloxane Resins. *J Inorg Organomet Polym Mater* **2014**, *24* (6), 1092–1095.

(34) Hofmann, R. J.; Vlatkovic, M.; Wiesbrock, F. Fifty Years of Hydrosilylation in Polymer Science: A Review of Current Trends of Low-Cost Transition-Metal and Metal-Free Catalysts, Non-Thermally Triggered Hydrosilylation Reactions, and Industrial Applications. *Polymers* **2017**, *9* (10), 534.

(35) Lukin, R. Y.; Kuchkaev, A. M.; Sukhov, A. V.; Bekmukhamedov, G. E.; Yakhvarov, D. G. Platinum-Catalyzed Hydrosilylation in Polymer Chemistry. *Polymers* **2020**, *12* (10), 2174.

(36) Zinchenko, G. A.; Mileshkevich, V. P.; Kozlova, N. Investigation of the Synthesis and Hydrolytic Degradation of Polyborodimethylsiloxanes. *Polymer Science U.S.S.R.* **1981**, *23* (6), 1421–1429.

(37) Porath, L. E.; Evans, C. M. Importance of Broad Temperature Windows and Multiple Rheological Approaches for Probing Viscoelasticity and Entropic Elasticity in Vitrimers. *Macromolecules* **2021**, *54* (10), 4782–4791.

(38) Christopher W. Macosko. *Rheology: Principles, Measurements, and Applications*; VCH, 1994.

(39) Montarnal, D.; Capelot, M.; Tournilhac, F.; Leibler, L. Silica-Like Malleable Materials from Permanent Organic Networks. *Science* **2011**, *334* (6058), 965–968.

(40) Cromwell, O. R.; Chung, J.; Guan, Z. Malleable and Self-Healing Covalent Polymer Networks through Tunable Dynamic Boronic Ester Bonds. *J Am Chem Soc* **2015**, *137* (20), 6492–6495.

(41) Robinson, L. L.; Self, J. L.; Fusi, A. D.; Bates, M. W.; Read De Alaniz, J.; Hawker, C. J.; Bates, C. M.; Sample, C. S. Chemical and Mechanical Tunability of 3D-Printed Dynamic Covalent Networks Based on Boronate Esters. *ACS Macro Lett* **2021**, *10*, 857–863.

(42) Li, L.; Chen, X.; Jin, K.; Torkelson, J. M. Vitrimers Designed Both to Strongly Suppress Creep and to Recover Original Cross-Link Density after Reprocessing: Quantitative Theory and Experiments. *Macromolecules* **2018**, *51* (15), 5537–5546.

(43) Breuillac, A.; Kassalias, A.; Nicolaÿ, R. Polybutadiene Vitrimers Based on Dioxaborolane Chemistry and Dual Networks with Static and Dynamic Cross-Links. *Macromolecules* **2019**, *52* (18), 7102–7113.

(44) Saed, M. O.; Gablier, A.; Terentejv, E. M. Liquid Crystalline Vitrimers with Full or Partial Boronic-Ester Bond Exchange. *Adv Funct Mater* **2020**, *30* (3), 1906458.

(45) Konuray, O.; Fernández-Francos, X.; Ramis, X. Structural Design of CANs with Fine-Tunable Relaxation Properties: A Theoretical Framework Based on Network Structure and Kinetics Modeling. *Macromolecules* **2023**, *56* (13), 4855–4873.

(46) Okayama, Y.; Eom, T.; Czuczola, M.; Abdilla, A.; Blankenship, J. R.; Albanese, K. R.; de Alaniz, J. R.; Bates, C. M.; Hawker, C. J. Heterotelechelic Silicones: Facile Synthesis and Functionalization Using Silane-Based Initiators. *Macromolecules* **2023**, *56* (21), 8806–8812.

(47) Lamers, B. A. G.; de Waal, B. F. M.; Meijer, E. W. The Iterative Synthesis of Discrete Dimethylsiloxane Oligomers: A Practical Guide. *Journal of Polymer Science* **2021**, *59* (12), 1142–1150.

Chapter 4. Enahnced tunability in polyborosiloxane networks through functionalized boronate ester crosslinkers

4.1 Introduction

Dynamic polymer networks are a rapidly developing class of materials due to the broad range of mechanical properties that arise from the frequency dependent bond exchange. Whereas traditional thermosets, like crosslinked silicone networks,[1] experience permanent damage, the incorporation of dynamic bonds into such a network allows for reprocessing and self-healing.[2–7] One notable dynamic motif is the transesterification of B–O–Si bonds.[8–10] Polymer networks that contain these borosiloxane crosslinks undergo rapid bond exchange that leads to unique viscoelastic properties, resulting in a material that flows over time but feels solid and can dampen the force of a high speed impact.[11–15] The most notable example of such a material is Silly Putty, which was developed in the 1940s by heating boric acid mixed into a polydimethylsiloxane (PDMS) fluid.[16,17]

Our group recently detailed a synthetic method for the facile preparation of dynamic PDMS-based networks with a borosiloxane-containing crosslinker using hydrosilylation, but the tunability was severely limited. Stress relaxation dynamics were tuned through network architecture and through the addition of a static crosslinker. However, mechanical properties are strongly connected to network architecture, and incorporation of a static crosslinker can cause buildups of residual stress due to the non-exchangeable crosslinks.[18] As such, a way to decouple the network architecture from the bond exchange dynamics would enable a significant increase in control over the resulting network properties.

Tunability in crosslinker chemistry has enabled significant advancements in the design of dynamic networks, leading to orders of magnitude of variability in the bond exchange timescales.[19–22] The Evans group has demonstrated such a strategy in PDMS networks crosslinked through boronic acid derivatives.[23] The authors synthesized a dimethylamine-containing boronic acid crosslinker that demonstrated a four order of magnitude increase in characteristic relaxation time compared to *p*-phenylenediboronic acid due to the internal catalysis of the amine. However, the authors were unable to achieve intermediate rates of stress relaxation. Since these networks are crosslinked through the condensation of boronic acid with linear PDMS terminated with silanol moieties, the crosslinkers must necessarily be bifunctional boronic acid derivatives with four reactive sites, which significantly increases the synthetic burden associated with synthesizing a library of crosslinkers.

Notably, the polyborosiloxane networks that were previously reported by our group can be formed from backbone-functionalized, Si–H containing PDMS. Since these PDMS substrates have numerous reactive sites, a difunctional boronic acid derivative can be used to form a crosslinked network. The prevalence of the Suzuki-Miyaura coupling reaction has led to the development and commercialization of numerous boronic acid derivatives with huge variability in functional groups. Taking advantage of such starting materials, we have synthesized a library of crosslinkers based on esterification of boronic acids where the substituents affect the electronic and steric environment surrounding the boron core, resulting in enhanced tunability in the rate of stress relaxation while retaining the convenience of hydrosilylation-based network formation.

4.2 Experimental

4.2.1 General Crosslinker Synthesis

Boronic acids were dissolved in THF, and 2 equivalents of triethylamine were added to a round bottom flask. Subsequently, the reaction vessel was placed into an ice bath. Subsequently a 1.8 M solution of dimethylvinylchlorosilane in THF was added to an addition funnel. Notably, the addition funnel was open to air, not an inert gas. To prevent unwanted formation of HCl after the reaction, 1.95 equivalents of dimethylvinylchlorosilane were added to ensure complete consumption. The reagent solution was added at a rate of 1 drop per second, causing triethylammonium chloride to precipitate as a white solid. The reaction vessel was then removed from the ice bath and left to react for an additional 30 minutes. The reaction solution was filtered through a cotton plug to remove the salt, flushing with ether. The solvent volume was reduced *in vacuo*, causing more salt to precipitate. The concentrated crude solution was filtered through a 0.45 μm filter. Finally, the solution was distilled into a Schlenk flask stored under nitrogen. Upon purification of the synthesized crosslinkers, the structure and purities were confirmed through nuclear magnetic resonance spectroscopy (^{1}H, ^{11}B, ^{13}C, and ^{29}Si), gas chromatography, and mass spectrometry.

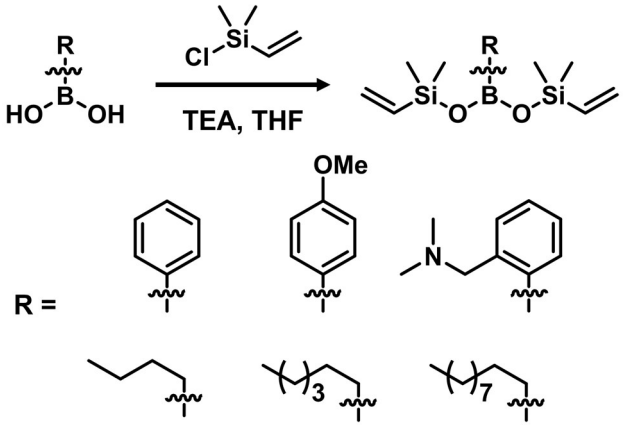

Figure 4.1. Scheme for the synthesis of boronate esters starting from the depicted commercially available boronic acids to generate borosiloxane crosslinkers amenable to hydrosilylation.

4.2.2 General Sample Preparation

The Si–H functional PDMS was degassed under high vacuum at 90 °C for 30 minutes to remove dissolved oxygen. Subsequently, the appropriate crosslinker was added to achieve a 1:1 ratio of Si–H:alkene units. A solution of Karstedt's catalyst inhibited by dimethyl fumarate was added to achieve a Pt concentration of 60 ppm. The mixture was briefly vortexed to mix the components, then briefly degassed to remove air bubbles. The clear solution was then poured into a polystyrene dish and heated to 90 °C for 15 minutes to form an approximately 2 mm thick elastomer. The elastomers were then heated to 140 °C on a hot plate and 25 mm discs were punched out and transferred to a rheometer. Samples were punched out at elevated temperatures to prevent the discs from expanding beyond the rheometer platform when heated during experimentation.

4.3 Results and Discussion

To introduce tunability into polyborosiloxane networks, vinyl-containing borosiloxane crosslinkers were synthesized through the esterification of commercially available boronic acids with dimethylvinylchlorosilane. To ensure the synthesis was successful and the products pure, ^{1}H, ^{11}B, ^{13}C, and ^{29}Si NMR were performed to obtain complementary information about the chemical environments of each nuclei (Figure 4.2). Three doublet of doublets between from 5.7 – 6.4 ppm in ^{1}H NMR and two singlet peaks in the ^{13}C NMR spectra at 130 and 140 ppm

confirmed the presence of vinyl moieties in the final product. To ensure the successful esterification of the boronic acid core, ^{11}B NMR was performed. After the reaction, the single peak shifted upfield due to the functionalization of boronic acid to a borosiloxane. The broad peak in the ^{11}B spectra, however, couldn't discern between the singly and doubly esterified species. As such, ^{29}Si NMR was used to track the number of unique silicon atoms present in the final product. A single peak dominated each Si spectrum with a small impurity present in some of the products, showing that there the product was predominantly a species with a single unique silicon atom with 0% – 5% impurity, which likely corresponded to the hydrolyzed product. To measure the purity while minimizing prolonged exposure to moisture, gas chromatography (GC) was performed, which showed that the products are < 97% pure. The combination of these characterization methods confidently proves that the boronate ester crosslinkers were synthesized with high purity.

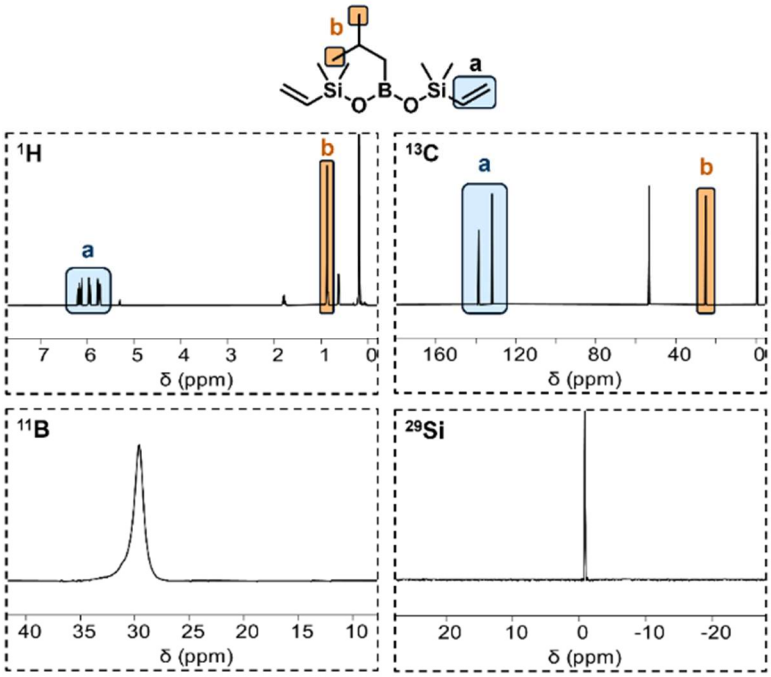

Figure 4.2. NMR spectra probing the ^{1}H, ^{11}B, ^{13}C, and ^{29}Si nuclei for the drawn chemical structure as a representation of the synthesized crosslinkers. The highlighted regions

correspond to the labeled functional groups and the ^{11}B and ^{29}Si spectra show a single peak, illustrating the high purity of the product.

The steric and electronic environments were tuned through alkyl and aryl substituents on the boron core. Three linear aliphatic chains of differing lengths were chosen to alter the sterics. Phenylboronic acid and 4-methoxyphenylboronic acid were synthesized to investigate the electron-donating effect of the methoxy substituent on the crosslinker kinetics—synthetic efforts using strongly electron withdrawing groups proved difficult due to the instability of the product. Additionally, a Wulff-type boronate ester was synthesized using 2-2-(N,N-dimethylamino(methyl))phenylboronic acid as the starting material. Wulff-type boronate esters have been shown to drastically increase the rate of transesterification and consequently the rate of stress relaxation when incorporated into dynamic polymer networks.[24,25]

One key element in the preparation of these networks is the solubility of the boronate crosslinkers in the polydimethylsiloxane matrix. While solvent could be used to ensure mixing, that solvent must then be removed after curing, a lengthy processing step that could cause sample-to-sample variation depending on the degree of solvent removal. Significantly, the synthesized crosslinkers are all liquids that proved to be miscible with the selected Si–H containing PDMS fluid without the need for added solvent.

Hydrosilylation between the alkene-containing crosslinkers and the Si–H containing PDMS fluid was conducted to induce network formation. To enable comparison between formulations, a 6 kDa PDMS fluid with 6 Si–H substituents along the polymer backbone was used for each synthesized network. The formulations were designed to a 1:1 stoichiometric ratio between Si–H and alkene functional groups. Additionally, a solution of Karstedt's catalyst inhibited by dimethyl fumarate was added such that the formulation contained 60 ppm

Pt. Consequently, the networks were bench stable for at least an hour but could react and form a solidified elastomeric network when heated for 15 minutes at 90 °C. Formulations prepared with each crosslinker cured into a solid elastomer (Figure 4.3) when heated in the presence of Karstedt's catalyst. Interestingly, the network crosslinked with the Wulff-boronate crosslinker was significantly more pliable and moldable than the networks prepared with the 5 other crosslinkers, suggesting that the network relaxed stress remarkably fast.

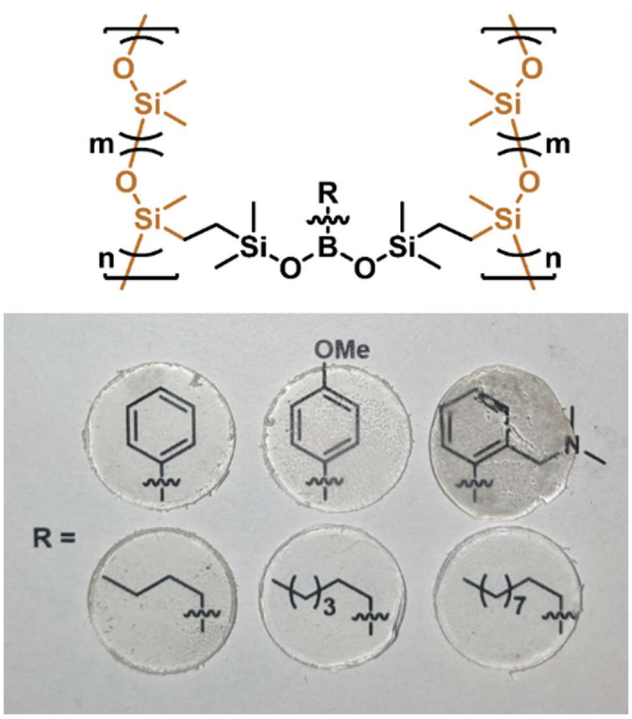

Figure 4.3. Chemical representation of the crosslinked network. The solid elastomeric films correspond to networks formed with the depicted R group.

4.3.1 Tunable Stress Relaxation

Systematic variation in the stress relaxation behavior of the dynamic networks with varying functionality on the boronate ester core was quantified through step-strain rheological measurements. A rapid strain was applied to the elastomers and the decay in modulus was

measured over time (Figure 4.4a and 4.4b). Interestingly, the Wulff-boronate crosslinker had such rapid stress relaxation that a comparison to the other crosslinkers at the same temperature was not possible. A characteristic time constant, τ, was as the time taken for the normalized modulus to decay to a value of e^{-1} where e is the mathematical constant. Importantly, the τ values are temperature dependent and display an Arrhenius temperature dependence with an activation energy corresponding to the bond-exchange mechanism. As such, plotting inverse temperature versus the natural log of τ produces a line where the slope can be used to calculate the aforementioned activation energy (Figure 4.4c). The activation energy values for each tested crosslinker lies in the range of 35 – 55 kJ/mol, which is in the expected value based on previous literature.[23,26]

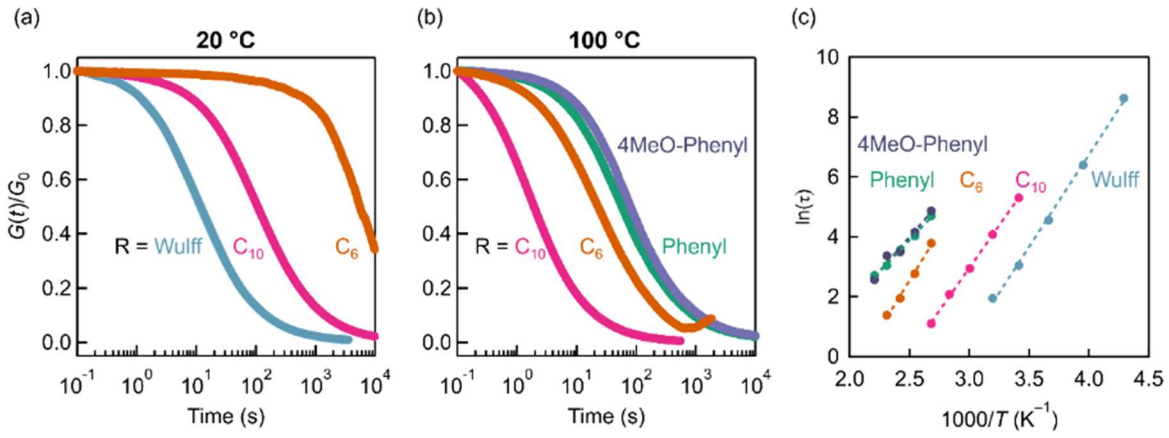

Figure 4.4. Stress relaxation behavior at 20 °C (a) or 100 °C (b) for polyborosiloxane networks prepared from a 6 kDa PDMS copolymer with an average of 6 Si–H containing monomers per chain. The labeled R groups correspond to the functionality on the boronate crosslinker. (c) Linear dependence of ln(τ) versus inverse temperature shows Arrhenius behavior for each tested crosslinker, and the wide span of τ values showcase the broad range of stress relaxation dynamics.

As indicated in Figure 4.4, networks prepared from different crosslinkers displayed different stress relaxation behavior. The electron-withdrawing effect of the methoxy substituent did not significantly impact the stress relaxation dynamics. Interestingly, the incorporation of the N,N-dimethylamino methyl group on the phenyl moiety led to a remarkable increase in the stress relaxation dynamics due to the interaction between the nitrogen lone-pair electrons and the vacant p-orbital on the boron atoms, leading an internal catalytic effect. The crosslinker with the larger aliphatic chain displayed a counterintuitive increase in the rate of stress relaxation compared to the shorter aliphatic chain. This change could be due to the increase in the non-polar character of the crosslinker, which would lead to less repulsion between the crosslinker and the neighboring PDMS chains. Further investigations into this phenomenon are necessary to confirm this hypothesis, and a crosslinker with a branched aliphatic chain could help decouple the effects of sterics and polarity on the resulting stress relaxation behavior.

The incorporation of the synthesized crosslinkers into polyborosiloxane networks demonstrates unprecedented tunability. The facile synthesis of the crosslinkers and the robust curing mechanism results in an approachable strategy to produce a variety of dynamic PDMS networks with a targeted rate of stress relaxation. This strategy enables new avenues of research and facile incorporation of these materials into novel composite systems.

4.4 Conclusions

We have developed a synthetic platform to generate borosiloxane crosslinkers through the esterification of commercially available boronic acid derivatives using dimethylvinylchlorosilane. The vinyl-containing chlorosilane was chosen to impart a reactive functional handle that could be used to crosslink Si–H containing PDMS copolymers through

hydrosilylation. Commercially available boronic acids containing various functional groups were used to vary the electronic and steric environment of the resulting boronate ester crosslinker. Three aromatic and three aliphatic functional groups were chosen to investigate the effects of an electron-withdrawing substituent, internal catalysis, and steric hindrance on the stress relaxation dynamics of polyborosiloxane networks. The boronate esters were characterized through NMR spectroscopy to confirm the expected chemical environment of ^{1}H, ^{11}B, ^{13}C, and ^{29}Si nuclei in the resulting products. Furthermore, gas chromatography was conducted to quantify the purity in the products and confirmed the synthesized products were > 95% pure. Subsequently, polyborosiloxane networks were prepared from a 6 kDa, Si–H containing PDMS copolymer with an average of 6 hydridosilane moieties per chain. Importantly, the crosslinkers were miscible with the PDMS fluid and the catalyst solution. The formulations rapidly crosslinked upon heating at 90 °C. Preliminary stress relaxation measurements showcase unprecedented tunability in polyborosiloxane dynamic networks, with the internally catalytic Wulff-boronate crosslinker showing the fastest rate of stress relaxation and the phenyl boronate and 4-methoxyphenyl boronate showing the slowest rates.

4.5 Materials and Methods

All materials were used as received unless specified. All siloxane samples were purchased from Gelest Inc. Karstedt's catalyst (2 wt% Pt in xylenes), dimethyl fumarate, toluene, tetrahydrofuran, dichloromethane, and dimethylvinylchlorosilane were purchased from Fisher Scientific. An inhibited catalyst solution (1 wt% Pt) was prepared by mixing 1 mL Karstedt's catalyst solution, 1 mL toluene, and 40 mg dimethyl fumarate (4 molar equivalents compared to Pt).

Synthesis of bis(dimethyl(vinyl)silyl) butylboronate

To a 100 mL round bottom flask was added a stirbar, butylboronic acid (2.50 g, 24.5 mmol, 1 eq), THF (50 mL), and triethylamine (4.96 g, 49.0 mmol, 2 eq). The flask was placed into an ice bath and stirred. An addition funnel was added to the flask and charged with THF (25 mL) and dimethyl(vinyl)chlorosilane (5.77 g, 47.8 mmol, 1.95 eq). The chlorosilane solution was added at a rate of 1 drop per second whereupon a white gas formed in the headspace of the flask and a white solid precipitated, indicating HCl and TEA•HCl formation, respectively. After adding the contents of the addition funnel, the flask was removed from the ice bath and left to react for an additional 10 minutes.* The salt was filtered through a piece of cotton plugged into a plastic funnel with diethyl ether being used to rinse the flask and funnel. The volume of solvent was reduced *in vacuo* and the crude mixture was filtered through a syringe plugged with a piece of cotton and a 0.45 μm filter on the end. The recovered solution was then distilled to recover a clear liquid with a boiling point of 75 °C at 340 mTorr (4.00 grams, 62% yield). The product had a 98% purity via GC.

*At this time, there was no visible HCl gas remaining. However, HCl gas released from the flask upon subsequent agitation during workup, so workup should be performed in fume hood to reduce the chances of exposure to the corrosive fumes.

^{1}H NMR (500 MHz, CD_2Cl_2): δ 6.15 (dd, *J* = 20.4, 14.9 Hz, 2H), 5.95 (dd, *J* = 14.8, 3.8 Hz, 2H), 5.74 (dd, *J* = 20.4, 3.8 Hz, 2H), 1.37 – 1.19 (m, 4H), 0.85 (t, *J* = 7.1 Hz, 3H), 0.66 (t, *J* = 7.5 Hz, 2H), 0.19 (s, 12H).

^{11}B NMR (160 MHz, CD_2Cl_2): δ 30.3.

^{13}C NMR (126 MHz, CD_2Cl_2): δ 138.87 , 131.77, 26.91, 25.24, 13.77, –0.62.

^{29}Si NMR (99 MHz, CD_2Cl_2): δ –0.86.

Synthesis of bis(dimethyl(vinyl)silyl) hexylboronate

To a 100 mL round bottom flask was added a stirbar, 1-hexylboronic acid (3.0 g, 23.1 mmol, 1 eq), THF (60 mL), and triethylamine (4.67 g, 46 mmol, 2 eq). The flask was placed into an ice bath and stirred. An addition funnel was added to the flask and charged with THF (20 mL) and dimethyl(vinyl)chlorosilane (5.43 g, 45 mmol, 1.95 eq). The chlorosilane solution was added at a rate of 1 drop per second whereupon a white gas formed in the headspace of the flask and a white solid precipitated, indicating HCl and TEA•HCl formation, respectively. After adding the contents of the addition funnel, the flask was removed from the ice bath and left to react for an additional 10 minutes.* The salt was filtered through a piece of cotton plugged into a plastic funnel with diethyl ether being used to rinse the flask and funnel. The volume of solvent was reduced *in vacuo* and the crude mixture was filtered through a syringe plugged with a piece of cotton and a 0.45 μm filter on the end. The recovered solution was then distilled to recover a clear liquid with a boiling point of 80 °C at 180 mTorr with 95% purity via GC.

*At this time, there was no visible HCl gas remaining. However, HCl gas released from the flask upon subsequent agitation during workup, so workup should be performed in fume hood to reduce the chances of exposure to the corrosive fumes.

^{1}H NMR (500 MHz, CD_2Cl_2) δ 6.15 (dd, J = 20.4, 14.9 Hz, 2H), 5.95 (dd, J = 14.8, 3.8 Hz, 2H), 5.75 (dd, J = 20.4, 3.9 Hz, 2H), 1.41 – 1.15 (m, 8H), 0.87 (t, J = 6.9 Hz, 3H), 0.67 (t, J = 7.5 Hz, 2H), 0.19 (d, J = 1.1 Hz, 12H).**^{11}B NMR** (160 MHz, CD_2Cl_2): δ. 30.3.

^{11}B NMR (160 MHz, CD_2Cl_2): δ 29.9.

^{13}C NMR (126 MHz, CD_2Cl_2): δ. 138.56 , 131.86, 32.16, 31.85, 24.63, 22.66, 13.89–0.61.

^{29}Si NMR (99 MHz, CD_2Cl_2): δ. –0.88.

Synthesis of bis(dimethyl(vinyl)silyl) decylboronate

To a 100 mL round bottom flask was added a stirbar, decylboronic acid (2.78 g, 14.9 mmol, 1 eq), THF (60 mL), and triethylamine (3.51 g, 29.9 mmol, 2 eq). The flask was placed into an ice bath and stirred. An addition funnel was added to the flask and charged with THF (15 mL) and dimethyl(vinyl)chlorosilane (3.02 g, 29.1 mmol, 1.95 eq). The chlorosilane solution was added at a rate of 1 drop per second whereupon a white gas formed in the headspace of the flask and a white solid precipitated, indicating HCl and TEA•HCl formation, respectively. After adding the contents of the addition funnel, the flask was removed from the ice bath and left to react for an additional 10 minutes.* The salt was filtered through a piece of cotton plugged into a plastic funnel with diethyl ether being used to rinse the flask and funnel. The volume of solvent was reduced *in vacuo* and the crude mixture was filtered through a syringe plugged with a piece of cotton and a 0.45 μm filter on the end. The recovered solution was then distilled to recover a clear liquid with a boiling point of 115 °C at 150 mTorr (1.33 grams, 26% yield). The product had a 97% purity via GC.

*At this time, there was no visible HCl gas remaining. However, HCl gas released from the flask upon subsequent agitation during workup, so workup should be performed in fume hood to reduce the chances of exposure to the corrosive fumes.

1H NMR (500 MHz, CD_2Cl_2) δ 6.21 (dd, J = 20.4, 14.9 Hz, 2H), 6.01 (dd, J = 14.9, 3.9 Hz, 2H), 5.80 (dd, J = 20.4, 3.8 Hz, 2H), 1.48 – 1.19 (m, 16H), 0.93 (t, J = 6.8 Hz, 3H), 0.72 (t, J = 7.6 Hz, 2H), 0.25 (s, 12H).

^{11}B NMR (160 MHz, CD_2Cl_2): δ 30.1.

^{13}C NMR (126 MHz, CD_2Cl_2): δ 138.56 , 131.86, 32.49, 31.94, 29.67. 29.60, 29.37, 24.67, 22.70, 13.89, –0.61.

^{29}Si NMR (99 MHz, CD_2Cl_2): δ –0.88.

Synthesis of bis(dimethyl(vinyl)silyl) phenylboronate

To a 100 mL round bottom flask was added a stirbar, phenylboronic acid (2.78 g, 14.9 mmol, 1 eq), DCM (60 mL), and triethylamine (3.51 g, 29.9 mmol, 2 eq). The flask was placed into an ice bath and stirred. An addition funnel was added to the flask and charged with DCM (15 mL) and dimethyl(vinyl)chlorosilane (3.02 g, 29.1 mmol, 1.95 eq). The chlorosilane solution was added at a rate of 1 drop per second whereupon a white gas formed in the headspace of the flask and a white solid precipitated, indicating HCl and triethylammonium chloride formation, respectively. After adding the contents of the addition funnel, the flask was removed from the ice bath and left to react for an additional 10 minutes.* The solution was washed with 50 mL DI water. The organic layer was collected and dried with $MgSO_4$. The volume of solvent was removed *in vacuo.* The recovered solution was then distilled to recover a clear liquid with a boiling point of 65 °C at 150 mTorr (3.2 grams, 52% yield). The product had a 97% purity via GC.

*At this time, there was no visible HCl gas remaining. However, HCl gas released from the flask upon subsequent agitation during workup, so workup should be performed in fume hood to reduce the chances of exposure to the corrosive fumes.

1H NMR (500 MHz, CD_2Cl_2) δ 7.89 – 7.65 (m, 2H), 7.58 – 7.38 (m, 2H), 7.39 – 7.28 (m, 1H), 6.28 (dd, J = 20.4, 14.9 Hz, 2H), 6.03 (dd, J = 14.9, 3.7 Hz, 2H), 5.85 (dd, J = 20.4, 3.7, 1.7 Hz, 2H), 0.33 (d, J = 2.2 Hz, 12H).

^{11}B NMR (160 MHz, CD_2Cl_2): δ 25.3.

^{13}C NMR (126 MHz, CD_2Cl_2): δ 138.43, 135.17, 132.34, 130.56, 127.41, –0.20.

^{29}Si NMR (99 MHz, CD_2Cl_2): δ –1.27.

Synthesis of bis(dimethyl(vinyl)silyl) 4-methoxyphenylboronate

To a 250 mL round bottom flask was added a stirbar, 4-methoxyphenylboronic acid (5.00 g, 32.9 mmol, 1 eq), THF (80 mL), and triethylamine (7.33 g, 65.8 mmol, 2 eq). The flask was placed into an ice bath and stirred. An addition funnel was added to the flask and charged with THF (20 mL) and dimethyl(vinyl)chlorosilane (7.74 g, 64.2 mmol, 1.95 eq). The chlorosilane solution was added at a rate of 1 drop per second whereupon a white gas formed in the headspace of the flask and a white solid precipitated, indicating HCl and TEA•HCl formation, respectively. After adding the contents of the addition funnel, the flask was removed from the ice bath and left to react for an additional 10 minutes.* The salt was filtered through a piece of cotton plugged into a plastic funnel with diethyl ether being used to rinse the flask and funnel. The volume of solvent was reduced *in vacuo* and the crude mixture was filtered through a syringe plugged with a piece of cotton and a 0.45 μm filter on the end. The recovered solution was then distilled to recover a clear liquid with a boiling point of 110 °C at 100 mTorr. The product had a 100% purity via GC.

*At this time, there was no visible HCl gas remaining. However, HCl gas released from the flask upon subsequent agitation during workup, so workup should be performed in fume hood to reduce the chances of exposure to the corrosive fumes.

1H NMR (500 MHz, CD_2Cl_2) δ 7.74 (d, J = 8.6 Hz, 2H), 6.91 (d, J = 8.6 Hz, 2H), 6.30 (dd, J = 20.4, 14.9 Hz, 2H), 6.05 (dd, J = 14.9, 3.7 Hz, 2H), 5.87 (dd, J = 20.4, 3.7 Hz, 2H), 3.85 (s, 3H), 0.35 (s, 12H).

^{11}B NMR (160 MHz, CD_2Cl_2): δ 25.4.

^{13}C NMR (126 MHz, CD_2Cl_2): δ 161.84, 138.60, 137.01, 132.21, 132.19, 112.88, 54.99, -0.22.

^{29}Si NMR (99 MHz, CD_2Cl_2): δ –1.73.

Synthesis of bis(dimethyl(vinyl)silyl) 2-(N,N-dimethylamino(methyl))phenylboronate

To a 250 mL round bottom flask was added a stirbar, 2-(N,N-dimethylamino(methyl))phenylboronate (5.00 g, 27.9 mmol, 1 eq), DCM (150 mL), and triethylamine (5.6 g, 55.9 mmol, 2 eq). The flask was placed into an ice bath and stirred. An addition funnel was added to the flask and charged with THF (15 mL) and dimethyl(vinyl)chlorosilane (6.6 g, 54.5 mmol, 1.95 eq). The chlorosilane solution was added at a rate of 1 drop per second whereupon a white gas formed in the headspace of the flask and a white solid precipitated, indicating HCl and triethylammonium chloride formation, respectively. After adding the contents of the addition funnel, the flask was removed from the ice bath and left to react for an additional 10 minutes.* After adding the contents of the addition funnel, the flask was removed from the ice bath and left to react for an additional 10 minutes.* The solution was washed with 50 mL DI water. The organic layer was collected and dried with $MgSO_4$. The volume of solvent was removed *in vacuo*. The recovered solution was then distilled to recover a clear liquid with a boiling point of 110 °C at 150 mTorr (1.33 grams, 26% yield). The product had a 100% purity via GC.

*At this time, there was no visible HCl gas remaining. However, HCl gas released from the flask upon subsequent agitation during workup, so workup should be performed in fume hood to reduce the chances of exposure to the corrosive fumes.

1H NMR (500 MHz, CD_2Cl_2) δ 7.43 (dd, J = 6.2, 2.1 Hz, 1H), 7.19 (tt, J = 7.4, 5.9 Hz, 2H), 7.10 – 6.91 (m, 1H), 6.12 (dd, J = 20.4, 14.8 Hz, 2H), 5.85 (dd, J = 14.8, 4.2 Hz, 2H), 5.66 (dd, J = 20.4, 4.2 Hz, 2H), 3.78 (s, 2H), 2.43 (s, 6H), 0.06 (s, 12H).

^{11}B NMR (160 MHz, CD_2Cl_2): δ 7.52.

^{13}C NMR (126 MHz, CD_2Cl_2): δ 142.20, 140.00, 130.54, 127.11, 123.21, 65.03, 45.46, 0.92.

^{29}Si NMR (99 MHz, CD_2Cl_2): δ –8.71.

Representative example of curing networks

To a 20 mL glass vial, 1.5 grams (0.6 mmol, HMS-082) of 6 kDa Si–H functional PDMS copolymer were added and degassed at 90 °C and 100 mTorr for at least 15 minutes. Next, 125 mg (0.4 mmol) of tris(dimethylvinylsilyl)borate, and 6 µL inhibited Karstedt's catalyst solution were added to achieve a 1:1 stoichiometric ratio of Si–H to alkene functional groups and 20 ppm Pt. This mixture was vortexed for 1 minute and briefly degassed at room temperature to remove any air bubbles. The solution was poured into a polystyrene dish and heated at 90 °C for 10 minutes to obtain a solid and flexible elastomer.

4.5.1 Chemical Characterization

Attenuated total reflectance Fourier transform infrared spectroscopy (ATR-FTIR) spectra were collected on a Nicolet is10 spectrometer with a diamond ATR accessory. All spectra were collected with 64 scans and a resolution of 4 cm^{-1} in absorbance mode, baseline corrected, and displayed in transmittance mode. Proton nuclear magnetic resonance (NMR) spectra were taken on a Varian Unity Inova AS600 600MHz at 25 °C with 16 scans and a

relaxation delay (d_1) of 15 seconds. Solution state ^{11}B, ^{13}C, and ^{29}Si NMR spectra were taken on a Bruker Avance NEO 500 MHz at 25 °C. ^{11}B spectra used a d_1 value of 2 seconds and 64 scans. ^{13}C used a d_1 value of 2 seconds and 256 scans. ^{29}Si used a d_1 value of 60 seconds and 32 scans.

4.6 Characterization Data

NMR spectra

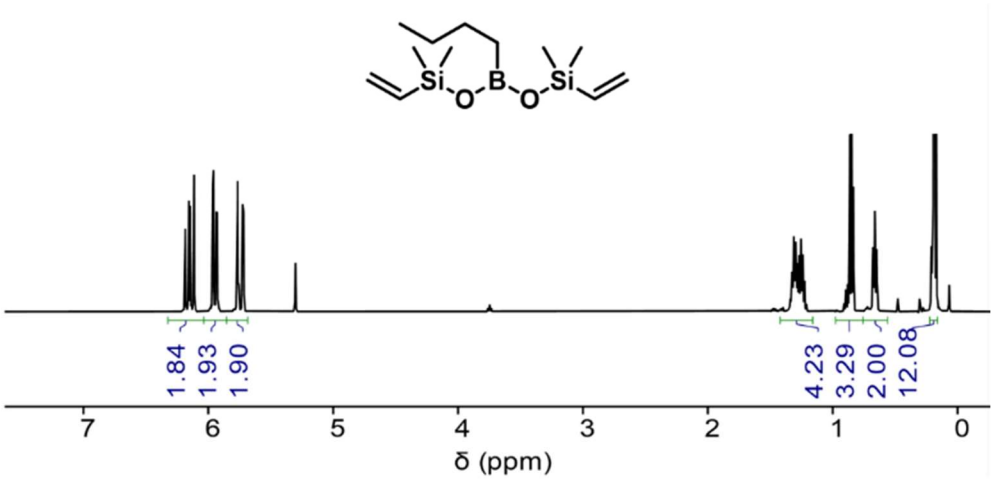

Figure 4.5. ^{1}H NMR spectrum of bis(dimethyl(vinyl)silyl) butylboronate (CD_2Cl_2, 500 MHz).

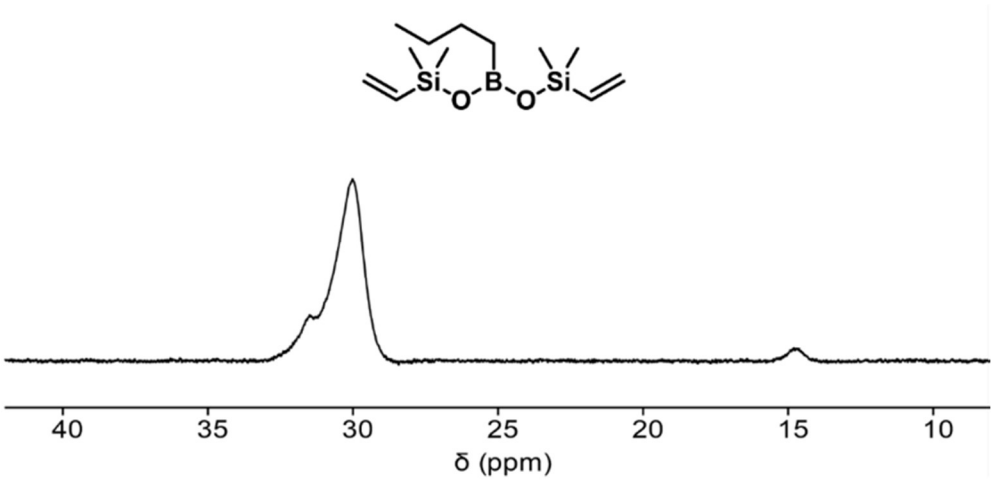

Figure 4.6. ^{11}B NMR spectrum of bis(dimethyl(vinyl)silyl) butylboronate (CD_2Cl_2, 160 MHz).

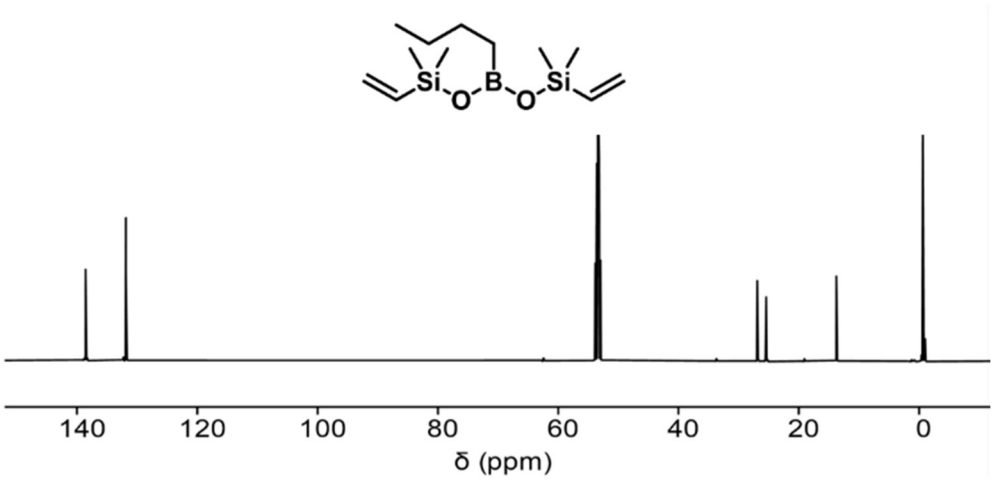

Figure 4.7. ^{13}C NMR spectrum of bis(dimethyl(vinyl)silyl) butylboronate (CD_2Cl_2, 126 MHz).

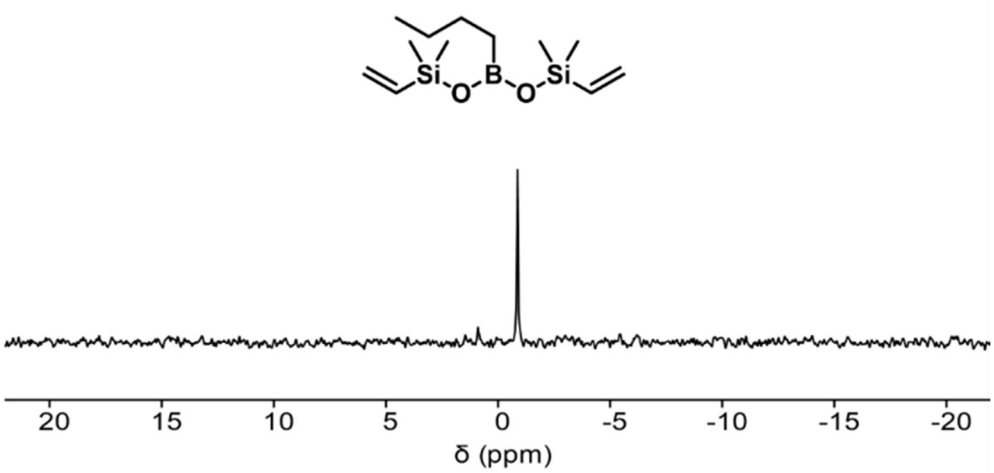

Figure 4.8. ^{29}Si NMR spectrum of bis(dimethyl(vinyl)silyl) butylboronate (CD_2Cl_2, 99 MHz).

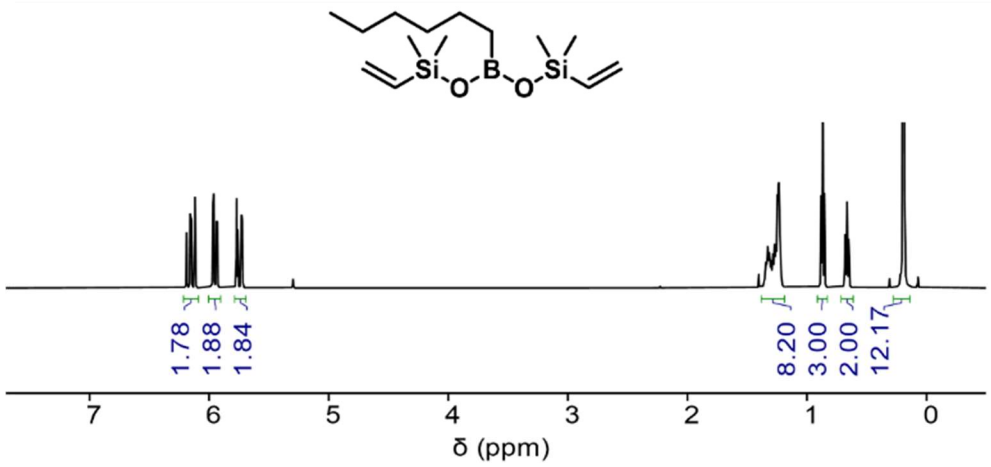

Figure 4.9. ^{1}H NMR spectrum of bis(dimethyl(vinyl)silyl) hexylboronate (CD_2Cl_2, 500 MHz).

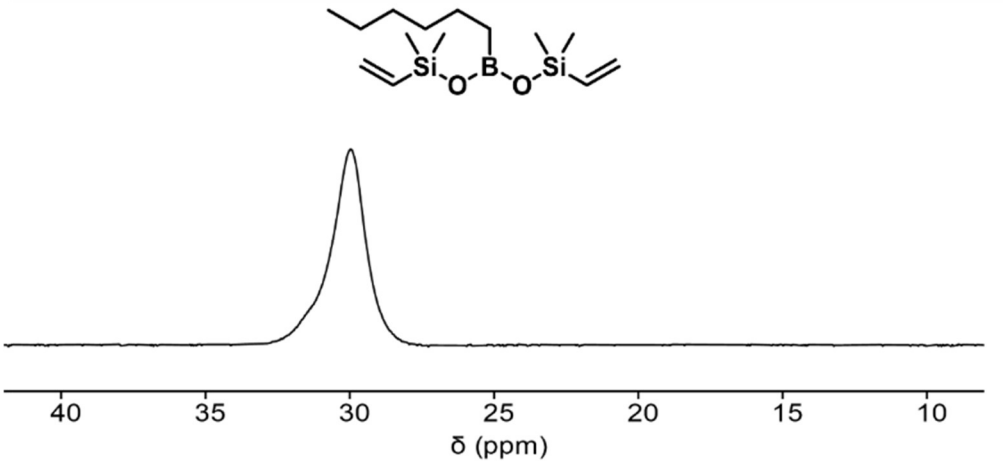

Figure 4.10. ^{11}B NMR spectrum of bis(dimethyl(vinyl)silyl hexylboronate (CD_2Cl_2, 160 MHz).

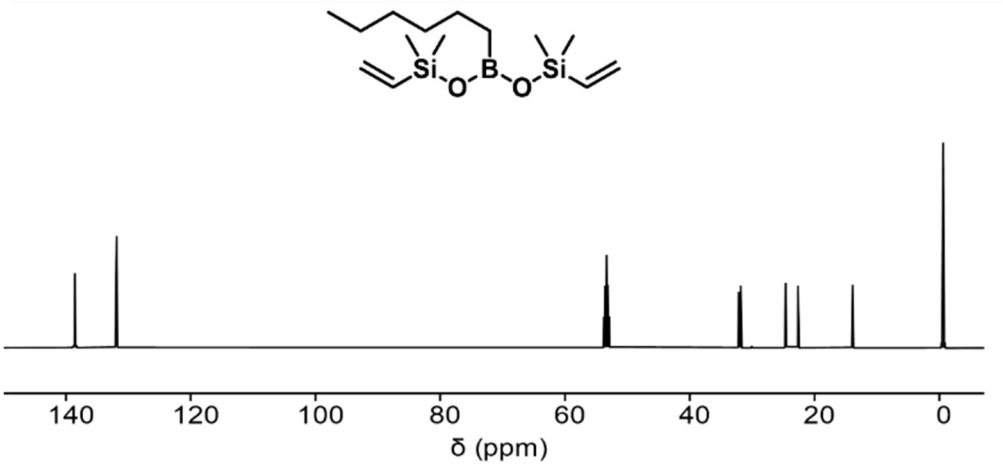

Figure 4.11. ^{13}C NMR spectrum of bis(dimethyl(vinyl)silyl) hexylboronate (CD_2Cl_2, 126 MHz).

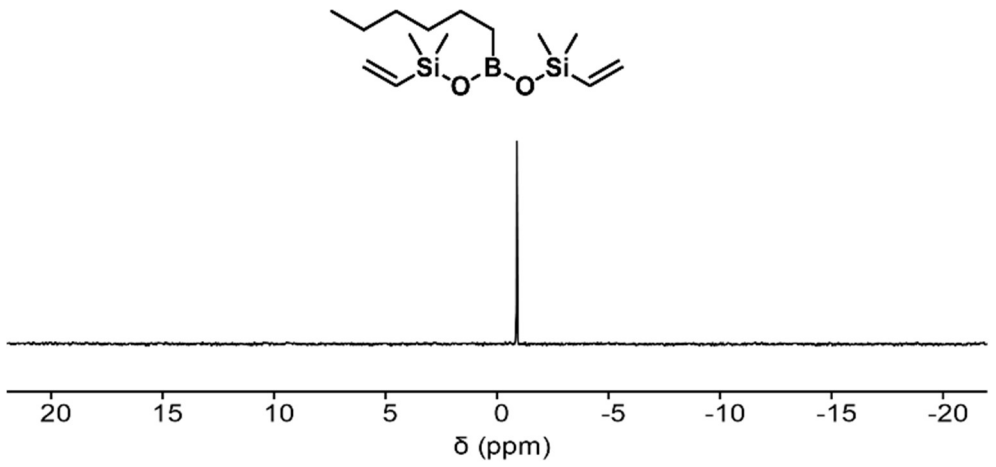

Figure 4.12. ^{29}Si NMR spectrum of bis(dimethyl(vinyl)silyl) hexylboronate (CD_2Cl_2, 99 MHz).

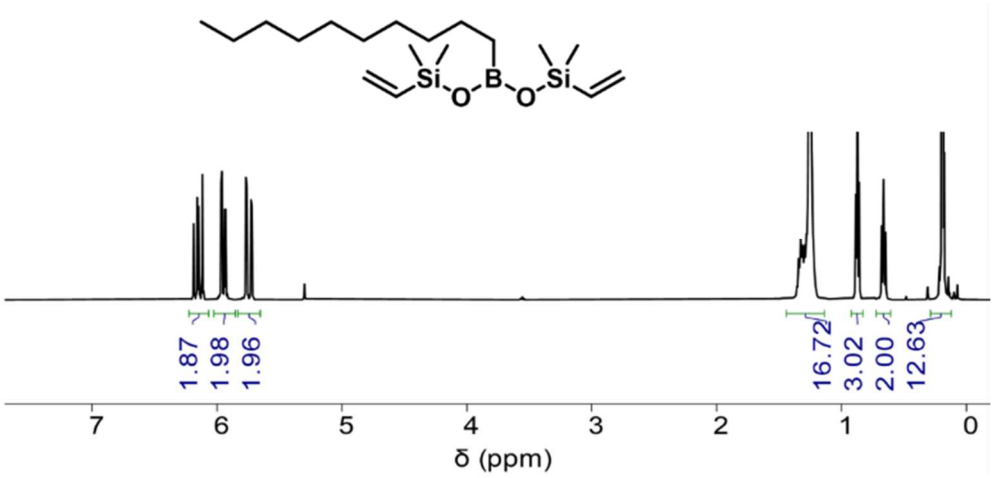

Figure 4.13. ^{1}H NMR spectrum of bis(dimethyl(vinyl)silyl) decylboronate (CD_2Cl_2, 500 MHz).

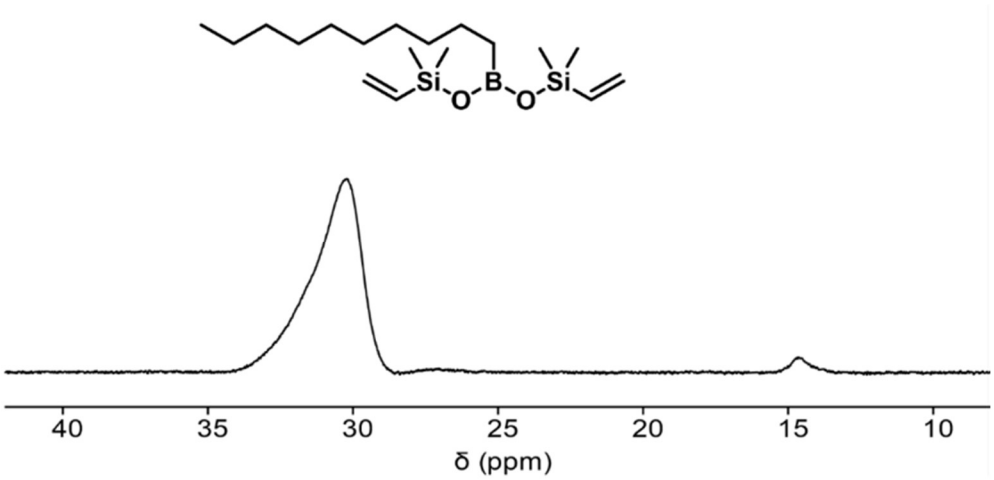

Figure 4.14. ^{11}B NMR spectrum of bis(dimethyl(vinyl)silyl) decylboronate (CD_2Cl_2, 160 MHz).

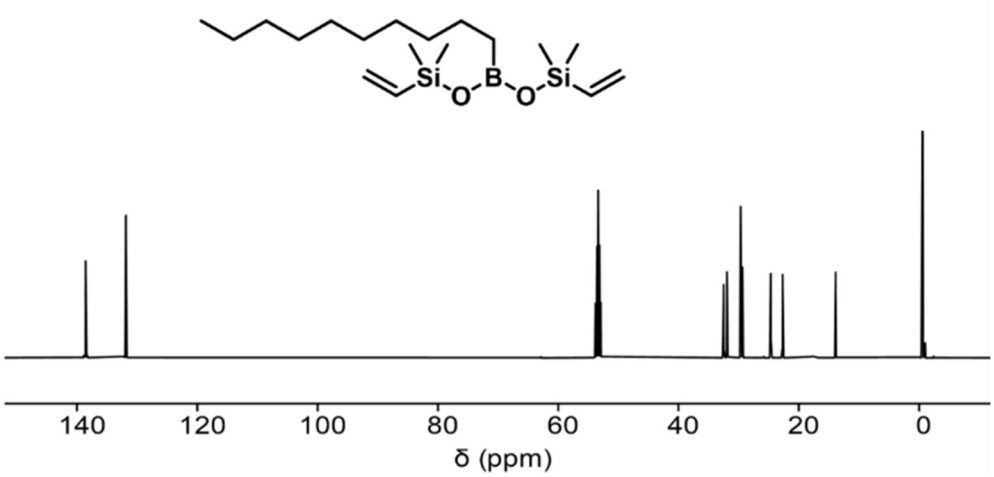

Figure 4.15. ^{13}C NMR spectrum of bis(dimethyl(vinyl)silyl) decylboronate (CD_2Cl_2, 126 MHz).

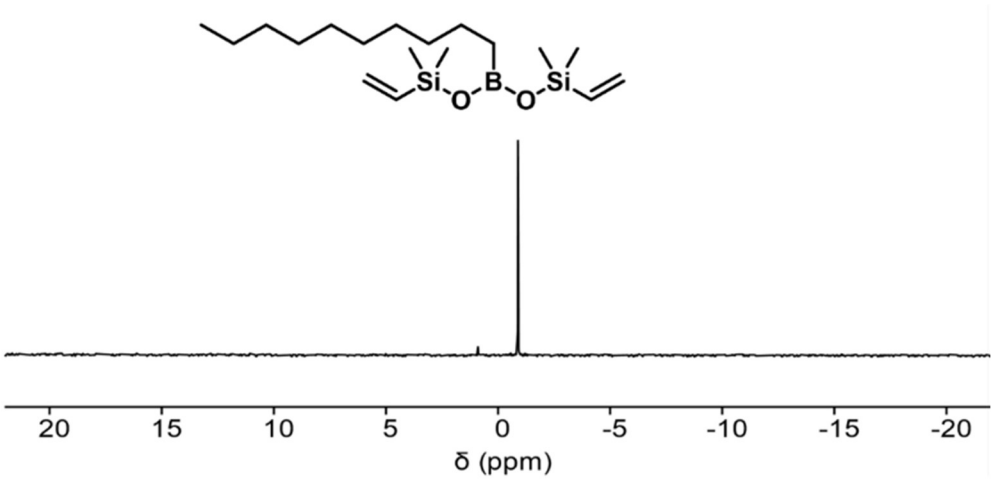

Figure 4.16. ^{29}Si NMR spectrum of bis(dimethyl(vinyl)silyl) decylboronate (CD_2Cl_2, 99 MHz).

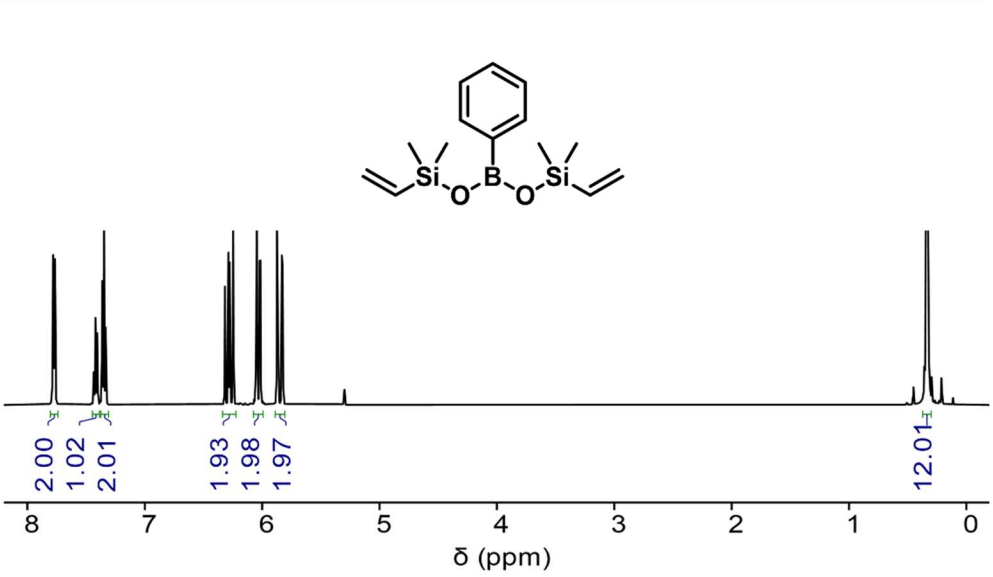

Figure 4.17. ^{1}H NMR spectrum of bis(dimethyl(vinyl)silyl) phenylboronate (CD_2Cl_2, 500 MHz).

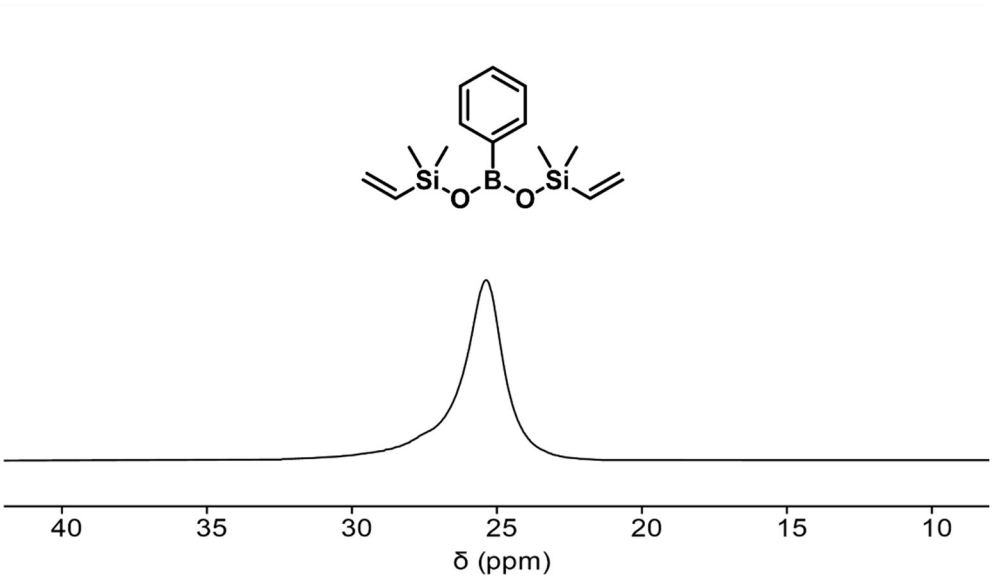

Figure 4.18. ^{13}B NMR spectrum of bis(dimethyl(vinyl)silyl) phenylboronate (CD_2Cl_2, 160 MHz).

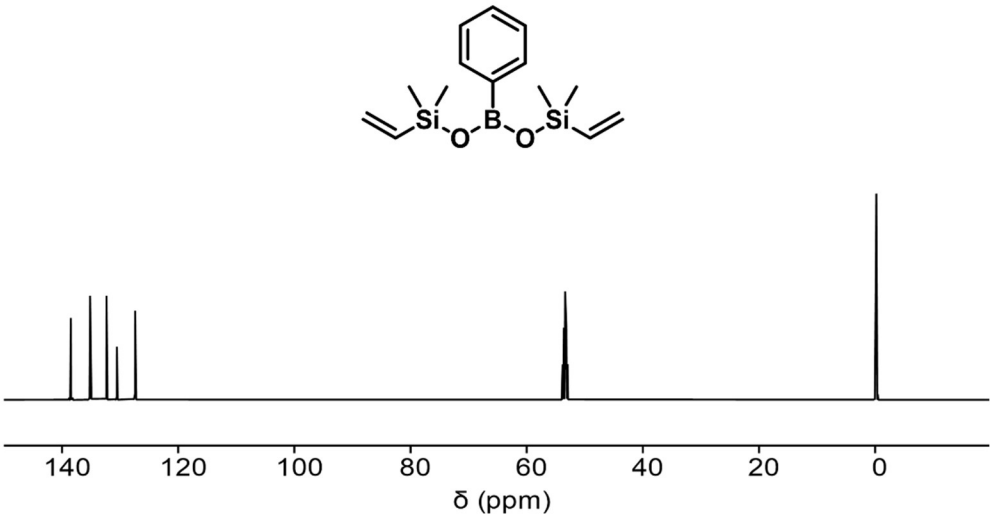

Figure 4.19. ^{1}H NMR spectrum of bis(dimethyl(vinyl)silyl) phenylboronate (CD_2Cl_2, 126 MHz).

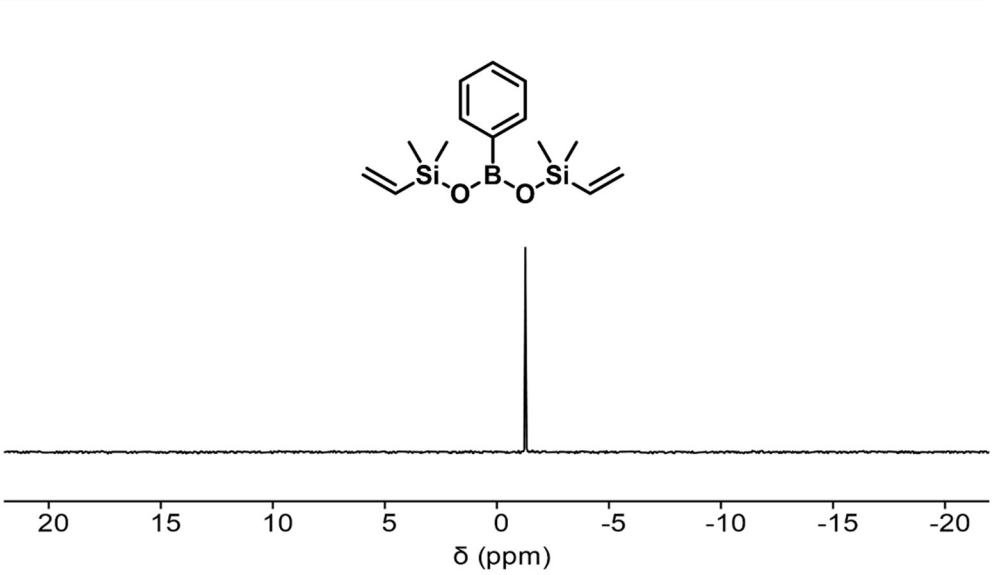

Figure 4.20. ^{29}Si NMR spectrum of bis(dimethyl(vinyl)silyl) phenylboronate (CD_2Cl_2, 99 MHz).

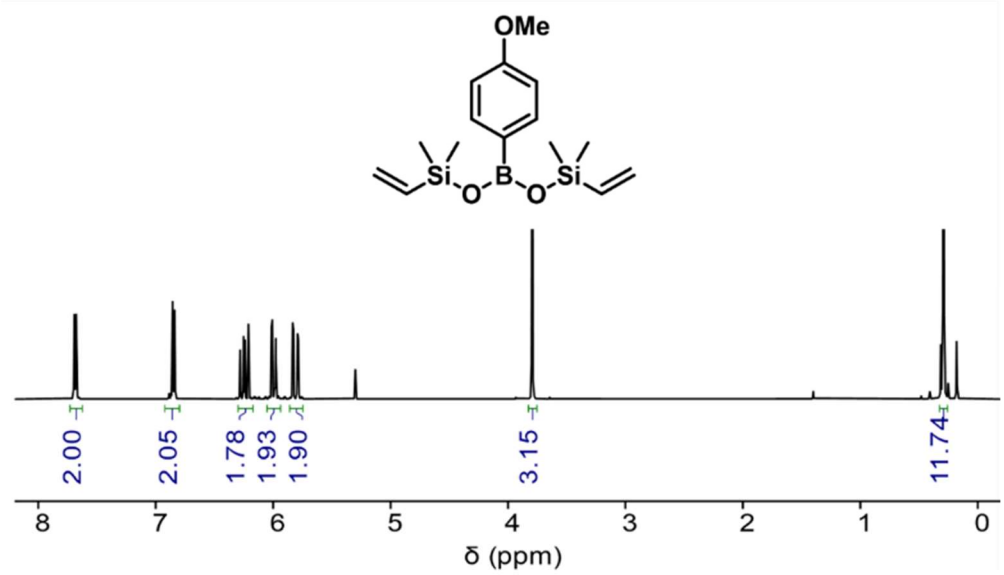

Figure 4.21. ^{1}H NMR spectrum of bis(dimethyl(vinyl)silyl) 4-methoxyphenylboronate (CD_2Cl_2, 500 MHz).

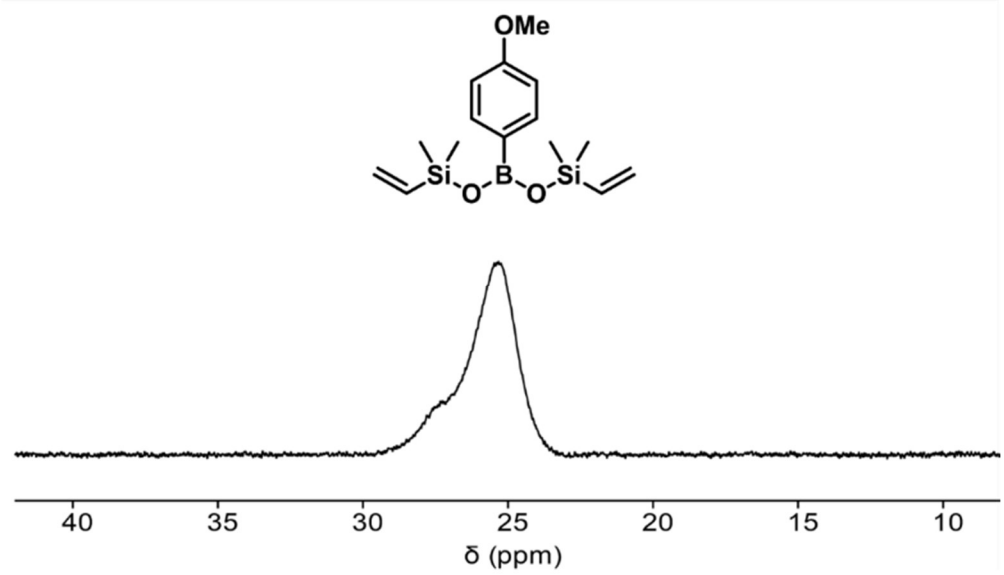

Figure 4.22. ^{13}B NMR spectrum of bis(dimethyl(vinyl)silyl) 4-methoxyphenylboronate (CD_2Cl_2, 160 MHz).

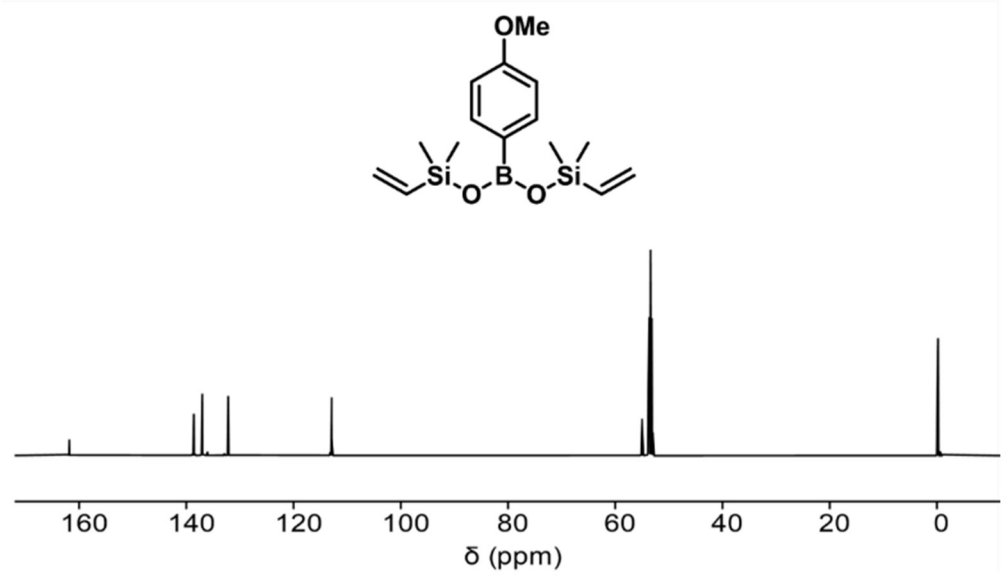

Figure 4.23. ^{1}H NMR spectrum of bis(dimethyl(vinyl)silyl) 4-methoxyphenylboronate (CD_2Cl_2, 126 MHz).

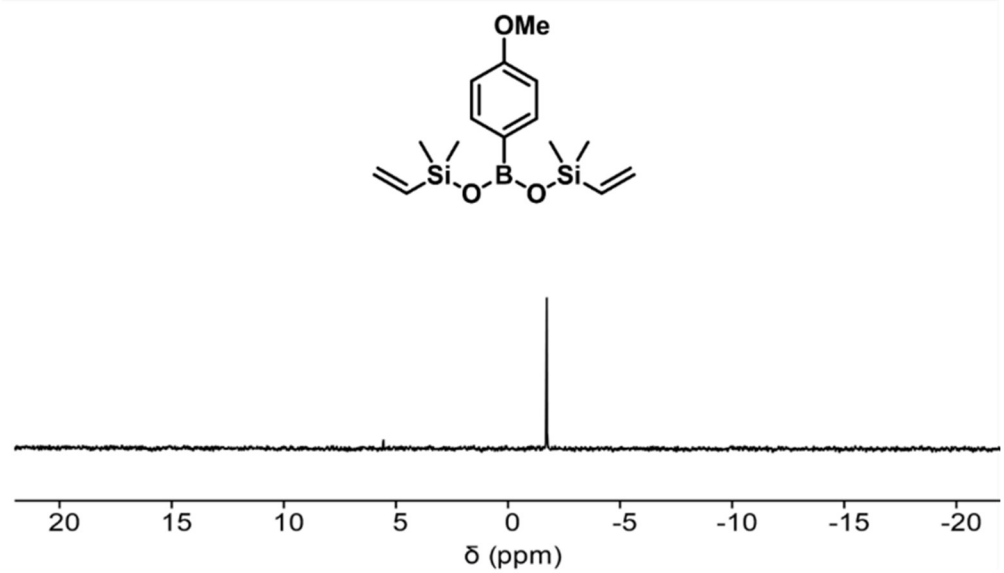

Figure 4.24. ^{29}Si NMR spectrum of bis(dimethyl(vinyl)silyl) 4-methoxyphenylboronate (CD_2Cl_2, 99 MHz).

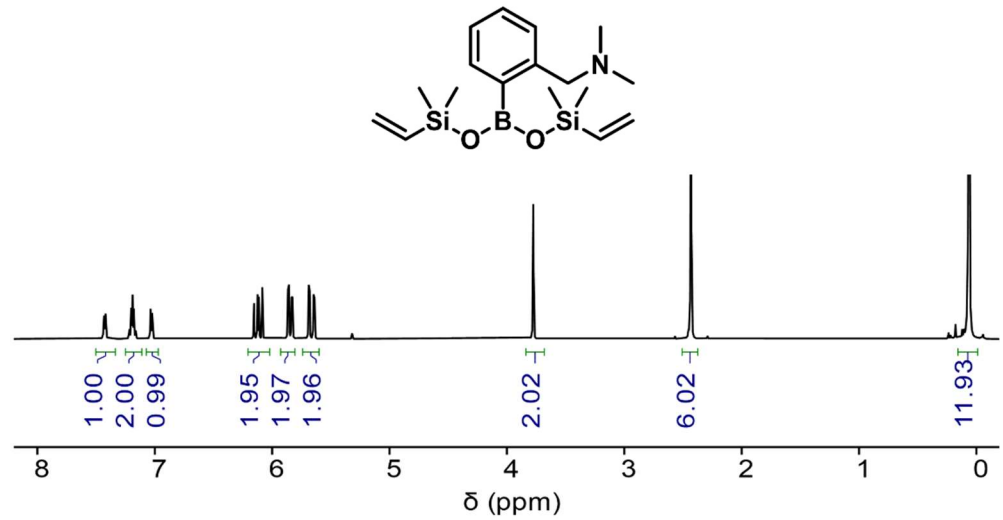

Figure 4.25. ^{1}H NMR spectrum of bis(dimethyl(vinyl)silyl) 2-(N,N-dimethylamino(methyl)) phenylboronate (CD_2Cl_2, 500 MHz).

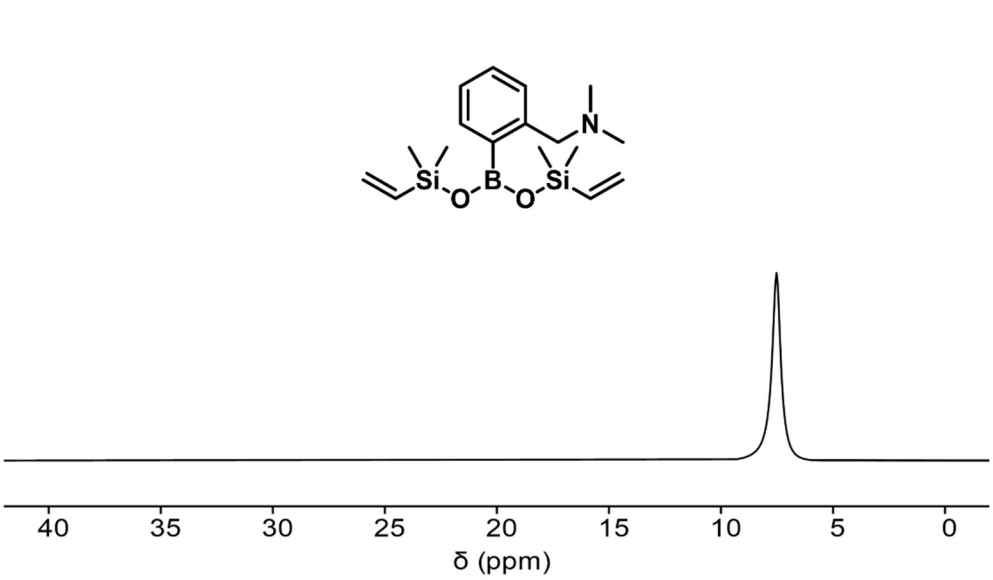

Figure 4.26. ^{13}B NMR spectrum of bis(dimethyl(vinyl)silyl) 2-(N,N-dimethylamino(methyl)) phenylboronate (CD_2Cl_2, 160 MHz).

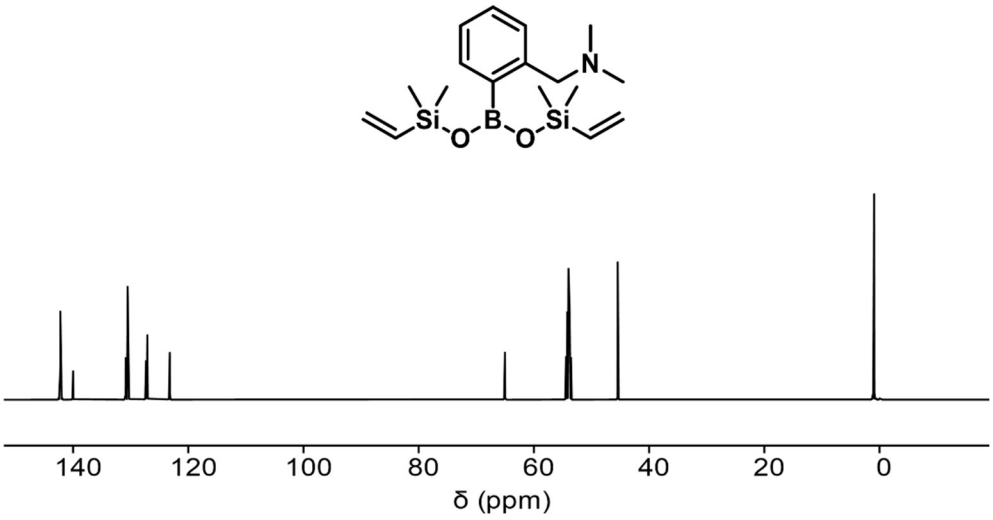

Figure 4.27. ^{1}H NMR spectrum of bis(dimethyl(vinyl)silyl) 2-(N,N-dimethylamino(methyl)) phenylboronate (CD_2Cl_2, 126 MHz).

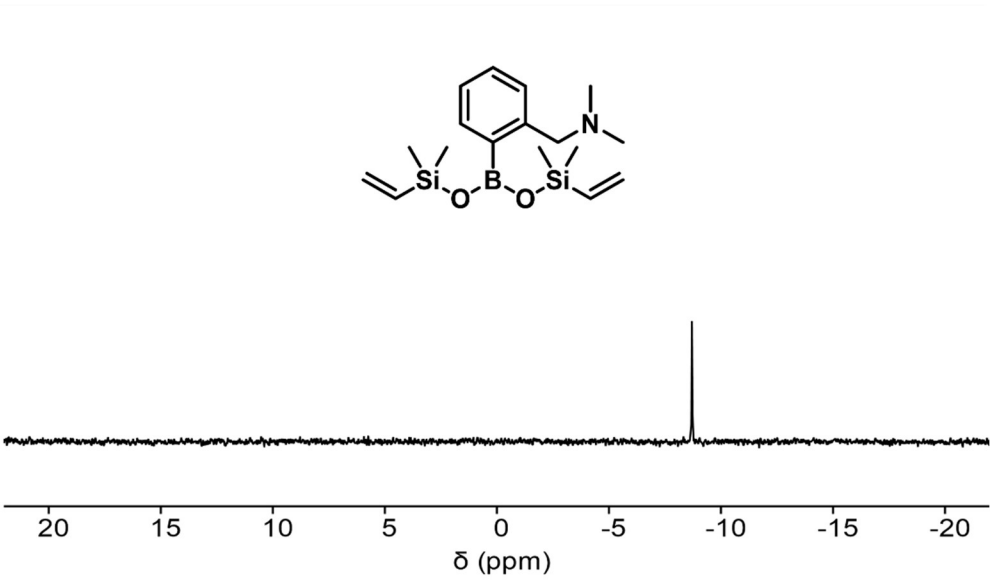

Figure 4.28. ^{29}Si NMR spectrum of bis(dimethyl(vinyl)silyl) 2-(N,N-dimethylamino(methyl)) phenylboronate (CD_2Cl_2, 99 MHz).

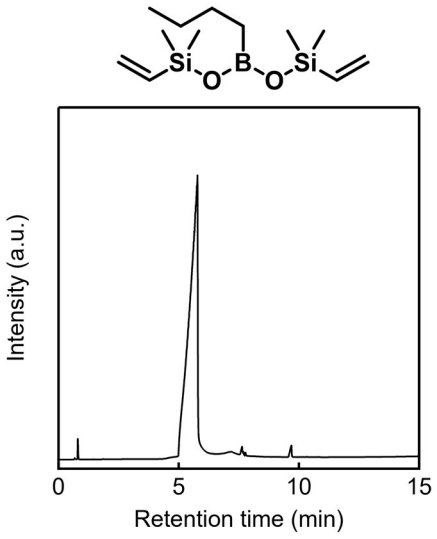

Figure 4.29. GC trace of bis(dimethyl(vinyl)silyl) butylboronate.

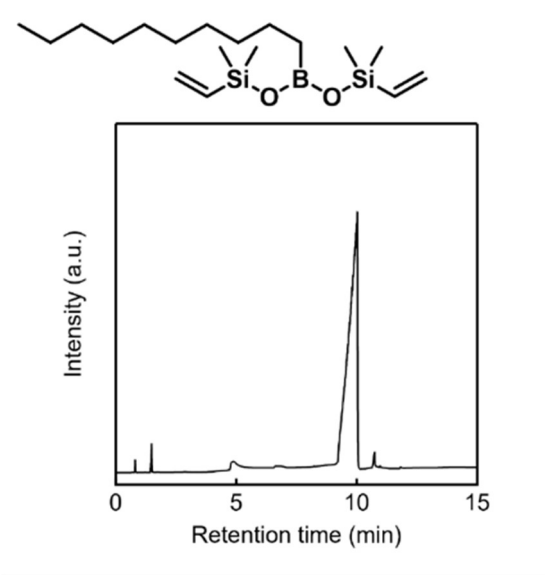

Figure 4.30. GC trace of bis(dimethyl(vinyl)silyl) decylboronate.

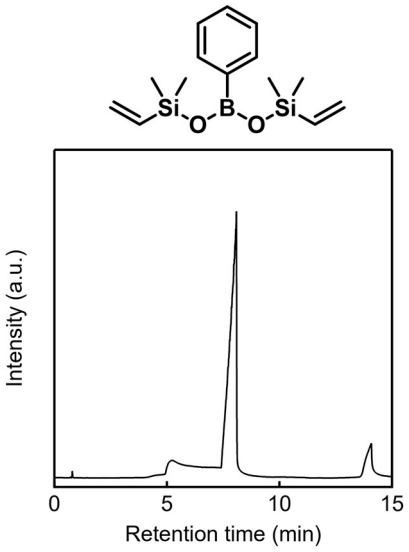

Figure 4.31. GC trace of bis(dimethyl(vinyl)silyl) phenylboronate.

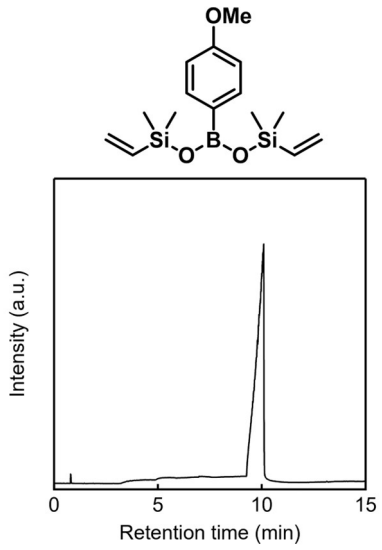

Figure 4.32. GC trace of bis(dimethyl(vinyl)silyl) 4-methoxyphenylboronate.

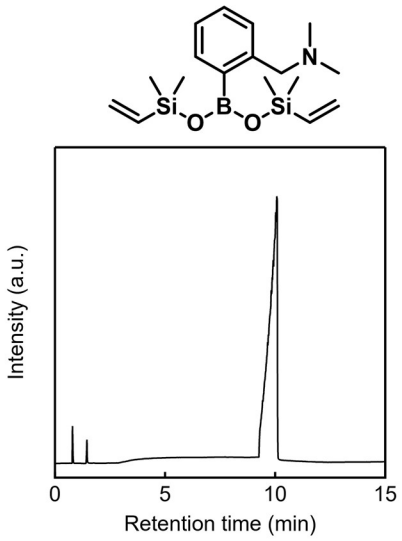

Figure 4.33. GC trace of bis(dimethyl(vinyl)silyl) 2-(N,N-dimethylamino(methyl)) phenylboronate.

4.7 References

(1) Mazurek, P.; Vudayagiri, S.; Skov, A. L. How to Tailor Flexible Silicone Elastomers with Mechanical Integrity: A Tutorial Review. *Chem Soc Rev* **2019**, *48* (6), 1448–1464.

(2) Chen, C.; Fei, H. F.; Watkins, J. J.; Crosby, A. J. Soft Double-Network Polydimethylsiloxane: Fast Healing of Fracture Toughness. *J Mater Chem A Mater* **2022**, *10* (21), 11667–11675.

(3) Chen, Z.; Sun, Y. C.; Wang, J.; Qi, H. J.; Wang, T.; Naguib, H. E. Flexible, Reconfigurable, and Self-Healing TPU/Vitrimer Polymer Blend with Copolymerization Triggered by Bond Exchange Reaction. *ACS Appl Mater Interfaces* **2020**, *12* (7), 8740–8750.

(4) Ma, J.; Porath, L. E.; Haque, M. F.; Sett, S.; Rabbi, K. F.; Nam, S. W.; Miljkovic, N.; Evans, C. M. Ultra-Thin Self-Healing Vitrimer Coatings for Durable Hydrophobicity. *Nat Commun* **2021**, *12* (1), 5210.

(5) Islam, S.; Bhat, G. Progress and Challenges in Self-Healing Composite Materials. *Mater Adv* **2021**, *2* (6), 1896–1926.

(6) Feng, Z.; Yu, B.; Hu, J.; Zuo, H.; Li, J.; Sun, H.; Ning, N.; Tian, M.; Zhang, L. Multifunctional Vitrimer-Like Polydimethylsiloxane (PDMS): Recyclable, Self-Healable, and Water-Driven Malleable Covalent Networks Based on Dynamic Imine Bond. *Ind Eng Chem Res* **2019**, *58* (3), 1212–1221.

(7) Yue, C.; Zhao, L.; Guan, L.; Zhang, X.; Qu, C.; Wang, D.; Weng, L. Vitrimeric Silicone Composite with High Thermal Conductivity and High Repairing Efficiency as Thermal Interface Materials. *J Colloid Interface Sci* **2022**, *620*, 273–283.

(8) Liu, Z.; Picken, S. J.; Besseling, N. A. M. Polyborosiloxanes (PBSs), Synthetic Kinetics, and Characterization. *Macromolecules* **2014**, *47* (14), 4531–4537.

(9) Drozdov, F. V.; Manokhina, E. A.; Vu, T. D.; Muzafarov, A. M. Polyborosiloxanes (PBS): Evolution of Approaches to the Synthesis and the Prospects of Their Application. *Polymers (Basel)* **2022**, *14* (22), 4824.

(10) Kurkin, A.; Lipik, V.; Tan, K. B. L.; Seah, G. L.; Zhang, X.; Tok, A. I. Y. Correlations Between Precursor Molecular Weight and Dynamic Mechanical Properties of Polyborosiloxane (PBS). *Macromol Mater Eng* **2021**, *306* (11), 2100360.

(11) Wu, Q.; Xiong, H.; Peng, Y.; Yang, Y.; Kang, J.; Huang, G.; Ren, X.; Wu, J. Highly Stretchable and Self-Healing "Solid-Liquid" Elastomer with Strain-Rate Sensing Capability. *ACS Appl Mater Interfaces* **2019**, *11* (21), 19534–19540.

(12) Zhao, Y.; Qin, T.; Jiang, C.; Li, J.; Xiong, Y.; Liu, S.; Qin, J.; Shi, X.; Zhang, G. Boronic Ester-Based Vitrimeric Methylvinyl Silicone Elastomer with "Solid-Liquid" Feature and Rate-Dependent Mechanical Performance. *Polymer* **2023**, *265*, 125545.

(13) Goertz, M. P.; Zhu, X. Y.; Houston, J. E. Temperature Dependent Relaxation of a ' "Solid-Liquid." *J Polym Sci B Polym Phys* **2009**, *47* (13), 1285–1290.

(14) Xu, C.; Wang, Y.; Wu, J.; Song, S.; Cao, S.; Xuan, S.; Jiang, W.; Gong, X. Anti-Impact Response of Kevlar Sandwich Structure with Silly Putty Core. *Compos Sci Technol* **2017**, *153*, 168–177.

(15) Lee, J.; Jing, B. B.; Porath, L. E.; Sottos, N. R.; Evans, C. M. Shock Wave Energy Dissipation in Catalyst-Free Poly(Dimethylsiloxane) Vitrimers. *Macromolecules* **2020**, *53* (12), 4741–4747.

(16) McGregor, R. R.; Warrick, E. Treating Dimethyl Silicone Polymer with Boric Oxide, 1947.

(17) Wright, J. G. E. Process for Making Puttylike Elastic Plastic, Siloxane Derivative Composition Containing Zinc Hydroxide, 1951.

(18) Li, L.; Chen, X.; Jin, K.; Torkelson, J. M. Vitrimers Designed Both to Strongly Suppress Creep and to Recover Original Cross-Link Density after Reprocessing: Quantitative Theory and Experiments. *Macromolecules* **2018**, *51* (15), 5537–5546.

(19) Schoustra, S. K.; Dijksman, J. A.; Zuilhof, H.; Smulders, M. M. J. Molecular Control over Vitrimer-like Mechanics – Tuneable Dynamic Motifs Based on the Hammett Equation in Polyimine Materials. *Chem Sci* **2021**, *12* (1), 293–302.

(20) Scheutz, G. M.; Lessard, J. J.; Sims, M. B.; Sumerlin, B. S. Adaptable Crosslinks in Polymeric Materials: Resolving the Intersection of Thermoplastics and Thermosets. *J Am Chem Soc* **2019**, *141* (41), 16181–16196.

(21) Robinson, L. L.; Taddese, E. S.; Self, J. L.; Bates, C. M.; Read de Alaniz, J.; Geng, Z.; Hawker, C. J. Neighboring Group Participation in Ionic Covalent Adaptable Networks. *Macromolecules* **2022**, *55* (21), 9780–9789.

(22) Van Lijsebetten, F.; Debsharma, T.; Winne, J. M.; Du Prez, F. E. A Highly Dynamic Covalent Polymer Network without Creep: Mission Impossible? *Angewandte Chemie International Edition* **2022**, *61* (48).

(23) Porath, L.; Huang, J.; Ramlawi, N.; Derkaloustian, M.; Ewoldt, R. H.; Evans, C. M. Relaxation of Vitrimers with Kinetically Distinct Mixed Dynamic Bonds. *Macromolecules* **2022**, *55* (11), 4450–4458.

(24) Zhao, Z.; Li, C.; Zuo, J. Dynamic Polymeric Materials Based on Reversible B–O Bonds with Dative Boron–Nitrogen Coordination. *SmartMat* **2023**, *4* (3).

(25) Wulff, G.; Lauer, M.; Böhnke, H. Rapid Proton Transfer as Cause of an Unusually Large Neighboring Group Effect. *Angewandte Chemie International Edition in English* **1984**, *23* (9), 741–742.

(26) Kang, B.; Kalow, J. A. Internal and External Catalysis in Boronic Ester Networks. *ACS Macro Lett* **2022**, *11* (3), 394–401.

Appendix A. Rapid and Selective Deposition of Patterned Thin Films on Heterogeneous Substrates via Spin Coating[2]

A.1 Introduction

An abundance of thin film patterning techniques — for example, optical lithography,[1] imprint lithography,[2] and microcontact printing[3] — underpin many types of contemporary technology ranging from microelectronics[4] to tailored bio-surfaces.[5] Frequently, three-dimensional design targets require iterative thin film processing to create structures that cannot be formed in a single step.[1, 6] The added complexity of overlay and alignment can create significant practical difficulties that amplify economic costs.[7] In principle, these challenges could be alleviated by self-aligned patterning, which uses existing chemical and/or topographic features to template subsequent layers.[8]

A variety of strategies have been developed to achieve self-aligned patterning of inorganic and organic materials in thin films.[9-12] Each involves manipulating selectivity during the deposition step by blocking or promoting film formation via interfacial engineering. One common approach leverages the preferential attachment of self-assembled monolayers (SAMs) to spatially control nucleation, growth, and/or wettability.[13] For example, Bent and co-workers have exploited alkylphosphonic acid SAMs to protect copper (Cu) and induce area-selective atomic layer deposition (AS-ALD) of inorganic oxides only on silicon dioxide (SiO_2).[14] SAMs can similarly influence the spatial distribution of polymer films through phase

[2] This Appendix was originally published in *ACS Applied Materials and Interfaces*. Reproduced with permission from *ACS Applied Materials and Interfaces* 2019, 11, 23, 21177–21183. Copyright 2019, American Chemical Society.

separation,[15-16] self-assembly,[17] localized brush growth,[18] and thermal dewetting.[19-20] Significantly, unlike inorganics, the majority of this past work on SAM-directed polymer thin film patterning placed SAMs on flat, homogeneous substrates, e.g., with microcontact printing.[21] Developing similar capabilities to selectively pattern polymer thin films on heterogeneous (e.g., metal/dielectric) surfaces would provide fundamental insight that might someday be useful in technological applications.

To address this opportunity, our attention was drawn to a technique known as spin dewetting, which results in the local segregation of polymers *during* spin coating and requires no post-processing or additional steps to generate patterns.[22-23] Past work has highlighted the simplicity of spin dewetting in comparison to more complex patterning approaches.[24] Bhandaru at al. explored using topographic poly(dimethylsiloxane) substrates and demonstrated an impressive array of resulting polymer structures depending on pre-pattern dimensions and coating conditions.[25-26] In addition, Lee et al. selectively deposited block copolymers on patterned surfaces via careful temperature control.[27] Despite promise, there still remains significant uncertainty surrounding the design rules that govern spin dewetting as a function of material selection and processing. Here, we systematically investigate SAM-promoted spin dewetting using homogeneous (SiO_2) and heterogeneous (Cu/SiO_2; TiN/SiO_2) substrates that are relevant to the microelectronics industry. Significantly, incomplete SAM layers are sufficient to induce spin dewetting, resulting in selective polymer deposition on Cu and TiN lines under optimal conditions.

A.2 Materials

Anhydrous toluene, dioxane, methanol, octyltrichlorosilane (OTS), and octadecyltrichlorosilane (ODTS) were purchased from Sigma-Aldrich and used without

further purification. Butyltrichlorosilane (BTS) and dodecyltrichlorosilane (DDTS) were purchased from Gelest, Inc. and used without further purification. Cu and TiN stripes on SiO_2 wafers were patterned by standard photolithography using lift-off.

A.3 General Methods

A.3.1 Silane deposition on Cu/SiO_2 and TiN/SiO_2.

Homogenous SiO_2 and heterogeneous TiN/SiO_2. Substrates (e.g. SiO_2 and TiN/SiO_2) were cleaned by sonication in acetone, isopropanol, and MilliQ® water for 3 minutes each, followed by UVO treatment in a Model 18 UVO cleaner (Jelight, USA) for 10 minutes. The substrates were immersed without stirring in 5 mM alkyltrichlorosilane solution in toluene for 5 minutes unless otherwise noted. The substrates were sonicated in toluene and acetone for 3 minutes each to remove excess silane. These conditions were adapted from literature procedures.[28] Water contact angle measurements indicate that silane preferentially covers TiN in the presence of SiO_2 (Figure A.9).

Heterogeneous Cu/SiO_2. Substrates were sonicated in acetone, isopropanol, and MilliQ® water for 3 minutes each, treated with the same UVO cleaner for 10 minutes, and sonicated in acetic acid for 5 minutes and acetone for 3 minutes prior to immersion in 5 mM alkyltrichlorosilane solution in toluene for 5 minutes unless otherwise noted. The substrates were then sonicated in toluene for 3 minutes, acetone for 3 minutes, acetic acid for 5 minutes, and acetone for 3 minutes.

A.3.2 Spin coating conditions

A droplet of 15 μL polymer solution (e.g., 50 mg/mL of PS in toluene or PAA in 50/50 vol% dioxane/methanol) was dispensed by a micropipette to fully cover the substrate and

immediately spun at 10,000 rpm for 60 s at a ramp rate of 3 s using a 6800 Spin Coater (Speciality Coating Systems, USA) unless otherwise described.

A.3.3 Surface Characterization

SIMS imaging was performed using a Camera IMS 7f system (Camera SAS, Gennevilliers, France) with a 15 keV caesium beam on an analytical area of 200 μm^2 by monitoring ^{28}Si and ^{12}C signals. About 100 images were taken over one spot and overlaid to generate the average image. Tapping mode (AFM) experiments were performed using a Multimode system (Veeco, USA) to investigate the surface. Measurements were conducted using commercial silicon cantilevers (resonant frequency: 190 kHz, force constant: 48 N/m, model: Tap190Al-G, NanoAndMore USA). Polymer film thickness on homogeneous surfaces was determined by an alpha-SE spectroscopic ellipsometer (J.A. Woollam Co.) or a DektakXT Stylus Profilometer (Bruker Corporation). Optical micrographs were captured with an Olympus BX51 optical microscope in reflectance mode. Contact angle measurements were performed using a ramé-hart Model 290 advanced goniometer. Deionized water was dispensed to measure static contact angles. Snapshots were taken immediately after deposition of the water droplets and analyzed by DROPimage Advanced.

A.4 Results and Discussion

A.4.1 Spin Dewetting on Homogeneous Surfaces

Spin dewetting on partially formed SAMs was initially examined using homogeneous surfaces. As depicted in Figure A.1a, SiO_2 substrates were submersed in alkyltrichlorosilane solutions and the surface silanol groups reacted for varying amounts of time (t) to control surface coverage. For example, using octyltrichlorosilane (OTS), an increase in the water contact angle with t (Figure A.1b) indicates a higher SAM coverage[29] due to alkyl chain

hydrophobicity. Spin coating of polystyrene (PS) on these surfaces was then quantified by ellipsometry and optical microscopy and correlated with the water contact angle of the surface. Figure A.1b demonstrates a transition from spin wetting to spin dewetting on OTS-functionalized SiO_2. This reproducible transition is observed at a critical time ($t_c \approx 1$ min) well before the plateau in water contact angle (onset circa 4 min), suggesting that silanol functionalization is incomplete at shorter times. Analogous experiments with poly(acrylic acid) (PAA) spin coated from 50/50 vol% dioxane/methanol yield identical conclusions (**Figure S2**). Homogeneous SiO_2 surfaces partially functionalized with OTS SAM thus induce spin dewetting of polar (PAA) and non-polar (PS) polymers. This behavior still persists after extended storage of the OTS–SiO_2 substrate (e.g., one year) under ambient conditions (Figure A.2), which illustrates the robustness of this surface functionalization process and the ability to control spin dewetting with incomplete grafting densities. As will be discussed below, the specific choice of alkyl group allows for further tuning of the critical deposition time t_c by varying the hydrophobic SAM chemistry.

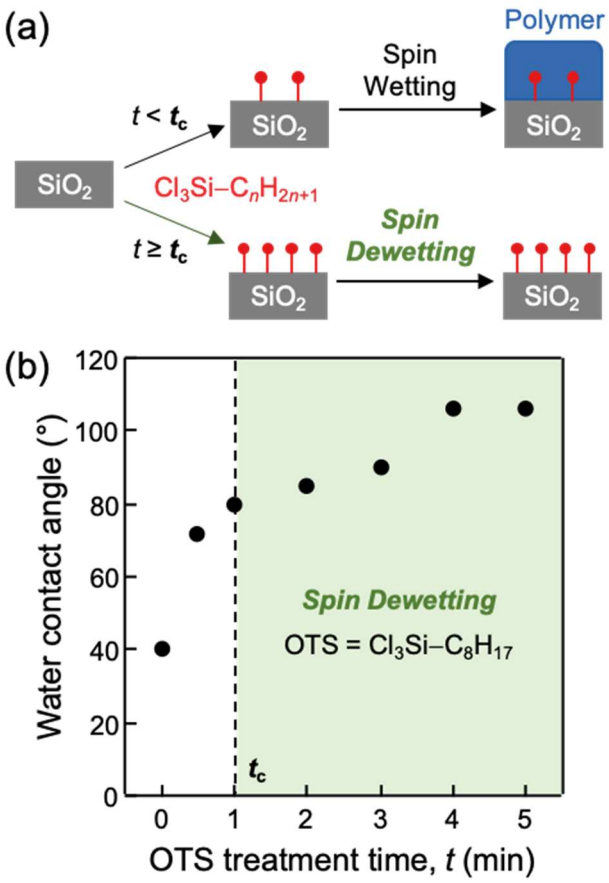

Figure A.1. (a) Illustration of homopolymer dewetting on homogeneous SiO_2 functionalized with an alkylsilane self-assembled monolayer. Spin dewetting or lack thereof depends on the SAM deposition time t. (b) Water contact angle measurements as a function of OTS SAM deposition time (t). Spin coating PS on these OTS-functionalized surfaces (see Figure A.11) indicates spin dewetting occurs after a critical time $t_c \approx 1$ min that corresponds with incomplete SAM coverage. Spin coating conditions: PS, 21.5 kDa, 5 wt% in toluene at 10k rpm.

Having established that spin dewetting can be induced by incomplete SAMs, the role of spin coating conditions was systematically investigated. For these experiments, SiO_2 substrates were treated with OTS for 5 min prior to spin coating PS with varying molecular weights at different spin speeds and concentrations. Figure A.2a shows the film thickness as a

function of spin speed for 5 wt% solutions of PS in toluene on unfunctionalized SiO_2 surfaces (open symbols). As expected, film thickness decreases monotonically with increasing spin speeds and lower solution viscosity (small molecular weight or solution concentration).[30-31] In direct contrast, on OTS–SiO_2 surfaces (filled red symbols) complete dewetting is observed at low spin speeds with no polymer deposited (see also Figure A.10).[32] Significantly, a sharp transition occurs at spin speeds of ≈4k rpm, termed ω^*, after which continuous films are formed with thicknesses comparable to those on native SiO_2 substrates and which follow the expected decreasing trend with increasing spin speeds. Similar abrupt transitions from spin dewetting to spin wetting are observed for increasing polymer concentration (≈2.3 wt%) (Figure A.2b) and polystyrene molecular weight (≈30 kDa) (Figure A.2c).

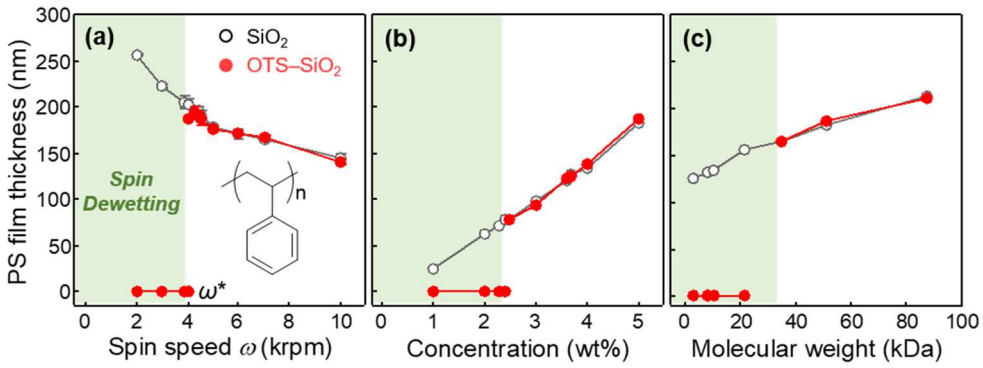

Figure A.2. Abrupt transitions are observed in the spin dewetting of PS from OTS–SiO_2 as indicated by the film thickness dependence on (a) spin speed, (b) weight concentration, and (c) molecular weight. Note that the PS film thickness is nearly identical on SiO_2 and OTS–SiO_2 after the spin-dewetting transition in all cases. Spin coating conditions: (a) PS, 51.0 kDa, 5 wt% in toluene at varying spin speeds from 2k to 10k rpm; (b) PS, 5 wt% in toluene at 5k rpm with varying molar mass; (c) PS, 51.0 kDa, in toluene at 5k rpm with varying weight concentration.

We attribute this unique transition between spin dewetting and spin wetting on homogeneous surfaces to a competition between polymer dewetting and solvent evaporation. During the course of spin coating, surface hydrophobicity of the grafted alkylsilane in conjunction with centrifugal forces exerted on the fluid drive polymer dewetting. This behavior is opposed by solvent evaporation, which increases solution viscosity and reduces polymer chain mobility until eventual film vitrification. Lower spin speeds, molecular weight, and polymer concentration all favor dewetting before solidification. Our interpretation is further supported by estimates of solution viscosity using an empirical equation reported by Grishchuk and Estrin;[33] the spin wetting to dewetting transitions observed herein for molecular weight and concentration occur around the same viscosity ≈0.584 mPa·s (Figure A.12).

Since dewetting during spin coating is driven by the unfavorable interfacial interactions between the substrate grafted with alkylsilane and the polymer solution, we hypothesized that tuning the SAM hydrophobicity should allow further control over spin dewetting. To investigate this possibility, SiO_2 wafers were functionalized with alkyltrichlorosilane ($Cl_3Si–C_nH_{2n+1}$) of different chain lengths: BTS (butyltrichlorosilane, n = 4), OTS (n = 8), DDTS (dodecyltrichlorosilane, n = 12), and ODTS (octadecyltrichlorosilane, n = 18) (Figure A.3). Note that all SAMs were deposited for 5 minutes and there may be different t_c and plateau times for each (Figure A.1). As expected, longer alkyl chains render the SiO_2 surface more hydrophobic as evidenced by static water contact angle measurements (Figure A.13). Significantly, for the longest alkyl chain, ODTS–SiO_2 (n = 18), PS dewets across the entire range of accessible spin speeds (2k–10k rpm), while decreasing the alkyl chain length from ODTS (n = 18) to DDTS (n = 12) and OTS (n = 8) results in well-defined transitions from spin

dewetting to spin wetting depending on the spin speed. This sharp transition ω^* is observed at 8.3k rpm for DDTS (n = 12) and 4.0k rpm for OTS (n = 8). Further decreasing the alkyl chain length to BTS (n = 4) results in the disappearance of a spin dewetting regime, with PS coating the surface across the entire range of tested spin speeds (2k – 10k rpm). The data in Figure A.3 clearly indicate that the spin dewetting regime can be controlled by varying the chemistry of grafted SAMs. Increased hydrophobicity leads to a wider window for spin dewetting.

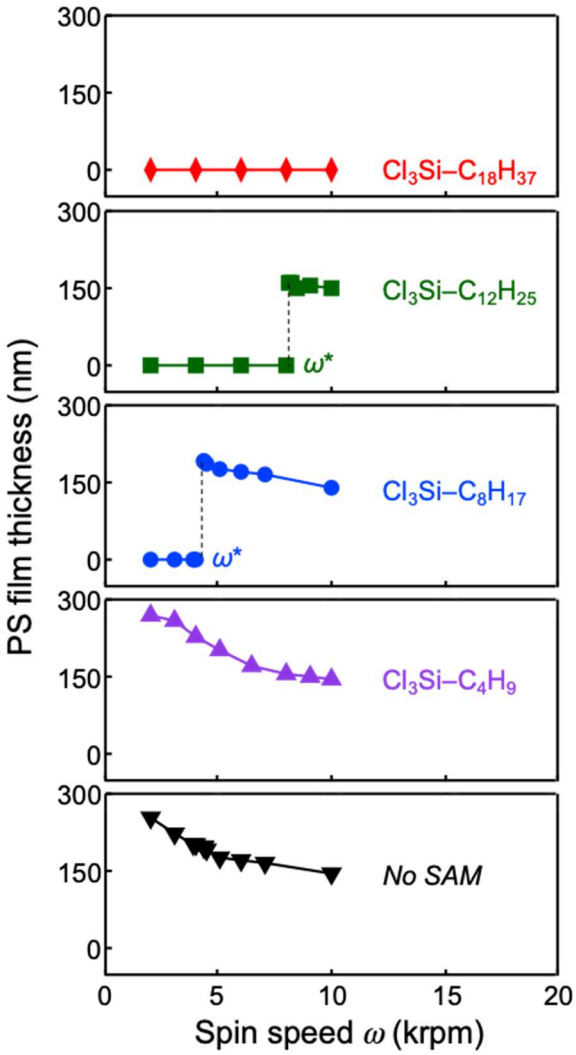

Figure A.3. SAM hydrophobicity is correlated with the range of spin speeds over which spin dewetting occurs and the location of an abrupt transition ω*. Data correspond to film thickness of PS versus spin speed on SiO_2 functionalized with alkyltrichlorosilanes ($Cl_3Si–C_nH_{2n+1}$, 5

min deposition time): BTS (butyltrichlorosilane, n = 4), OTS (n = 8), DDTS (dodecyltrichlorosilane, n = 12), and ODTS (octadecyltrichlorosilane, n = 18). Note that the silane deposition time in all cases was 5 min. Spin coating conditions: PS, 51.0 kDa, 5 wt% in toluene at varying spin speeds from 2k−10k rpm.

The versatility of SAM-induced spin dewetting was then demonstrated by extension to a wide range of other polymers. For example, a variety of glassy polymers spanning different polarities, including poly(acrylic acid) (PAA), poly(lactide) (PLA), poly(vinyl chloride) (PVC), poly(methyl methacrylate) (PMMA), and polt(*tert*-butyl acrylate) (PtBA) all exhibit a spin dewetting-to-wetting transition. Interestingly, the critical concentration at which this crossover occurs depends on polymer polarity (Figure A.14). This transition is also evident for rubbery polymers (at 25 °C) such as poly(butadiene) and poly(ethylene oxide), with two important differences. The crossover from spin wetting to dewetting is not as sharp and in this intermediate zone the polymer partially dewets to form holes or droplets (Figure A.14). In addition, the structures formed in the intermediate regime are unpredictable and inconsistent. Finally, a wetting/dewetting transition is also evident for poly(methyl acrylate) bottlebrush polymers, indicating that the spin dewetting transition is not limited to linear polymers. The ubiquitous presence of a spin wetting/dewetting transition in all the materials described above suggests this is a general phenomenon that can be tuned through structural as well as processing factors.

A.4.2 Spin Dewetting on Heterogeneous Surfaces

Having demonstrated spin dewetting on homogeneous substrates, heterogeneous surfaces were then investigated to probe the relationship between selectivity and SAM coverage. Equal line–space patterns of copper (Cu) or titanium nitride (TiN) on SiO_2 were prepared by photolithography (Figures A.15–A.16) with the deposition of Cu and TiN resulting in minimal topography (circa 5 nm) when compared to the lateral pitch (≥10 μm). In examining the spin dewetting process on heterogeneous surfaces, two key steps were considered (Figure A.4): (1) preferential deposition of a SAM on select surfaces to promote local dewetting, and (2) selective deposition of polymer over other regions via subsequent spin coating. Based on the data presented in Figure A.3, OTS (n = 8) was chosen as a model for preliminary studies since it places ω^* at a convenient spin speed.

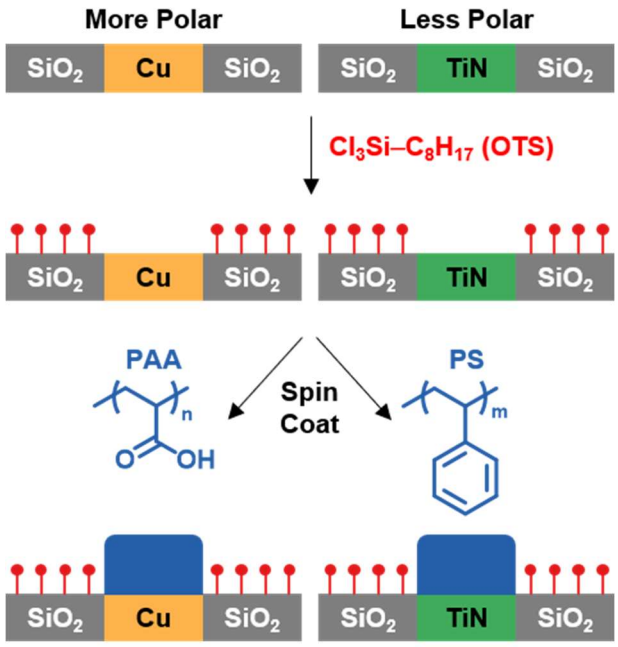

Figure A.4. Illustration of spin dewetting on heterogeneous surfaces. The preferential functionalization of SiO_2 with a hydrophobic alkylsilane induces selective polymer deposition on the opposing material during spin coating.

As-fabricated Cu/SiO_2 and TiN/SiO_2 line-space patterns were therefore treated with OTS ($n = 8$) for different lengths of time (t). At times greater than $t_c > 1$ min (c.f., homogeneous surfaces shown in Figure A.1), OTS induces spin dewetting of both poly(acrylic acid) (PAA) on Cu/OTS–SiO_2 and PS on TiN/OTS–SiO_2 to give spatial localization of the polymer film only on the Cu or TiN areas (Figure A.5). In contrast, below t_c, PS and PAA solutions were observed to coat the entire substrate leading to a continuous film. This significant difference illustrates the role that partial SAM functionalization (with application time $t > t_c$) plays in promoting spin dewetting on heterogeneous surfaces. Note the contrast with other selective deposition techniques that require much more uniform SAMs to achieve area selectivity, for example AS-ALD.[14]

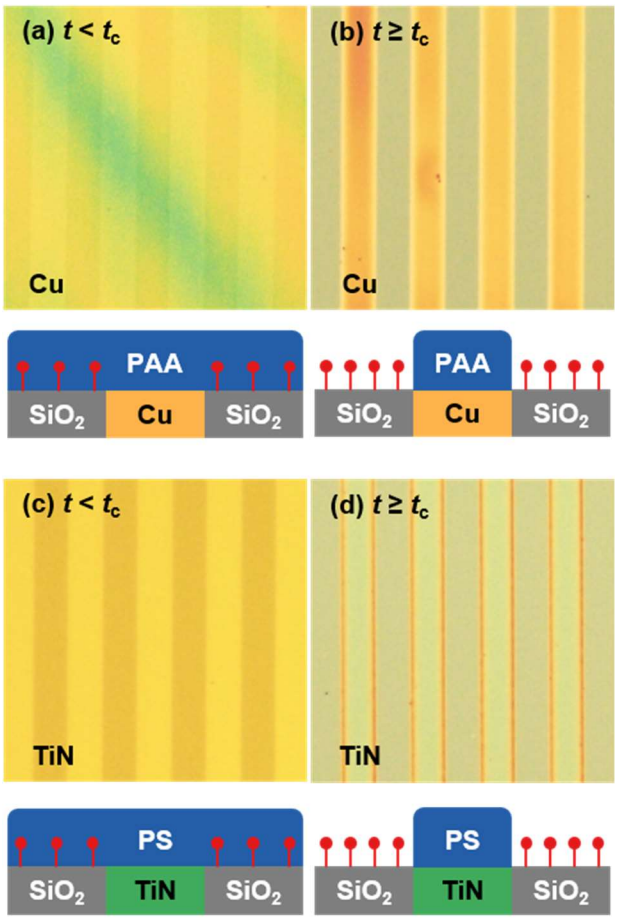

Figure A.5. The critical SAM deposition time (t_c) identified with homogeneous substrates also distinguishes spin wetting ($t < t_c$) and spin dewetting ($t > t_c$) regimes on heterogeneous surfaces. (a ,b) Optical micrographs of spun cast PAA films on Cu/SiO_2 substrates treated with OTS for (a) t = 30 s < t_c = 1 min, and (b) $t = t_c$. (c, d) Optical micrographs of spun cast PS films on TiN/SiO_2 substrates treated with OTS for (c) t = 30 s < t_c = 1 min, and (d) $t < t_c$. Spin coating conditions: PS, 21.5 kDa, 5 wt% in toluene at 10k rpm, and PAA, 20.5 kDa, 5 wt% in 50/50 vol% dioxane/methanol at 10k rpm.

To further probe film coverage on heterogeneous surfaces, patterns of PAA formed by spin dewetting on equal line–space patterns of Cu/OTS–SiO_2 (40 μm pitch) were analyzed by

secondary ion mass spectrometry (SIMS). When compared to background and control samples, carbon signals for PAA films were only observed over areas corresponding to the underlying Cu lines, which indicates a high degree of pattern fidelity (Figure A.6 and A.17). Similarly, spin coating polystyrene on TiN/OTS–SiO_2 results in the deposition of polymer only on the patterned TiN areas as evidenced by SIMS analysis (Figure A.18). In both cases, deposition of the polymers also creates templated films that are observable by atomic force microscopy (AFM) (Figures S19–S20). Collectively, these data indicate the spin dewetting process — under optimal conditions — is efficient at selectively coating heterogeneous substrates with no detectable deposition of polymers over regions that dewet.

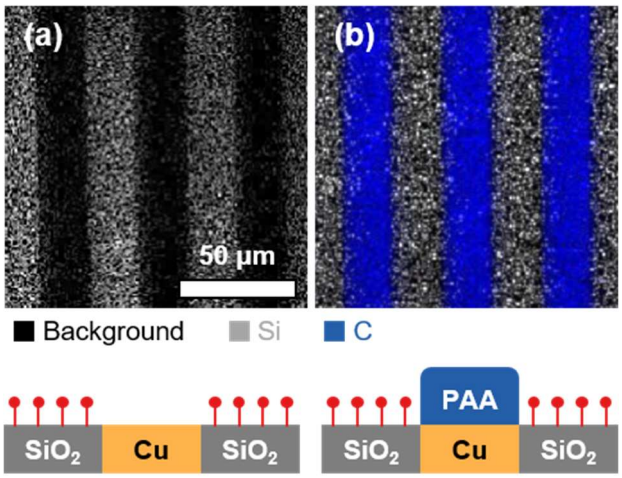

Figure A.6. SIMS chemical mapping reveals that spin dewet poly(acrylic acid) on Cu/OTS–SiO_2 exclusively covers Cu. (a) Cu/OTS–SiO_2 before polymer deposition. (b) PAA on Cu/OTS–SiO_2. Spin coating condition: PAA, 20.5 kDa, 5 wt% in 50/50 vol% dioxane/methanol at 10k rpm.

To illustrate the broad applicability of this spin dewetting approach, selective deposition over different pitch sizes ranging from 10 to 40 µm was examined. Figure A.7

shows AFM data demonstrating the dependence of spin dewetting on pre-pattern dimensions for both PAA on Cu/OTS–SiO_2 and PS on TiN/OTS–SiO_2. In both cases, the height of resulting polymer features decreases with pitch (P), reaching approximately 30 nm for 5 μm lines of Cu or TiN. Also note that there is some variability in the height profile of different lines at the same pitch on a given wafer. For example, the downward slope of PAA covering Cu at P = 40 μm (Figure A.7b, left) can be more or less prominent, and the difference between PS spike height at the boundaries of TiN lines (Figure A.7d) varies on the order of 20 nm.

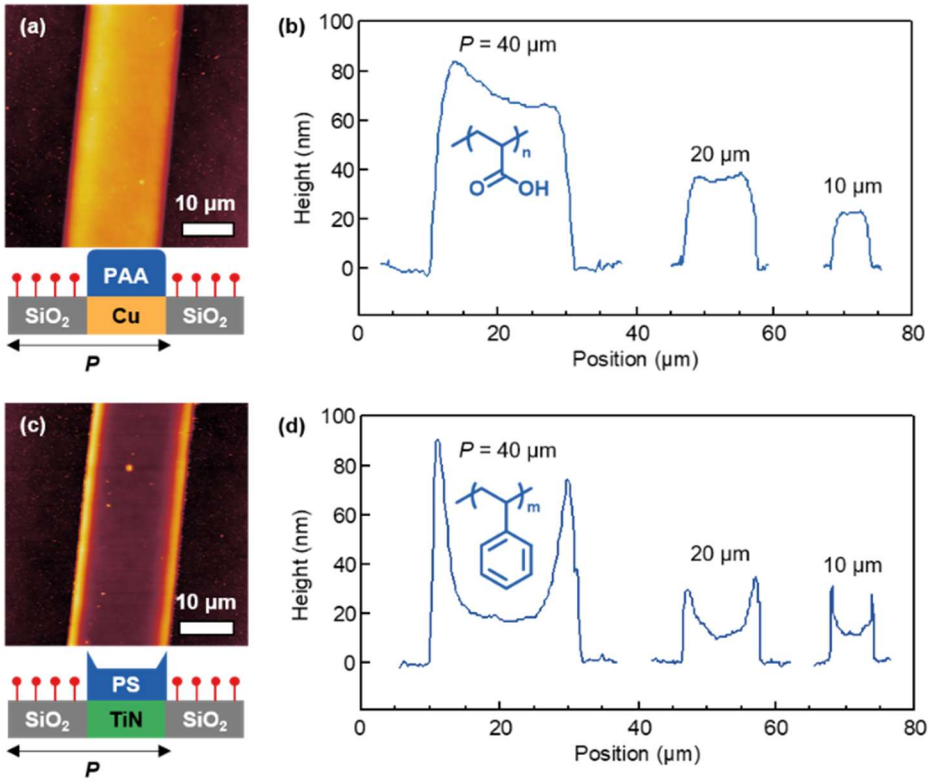

Figure A.7. Polymer and surface chemistry influence film coverage after spin dewetting on heterogeneous surfaces. (a) Atomic force micrograph of PAA on Cu/OTS–SiO_2 (40 μm), and (b) height profiles at three different pitches. (c) Atomic force micrograph of PS on TiN/OTS–SiO_2, and (d) height profiles at three different pitches. Spin coating conditions: PS,

21.5 kDa, 5 wt% in toluene at 10k rpm, and PAA, 20.5 kDa, 5 wt% in 50/50 vol% dioxane/methanol at 10k rpm.

As is apparent in Figure A.7, there are also distinct differences between the morphology of spin dewet PAA and PS, a result that is consistently observed across replicate samples. PS tends to form spikes at the boundaries of TiN (and Cu, Figure A.21), while PAA features on Cu are more rounded. We speculate that a complicated interplay involving polymer, solvent, and surface interactions influences these results.[34] Water contact angles indicate the native Cu surface is significantly more polar than TiN (Figure A.22), which would further explain (1) why PS (non-polar) coats Cu/OTS–SiO_2 (Figure A.21) with worse fidelity compared to TiN/OTS–SiO_2 (Figure A.7c), and (2) why PAA (polar) dewets from TiN (Figure A.23). As expected, the thickness of as-deposited material and to a lesser extent the shape of polymer features also depends on solution concentration (Figure A.24). However, we have not identified any processing conditions that circumvent the formation of U-shaped films with polystyrene on TiN, in contrast to a literature report by Wang et al. using polymer/polymer pre-patterns.[35]

Based on the successful patterning of disparate polymeric thin films on TiN- and Cu-based substrates, we expect that the general principle of spin dewetting will enable additional combinations of polymers and substrates to be rationally designed. This versatility will also prove critical for scaling the selective deposition of polymers to higher resolution pre-patterns. Preliminary data across 40, 20, and 10 μm pitches indicate PS scales well on TiN (Figure A.7c–d) but not Cu (Figure A.21). PAA exhibits the opposite trend (Figure A.7a–b, Figure

A.23). These observations further support the aforementioned importance of surface−polymer interactions[36] in mediating effective spin dewetting.

A.4.3 Comparison to Traditional Dewetting

The kinetic arrest of polymer thin films during spin dewetting on heterogeneous substrates can generate unique structures that are otherwise inaccessible with traditional types of dewetting or self-assembly. Figure A.8 compares thermal dewetting on a TiN/OTS−SiO_2 pattern starting from: (1) PS confined over the TiN via spin dewetting from toluene (Figure A.8b), and (2) a continuous film of PS formed using THF as the casting solvent (Figure A.8c). In both cases, thermal dewetting creates droplets (Figure A.8d−e) that are distinct from Figure A.7. We attribute the propensity of PS to thermally dewet from TiN (and Cu, Figure A.25) to the weak attractive forces mentioned above. In contrast, PAA still adheres to Cu at 170 °C after one hour; further thermal annealing at 240 °C results in a crosslinked film (Figure A.26) that remains essentially indistinguishable from the as-spin-dewet structure. One could envision exploiting this concept with other types of crosslinkers to immobilize various polymer chemistries using heat[37] and/or light.[38] Finally, solvent evaporation on tilted surfaces can produce interesting multi-scale dewetting patterns of polymer blends[39] that exhibit macroscopic alignment; these too are different than the spin dewet structures described herein.

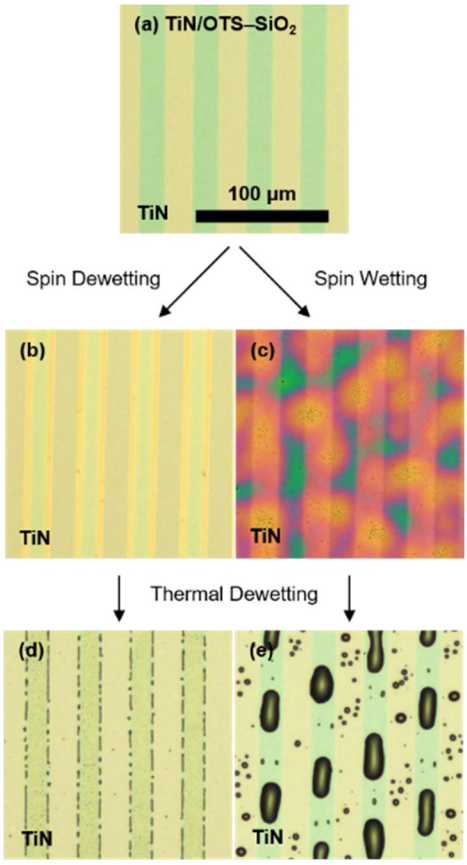

Figure A.8. Spin dewetting leads to non-equilibrium structures that are not necessarily accessible by thermal dewetting. Optical micrographs collected for: (a) TiN/OTS–SiO_2 prior to spin coating, (b) PS confined over TiN via spin dewetting, and (c) a continuous but rough film of PS formed via spin wetting using a different casting solvent. (d, e) Thermal dewetting at 170 °C for 1 hour of the (d) spin dewetting and (e) spin wetting films. All images were taken with the same light intensity and exposure time. Spin coating conditions: PS, 21.5 kDa, 5 wt% at 10k rpm in (b) toluene and (c) tetrahydrofuran. Thermal dewetting conditions: substrates with polymer films were annealed at 170 °C for 1 hr in high vacuum ($\approx 4\times10^{-8}$ Torr). The scale bar is valid for all micrographs.

A.5 Conclusions

In summary, spin dewetting is a powerful technique for controlling polymer thin formation on homogeneous and heterogeneous surfaces using incomplete self-assembled monolayers to drive dewetting. The transition between complete wetting and dewetting for glassy polymers is sharp and depends on polymer chemistry, processing variables, and SAM selection. Using octyltrichlorosilane-functionalized SiO_2, the selective deposition of polystyrene on TiN/SiO_2 and poly(acrylic acid) on Cu/SiO_2 was successfully demonstrated. Secondary ion mass spectrometry indicates clean dewetting over the SAM-functionalized region at the pitches tested (10–40 μm). The morphology of polymer spin dewet onto Cu or TiN significantly varies from rounded edges to spike-like boundary features. Under optimized processing conditions, spin dewetting generates structures that complement those available via other thermal dewetting or self-assembly techniques. We anticipate these results will prove enabling for applications that necessitate simple control over the spatial distribution of polymeric thin films.

A.6 Material Details

Table A.1. Characterization data of the polymers used herein.

Polymer	Sample ID	M_n (kDa)	$Đ$	Source
Polystyrene	PS1	2.8	1.05	Polymer Source
	PS2	8.0	1.10	Polymer Source
	PS3	10.2	1.05	Polymer Source
	PS4	21.5	1.05	Polymer Source
	PS5	35.0	1.10	Sigma-Aldrich
	PS6	51.0	1.10	Polymer Source
	PS7	87.2	1.20	Synthesized[40]
Poly(acrylic acid)	PAA1	20.5	1.10	Synthesized[41–42]
	PAA2	750	N.A.	Sigma-Aldrich
Poly(methyl methacrylate)	PMMA	24.0	1.25	Polymer Source
Poly(vinyl chloride)	PVC	35.0	1.77	Sigma-Aldrich

Poly(*tert*-butyl acrylate)	PtBA	12.0	1.16	Synthesized[41]

A.7 **Surface characterization**

SIMS imaging was performed using a Camera IMS 7f system (Camera SAS, Gennevilliers, France) with a 15 keV caesium beam on an analytical area of 200 μm^2 by monitoring ^{28}Si and ^{12}C signals. Tapping mode (AFM) experiments were performed using a Multimode system (Veeco, USA) to investigate the surface. Measurements were conducted using commercial silicon cantilevers (resonant frequency: 190 kHz, force constant: 48 N/m, model: Tap190Al-G, NanoAndMore USA). Polymer film thickness on homogeneous surfaces was determined by an alpha-SE spectroscopic ellipsometer (J.A. Woollam Co.) or a DektakXT Stylus Profilometer (Bruker Corporation). Optical micrographs were captured with an Olympus BX51 optical microscope in reflectance mode. Contact angle measurements were performed using a ramé-hart Model 290 advanced goniometer. Deionized water was dispensed to measure static contact angle. Snapshots were taken immediately after deposition of the water droplets and analyzed by DROPmage Advanced.

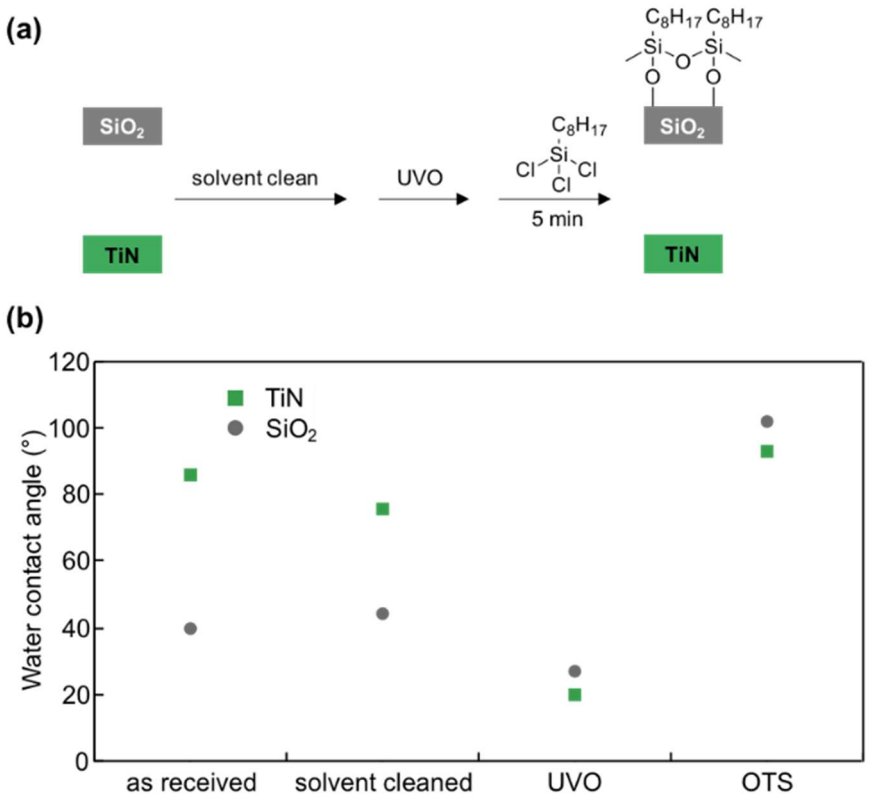

Figure A.9. Selective deposition of OTS only on SiO_2 (vs. TiN) as evidenced by water contact angles. (a) Illustration of the OTS treatment process. (b) Water contact angles monitored after each step.

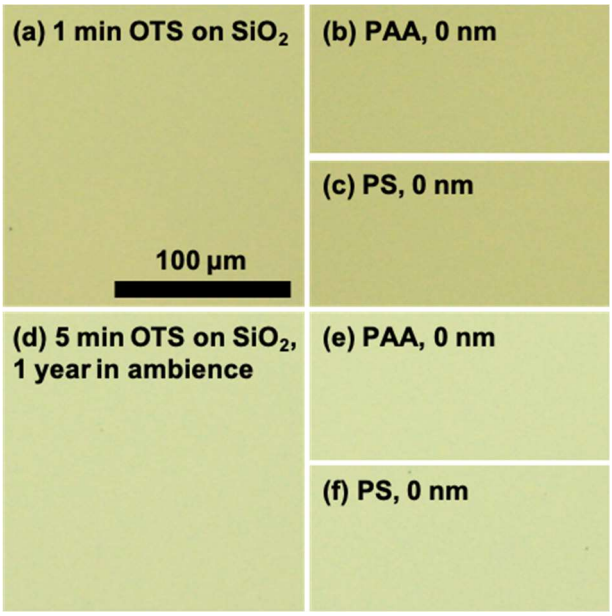

Figure A.10. For OTS-treated SiO_2, spin dewetting leads to complete dewetting; no polymer is deposited. Even after 1 year, OTS-treated SiO_2 still induces spin dewetting. Optical micrographs of (a) SiO_2 after 1 min OTS treatment, and subsequent spin coating of (b) PAA or (c) PS. (d) SiO_2 after 5 min OTS treatment stored for 1 year under ambient conditions, and subsequent spin coating of (e) PAA or (f) PS. All images were collected with the same light intensity and exposure time. Film thicknesses were determined by ellipsometry, except a profilometer was used for (e) and (f). Spin coating conditions: PS, 21.5 kDa 5 wt% in toluene at 10k rpm; PAA, 20.5 kDa, 5 wt% in 50/50 vol% dioxane/methanol at 10k rpm.

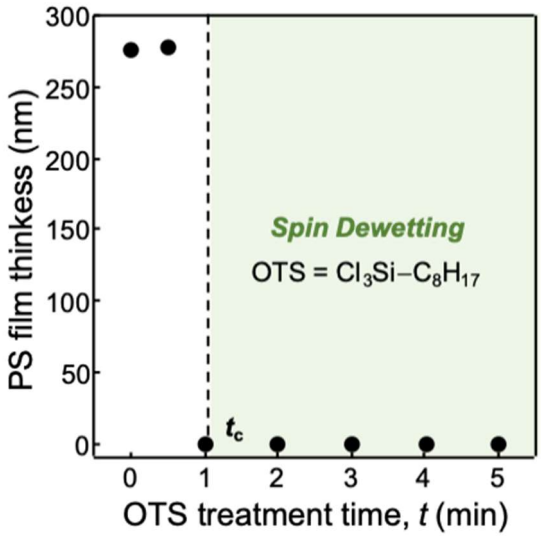

Figure A.11. Spin dewetting of PS occurs after a critical OTS treatment time as indicated by the PS film thickness as a function of OTS treatment time. Spin coating conditions: PS, 21.5 kDa, 5 wt% in toluene at 10k rpm. The data points correspond to the samples of Figure A.1b.

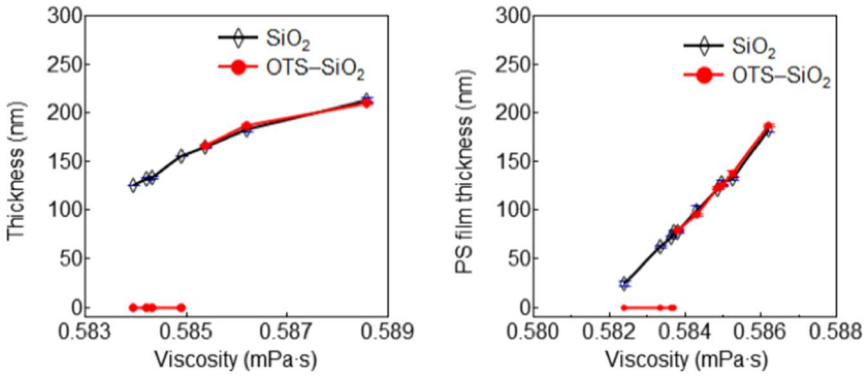

Figure A.12. Film thicknesses and dewetting conditions are comparable when varying **(a)** molecular weight and **(b)** weight concentration. The viscosity was calculated using the following empirical equation from Grishchuk and Estrin:[43]

$$\ln \mu_0 = -5.26 + \left(6.51\times10^{-2} + 1.326 \times 10^{-6}M\right)c + \left(1.52\times10^{-3} - 3.497 \times 10^{-8}M\right)c^2 - \left(4.309 \times 10^{-6} - 3.022 \times 10^{-10}M\right)c^3 + (8280 + 458c - 15.55c^2 + 0.255c^3)(1/T - 0.0033)/8.31$$

Where μ_0 is the viscosity at zero shear rate, M is the weight-average molecular weight of **polystyrene, *c* is the** solution concentration (wt%), and T is absolute temperature (K).[4] Note that this equation was developed for polystyrene with a weight average molecular weight from 28 kDa to 780 kDa in toluene and is therefore an approximation for the samples used herein. The data points correspond to the samples of Figure A.2.

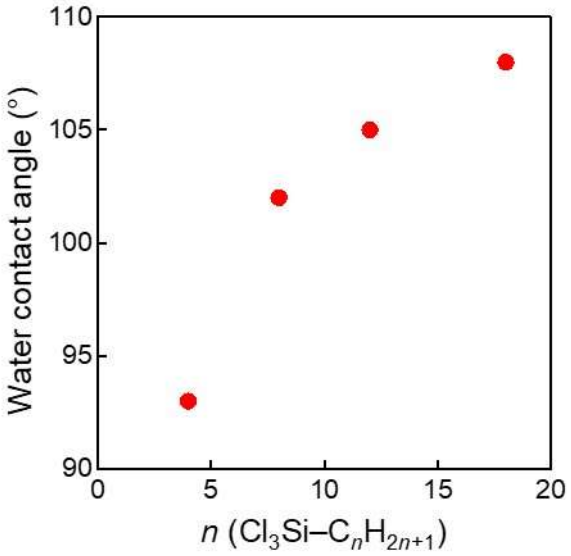

Figure A.13. Longer alkyl chains render the SiO_2 surface more hydrophobic. Water contact angle measurements for butyltrichlorosilane (n = 4), octyltrichlorosilane (n = 8), dodecyltrichlorosilane (n = 12), and octadecyltrichlorosilane (n = 18) coated on a homogeneous SiO_2 substrate for 5 minutes.

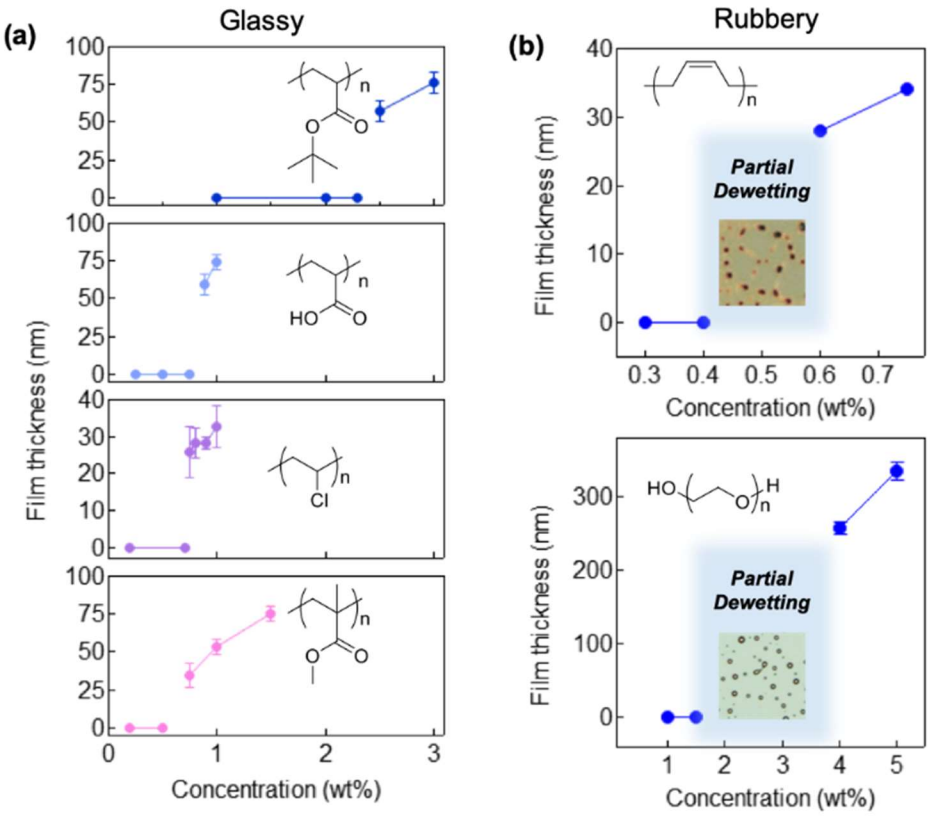

Figure A.14. Spin dewetting occurs with both glassy and rubbery polymers across a range of polarities. Step changes in polymer heights are shown in (a) glassy polymers: poly(acrylic acid) (PAA), poly(vinyl chloride) (PVC), poly(*tert*-butyl acrylate) (PtBA), and poly(methyl methacrylate) (PMMA). Vertical shifts were applied to improve clarity. (b) Rubbery polymers polybutadiene (PB) and poly(ethylene oxide) (PEO) exhibit a region between wetting and dewetting where droplets form as evidenced by optical micrographs. Error bars represent the standard deviation from three experiments. The optical images inserted in (b) are 12 μm x 12 μm. Spin coating conditions: (a) PAA2: 750 kDa, 6k rpm, varying concentrations in methanol; PVC: 35 kDa, 4k rpm, varying concentration in methyl ethyl ketone; PtBA: 12 kDa, 5k rpm, varying concentration in toluene; PMMA: 24 kDa, 4k rpm, varying concentration in toluene; (b) PB: 93 kDa, 5k rpm, varying concentration in toluene; PEO: 36 kDa, 3k rpm, varying concentration in 1:1 ethanol and toluene mixture.

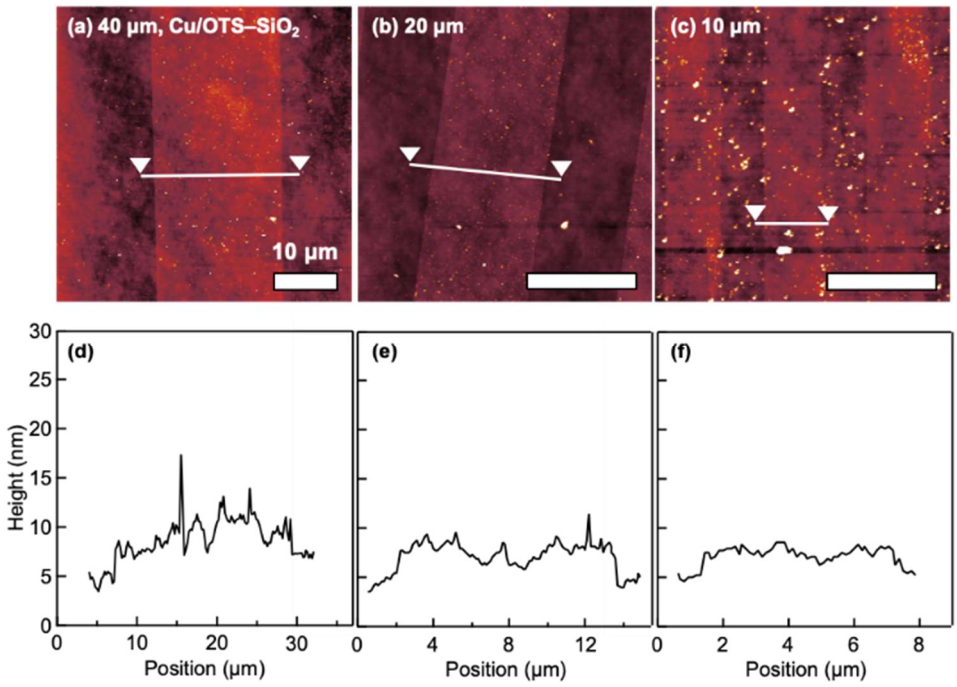

Figure A.15. AFM images of Cu/OTS–SiO_2 with different underlying pre-pattern pitches: (a) 40 µm, (b) 20 µm, and (c) 10 µm. (d), (e), and (f) are the corresponding height profiles of (a), (b), and (c), respectively. The *y*-axis scale in (d) is also valid for (e) and (f).

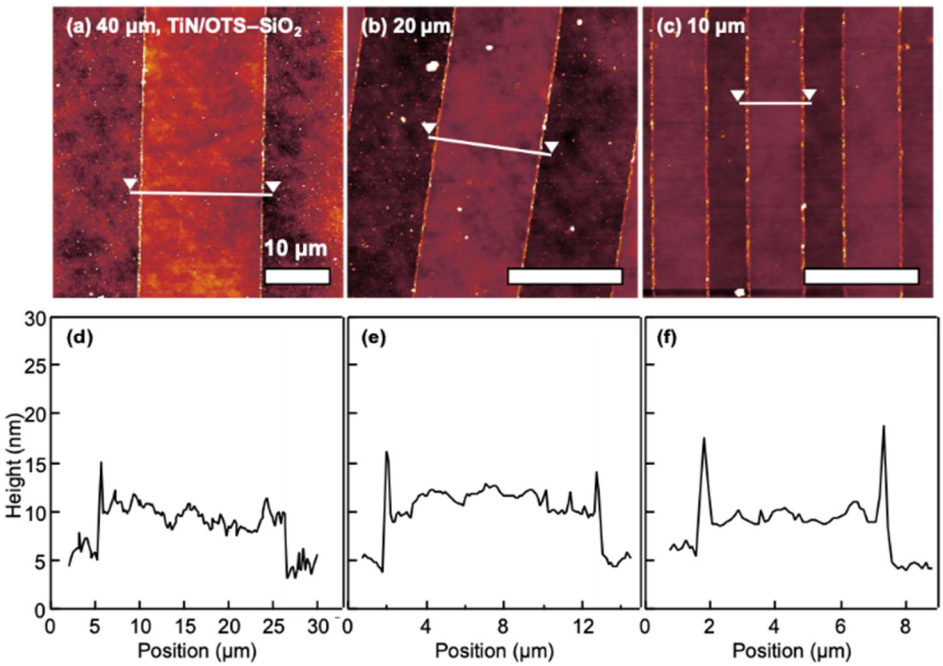

Figure A.16. AFM images of TiN/OTS–SiO_2 with different underlying pre-pattern pitches: (a) 40 µm, (b) 20 µm, and (c) 10 µm. (d), (e), and (f) are the corresponding height profiles of (a), (b), and (c), respectively. The *y*-axis scale in (d) is also valid for (e) and (f).

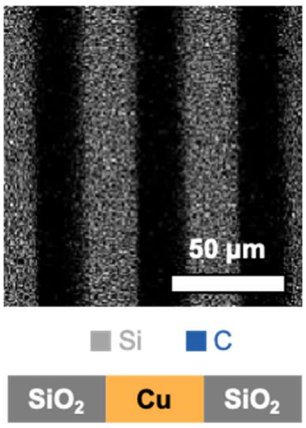

Figure A.17. Cu/SiO_2 patterns made by photolithography exhibit no carbon signals as evidenced by SIMS chemical mapping.

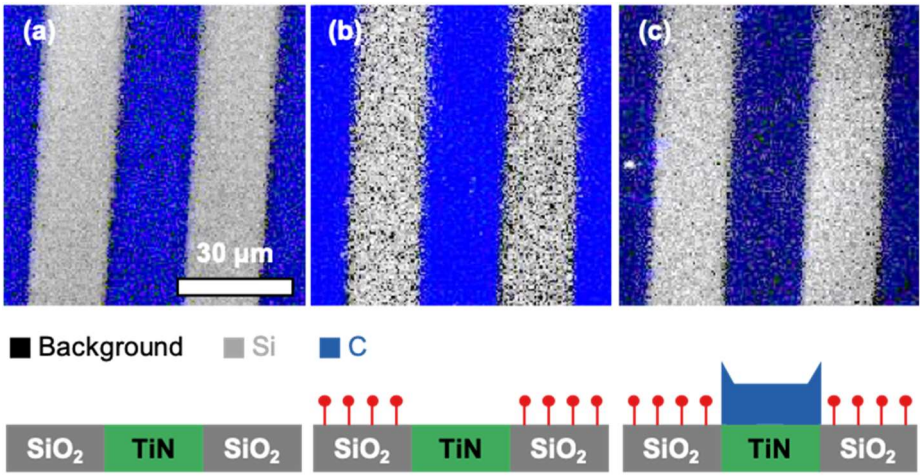

Figure A.18. SIMS chemical mapping reveals spin dewetting of polystyrene on TiN/OTS–SiO_2 exclusively covers TiN. (a) TiN/SiO_2 as-fabricated by photolithography. (b) TiN/OTS–SiO_2 after SAM deposition but before spin dewetting. (c) PS on TiN/OTS–SiO_2 after spin dewetting. The presence of carbon signals over TiN in the as-fabricated pattern is consistent with literature that indicates TiN can absorb carbon upon exposure to air.[5] After spin dewetting, the exclusive presence of carbon on TiN stripes indicates no polymer deposited on OTS–SiO_2. Together with the height change before and after spin coating (Figures A.7d and A.17), we conclude that polymer only coats TiN. Spin coating condition: PS4, 21.5 kDa 5 wt%

in toluene at 10k rpm. Also note that experimentally, the images represent an average over approximately 100 slices at different distances from the substrate. Carbon signals were in fact observed on SiO_2 in Figure A.6b during some individual scans, but given the extremely thin nature of the SAM, this effect is washed out during averaging.

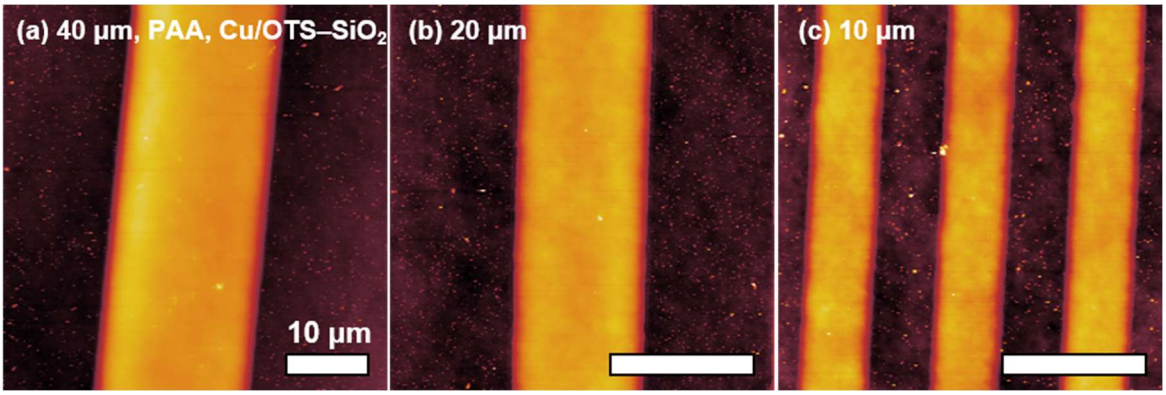

Figure A.19. AFM images of PAA on Cu/OTS–SiO_2 with different underlying pre-pattern pitches: (a) 40 µm, (b) 20 µm, and (c) 10 µm. All scale bars are 10 µm. Spin coating condition: PAA1, 20.5 kDa, 5 wt% in 50/50 vol% dioxane/methanol at 10k rpm.

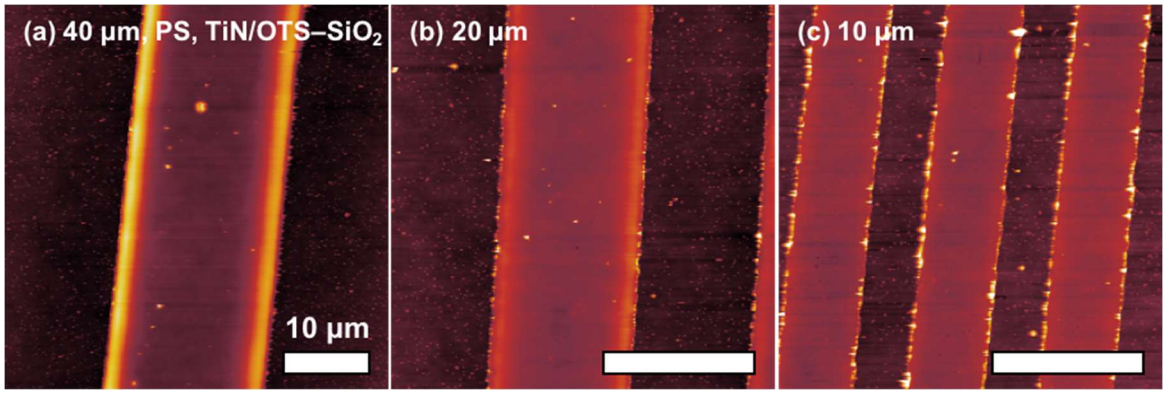

Figure A.20. PS films on TiN/OTS–SiO_2 have better fidelity than those on Cu/OTS–SiO_2. PS fully covers TiN with different underlying pre-pattern pitches: (a) 40 µm, (b) 20 µm, and (c) 10 µm. Spin coating condition: PS4, 21.5 kDa 5 wt% in toluene at 10k rpm.

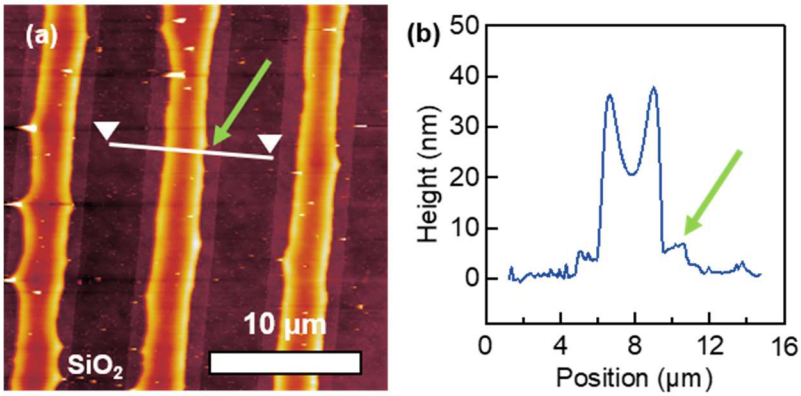

Figure A.21. PS films on Cu/OTS–SiO_2 exhibit U shapes with worse coverage than those on TiN/OTS–SiO_2 (Figure 7c) under the same spin dewetting processing conditions. (a) AFM image of PS on Cu/OTS–SiO_2. (b) Height profile of the line cut; the green arrow corresponds to the edges of a Cu stripe, which is not covered by polymer. Spin coating condition: PS4, 21.5 kDa 5 wt% in toluene at 10k rpm.

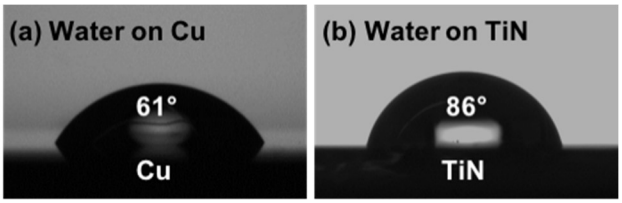

Figure A.22. Water contact angles of (a) Cu and (b) TiN suggest a difference in native surface polarity.

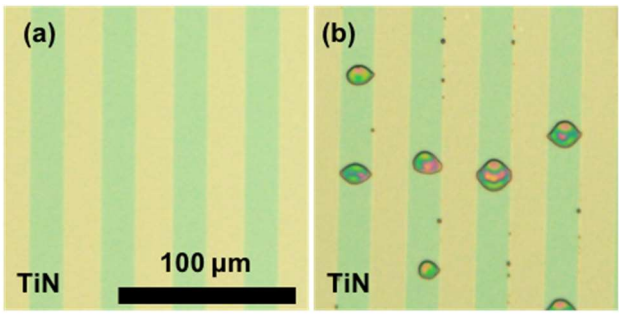

Figure A.23. PAA completely dewets from TiN/OTS–SiO_2. Optical images of (a) TiN/OTS–SiO_2 and (b) PAA spin-dewet on TiN/OTS–SiO_2. Spin coating condition: PAA1, 20.5 kDa, 5 wt% in 50/50 vol% dioxane/methanol at 10k rpm.

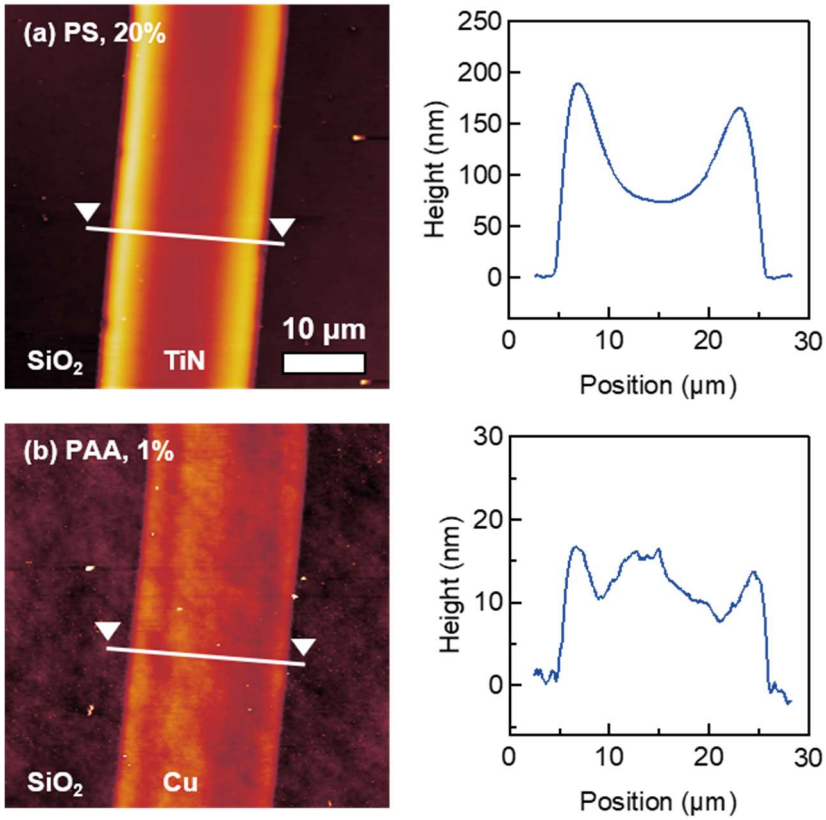

Figure A.24. Changing spin coating solution concentration somewhat alters the shape of deposited films. (a) Increasing PS4 solution concentration to 20 wt% (c.f., 5 wt%, Figure A.7c–d). (b) Decreasing PAA1 solution concentration to 1 wt% (c.f., 5 wt%, Figure A.7a–b).

In contrast, the deposited film thickness changes significantly with concentration. For PS, the edge spike height increases from ≈80 nm (5 wt%) to 160 nm (20 wt%), while the center increases from ≈20 nm (5 wt%) to 75 nm (20 wt%). Similarly, for PAA, the average film thickness decreases from ≈70 nm (5 wt%) to 12 nm (1 wt%).

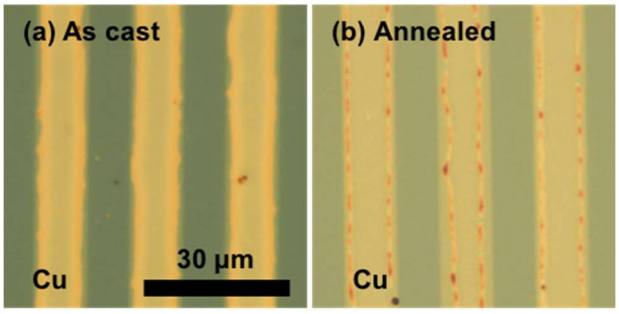

Figure A.25. PS4 dewets from Cu upon thermal annealing. Optical micrographs (a) of an as-cast PS film on Cu/OTS–SiO_2, and (b) after annealing at 170 °C for 1 hr.

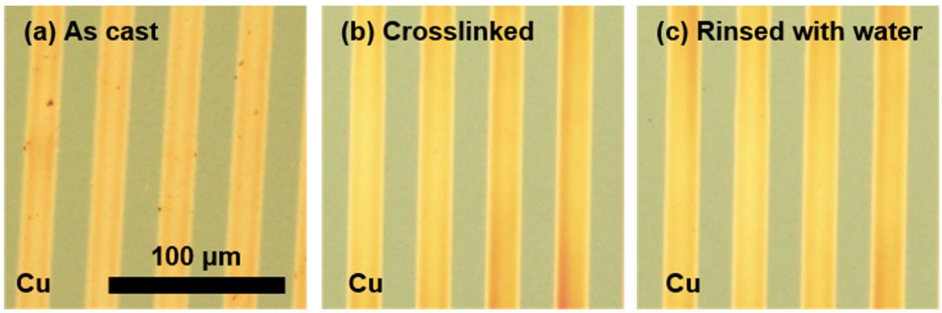

Figure A.26. PAA1 crosslinks at 240 °C on Cu/OTS–SiO_2 and thereafter becomes insoluble in water. Optical images of (a) as-spin-dewet PAA, (b) crosslinked at 240 °C for 1 hr, and (c) rinsed with water.

A.8 References

(1) Sanders, D. P. Advances in Patterning Materials for 193 nm Immersion Lithography. *Chem. Rev.* **2010,** *110* (1), 321-360.

(2) Chou, S. Y.; Krauss, P. R.; Renstrom, P. J. Imprint Lithography with 25-Nanometer Resolution. *Science* **1996,** *272* (5258), 85-87.

(3) Wilbur, J. L.; Kumar, A.; Kim, E.; Whitesides, G. M. Microfabrication by Microcontact Printing of Self-Assembled Monolayers. *Adv. Mater.* **1994,** *6* (7–8), 600-604.

(4) Peercy, P. S. The Drive to Miniaturization. *Nature* **2000,** *406* (6799), 1023-1026.

(5) von der Mark, K.; Park, J.; Bauer, S.; Schmuki, P. Nanoscale Engineering of Biomimetic Surfaces: Cues from the Extracellular Matrix. *Cell Tissue Res.* **2009,** *339* (1), 131.

(6) Javey, A.; Nam; Friedman, R. S.; Yan, H.; Lieber, C. M. Layer-by-Layer Assembly of Nanowires for Three-Dimensional, Multifunctional Electronics. *Nano Lett.* **2007,** *7* (3), 773-777.

(7) Chen, Y.; Cheng, Q.; Kang, W. In Technological Merits, Process Complexity, and Cost Analysis of Self-Aligned Multiple Patterning, SPIE Advanced Lithography, SPIE: 2012; p 832620.

(8) Yaegashi, H. In Pattern Fidelity Control in Multi-Patterning towards 7nm Node, International Conference on Nanotechnology (IEEE-NANO), 2016; pp 452-455.

(9) Kalanyan, B.; Lemaire, P. C.; Atanasov, S. E.; Ritz, M. J.; Parsons, G. N. Using Hydrogen to Expand the Inherent Substrate Selectivity Window during Tungsten Atomic Layer Deposition. *Chem. Mater.* **2016,** *28* (1), 117-126.

.; Azucena, C.; Welle, A.; Ross, A. M.; Wöll, C.; Lahann, J. Free-Standing Nanomembranes Based on Selective CVD Deposition of Functional Poly-p-xylylenes. *ACS Nano* **2015,** *9* (2), 1400-1407.

(11) Zhang, H.-L.; Bucknall, D. G.; Dupuis, A. Uniform Nanoscopic Polystyrene Patterns Produced from a Microscopic Mold. *Nano Lett.* **2004,** *4* (8), 1513-1519.

(12) Prasittichai, C.; Zhou, H.; Bent, S. F. Area Selective Molecular Layer Deposition of Polyurea Films. *ACS Appl. Mater. Interfaces* **2013,** *5* (24), 13391-13396.

(13) Seo, E. K.; Lee, J. W.; Sung-Suh, H. M.; Sung, M. M. Atomic Layer Deposition of Titanium Oxide on Self-Assembled-Monolayer-Coated Gold. *Chem. Mater.* **2004,** *16* (10), 1878-1883.

(14) Hashemi, F. S. M.; Prasittichai, C.; Bent, S. F. A New Resist for Area Selective Atomic and Molecular Layer Deposition on Metal–Dielectric Patterns. *J. Phys. Chem. C* **2014,** *118* (20), 10957-10962.

(15) Böltau, M.; Walheim, S.; Mlynek, J.; Krausch, G.; Steiner, U. Surface-Induced Structure Formation of Polymer Blends on Patterned Substrates. *Nature* **1998,** *391*, 877.

(16) Ming, W.; Liang, F.; Jun, L.; Sivasubramanian, S.; Xugang, X.; Carol, B.; Ahmed, B.; Joey, M. Directed Assembly of Polymer Blends Using Nanopatterned Templates. *Adv. Mater.* **2009,** *21* (7), 794-798.

(17) Heier, J.; Kramer, E. J.; Walheim, S.; Krausch, G. Thin Diblock Copolymer Films on Chemically Heterogeneous Surfaces. *Macromolecules* **1997,** *30* (21), 6610-6614.

(18) Johnson, A.; Madsen, J.; Chapman, P.; Alswieleh, A.; Al-Jaf, O.; Bao, P.; Hurley, C. R.; Cartron, M. L.; Evans, S. D.; Hobbs, J. K.; Hunter, C. N.; Armes, S. P.; Leggett, G. J. Micrometre and Nanometre Scale Patterning of Binary Polymer Brushes, Supported Lipid Bilayers and Proteins. *Chem. Sci.* **2017,** *8* (6), 4517-4526.

(19) Sehgal, A.; Ferreiro, V.; Douglas, J. F.; Amis, E. J.; Karim, A. Pattern-Directed Dewetting of Ultrathin Polymer Films. *Langmuir* **2002,** *18* (18), 7041-7048.

(20) Geoghegan, M.; Wang, C.; Rehse, N.; Magerle, R.; Krausch, G. Thin Polymer Films on Chemically Patterned, Corrugated Substrates. *J. Phys.: Condens. Matter* **2005,** *17* (9), S389-S402.

(21) Zhang, Z.; Wang, Z.; Xing, R.; Han, Y. Patterning Thin Polymer Films by Surface-Directed Dewetting and Pattern Transfer. *Polymer* **2003,** *44* (13), 3737-3743.

(22) Nicholas, F.; Derek, H. Fabrication of Micro- and Nanoscale Polymer Structures by Soft Lithography and Spin Dewetting. *Macromol. Rapid Commun.* **2007,** *28* (8), 966-971.

(23) Chiu, M.; Wood, J. A.; Widmer-Cooper, A.; Neto, C. Aligned Droplet Patterns by Dewetting of Polymer Bilayers. *Macromolecules* **2018,** *51* (15), 5485-5493.

(24) Dhara, P.; Bhandaru, N.; Das, A.; Mukherjee, R. Transition from Spin Dewetting to Continuous Film in Spin Coating of Liquid Crystal 5CB. *Sci. Rep.* **2018,** *8* (1), 7169.

(25) Bhandaru, N.; Das, A.; Salunke, N.; Mukherjee, R. Ordered Alternating Binary Polymer Nanodroplet Array by Sequential Spin Dewetting. *Nano Lett.* **2014,** *14* (12), 7009-7016.

(26) Bhandaru, N.; Karim, A.; Mukherjee, R. Directed Ordering of Phase Separated Domains and Dewetting of Thin Polymer Blend Films on a Topographically Patterned Substrate. *Soft Matter* **2017,** *13* (27), 4709-4719.

(27) Lee, J. H.; Choi, H.-J.; Lee, C.; Song, S. W.; Lee, J. B.; Huh, D.; Nam, Y. S.; Jeon, D. Y.; Lee, H.; Jung, Y. S. Spontaneous Registration of Sub-10 nm Features Based on Subzero Celsius Spin-Casting of Self-Assembling Building Blocks Directed by Chemically Encoded Surfaces. *ACS Nano* **2018,** *12* (8), 8224-8233.

(28) Glass, N. R.; Tjeung, R.; Chan, P.; Yeo, L. Y.; Friend, J. R. Organosilane Deposition for Microfluidic Applications. *Biomicrofluidics* **2011,** *5* (3), 036501.

(29) Efimenko, K.; Novick, B.; Carbonell, R. G.; DeSimone, J. M.; Genzer, J. Formation of Self-Assembled Monolayers of Semifluorinated and Hydrocarbon Chlorosilane Precursors on Silica Surfaces from Liquid Carbon Dioxide. *Langmuir* **2002,** *18* (16), 6170-6179.

(30) Meyerhofer, D. Characteristics of Resist Films Produced by Spinning. *J. Appl. Phys.* **1978,** *49* (7), 3993-3997.

(31) Hall, D. B.; Underhill, P.; Torkelson, J. M. Spin Coating of Thin and Ultrathin Polymer Films. *Polym. Eng. Sci.* **1998,** *38* (12), 2039-2045.

(32) Reiter, G. Dewetting of Thin Polymer Films. *Phys. Rev. Lett.* **1992,** *68* (1), 75-78.

(33) Grishchuk, A. A.; Estrin, Y. I. Viscosity of Concentrated Solutions of Polystyrene and Poly(Vinyl Acetate) (Empirical Equations). *Russ. J. Appl. Chem.* **2007,** *80* (11), 1940-1944.

(34) Hu, H.; Larson, R. G. Marangoni Effect Reverses Coffee-Ring Depositions. *J. Phys. Chem. B* **2006,** *110* (14), 7090-7094.

(35) Wang, X.; Östblom, M.; Johansson, T.; Inganäs, O. PEDOT Surface Energy Pattern Controls Fluorescent Polymer Deposition by Dewetting. *Thin Solid Films* **2004,** *449* (1), 125-132.

(36) Bauer, E.; Maurer, E.; Mehaddene, T.; Roth, S. V.; Müller-Buschbaum, P. Flow in Confined Geometry Introduced by Dewetting of Ultrathin Polystyrene Films. *Macromolecules* **2006,** *39* (15), 5087-5094.

(37) Spruell, J. M.; Wolffs, M.; Leibfarth, F. A.; Stahl, B. C.; Heo, J.; Connal, L. A.; Hu, J.; Hawker, C. J. Reactive, Multifunctional Polymer Films through Thermal Cross-linking of Orthogonal Click Groups. *J. Am. Chem. Soc.* **2011,** *133* (41), 16698-16706.

(38) Harnish, B.; Robinson, J. T.; Pei, Z.; Ramström, O.; Yan, M. UV-Cross-Linked Poly(Vinylpyridine) Thin Films as Reversibly Responsive Surfaces. *Chem. Mater.* **2005,** *17* (16), 4092-4096.

(39) Müller-Buschbaum, P.; Bauer, E.; Pfister, S.; Roth, S. V.; Burghammer, M.; Riekel, C.; David, C.; Thiele, U. Creation of Multi-Scale Stripe-Like Patterns in Thin Polymer Blend Films. *Europhys. Lett.* **2006,** *73* (1), 35-41.

(40) Worsfold, D. J. Anionic Copolymerization of Styrene and Isoprene in Cyclohexane. *J. Polym. Sci., Part A-1: Polym. Chem.* **1967,** *5* (11), 2783-2789.

(41) Anastasaki, A.; Willenbacher, J.; Fleischmann, C.; Gutekunst, W. R.; Hawker, C. J. End Group Modification of Poly(Acrylates) Obtained via ATRP: a User Guide. *Polym. Chem.* **2017,** *8* (4), 689-697.

(42) Burguière, C.; Pascual, S.; Bui, C.; Vairon, J.-P.; Charleux, B.; Davis, K. A.; Matyjaszewski, K.; Bétremieux, I. Block Copolymers of Poly(Styrene) and Poly(Acrylic Acid) of Various Molar Masses, Topologies, and Compositions Prepared via Controlled/Living Radical Polymerization. Application as Stabilizers in Emulsion Polymerization. *Macromolecules* **2001,** *34* (13), 4439-4450.

(43) Grishchuk, A. A.; Estrin, Y. I. Viscosity of Concentrated Solutions of Polystyrene and Poly(Vinyl Acetate) (Empirical Equations). *Russ. J. Appl. Chem.* **2007,** *80* (11), 1940-1944.

(44) Ohya, S.; Chiaro, B.; Megrant, A.; Neill, C.; Barends, R.; Chen, Y.; Kelly, J.; Low, D.; Mutus, J.; O'Malley, P. J. J.; Roushan, P.; Sank, D.; Vainsencher, A.; Wenner, J.; White, T. C.; Yin, Y.; Schultz, B. D.; Palmstrøm, C. J.; Mazin, B. A.; Cleland, A. N.; John, M. M. Room Temperature Deposition of Sputtered TiN Films for Superconducting Coplanar Waveguide Resonators. *Supercond. Sci. Technol.* **2014,** *27* (1), 015009.

Appendix B. Multi-Wavelength Photodetectors Based on an Azobenzene Polymeric Ionic Liquid[3]

B.1 Introduction

Organic photodetectors (OPDs) have a tunable wavelength response and are compatible with flexible/lightweight form factors.[1–4] The chemical versatility of the organic semiconducting materials used to fabricate OPDs provides a wide range of accessible absorption profiles and physical properties that are important in various applications. For example, these materials can be deposited over large areas with solution-based methods (e.g., spin coating, inkjet printing, and roll-to-roll printing) and are processable under ambient (or convenient) conditions.[2–6]

One strategy to create OPDs and other light responsive devices leverages molecular photoswitches (including spiropyran, azobenzene, and diarylethene), which remotely modify the properties of organic semiconductors in response to light.[7–9] Among these photoswitches, azobenzenes have been widely studied due to their synthetic accessibility and stable cycling performance.[10] Azobenzenes have been used to modulate the electrical properties of thin film transistors both under and after illumination when incorporated as the gate insulator or directly in the semiconductor layer.[11–17] Generally, these effects are related to charge trapping[11–15] or photomediated changes in the azobenzene dipole moment that accompanies *cis–trans* isomerization.[16,17]

Despite the appeal of OPD devices containing organic semiconductors and

[3] This Appendix was originally published in *ACS Applied Polymeric Materials*. Reproduced with permission from *ACS Applied Polymeric Materials* 2021, 3, 10, 5125–5133. Copyright 2021, American Chemical Society.

photoswitches, there are two major challenges associated with practical implementation. First, the wavelength range over which they respond to light is typically limited to a narrow region around the absorption profile of the two photoswitch states, e.g., *trans*- and *cis*-azobenzene. Second, there are often processing difficulties in forming thin film stacks containing organic semiconductors and light-responsive azobenzene-based materials because of their similar solubilities.[16] Here, we overcome these limitations by exploiting azobenzene-containing polymeric ionic liquids (PILs) as efficient materials for multi-wavelength detection in OPDs when used as a gate layer with the semiconducting *p*-type polymer poly{(4,4-dihexadecyl-4H-cyclopenta[1,2-b:5,4- b′]dithiophene-2,6-diyl)-*alt*-(2,3-difluoro-1,4-phenylene)} (PhF-2,3). PILs are advantageous as light-responsive gate materials because they exhibit good solubility in polar solvents, which allows for direct deposition via spin-coating onto less polar semiconducting conjugated polymers. Moreover, PILs retains the advantageous qualities of ionic liquids (ILs) such as good thermal stability and low volatility while providing tunable mechanical and physical properties through synthesis.[18] Our photoswitch-based photodetector platform shows an increase in photocurrent over two-to-three orders of magnitude when exposed to different wavelengths of light, as well as an attenuated response across the visible spectrum. These multi-wavelength sensing capabilities expand the applicability of photoswitches and PILs in flexible, solution- processable devices for broadband light detection.

B.2 Results and Discussions

B.2.1 Design and Synthesis of a Photoresponsive PIL with Pendant Azobenzene Groups

We sought to develop a PIL-containing photoswitch as a light-responsive unit with high solubility in orthogonal solvents to the organic semiconducting polymer PhF-2,3. PhF-2,3

is a donor–acceptor-type semiconducting polymer based on 4,4-dihexadecyl-4H-cyclopenta[1,2- b:5,4]dithiophene (CDT) and 2,3-difluorophenylene (2,3-DFPh) that was chosen for its high hole mobility.[19,20] The electron-withdrawing property of 2,3-DFPh is relatively weak in comparison with conventional acceptor units, which results in a higher-lying LUMO level that provides a sufficient energetic barrier for minimizing electron injection from gold, thereby facilitating unipolar hole transport in the semiconductor.

For the light-responsive PIL layer, we designed a polymer with covalently-attached azobenzene units and, importantly, fixed charge groups that would solubilize the material in polar solvents for direct deposition onto PhF-2,3 (which is soluble in nonpolar solvents). Poly(ethylene oxide) was chosen as the PIL polymer backbone because it is a synthetically-accessible and soluble scaffold that has a low T_g to avoid aggregation of the azobenzene chromophore, which could lead to non-uniform and irreversible performance in devices.[13,17] A poly(ethylene oxide) homopolymer with side chains containing neutral imidazoles (T_g = –20 °C) was synthesized as the PIL precursor through a thiol–ene click reaction according to previously reported literature.[21] Post-polymerization modification of this PIL precursor by partial quaternization of the imidazoles with 1-(4-(bromomethyl)phenyl)-2-phenyldiazene[22] yielded a photoresponsive azobenzene PIL (Figure B.1). This simple synthetic approach installs the charged imidazolium group and covalently-bound azobenzene in tandem with stoichiometric control over the level of functionalization. The extent of quaternization as measured by ^{1}H NMR (details shown in Supporting Information) was 37 mol%, which agrees well with the target of 40 mol% azobenzene-IL incorporation. This concentration of PIL and azobenzene represents a suitable balance between ionicity for solubility without making the material too optically dense for effective light penetration.[23,24] The bromide anion was then

exchanged for bis(trifluoromethanesulfonyl)imide (TFSI) (Figure B.12) via ion metathesis to form a PIL denoted Azo-PIL (T_g = –11 °C). The larger, more diffuse TFSI anion improves solubility in organic solvents and reduces the T_g compared to other possible PIL counterions.[25,26]

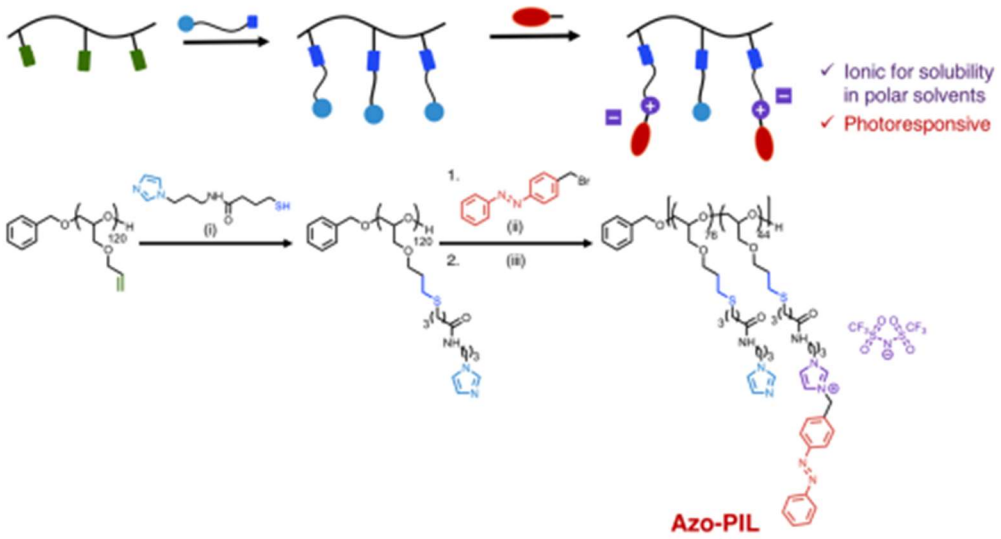

Figure B.1. Synthesis of Azo-PIL via post-polymerization modification of poly(allyl glycidyl ether). (i) Light-mediated thiol–ene click with pendant alkenes initiated by 2,2-dimethoxy-2-phenylacetophenone (DMPA) in methanol over 2 hours at room temperature. (ii) Partial quaternization of imidazole side chains with 1-(4-(bromomethyl)phenyl)-2-phenyldiazene in 1:1 methanol:acetonitrile at 100 °C for 15 hours. (iii) Ion exchange with lithium bis(trifluoromethanesulfonyl)imide (LiTFSI) in 20% water in methanol at 50 °C for 18 hours.

B.2.2 Fatigue resistant trans–cis isomerization

Upon covalent attachment to Azo-PIL via side-chain imidazoles, the isomerization of azobenzene in the solid state was photochemically characterized by UV–vis spectroscopy. Azo-PIL in acetone was spin-coated onto quartz substrates to prepare 400 nm thin-film

samples. The penetration depth of light in a thin film can be calculated as $l = \alpha^{-1}$, where l is the penetration depth and α is the attenuation coefficient at a specific wavelength of light (Table B.1).[27] At the wavelengths of interest for azobenzene (365 nm and 470 nm),[10] the penetration depth is roughly 430 nm and 620 nm, respectively, based on 37% azobenzene in the PIL. Thus, at the film thicknesses used in UV–vis experiments, some incident light will be transmitted through the film. We first irradiated these samples with 365 nm light (80 mW cm^{-2}) to induce *trans*-to-*cis* isomerization. In the UV–vis spectrum of Azo-PIL (Figure B.2), isomerization to the *cis* isomer corresponds with a decrease in the λ_{max} at 323 nm, largely associated with the $\pi \rightarrow \pi^*$ transition of *trans*-azobenzene. The concomitant increase in λ_{max} at 430 nm is related to the $n \rightarrow \pi^*$ transition of *cis*-azobenzene, which was observed after 1 minute of irradiation with 365 nm light. Subsequent irradiation with 470 nm light (200 mW cm^{-2}) for 1 minute resulted in back isomerization from *cis* to *trans*. Prolonged irradiation with either 365 nm or 470 nm did not induce further changes in the UV–vis spectrum of Azo-PIL, indicating 1 minute of irradiation is sufficient to reach a photostationary state (PSS) (Figure 2.15 and Figure 2.16). The *cis–trans* ratio at the photostationary state was quantified by UV–vis spectroscopy and ^{1}H NMR by extrapolating the *trans* and *cis* extinction coefficients (Table B.2 and Figure B.17).[28] Calculated by this method, the PSS corresponds with 67% *cis* under 365 nm light. Partially overlapping absorbances of the *trans* and *cis* states around 365 nm, which presumably results from the proximity of the azobenzene to an electron-withdrawing imidazolium, contributes to the modest *cis* content of the PSS;[23] in comparison with other polymers that are covalently conjugated to an azobenzene unit, we observe a slightly lower percentage of *cis* isomer in Azo-PIL at the PSS (typically ~89–95% *cis* form is observed after exposure to UV light).[29–31] However, the *trans*-to-*cis* ratio under UV light in Azo-PIL is consistent with the switching

efficiency of a previously reported small-molecule azobenzene ionic liquid.[22]

Next, we performed cyclic irradiation UV–vis studies of the Azo-PIL under 365 nm and 470 nm light to mimic the irradiation conditions used in devices. Exposing Azo-PIL films to alternating 365 nm and 470 nm light demonstrates the excellent reversibility of the *cis–trans* isomerization with a negligible decay in performance (Figure B.2). Once deposited on the semiconducting polymer PhF-2,3, the Azo-PIL preserves its reversible isomerization characteristics with a decreased absorbance in the $\pi \longrightarrow \pi^*$ transition at 323 nm upon UV light irradiation and a return to the original UV–vis spectrum with visible light (Figure B.18).

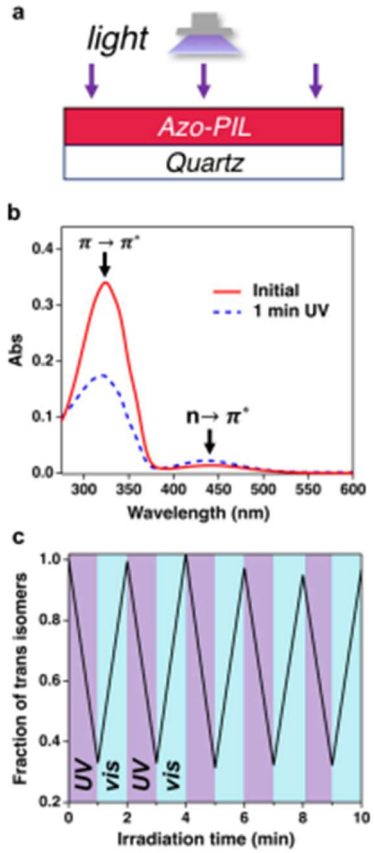

Figure B.2. UV–vis studies of Azo-PIL thin films were conducted on quartz. (a) Schematic of the irradiation setup (b) UV–vis spectra of thin-film Azo-PIL before (solid red trace) and after (dashed blue trace) exposure to 365 nm irradiation for 1 minute. (c) Fraction of the *trans*

azobenzene isomer during multiple irradiation cycles with UV (365 nm, 80 mW cm^{-2}) and visible (470 nm, 200 mW cm^{-2}) light.

B.2.3 Multi-wavelength-stimulated increase in photocurrent driven by absorption of azobenzene

With the reversible photochemical properties of Azo-PIL confirmed by UV–vis studies, both two- and three-terminal lateral organic bilayer photodetectors were fabricated to investigate the light-induced device response and associated molecular mechanism. Azo-PIL and PhF-2,3 were introduced as photoactive and semiconducting layers, respectively. Due to the orthogonal solubilities of Azo-PIL and PhF-2,3, Azo-PIL could be spin coated onto PhF-2,3 without the need for an intermediate layer (Figure B.3). Details about the fabrication methods for the devices are further described in Section B.4.5.

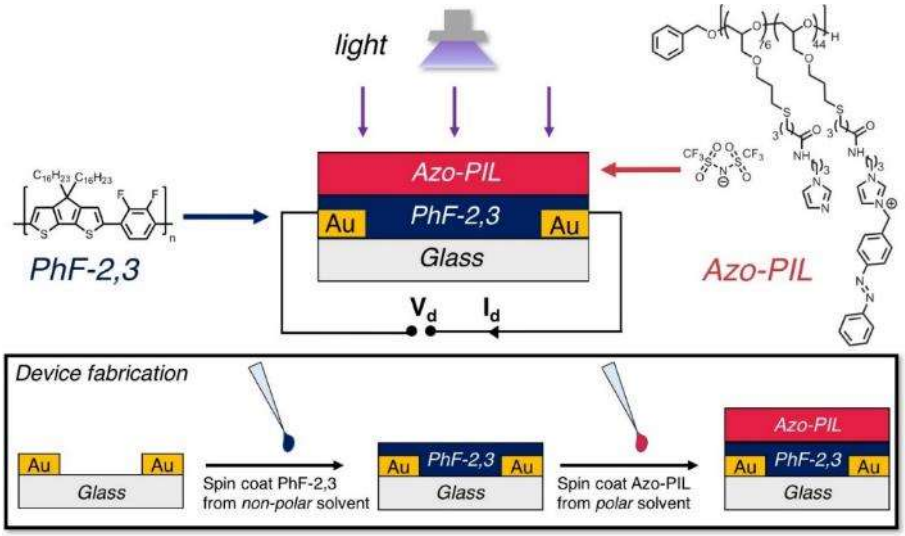

Figure B.3. Schematic of the two-terminal photodetector device fabrication by spin-coating Azo-PIL directly onto the semiconducting polymer PhF-2,3 on a glass substrate (previously

passivated with *n*-decyltrichlorosilane (DTS)).

The response produced in these bilayer devices under irradiation was studied by monitoring the drain current as a function of time under exposure to 365 nm and 470 nm light. When the photodetector was initially illuminated with 365 nm light (80 mW cm^{-2}), a 600-fold increase over three orders of magnitude in drain current was observed with a rise-time of 10 seconds (Figure B.4). After approximately a rise-time of 50 seconds, saturation at 99% of the final current was reached. Notably, a 90% relaxation of the current was observed within a fall-time of 5 seconds when the 365 nm light was shut OFF, eventually resulting in a 99% decrease in current after a fall-time of 70 seconds in the dark. To test the response to light within a timespan of minutes, the device was subsequently irradiated with 470 nm light (200 mW cm^{-2}), eliciting an increase over 2 orders of magnitude to the same maximum value in current. In the following irradiation cycles, the increase in current and decay with 470 nm is nearly identical to the response under 365 nm light. This fast ON–OFF performance is maintained upon repeated cycling between 365 nm and 470 nm light (Figure B.4a), performance that is within the range of[14,15] or exceeds[7,16] other photochromism-based devices.

As the increase in current was shown to be consistent with multiple cycles of irradiation with 365 nm and 470 nm light, the sensitivity of the device was then examined by comparing the effect of incident power at 470 nm (0.3 and 200 mW cm^{-2}) (Figure B.4b). Bias stress measurements of the two-terminal device under 470 nm at 0.3 mW cm^{-2} show an increase in current of approximately one order of magnitude, smaller than the 3 orders of magnitude increase observed under higher power (200 mW cm^{-2}). Although the irradiation with our high-powered 470 nm LED (200 mW cm^{-2}) is 670 times higher than that of the low-powered LED

(0.3 mW cm^{-2}), the current increase observed is only 25 times larger. Additionally, a responsivity of 0.23 A W^{-1} and an external quantum efficiency (EQE) of 59% was calculated at this low-powered 470 nm, comparable to what is found in other planar heterojunction OPDs (Table B.1). This non-linear dependence on power density reveals the limits of the current increase and the sensitivity and performance of this device as an OPD.

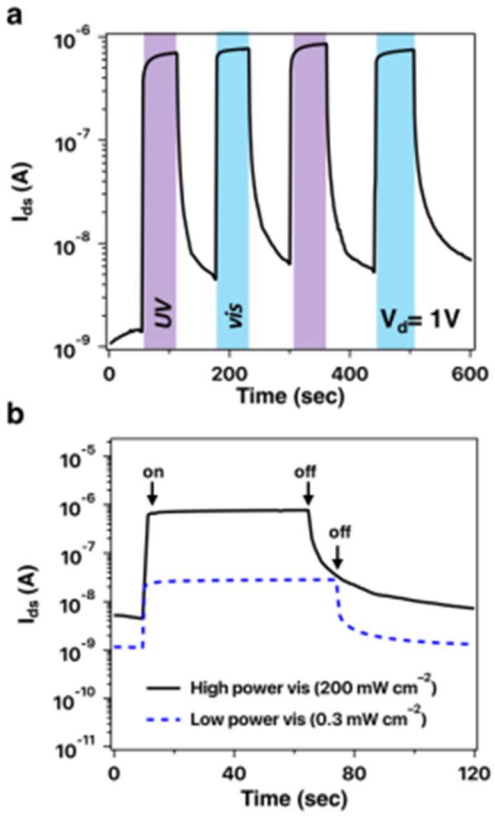

Figure B.4. Time-dependent current of the two-terminal device in response to (a) alternating UV (365 nm, 80 mW cm^{-2}) and visible (470 nm, 200 mW cm^{-2}) light, and (b) high (200 mW cm^{-2}) and low (0.3 mW cm^{-2}) power visible light.

Encouraged by these results, we next sought to determine if the Azo-PIL device would be applicable as a broadband photodetector through exposure to different wavelengths of light beyond the Azo-PIL wavelengths of maximum absorption. We selected three wavelengths of light with three different photon fluxes. Specifically, the device response under 470 nm was

compared to 600 and 700 nm wavelengths, which are lower energy than the π → π* and n → π* transitions of *trans*-Azo-PIL and are near the absorption edge of PhF-2,3 (Figure B.5b).

Bias stress measurements of the two-terminal photodetector under lower power 470 nm light (0.32 mW cm^{-2}; 7.7×10^{14} photons s^{-1} cm^{-2}) show an increase in current of approximately one order of magnitude (Figure B.5a). In comparison, the current increase under a 660 nm LED (2.1 mW cm^{-2}; 6.9×10^{15} photons s^{-} cm^{-2}) is 37% of the current increase seen with 470 nm light, despite a higher photon flux. With 700 nm light (1.5 mW cm^{-2}; 5.2×10^{15} photons s^{-} cm^{-2}), the increase in drain current under constant bias stress was 3% of the increase in current seen with 470 nm light (Figure B.5a). For all three wavelengths of light with differing photon fluxes, we see an increase in current, demonstrating the capability of this device to detect light of various wavelengths and corresponding energies.

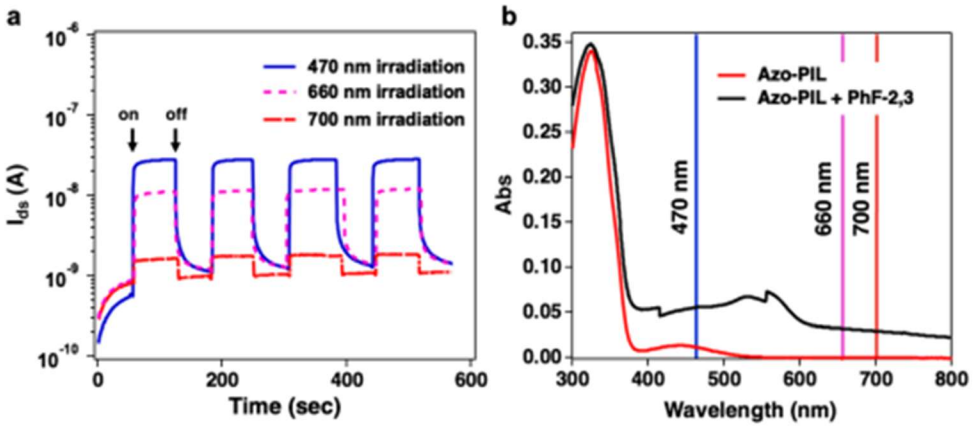

Figure B.5. (a) Time-dependent current of the two-terminal device under irradiation with three wavelengths of light. (b) UV–vis spectrum of *trans*-Azo-PIL and trans-Azo-PIL + PhF-2,3 on quartz with the wavelengths of irradiation from (a) highlighted. Figure 5b shows 470 nm has absorption from both Azo-PIL and PhF-2,3, whereas PhF-2,3 contributes to the majority of the absorption at 660 nm and 700 nm.

To evaluate if the increase in photocurrent was dependent on the concentration of *trans* or *cis* isomers in the Azo-PIL layer, the light-response of the bilayers was compared in the presence and absence of the *trans* → *cis* isomerization. A three-terminal device where the bilayer was formed on an SiO_2 dielectric with a doped silicon bottom gate provided a means to modulate the number of carriers in Ph-2,3 at the SiO_2 interface and into the bulk by application of a gate bias. Measurements were performed in the saturation regime (V_D = –80 V) of the device under irradiation with 365 nm and 470 nm light. The devices were first kept in the dark to ensure that the Azo-PIL layer was initially in the *trans* form. These three-terminal Azo-PIL devices were then irradiated with 365 or 470 nm light. Note that little *trans* → *cis* isomerization is observed when the Azo-PIL film in the *trans* form is illuminated with 470 nm LED light (Figure B.12). As expected from Figure B.4a, an increase in current at all voltages was observed with 365 nm light (Figure B.6). Notably, a similar shift in the transfer curve was observed with 470 nm illumination that corresponds with minimal *trans* → *cis* isomerization, presumably due to minor absorbance from the n → π* transition of *trans*-azobenzene.

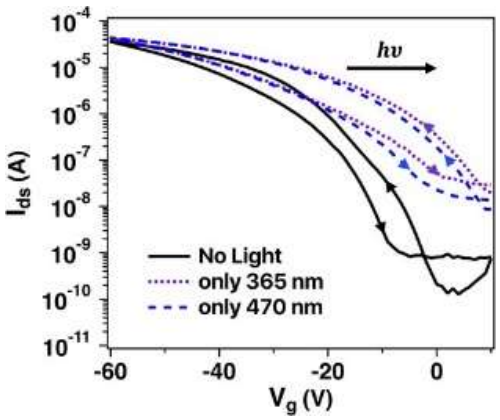

Figure B.6. Transfer characteristics of the three-terminal Azo-PIL device under dark conditions (trans form), after 365 nm irradiation (*trans* → *cis* isomerization), and after 470 nm irradiation (still in the trans form).

B.2.4 Mechanism

The increase in current observed with UV light could be consistent with either the isomerization of azobenzene—which yields a change in dipole moment[16,17]—or a light-induced charge-transfer mechanism.[11–15] With Azo-PIL, evidence suggests charge transfer between the Azo-PIL and PhF-2,3 semiconducting layers is responsible for the current increase. First, as shown above in Figure B.6, molecules that remain in the *trans* configuration still increase device current when illuminated. Second, a change in dipole driving the conductivity does not fully explain why the current increase is the same with both 365 nm and 470 nm light sources; as shown in Figure B.2, Azo-PIL undergoes a reversible isomerization with 365 nm and 470 nm light. If the change in dipole controlled the increase in current, a *cis-trans* isomerization would decrease the current as *cis* reverts back to *trans* if molecular dipole effects were at play, further supporting that charge-transfer is the mechanism in the Azo-PIL device.

Our hypothesis of charge-transfer is further supported by the higher OFF current under 365 and 470 nm light for the reverse scan of the transfer curve. Full current recovery was not observed during the reverse bias scans, which can be attributed to incomplete charge depletion in the bulk PhF-2,3 layer. The trapped charges in the PhF-2,3 layer are believed to keep the device ON during the reverse bias scan above 0 V, which indicates that charge transfer occurs at the Azo-PIL and PhF-2,3 interface.

Furthermore, this device shows the largest increases in current for the wavelengths of light associated with Azo-PIL absorbance. As shown in Figure B.5, we observed a difference in the increase in photocurrent under 470 nm light, associated with the Azo-PIL, and that under 660 nm and 700 nm light, outside of the Azo-PIL absorbance spectrum. Although the

respective photon fluxes of light with 660 nm (6.9×10^{15} photons s^{-} cm^{-2}) and 700 nm (5.2×10^{15} photons s^{-} cm^{-2}) are larger than that of the 470 nm LED (7.7×10^{14} photons s^{-} cm^{-2}) used in this experiment, a smaller current increase was observed, resulting in smaller responsivities and EQEs at these longer wavelengths (Table B.3). Additionally, the PhF-2,3 absorbs at 660 nm and 700 nm and shows a small amount of charge carriers generated compared to the wavelengths where Azo-PIL absorbs, implying formation of the exciton in the Azo-PIL layer (Table B.1).

Finally, in the absence of the Azo-PIL layer, the device containing only PhF-2,3 shows minimal increases in current with irradiation of multiple wavelengths of light despite the fact that PhF-2,3 does show some absorbance at 470 nm, 660 nm, and 700 nm in the UV–vis spectrum[19] (Figure B.20 and Figure B.21). Taken altogether, these results strongly support that the device response is driven by Azo-PIL absorption and subsequent charge transfer with the PhF-2,3 semiconductor.

Frontier energy levels of PhF-2,3 and Azo-PIL were determined experimentally by cyclic voltammetry to further support the interfacial charge transfer mechanism (Figure B.21). The highest-occupied molecular orbital (HOMO) and lowest-unoccupied molecular orbital (LUMO) of Azo-PIL were calculated using a ferrocene reference (4.8 eV), yielding a HOMO energy of –5.3 eV and LUMO energy of –4.1 eV. We believe these HOMO and LUMO levels are due to the azobenzene units on the Azo-PIL as the corresponding oxidation and reduction peaks used for HOMO-LUMO determination are present in the Azo-PIL, but are absent from the unfunctionalized imidazole homopolymer (Figure B.22 and Figure B.23). The HOMO and LUMO energies of PhF-2,3 have previously been reported as –5.3 eV and –3.3 eV, respectively.[19] With the similar HOMO levels of Azo-PIL and PhF-2,3 coupled with the fact

that PhF-2,3 does not absorb light at 365 nm,[19] it is plausible that the generation of an exciton in the Azo-PIL layer would allow for hole transfer from the HOMO of Azo-PIL to the HOMO of PhF-2,3, thereby reducing azobenzene in the Azo-PIL layer and yielding holes in PhF-2,3 (Figure B.7). This photoinduced interfacial hole transfer increases the hole current within the semiconductor, even with multiple wavelengths of light. In addition, the quick decay of current in the absence of light is consistent with recombination between carriers near the interface of the Azo-PIL and PhF-2,3 layers. This decay that begins as soon as the light is turned OFF contrasts with the behavior of past devices which exploit azobenzene charge transfer; typically, slow decay rates on the order of minutes to hours after UV irradiation are observed due to sluggish hole recombination between the semiconducting polymer and azobenzene additive, maintaining a metastable ON state.[11,14,15] In the Azo-PIL device described here, the reduced azobenzene in the Azo-PIL layer can readily transfer an electron back to holes in PhF-2,3 resulting in fast current decay.

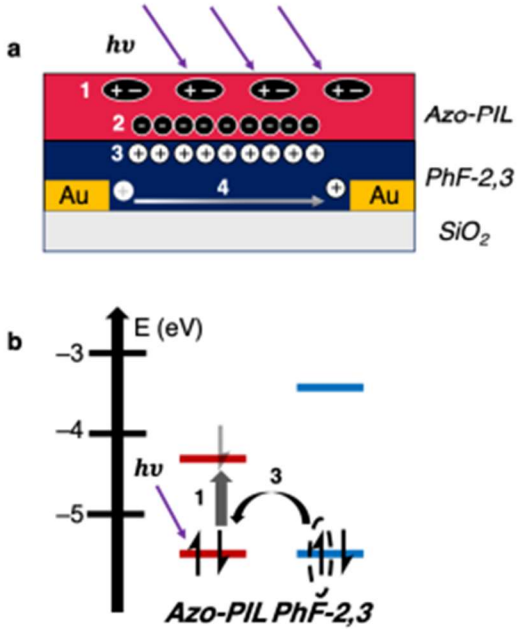

Figure B.7. Schematic of the charge transport mechanism as depicted with (a) an interfacial

diagram and (b) frontier energy levels. When the device is illuminated with either 365 nm or 470 nm light, an electron in Azo-PIL is promoted from the low-lying doubly-occupied HOMO to the LUMO, generating excitons in the PIL layer (step 1). These excitons diffuse throughout the PIL gate layer to the interface (step 2, not depicted in 7b), stimulating electron transfer from the doubly-occupied HOMO of PhF-2,3 to the now singly-occupied HOMO of azobenzene and creating holes in the semiconducting layer (step 3). The generation of holes in the semiconducting PhF-2,3 layer then allows for the lateral flow of electrons (step 4, not depicted in 2.7b), resulting in an increase in current under multiple wavelengths of light.

To further rationalize the interfacial charge transfer mechanism between Azo-PIL and PhF-2,3, measurements from two- and three-terminal devices were used to estimate the surface carrier number density. For the two-terminal device, a model for the charge-transfer mechanism was used, and the resulting estimated photo-generated carrier number density was compared to the carrier number density estimated for the three-terminal device. The agreement between these numbers would further support the proposed photo-induced interfacial charge transfer mechanism.

For the two-terminal device, the expected charge carrier number density can be extracted from the observed current increase, assuming the current increase is solely due to photo- induced charge transfer at the interface of the two polymers. The photo-generated current of a two-terminal, lateral organic bilayer heterojunction photoconductor can be described by Equation B.1.[32,33]

Equation B.1 $$J_{\text{photo}} = qn(\mu_{\text{n}} + \mu_{\text{p}})E$$

where q is the electric charge, n is the charge carrier density, E is the applied electric field, and

μ_n and μ_p are the electron and hole mobilities, respectively, such that $\mu_p = 1.1$ cm^2 V$^-$ s [20] and $\mu_p \gg \mu_n$. With a current increase of 0.44 μA, the surface photo-generated carrier number density is estimated to be 3×10^{11} carriers cm^{-2}. To further validate the application of a two- terminal photoconductor model to our system, the carrier number density for the three-terminal device was estimated from the transfer curve in Figure B.6. If the values of carrier number density from the two-terminal photoconductor model and calculations based on data from the three-terminal device match, this would support the hypothesis that the current increase is due to photoexcitation of the Azo-PIL followed by interfacial charge transfer. The capacitance of the gate (~4 pF) was estimated from the capacitance per unit area of 300 nm-thick Si (10.5 nF cm^{-2}) and the area of the channel (40 μm × 1000 μm). By assuming the applied voltage is equal to the shift in the threshold voltage (30 V), the accumulated charge was calculated to be 1.2×10^{-10} coulombs. The carrier number density from the three-terminal device is estimated to be 2×10^{12} carriers cm^{-2}. A small difference in respective calculated carrier density values can be attributed to an overestimation of the hole mobility in the calculations pertaining to the two-terminal device. This difference can also be due to limitations in exciton diffusion and deviations in the PIL photoluminescence efficiency from 100%, which is seen with both the two-terminal and three-terminal devices. As the value calculated for carrier density of the three-terminal device is within one order of magnitude to that of the two-terminal photoconductor model, this finding supports the proposed charge-transfer mechanism and the validity of using this model.[33] Since the photoconductor model is applicable to this system, it can be used to estimate the charge carrier lifetime by extending Equation 2.1 as follows:[33]

Equation 2.2

$$J_{photo} = q\eta\phi \frac{L}{d} \tau \left(\frac{1}{t_n} + \frac{1}{t_p}\right)$$

where η is the photoluminescence efficiency, Φ is the photon flux per unit area, L is the channel length, d is the device thickness, τ is the carrier lifetime, and t_n and t_p are the transit times of electron and holes, respectively. With the known surface power density of both light sources at each wavelength, the device geometry, and the photon flux attenuated by the Azo- PIL layer, the carrier lifetime (τ) of PhF-2,3 at both wavelengths was extracted and found to be in the microsecond range (details shown in Table B.1). These results assume the photoluminescence efficiency to be around 0.05, which is typical for organic semiconducting polymers.[34–36] Along with the matching frontier energy levels, this analysis leads us to the conclusion that charge transfer occurs at the interface of the Azo-PIL and the PhF-2,3 and induces a current increase at operating wavelengths across the UV and visible spectrum.

In comparison to other light-responsive devices made with azobenzene as a photoresponsive motif, the performance of the Azo-PIL device described here performs well in terms of minimal decay over multiple cycles and fast response times.[11–17] Our report also explicitly shows that the *trans* → *cis* does not have a large effect on the interfacial charge-transfer capabilities of azobenzene as demonstrated by the same increase in current with both 365 nm (*trans* → *cis*) and 470 nm (*cis* → *trans*) light excitation. In general, larger light-induced increases in current are observed with the azobenzene devices that report operation via charge transfer as opposed to a change in dipole, consistent with the 2–3 orders of magnitude increase in current observed herein.[12,14–16] Although there are examples of larger increases in current, for example, over 6 orders of magnitude in devices that include azobenzene as a charge-trap, the application of a large negative gate voltage or irradiation with another wavelength of light was required to cause the current to return to its initial state.[12,14,15] In contrast, our device shows an immediate decrease in current in the absence of a light source. However, both devices hold

importance in the application of photochromic devices, with previous literature examples more useful as writing/erasing photo-memory devices and the Azo-PIL device described here applicable as a light sensor. As a photodetector, our device senses longer wavelengths of light than are common in other photochromic devices.[7]

B.3 Conclusions

In conclusion, we have reported the fabrication of a photodetector which functions via charge transfer between an azobenzene PIL layer and a *p*-type semiconducting polymer. The Azo-PIL layer was designed to have complementary solubility to the semiconducting polymer, PhF-2,3, which facilitates device fabrication by spin coating. The Azo-PIL was shown to have a reversible *trans* → *cis* isomerization through UV–vis spectroscopy under 365 nm and 470 nm irradiation. However, once incorporated into devices, an increase in current was observed with both wavelengths of light, indicating the response is surprisingly not due to the reversible *trans* → *cis* isomerization of azobenzene. Instead, we conclude that charge transfer occurs at the interface of the Azo-PIL and PhF-2,3 layers as evidenced by CV measurements and supporting calculations. This charge transfer mechanism results in a fast current response because the HOMO energy levels of Azo-PIL and PhF-2,3 are nearly equivalent. This report reinforces the importance of tailoring materials for contemporary applications, which can increase the processability and performance of advanced devices.

B.4 Materials and Methods

B.4.1 Materials

Methanol, acetonitrile, carbon tetrachloride, acetic acid, ethanol, 2,2-dimethoxy-2-phenylacetophenone, lithium bis(trifluoromethanesulfonyl)imide (LiTFSI), nitrosobenzene (>97%), toluidine (99%), *n*-bromosuccinimide (99%, Alfa Aesar), benzoyl peroxide (with 25%

H_2O, for synthesis), and carbon tetrachloride (anhydrous, >99.5%), were purchased from *Sigma-Aldrich* and *Fisher Scientific* and used as received. Benzoyl peroxide was recrystallized in ethanol before use.

B.4.2 Instrumentation

^{1}H NMR spectra were recorded on a Varian Unity Inova 500 MHz or a Varian Unity Inova AS600 600 MHz spectrometer at a regulated temperature of 25 °C. ^{1}H NMR chemical shifts were calibrated to the resonances of dimethylsulfoxide at δ = 2.50 ppm and MeOD at δ = 3.31 ppm. ^{19}F NMR spectra were recorded on an Agilent Technologies 400-MR DD2 400 MHz with hexafluorobenzene as an internal standard at δ = –164.9 for calibration. UV–Vis spectra were recorded on an Agilent UV–Vis Spectrometer. To induce photochemical isomerizations, a 365 nm Thorlabs collimated LED lamp (80 mW/cm^2), a 470 nm Thorlabs collimated LED lamp (0.2 W/cm^2), a 660 nm Thorlabs fiber LED (2.1 mW/cm^2), and a 700 nm Thorlabs fiber LED (1.5 mW/cm^2) were used. Glass transition temperatures were measured on a PerkinElmer DSC 8000. Devices were tested in a nitrogen environment using a Keithley semiconductor parametric analyzer (model 4200-SCS).

B.4.3 Synthesis

Synthesis of 1-(4-(bromomethyl)phenyl)-2-phenyldiazene

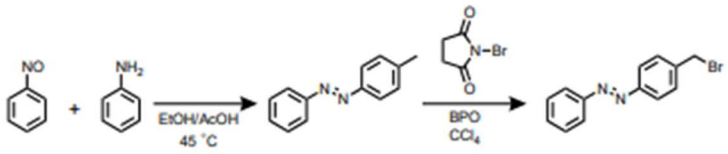

1-(4-(bromomethyl)phenyl)-2-phenyldiazene was synthesized in 2 steps from a previously published literature procedure.[1]

Synthesis of Azo-PIL

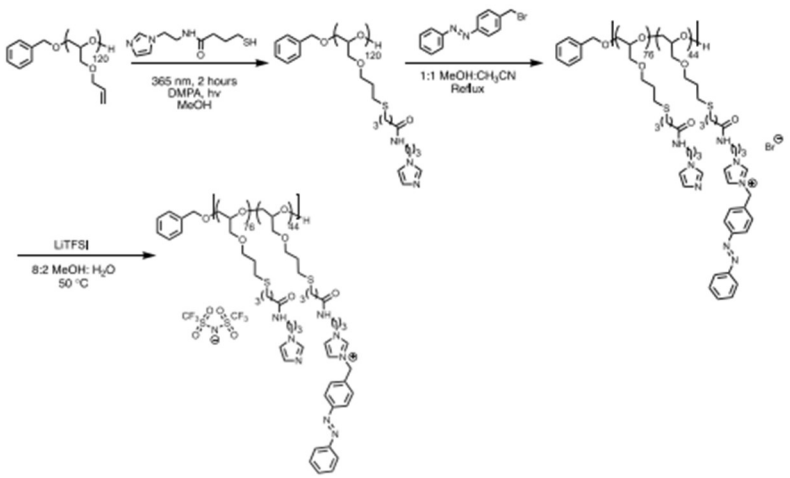

Synthesis of alkene-functionalized PEG polymer

The synthesis of the starting alkene-functionalized polymer was based on a previously published literature procedure.[2]

Synthesis of imidazole-functionalized PEG polymer (Poly(im))

The starting homopolymer with alkene pendant groups (n = 120), a thiol-imidazole small molecule, DMPA, and MeOH were added to a 250 mL round bottom flask and capped with a rubber septum. The reaction mixture was sparged with N_2 for 15 minutes before being exposed to 365 nm light to initiate the thiol–ene click reaction. After 2 hours of irradiation, the reaction mixture was exposed to air, and solvent was reduced with rotary evaporation. The resulting mixture was purified via dialysis (MW 10k) in MeOH over 48 hours and dried under high vacuum to yield a 100% imidazole-functionalized PAGE polymer (5.63 g, 85% yield).

Synthesis of 37% azobenzene-PIL with bromide counterion

Synthesis of PIL with azobenzene-imidazolium side chain Poly(im), 1-(4-(bromomethyl)phenyl)-2-phenyldiazene (0.4 eq), and 20 mL 1:1 MeOH:Acetonitrile were added to a 100 mL round bottom flask equipped with a stir bar. The flask was attached to a

findenser and refluxed at 97 °C overnight. After 15 hours, heating was stopped and the solvent was removed via rotary evaporation. The resulting crude material was dissolved in minimal MeOH and precipitated into 30 mL cold ether. The precipitation solution was centrifuged for 2 minutes at 2000 rpm. The supernatant was decanted and the residual polymer was washed with minimal MeOH before being dried under high vacuum to recover the resulting red azobenzene PIL (1.29 g, 74% mass recovery).

Ion exchange with LiTFSI to synthesize final Azo-PIL

The azobenzene-imidazolium (Br^-) PIL, LiTFSI, and a mixture of 8:2 MeOH:H_2O were added to a 100 mL round bottom flask equipped with a stir bar. A reflux condenser was fitted to the round bottom flask and the reaction was stirred at 50 °C for 18 hours. The reaction mixture was then concentrated via rotary evaporation and precipitated into cold deionized H_2O. The precipitation solution was centrifuged at 2000 rpm for 50 minutes. The supernatant was decanted and the residual polymer was washed with cold H_2O before being dried under high vacuum to recover the resulting TFSI polymer (1.15 g, 97% mass recovery).

B.4.4 Spin-coating for UV–vis spectroscopy

Solutions of Azo-PIL (30 mg/mL) were dissolved in acetone for spin-coating onto solvent- cleaned quartz slides. Thin films on quartz were made with the following conditions: 35 µL of solution, 2k rpm, and 1 minute of spin-coating.

B.4.5 Device preparation

Bottom-gate/bottom-contact two-terminal devices were fabricated on silica glass substrates with 300-nm-thick SiO_2. Thermally evaporated gold contacts with a chromium adhesion layer were patterned on the substrates using standard lithography techniques in a

cleanroom. The patterned substrates were cleaned by sonication in acetone followed by isopropyl alcohol. Upon drying in an oven, the substrates were treated in a UV-O_3 cleaner. Decyltrichlorosilane (DTS) was used to form a self-assembled monolayer (SAM) on the surface of the SiO_2 substrate to reduce charge trapping at the semiconductor–dielectric interface. PhF-2,3 in chlorobenzene (35 μL, 5 mg/mL) and the photoresponsive Azo-PIL layer in methanol (35 μL, 30 mg/mL) were deposited on top of the semiconducting layer sequentially by spin coating. The resulting film thicknesses for PhF-2,3 and Azo-PIL were 100 nm and 440 nm, respectively. The devices were then stored under vacuum overnight to remove trace solvent in the active layers. Prior to testing, all devices were kept in the dark so that the initial azobenzene layer would be mostly trans as shown by UV–vis of the polymeric azobenzene on the semiconducting polymer on quartz.

B.4.6 Cyclic voltammetry

Cyclic voltammetry (CV) was conducted using a standard three-electrode cell and a Biologic SP-300 potentiostat. Glassy carbon was used as the working electrode, Ag/Ag^+ as the reference electrode, and platinum as the counter electrode. Ferrocene was used as an external reference. The measurements were performed at a scan rate of 100 mV/s in acetonitrile with tetrabutylammonium hexafluorophosphate (TBAF) (0.1M) as the supporting electrolyte. A solution of 100 μM Azo-PIL was prepared and degassed for 15 min with nitrogen prior the electrochemical measurement.

B.4.7 Characterization

^{1}H NMR Spectra

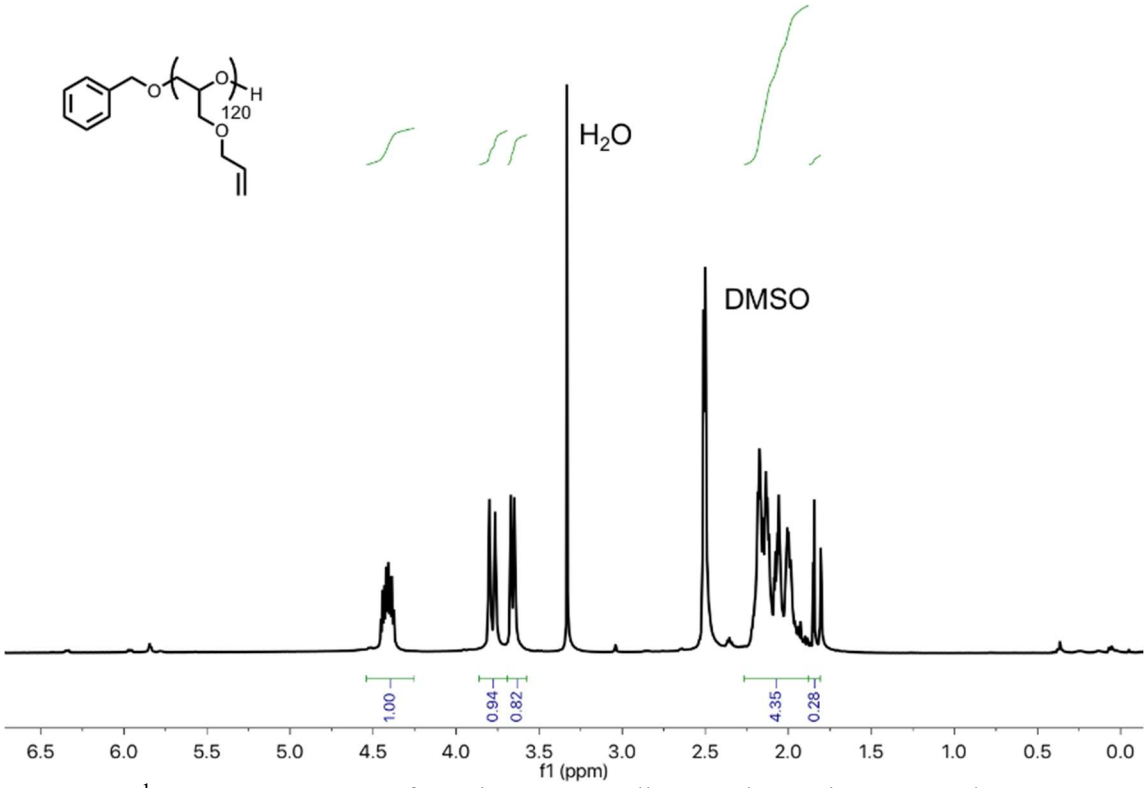

Figure B.8. ^{1}H NMR spectrum of starting PAGE-alkene polymer in DMSO-d_6.

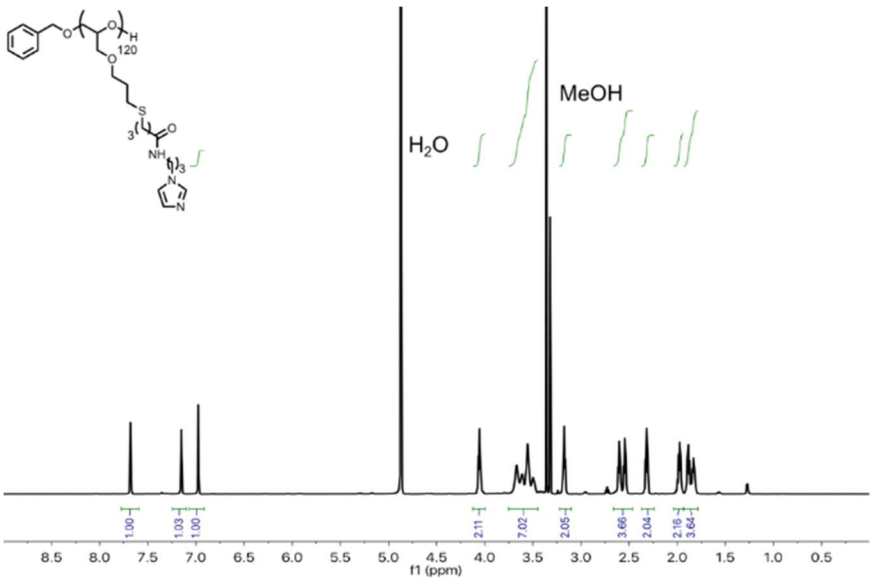

Figure B.9. [1]H NMR spectrum of polymer after the click reaction in MeOD.

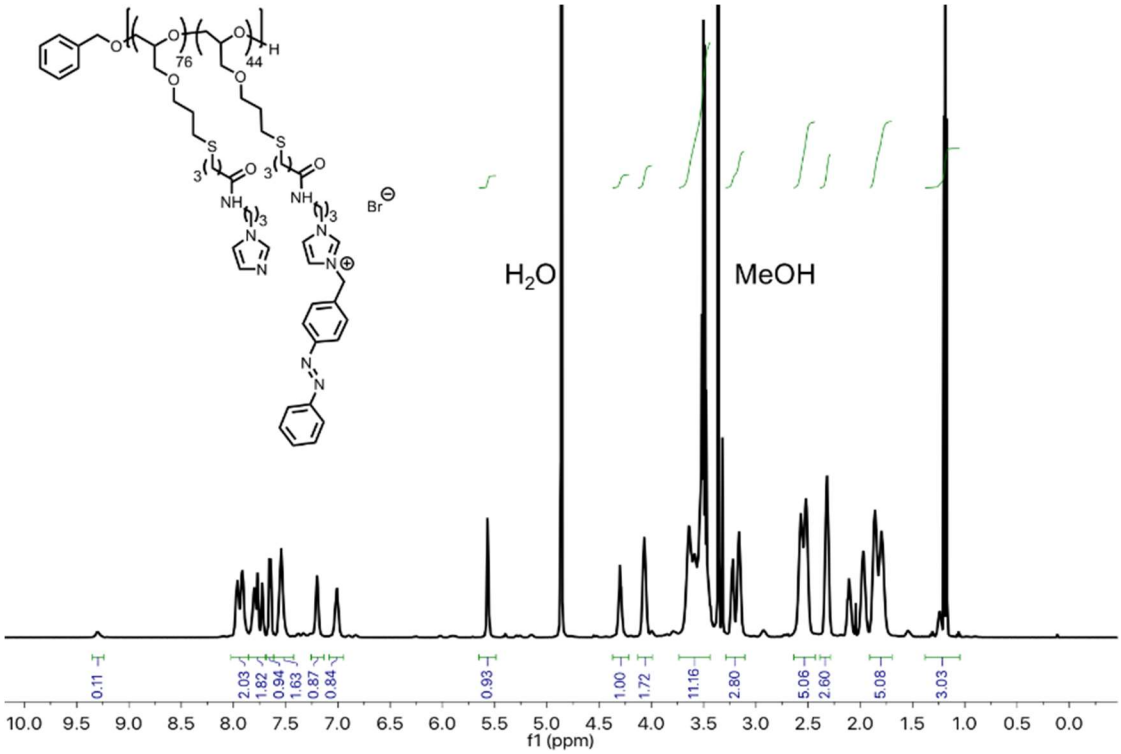

Figure B.10. [1]H NMR spectrum of azobenzene-PIL with a bromide anion in MeOD.

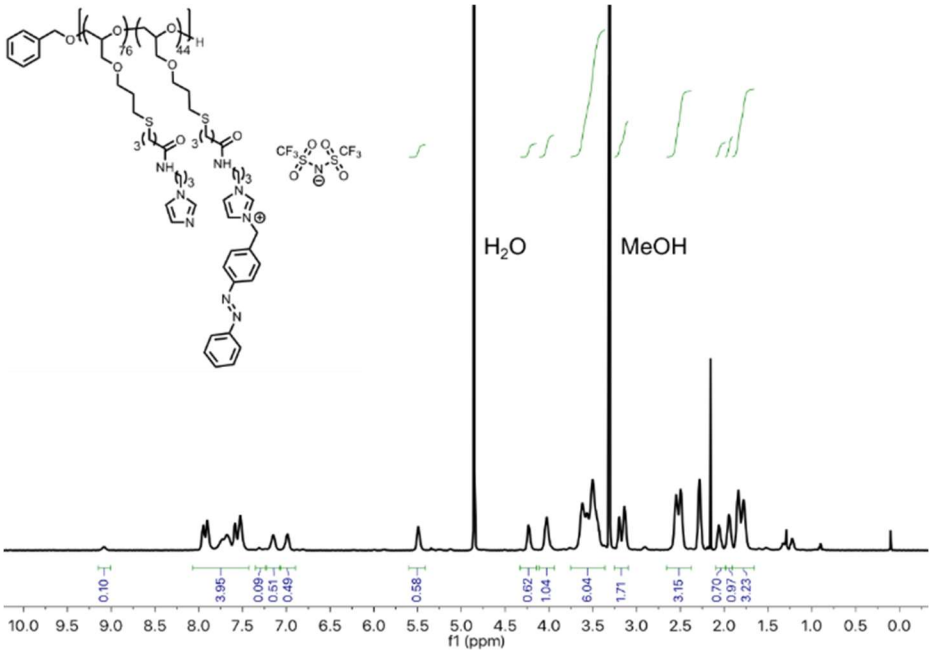

Figure B.11. ^{1}H NMR spectrum of Azo-PIL (with a TFSI counterion) in MeOD.

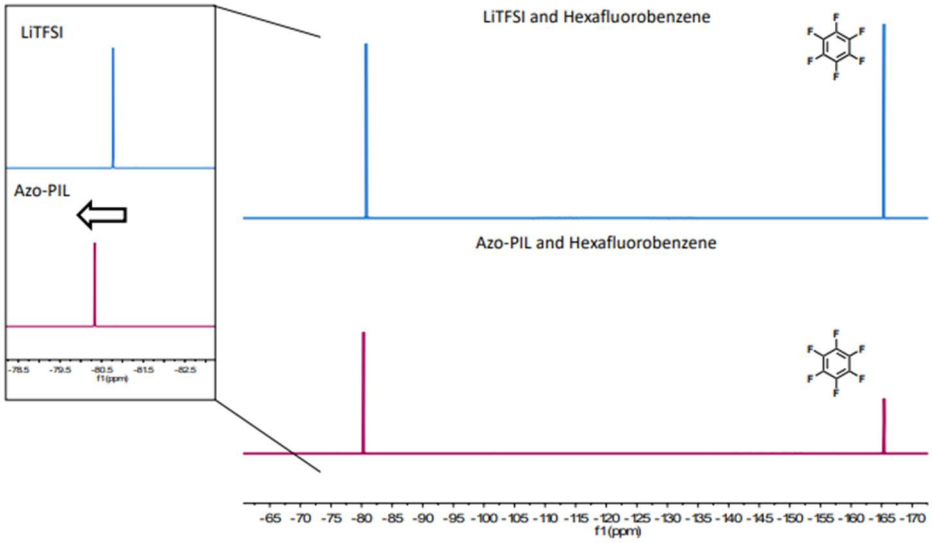

Figure B.12. ^{19}F of LiTFSI compared to azo-PIL in MeOD with hexafluorobenzene included as an internal standard (δ= –164.9 ppm).

DSC Measurements

For T_g measurements of Poly(im) and Azo-PIL in the dark (*trans*-azobenzene), the polymers were dried under vacuum at 10^{-8} Torr at 50 °C. 5–10 mg of each dried polymer sample was placed in respective aluminum hermetic pan. The sample of Poly(im) was subjected to 2 cycles of the following protocol: cooling at a rate of –20 °C/min from 25 ˚C to –90 °C and then heating at a rate of 20 °C/min to 25 ˚C. The sample of Azo-PIL was subjected to 2 cycles of a similar protocol: cooling at a rate of –20 °C/min from 25 ˚C to –90 °C and then heating at a rate of 20 °C/min to 90 ˚C. T_g measurements were recorded from the second cool/heat cycle.

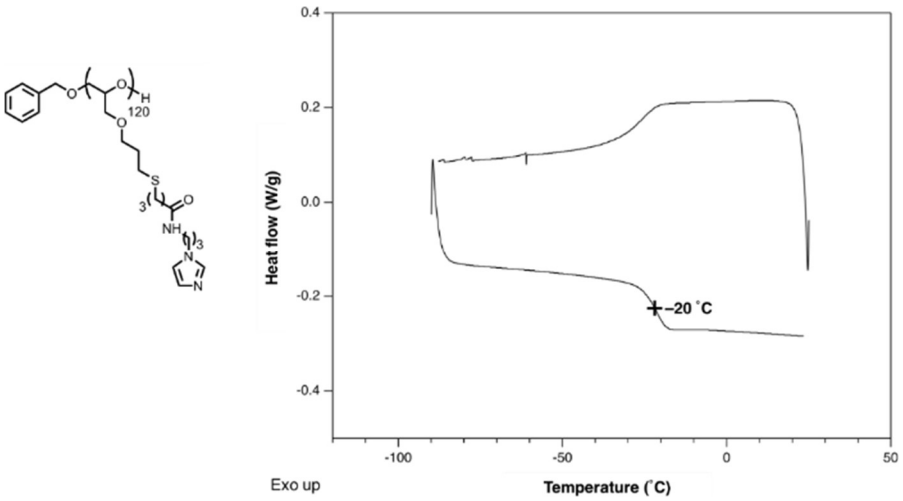

Figure B.13. DSC trace of Poly(im).

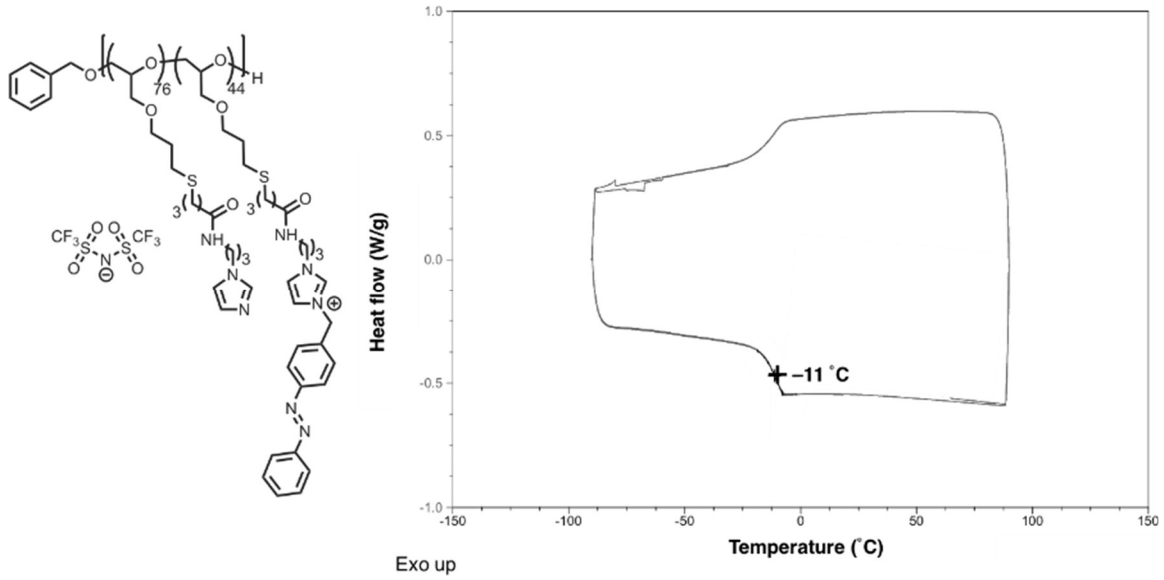

Figure B.14. DSC trace of final Azo-PIL polymer with 37% azobenzene-TFSI incorporation.

Table B.1 Experimental parameters used to extract the product of the carrier transit time and photoluminescence efficiency.

Wavelength (nm)	365 nm	470 nm	600 nm	700 nm
Photon energy (J)	5.4×10^{-19}	4.2×10^{-19}	3.0×10^{-19}	2.8×10^{-19}
Power density (mW cm^{-2})	80	200	2	1.5
Incident photon flux (photons s^{-1} cm^{-2})	1.47×10^{17}	4.74×10^{17}	6.86×10^{15}	5.24×10^{15}
Absorption coefficient[a] (cm^{-1})	9.34×10^{3}	1.61×10^{3}	50.0	42.2
Attenuated photon flux (photons s^{-1} cm^{-2})	9.75×10^{16}	4.41×10^{17}	6.84×10^{15}	5.23×10^{15}
Percentage of light absorbed	33	6.8	0.22	0.19
***J*photo (A cm^{-2})**	0.44	0.74	1.69×10^{-4}	4.81×10^{-4}
ht (s)	9.0×10^{-8}	3.3×10^{-8}	4.89×10^{-10}	1.82×10^{-10}

[a]Extracted from the Azo-PIL film thickness of 440 nm using $\alpha = \varepsilon c / \log_{10} e$.

B.4.8 UV–Vis Spectra (on quartz substrates) and calculation of extinction coefficients (ε)

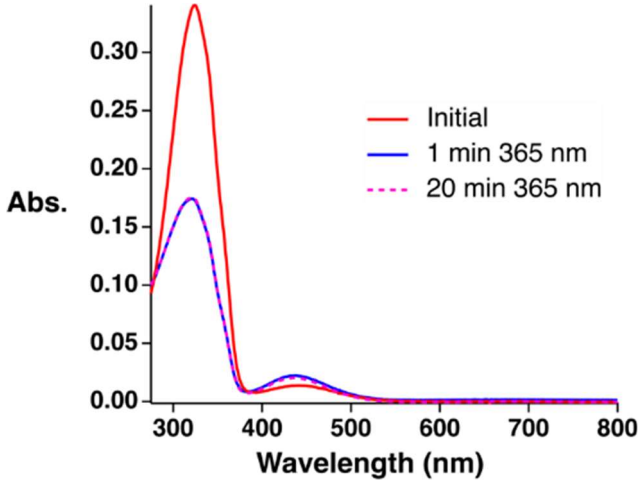

Figure B.15. UV–vis spectra of Azo-PIL initially (solid red trace) and after irradiation with 365 nm light for 1 minute (solid blue trace) or 20 minutes at the photostationary state (PSS, dashed pink trace).

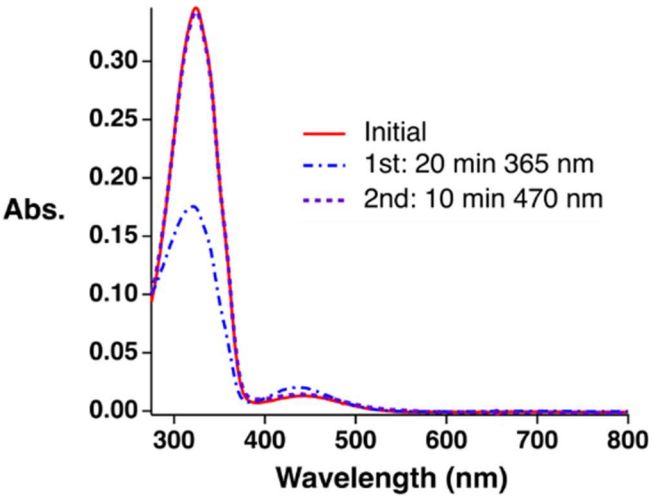

Figure B.16. UV–vis spectra of the Azo-PIL initially (solid red trace), after irradiation with 365 nm light for 20 minutes (dotted blue trace), and after irradiation with 470 nm light for 10 minutes (dashed purple trace).

B.4.9 Calculation of ε_{trans} and ε_{cis}

Solution-based UV–Vis spectroscopy was used to extrapolate the extinction coefficient of the trans form (ε_{trans}) and the extinction coefficient of the cis form (ε_{cis}). To find the ε_{trans}, a series of solutions of the azo-PIL (10^{-5} M of azobenzene) were prepared and the absorbance measured by UV–Vis. Linear regression of the absorbance, A, was then plotted versus cl, the concentration of the solution multiplied by the path length, to calculate the extinction coefficient of the trans form by Beer's law.

To calculate the extinction coefficient of the cis form, we also used Beer's law. (Eq. S1) A solution of azobenzene-PIL in MeOD (15 mg/mL) was stirred and irradiated with 365 nm LED (80 mW/cm^2). At each time point, t, the extent of trans–cis isomerization was monitored via ^{1}H NMR and diluted to 10^{-5} M of azobenzene in methanol for UV–Vis spectroscopy. The concentration of trans and cis azobenzene was calculated via the ratio of methylenes connecting the azobenzene to the imidazolium ring in the ^{1}H NMR spectrum (Figure S10A, blue and pink squares). The absorbance at a particular wavelength λ represents a mixture of the cis and trans forms at each time, t. We monitored the absorbance at λ = 323 nm as a function of exposure to 365 nm irradiation and calculated ε_{cis} by linear regression of $A/l - c_{\text{trans}}\varepsilon_{\text{trans}}$ vs. c_{cis}.

Table 2.2 Extinction coefficients of Azo-PIL calculated by solution-based UV-vis spectroscopy measurements.

Isomer of azobenzene	Extinction coefficient (ε) at 323 nm [L mol^{-1} cm^{-1}]
trans	23000
cis	2780

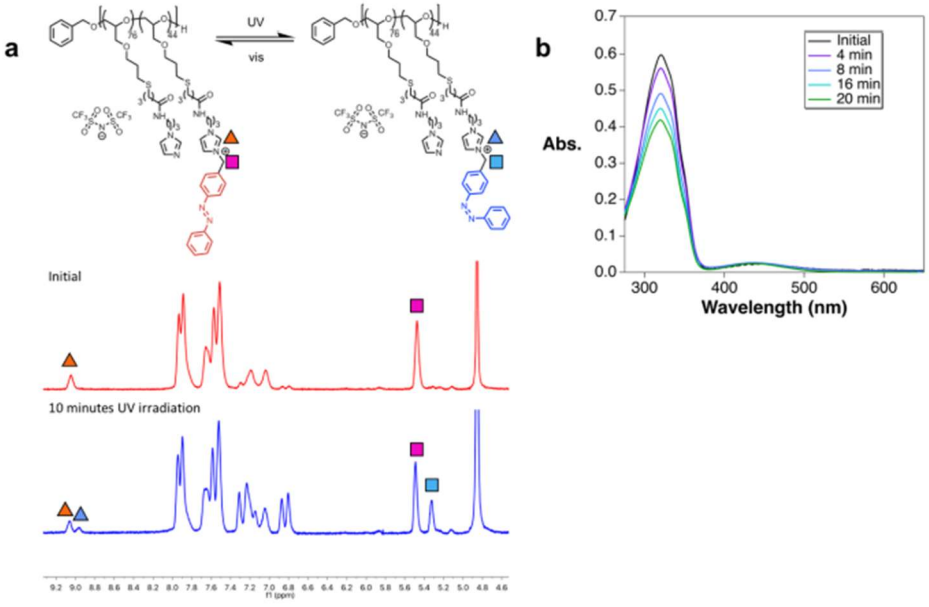

Figure B.17. (a) ^{1}H NMR of azobenzene PIL initially (at t = 0) and at t = 10 min of 365 nm light (UV) exposure, which was used to calculate the concentration of trans and cis. (b) Monitoring the changing absorbance at different time points under 365 nm LED irradiation.

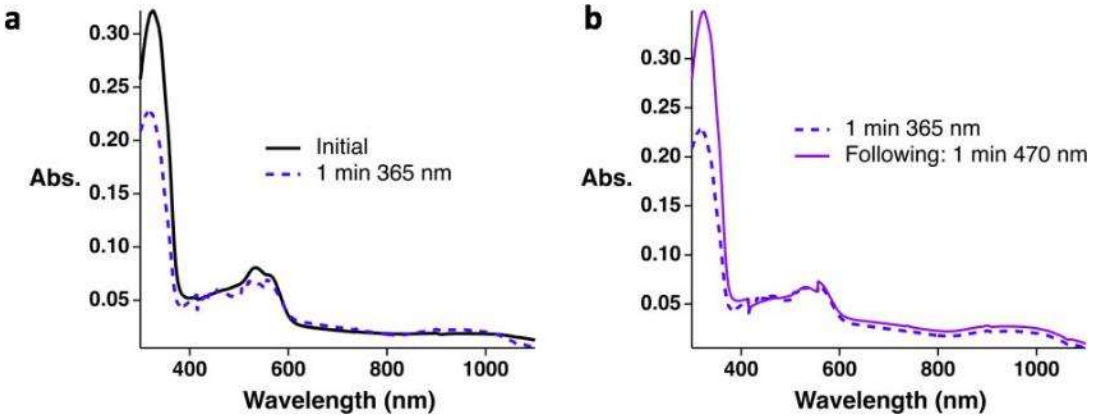

Figure B.18. UV–vis spectra of Azo-PIL on PhF-2,3 (a) initially in the trans form (solid black trace) and then after 365 nm irradiation (dashed blue trace) and (b) in the same 365 nm irradiated state (dashed blue trace) and after an additional 1 minute exposure to 470 nm light (solid purple trace).

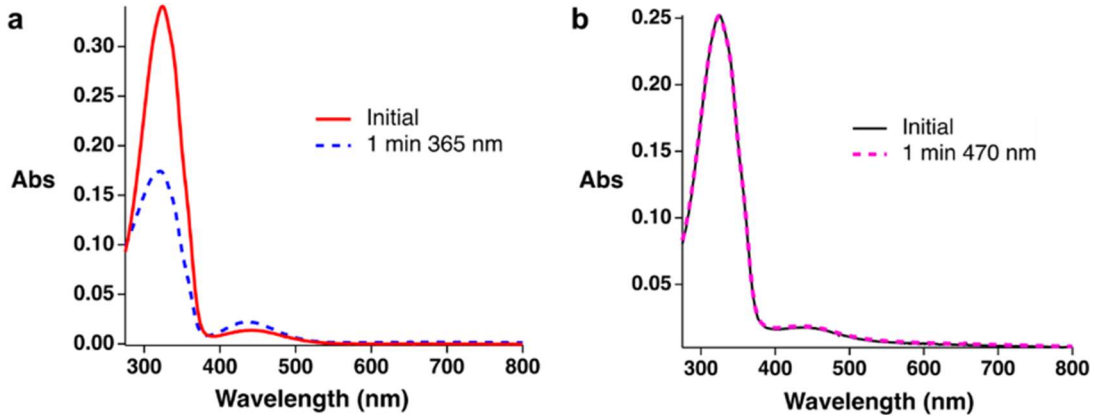

Figure B.19. UV–Vis spectra of Azo-PIL in the trans form and then exposed to (a) 365 nm or (b) 470 nm light.

Table B.3 Calculation of Responsivities and External Quantum Efficiency (EQE) based on various light sources used and corresponding photocurrents.

Light Source	Power density (W cm^{-2})	Power (W)	Photocurrent (A)	Responsivity (A/W)	External Quantum Efficiency (EQE)
High power 365 nm	0.080	3.2×10^{-5}	7.5×10^{-7}	0.023	8%
High power 470 nm	0.20	8×10^{-5}	7.6×10^{-7}	0.0095	2.5%
Low power 470 nm	0.0030	1.2×10^{-7}	2.7×10^{-8}	0.23	59%
660 nm	0.0020	8.0×10^{-7}	1.0×10^{-8}	0.013	2.3%
700 nm	0.0015	6.0×-10^{-7}	8.0×10^{-10}	0.0013	0.24%

*Power calculated based on a channel area of 40 μm × 1000 μm

B.4.10 Bias stress measurements

In the absence of the Azo-PIL layer

Control experiments were performed to see the influence of the PhF-2,3 semiconductor (no Azo-PIL) under light irradiation.

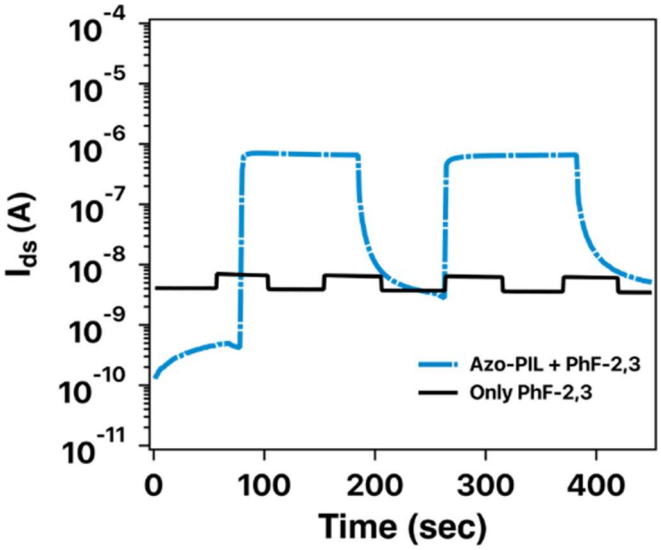

Figure B.20. Comparison of the time-dependent current at constant drain voltage V_D = 1 V in response to 365 nm (80 mW cm^{-2}) irradiation with the Azo-PIL–PhF-2,3 device (dotted blue trace) and only the PhF-2,3 semiconducting layer (solid black trace).

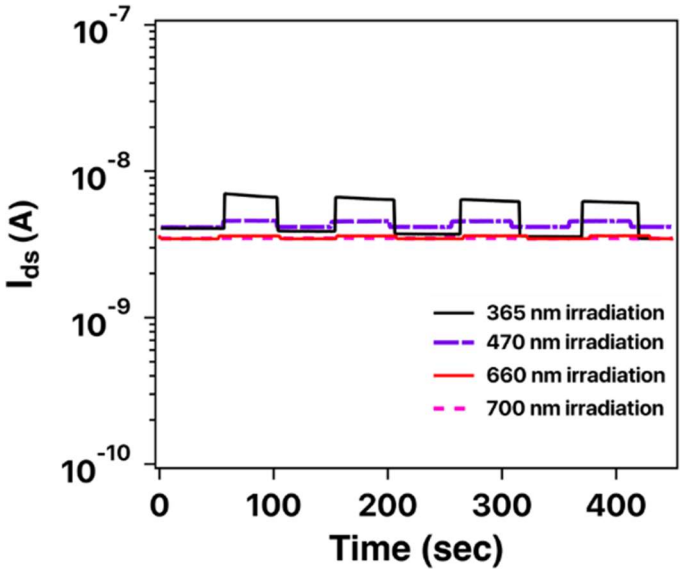

Figure B.21. Time-dependent current with only PhF-2,3 semiconductor (no Azo-PIL) at constant V_D=1V in response to one of the four light sources: 365 nm light (80 mW cm^{-2}, solid black trace), 470 nm light (200 mW cm^{-2}, dotted purple trace), 660 nm only (2.1 mW cm^{-2}, solid red trace). 700 nm (1.5 mW cm^{-2}, dashed pink trace).

B.4.11 Cyclic voltammograms

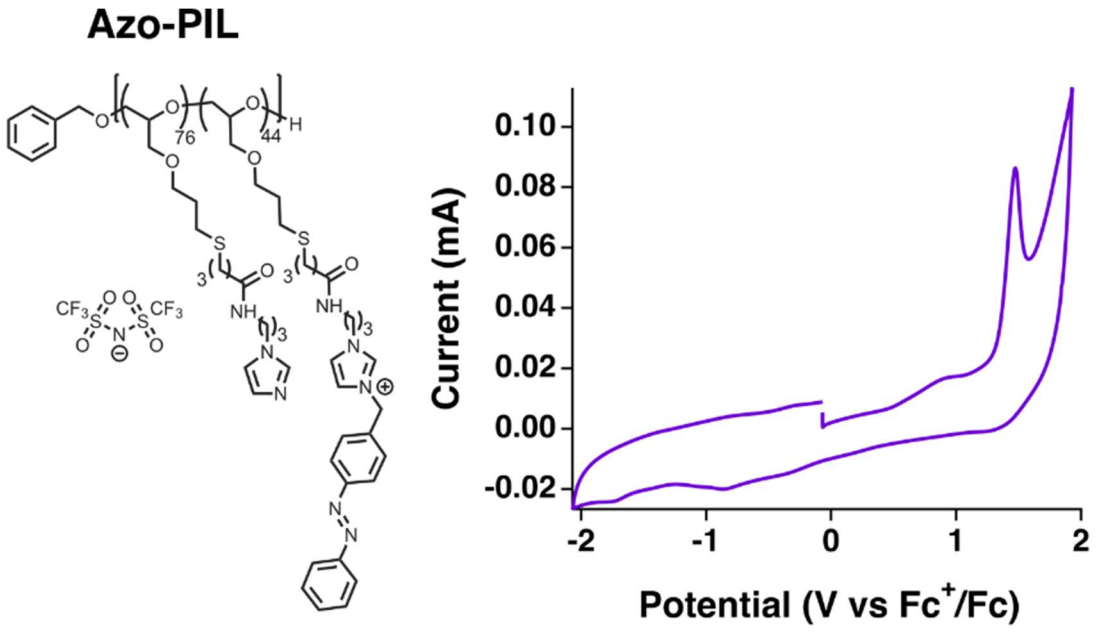

Figure B.22. Cyclic voltammogram of Azo-PIL (0.1 M TBAF in acetonitrile).

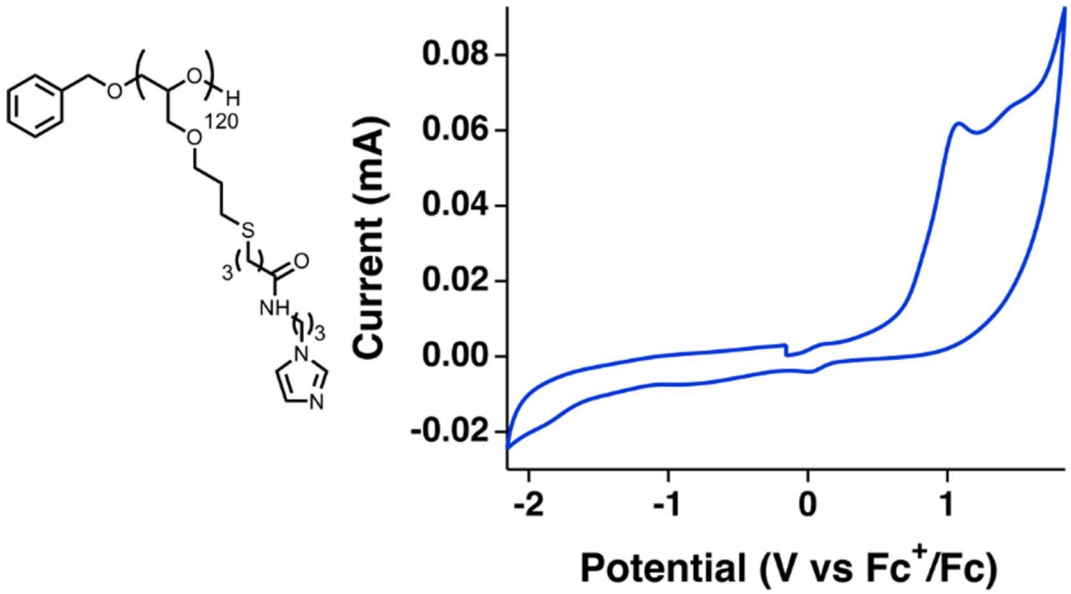

Figure B.23. Cyclic voltammogram of unfunctionalized Poly(im) (0.1 M TBAF in acetonitrile).

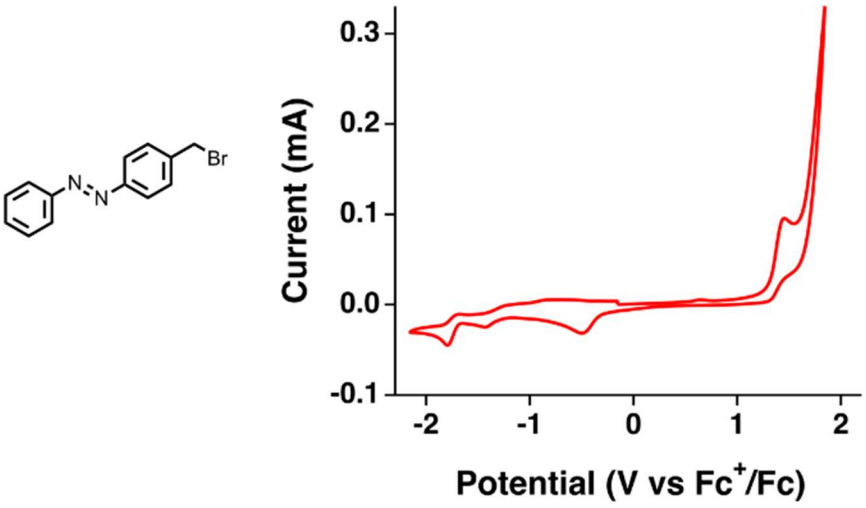

Figure B.24. Cyclic voltammagram of small-molecule Azo-Br (0.1 M TBAF in acetonitrile).

B.5 References

(1) Natali, D.; Caironi, M. Organic Photodetectors. In *Photodetectors*; Elsevier, 2016; pp 195–254.

(2) Ren, H.; Chen, J.; Li, Y.; Tang, J. Recent Progress in Organic Photodetectors and Their Applications. *Adv. Sci.* **2021**, *8* (1), 2002418.

(3) Simone, G.; Dyson, M. J.; Meskers, S. C. J.; Janssen, R. A. J.; Gelinck, G. H. Organic Photodetectors and Their Application in Large Area and Flexible Image Sensors: The Role of Dark Current. *Adv. Funct. Mater.* **2020**, *30* (20), 1904205.

(4) Xu, Y.; Lin, Q. Photodetectors Based on Solution-Processable Semiconductors: Recent Advances and Perspectives. *Applied Physics Reviews* **2020**, *7* (1), 011315.

(5) Moonen, P. F.; Yakimets, I.; Huskens, J. Fabrication of Transistors on Flexible Substrates: From Mass-Printing to High-Resolution Alternative Lithography Strategies. *Adv. Mater.* **2012**, *24* (41), 5526–5541.

(6) Gelinck, G.; Heremans, P.; Nomoto, K.; Anthopoulos, T. D. Organic Transistors in Optical Displays and Microelectronic Applications. *Adv. Mater.* **2010**, *22* (34), 3778–3798.

(7) Xu, C.; Zhang, J.; Xu, W.; Tian, H. Multifunctional Organic Field Effect Transistors Constructed with Photochromic Molecules. *Mater. Chem. Front.* **2021**, *5* (3), 1060–1075.

(8) Tian, J.; Liu, Z.; Jiang, W.; Shi, D.; Chen, L.; Zhang, X.; Zhang, G.; Di, C.; Zhang, D. A Conjugated Polymer Containing Arylazopyrazole Units in the Side Chains for Field- Effect Transistors Optically Tunable by Near Infra-Red Light. *Angew. Chem. Int. Ed.* **2020**, *59* (33), 13844–13851.

(9) Tian, J.; Liu, Z.; Wu, C.; Jiang, W.; Chen, L.; Shi, D.; Zhang, X.; Zhang, G.; Zhang, D. Simultaneous Incorporation of Two Types of Azo-Groups in the Side Chains of a Conjugated D–A Polymer for Logic Control of the Semiconducting Performance by Light Irradiation. *Adv. Mater.* **2021**, *33* (8), 2005613.

(10) Bandara, H. M. D.; Burdette, S. C. Photoisomerization in Different Classes of Azobenzene. *Chem. Soc. Rev.* **2012**, *41* (5), 1809–1825.

(11) Tseng, C.-W.; Huang, D.-C.; Tao, Y.-T. Electric Bistability Induced by Incorporating Self-Assembled Monolayers/Aggregated Clusters of Azobenzene Derivatives in Pentacene-Based Thin-Film Transistors. *ACS Appl. Mater. Interfaces* **2012**, *4* (10), 5483–5491.

(12) Peimyoo, N.; Li, J.; Shang, J.; Shen, X.; Qiu, C.; Xie, L.; Huang, W.; Yu, T. Photocontrolled Molecular Structural Transition and Doping in Graphene. *ACS Nano* **2012**, *6* (10), 8878–8886.

(13) Raimondo, C.; Crivillers, N.; Reinders, F.; Sander, F.; Mayor, M.; Samori, P. Optically

Switchable Organic Field-Effect Transistors Based on Photoresponsive Gold Nanoparticles Blended with Poly(3-Hexylthiophene). *Proceedings of the National Academy of Sciences* **2012**, *109* (31), 12375–12380.

(14) Smithson, C. S.; Wu, Y.; Wigglesworth, T.; Zhu, S. A More Than Six Orders of Magnitude UV-Responsive Organic Field-Effect Transistor Utilizing a Benzothiophene Semiconductor and Disperse Red 1 for Enhanced Charge Separation. *Adv. Mater.* **2015**, *27* (2), 228–233.

(15) Smithson, C. S.; Ljubic, D.; Wu, Y.; Zhu, S. The Effect of Azobenzene Derivatives on UV-Responsive Organic Thin-Film Transistors with a 2,7-Dipentylbenzo[b]Benzo[4,5]Thieno[2,3-d]Thiophene Semiconductor. *J. Mater. Chem. C* **2015**, *3* (31), 8090–8096.

(16) Lee, K. E.; Lee, J. U.; Seong, D. G.; Um, M.-K.; Lee, W. Highly Sensitive Ultraviolet Light Sensor Based on Photoactive Organic Gate Dielectrics with an Azobenzene Derivative. *J. Phys. Chem. C* **2016**, *120* (40), 23172–23179.

(17) Tian, J.; Fu, L.; Liu, Z.; Geng, H.; Sun, Y.; Lin, G.; Zhang, X.; Zhang, G.; Zhang, D. Optically Tunable Field Effect Transistors with Conjugated Polymer Entailing Azobenzene Groups in the Side Chains. *Adv. Funct. Mater.* **2019**, *29* (12), 1807176.

(18) Qian, W.; Texter, J.; Yan, F. Frontiers in Poly(Ionic Liquid)s: Syntheses and Applications. *Chem. Soc. Rev.* **2017**, *46* (4), 1124–1159.

(19) Wang, M.; Ford, M. J.; Zhou, C.; Seifrid, M.; Nguyen, T.-Q.; Bazan, G. C. Linear Conjugated Polymer Backbones Improve Alignment in Nanogroove-Assisted Organic Field-Effect Transistors. *J. Am. Chem. Soc.* **2017**, *139* (48), 17624–17631.

(20) Wang, M.; Ford, M. J.; Lill, A. T.; Phan, H.; Nguyen, T.-Q.; Bazan, G. C. Hole Mobility and Electron Injection Properties of D-A Conjugated Copolymers with Fluorinated Phenylene Acceptor Units. *Adv. Mater.* **2017**, *29* (7), 1603830.

(21) Sanoja, G. E.; Schauser, N. S.; Bartels, J. M.; Evans, C. M.; Helgeson, M. E.; Seshadri, R.; Segalman, R. A. Ion Transport in Dynamic Polymer Networks Based on Metal– Ligand Coordination: Effect of Cross-Linker Concentration. *Macromolecules* **2018**, *51* (5), 2017–2026.

(22) Wang, C.; Ma, X.; Kitazawa, Y.; Kobayashi, Y.; Zhang, S.; Kokubo, H.; Watanabe, M. From Macromolecular to Small-Molecular Triggers: Facile Method toward Photoinduced LCST Phase Behavior of Thermoresponsive Polymers in Mixed Ionic Liquids Containing an Azobenzene Moiety. *Macromol. Rapid Commun.* **2016**, *37* (23), 1960–1965.

(23) Weis, P.; Wu, S. Light-Switchable Azobenzene-Containing Macromolecules: From

UV to Near Infrared. *Macromol. Rapid Commun.* **2018**, *39* (1), 1700220.

(24) Weis, P.; Tian, W.; Wu, S. Photoinduced Liquefaction of Azobenzene-Containing Polymers. *Chem. Eur. J.* **2018**, *24* (25), 6494–6505.

(25) Jangu, C.; Schultz, A. R.; Wall, C. E.; Esker, A. R.; Long, T. E. Diphenylphosphino Styrene-Containing Homopolymers: Influence of Alkylation and Mobile Anions on Physical Properties. *Macromol. Rapid Commun.* **2016**, *37* (14), 1212–1217.

(26) Chen, M.; Dugger, J. W.; Li, X.; Wang, Y.; Kumar, R.; Meek, K. M.; Uhrig, D. W.; Browning, J. F.; Madsen, L. A.; Long, T. E.; Lokitz, B. S. Polymerized Ionic Liquids: Effects of Counter-Anions on Ion Conduction and Polymerization Kinetics. *J. Polym. Sci. Part A: Polym. Chem.* **2018**, *56* (13), 1346–1357.

(27) Goetzberger, A.; Knobloch, J.; Voss, B. *Crystalline Silicon Solar Cells*; John Wiley & Sons Inc.: Chichester, 1998.

(28) Vetráková, Ľ.; Ladányi, V.; Al Anshori, J.; Dvořák, P.; Wirz, J.; Heger, D. The Absorption Spectrum of *Cis* -Azobenzene. *Photochem. Photobiol. Sci.* **2017**, *16* (12), 1749–1756.

(29) Zhou, H.; Xue, C.; Weis, P.; Suzuki, Y.; Huang, S.; Koynov, K.; Auernhammer, G. K.; Berger, R.; Butt, H.-J.; Wu, S. Photoswitching of Glass Transition Temperatures of Azobenzene-Containing Polymers Induces Reversible Solid-to-Liquid Transitions. *Nature Chem* **2017**, *9* (2), 145–151.

(30) Yue, Y.; Norikane, Y.; Azumi, R.; Koyama, E. Light-Induced Mechanical Response in Crosslinked Liquid-Crystalline Polymers with Photoswitchable Glass Transition Temperatures. *Nat Commun* **2018**, *9* (1), 3234.

(31) Kuenstler, A. S.; Clark, K. D.; Read de Alaniz, J.; Hayward, R. C. Reversible

Actuation via Photoisomerization-Induced Melting of a Semicrystalline Poly(Azobenzene). *ACS Macro Lett.* **2020**, *9* (6), 902–909.

(32) Sze, S. M.; Ng, K. K. *Physics of Semiconductor Devices*, Third.; John Wiley & Sons Inc.: Hoboken, NJ.

(33) Ho, J. C.; Arango, A.; Bulović, V. Lateral Organic Bilayer Heterojunction Photoconductors. *Appl. Phys. Lett.* **2008**, *93* (6), 063305.

(34) Nojima, H.; Kobayashi, T.; Nagase, T.; Naito, H. Modulated Photocurrent Spectroscopy for Determination of Electron and Hole Mobilities in Working Organic Solar Cells. *Sci Rep* **2019**, *9* (1), 20346.

(35) Maruhashi, H.; Oku, T.; Suzuki, A.; Akiyama, T.; Yamasaki, Y. Fabrication and Characterization of P3HT:PCBM-Based Thin Film Organic Solar Cells with Zinc Phthalocyanine; Tsukuba-city, Ibaraki, Japan, 2015; pp 89–95.

(36) Mauer, R.; Kastler, M.; Laquai, F. The Impact of Polymer Regioregularity on Charge Transport and Efficiency of P3HT:PCBM Photovoltaic Devices. *Adv. Funct. Mater.* **2010**, *20* (13), 2085–2092.

Appendix C. Silicone-based Polymer Blends: Enhancing Properties through Compatibilization[4]

C.1. Introduction

Blending polymers is a powerful technique to obtain materials with improved properties,[1-4] often at a lower cost than the design of novel monomers and/or polymerization routes. Procedurally, blending typically takes place using common processing equipment such as twin-screw extruders, further reducing the financial investment associated with developing new materials. An additional advantage is that a wide range of properties can be obtained by simply changing the composition of blends, leading to considerable interest in a variety of real-world applications.

The exceptional properties of silicones[5], like the chain flexibility imparted by the wide silicon-oxygen bond angle paired with high bond strength, are a key driver for investigating the preparation of polymer blends based on mixtures of silicones with a wide variety of organic polymers. These unique properties arise from the substantial dipolar character of Si–O–Si bonds situated along a polysiloxane backbone, coupled with an ability to readily control the organic substituents at each silicon atom.[6] This versatile molecular design toolbox provides excellent tunability over surface properties, the glass transition temperature, flexibility, chemical resistance, and thermal/oxidative stability.[7] Consequently, many polysiloxane-based materials have been manufactured in the form of fluids, resins, and as crosslinked elastomers for thousands of commercial products.[8]

[4] This Appendix was originally published in *Journal of Polymer Science*. Reproduced with permission from *Journal of Polymer Science* 2021, 59, 11, 2114–2128. Copyright 2021, John Wiley and Sons.

Although the unique nature of Si–O bonds gives rise to the enhanced properties of silicones, a major processing challenge lies in their immiscibility with other polymers.[9] When incorporated into blends, macrophase separation usually yields undesirable mechanical properties, and while good dispersions can sometimes be obtained with careful control of mixing conditions, the resulting blends are often thermodynamically unstable and undergo further phase separation over time.[10] Strategies to compatibilize polysiloxanes with organic polymers are therefore needed to develop novel, hybrid blends for advanced materials applications.

In this report, we review state-of-the-art polysiloxane compatibilization strategies as divided into four categories: 1) block copolymer compatibilization, 2) reactive blending, 3) interpenetrating polymer networks, and 4) end-group functionalization. The impact of these different approaches will be discussed in terms of phase behavior and properties.

C.2. Results and Discussion

C.2.1. Block Copolymer Compatibilization

The emulsification of immiscible polymer blends by the addition of an interfacial modifier can lead to controllable morphologies with good mechanical properties and thermal stability.[11] These modifiers, referred to as compatibilizers, are often block copolymers where each block is miscible with one of the blend components.[12] Block copolymer compatibilizers typically segregate to the interface between immiscible homopolymers, resulting in increased interfacial adhesion, decreased interfacial tension and domain size, and minimal coalescence during subsequent processing (Figure C.1).[13,14] Block copolymer additives that sufficiently reduce interfacial tension can also prevent brittle fracture due to debonding, allowing for toughening mechanisms such as shear yielding and crazing to occur while limiting crack propagation.[14]

This interfacial toughening effect can be enhanced if the molecular weight of the copolymer is high enough to form entanglements with the surrounding homopolymer matrix.

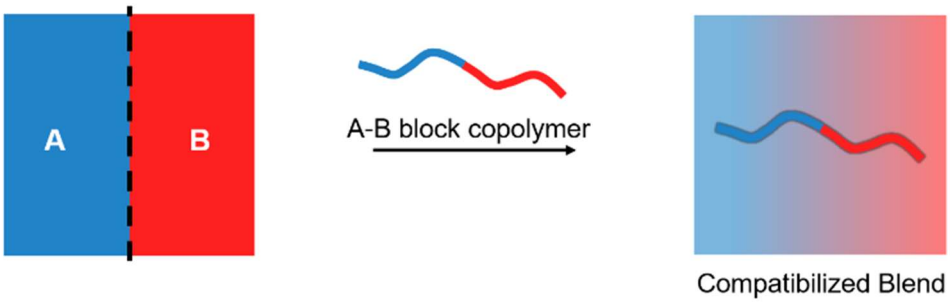

Figure C.1. Depiction of interfacial broadening in an immiscible polymer blend of homopolymers A and B after compatibilization by an AB block copolymer. The block copolymer segregates to the interface and lowers the interfacial tension.

Ternary blends of two homopolymers with copolymer compatibilizers are frequently studied systems in statistical physics. Various theories can be used to calculate equilibrium and non-equilibrium phase behavior, modes of phase separation, and diffusion processes,[15] with significant experimental and theoretical work having been summarized in numerous in-depth reviews.[16-18] Traditionally, block copolymers (BCPs) such as AB diblocks, ABA triblocks, or graft copolymers are used to manipulate the phase behavior of homopolymer blends as they segregate to A/B interfaces and suppress macroscopic phase separation.[2] The resulting blend morphology is governed by experimental factors including molecular weights, composition, and processing conditions.[19]

Useful insights regarding the miscibility and phase behavior of polymers can be inferred from the Flory–Huggins interaction parameter, χ, which captures the binary interactions between chemically dissimilar polymers.[15] Theoretically, χ reflects the enthalpy associated with mixing two dissimilar polymers (A and B) normalized by thermal energy,

where positive values indicate repulsion, which drives phase separation. In practice, Flory–Huggins theory only accounts for the ideal combinatorial entropy of mixing with non-ideal entropy contributions collapsed into an effective χ parameter which is modeled empirically as $\chi = A/T + B$, where T is absolute temperature and A and B are polymer specific parameters (note that additional terms with a higher-order temperature dependence can also be included).[20-22] Polysiloxanes are generally incompatible with organic materials and silicone-based BCPs are widely studied as strongly segregating, high-χ systems.[23-26] Table C.1 provides a summary of χ values found in the literature for BCPs with polydimethylsiloxane (PDMS) as the A block and various organic components as the B block. We also note that experimentally measured values of χ can vary depending on the material system (e.g., blends vs. blocks) and measurement technique (e.g., scattering vs. rheology).[27]

Table C.1. $\chi(T)$ interaction parameters for AB diblock copolymers, where A = PDMS.

B Block	$\chi(T)$[a)]	χ(298 K)	Reference
Poly(D,L-lactide)	$360/T + 0.21$	1.42	28
poly(3-hydroxystyrene)	$33.5/T + 0.31$	0.42	29
Poly(2-vinylpyridine)	$33.2/T + 0.14$	0.26	30
Poly(4-vinylpyridine)	$35.2/T + 0.18$[b)]	0.30	30

Poly(methyl methacrylate)	$26.7/T + 0.11$ $20.8/T + 0.11$	0.19 0.18	31
Poly(ethylene oxide)	$19.3/T + 0.14$ $13.9/T + 0.14$	0.20 0.29	32
Polyethylene	$89.9/T - 0.094$	0.21	33
Polyisoprene	$43.6/T - 0.011$	0.14 0.19	34,35
Poly(ethylene−propylene)	$41.0/T - 0.024$	0.12	33
Polystyrene	$5.80/T + 0.060$	0.076	31
Poly(ethyl ethylene)	$25.2/T - 0.021$	0.059	33

[a)] Values normalized to a monomer reference volume, v_0, of 118 Å^3 unless specified otherwise.

[b)] Reference volume not mentioned in source.

[c)] Only value given, not equation for $\chi(T)$.

While the high-χ nature of polysiloxanes with organic polymers facilitates the development of small features in applications such as photolithography and patterning, strong segregation presents a challenge for blend compatibilization.[8,31] Morse and coworkers have investigated the impact of adding pre-made BCPs to emulsify and stabilize PDMS droplets within an organic matrix.[36] The compatibility and morphology of the resulting blends were estimated by interfacial tension measurements, transmission electron microscopy (TEM), scanning electron microscopy (SEM), and calorimetry. Only minor amounts of a copolymer modifier, ranging from 0.01% to 5%, were required to compatibilize A/B blend interfaces. The addition of compatibilizer decreases the interfacial tension of a polymer blend until the A/B interface is saturated with BCP chains and the critical micellar concentration (CMC) is reached, beyond which BCP micelles lacking homopolymer begin to form and there is little change in bulk physical properties.

Leibler developed a theory to describe the interface between immiscible polymers and to predict the interfacial tension in highly immiscible A/B/AB ternary blends.[37] The theory models copolymer chains at the interface as brushes, with one brush in homopolymer A, the other brush in homopolymer B, and the interface separating the two brushes as a discrete plane. "Wet brush" and "dry brush" regimes are distinguished by the molecular weight ratio of a copolymer block relative to its homopolymer and the grafting density, σ, which is defined as the number of chains per unit area. A wet brush, where homopolymer chains intermingle with the copolymer, is obtained for small σ and relatively low homopolymer molecular weights relative to the block molecular weight. In contrast, a dry brush describes densely packed, highly extended copolymer interfaces where the brush resembles a neat block copolymer lamella. The

ability to distinguish these regimes is critical as interfacial adhesion is dependent on the degree of homopolymer penetration and entanglement with the block copolymer brush.

Hu and coworkers explored this concept experimentally in immiscible polystyrene (PS), polydimethylsiloxane (PDMS), and poly(styrene-*b*-dimethylsiloxane) (PS-*b*-PDMS) ternary blends (Figure C.2).[38] The interfacial tension was measured using an automated drop tensiometer to evaluate the compatibilization as a function of diblock copolymer concentration and PDMS molecular weight. When a nearly symmetric PS-*b*-PDMS (M_n = 13 KDa, 50 wt% PS) was added into a PDMS homopolymer phase of a $PS_{4K}/PDMS_{4.5K}$ blend, the interfacial tension decreased as the copolymer concentration increased. A reduction in interfacial tension of 82% was achieved at the CMC (0.002 wt.%), above which no further change was observed. These results follow Leibler's theory for dry brush behavior and a calculated saturation concentration of 0.003 wt.%. In contrast, a ~70% reduction in interfacial tension was observed for a lower molecular weight PDMS blend ($PS_{4K}/PDMS_{1.6K}$) with a significantly higher CMC of 0.03%. In this case, the interfacial tension observed is larger than Leibler's theory predicts for a dry brush, suggesting lower molecular weight PDMS chains penetrate the copolymer brush layer, leading to repulsive interactions between the PDMS/PS homopolymers that increase interfacial tension. Furthermore, a higher interfacial tension was observed when the PS-*b*-PDMS compatibilizer was first mixed into the PS phase, likely due to the formation of micelles with diffusion also limited by viscosity effects.

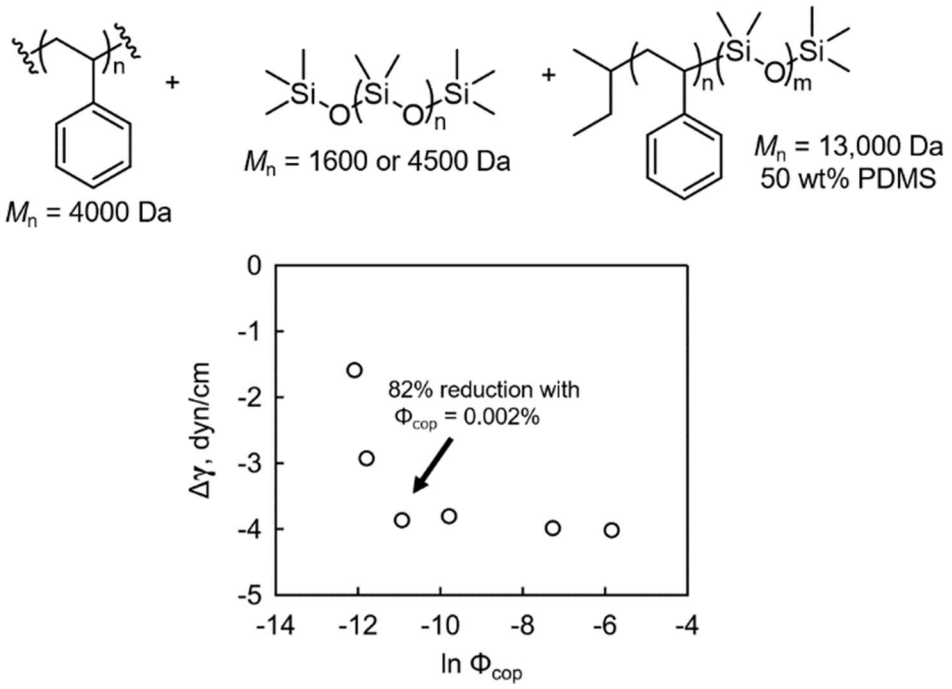

Figure C.2. Reduction of interfacial tension (γ) for PS/PDMS blends as a function of the mass concentration of a PS-*b*-PDMS copolymer additive (Φ_{cop}) formed at 180 °C. Adapted with permission.[38] 1995, American Chemical Society.

In addition to the compatibilizer concentration, the phase behavior of ternary A/B/AB blends heavily depends on the composition of the AB diblock copolymer additive.[39] Self-consistent field theory (SCFT) calculations predict that the interfacial tension, γ, for homopolymer mixtures with equal degrees of polymerization and statistical segment lengths should extrapolate to zero in the limit of a symmetric block copolymer and vary quadratically around the minimum of $f_A = 0.5$. To experimentally test these SCFT predictions, Chang and coworkers measured γ between polyisoprene (PI) and PDMS homopolymers mixed with a poly(isoprene-*b*-dimethylsiloxane) diblock copolymer using a spinning drop tensiometer (Figure C.3).[35] Measurements were conducted on symmetric homopolymer mixtures with

PDMS copolymer volume fractions, f_{PDMS}, ranging from 0.49 to 0.73. Mixtures containing nearly symmetric compatibilizers exhibited ultralow interfacial tension, up to three orders of magnitude less than observed for the homopolymer PI/PDMS interface. Optical microscopy and small-angle X-ray scattering (SAXS) confirmed that these symmetric mixtures form lamellar or bicontinuous microemulsion phases depending on the surfactant concentration. However, the equilibrium γ was found to be a discontinuous function of f_{PDMS}, particularly between f_{PDMS} = 0.60–0.63, where γ changes by an order of magnitude. Chang and coworkers concluded that the discrepancy with SCFT calculations may arise from the limiting rate at which micelles in the PDMS phase emulsify PI homopolymer chains as they approach the interface.

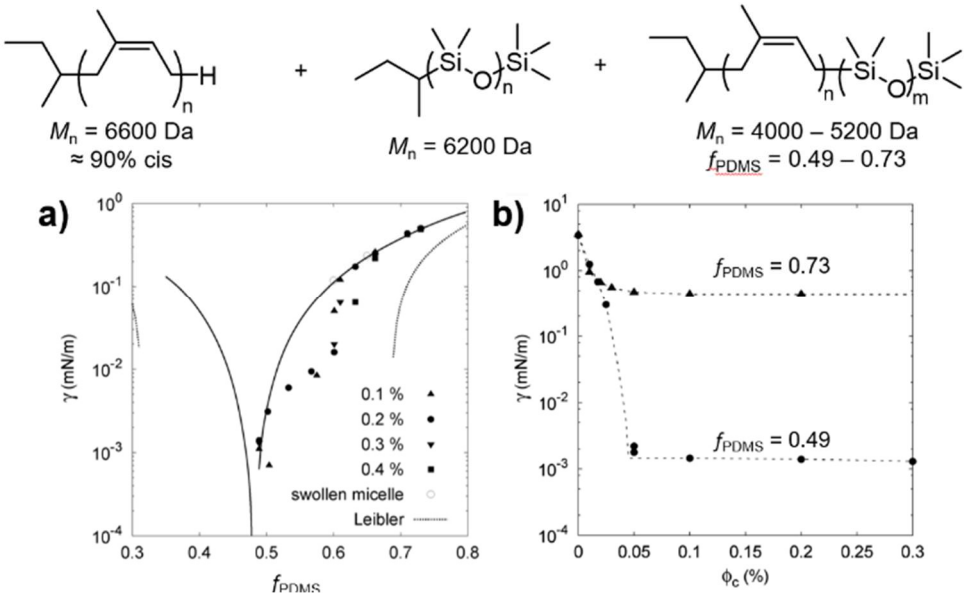

Figure C.3. Reduction of interfacial tension (γ) between polyisoprene and PDMS through the addition of a poly(isoprene-*b*-dimethylsiloxane) copolymer. a) Experimental data was gathered from a spinning drop tensiometer by varying the copolymer volume fraction (f_{PDMS}) and concentration (ϕ_c) and compared to Leibler's theory and SCFT predictions, denoted by the solid line. b) Direct comparison of two different volume fractions shows a larger decrease in

interfacial tension for a symmetric copolymer. Adapted with permission.[35] 2007, American Chemical Society.

The architecture of copolymer compatibilizers also strongly impacts the interfacial structure of macrophase-separated polymer blends. Both theoretical and experimental studies have shown that a diblock copolymer crosses the interface only once (Figure C.4).[40-43] Notably, the number of interfacial crossings for blocky compatibilizers can be increased with multiblock copolymers,[42] for example, a triblock copolymer can cross the interface twice, and a pentablock four times, creating multiple joints or "stitches" that improves interfacial adhesion. With low interfacial adhesion, brittle fracture can occur due to interfacial debonding, but when multiblock polymers are used as compatibilizers, the resulting blends are substantially tougher.[14] A caveat to the use of complex copolymer architectures is often the limited improvement in properties due to their poor entanglement with linear homopolymer chains and micelle formation that constrains diffusion to the homopolymer–homopolymer interface.[14]

The impact of compatibilizer architecture was also examined experimentally by Jorzik and Wolf, who measured the interfacial tension of poly(ethylene oxide) (PEO) blended with PDMS.[43] They compared the reduction in interfacial tension of diblock, triblock, and bottlebrush PEO-*b*-PDMS copolymers as a function of concentration (Figure C.4).

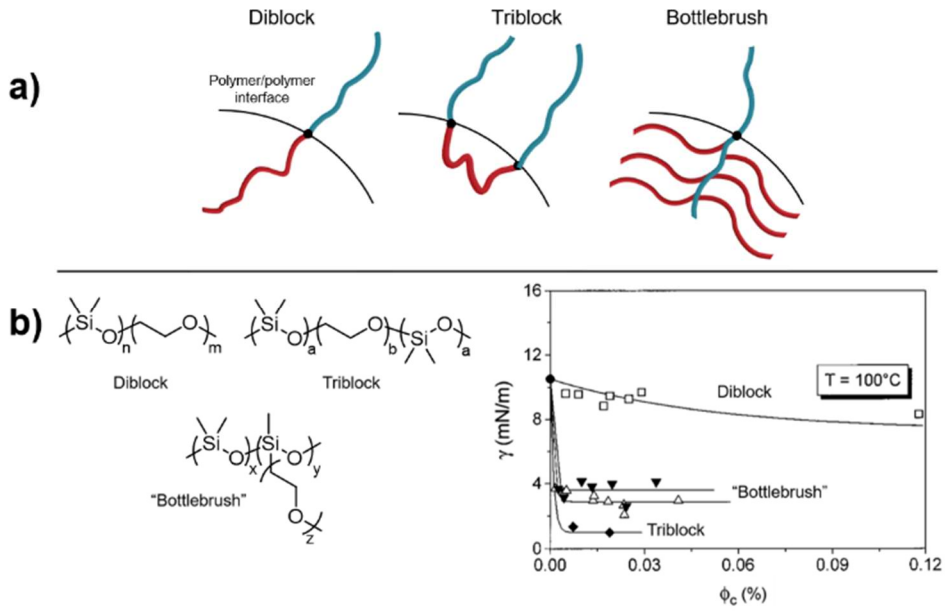

Figure C.4. a) Arrangement of BCP compatibilizers with various architectures at an A/B interface. b) Interfacial tension of compatibilized PEO/PDMS blends for different copolymer architectures. Adapted with permission.[43] 1997, American Chemical Society.

The efficiency of the additives with respect to the maximum reduction of γ follows the sequence triblock > "bottlebrush" > diblock. However, caution should be exercised in generalizing this trend since it does not appear that total molecular weight nor block molecular weight of the copolymers were controlled or varied systematically in the investigation. This presents an opportunity for further theoretical and experimental studies as the connectivity of blocks in the compatibilizer can play a decisive role in reducing interfacial tension. Furthermore, insights from architectures beyond classic diblock copolymers such as tapered block, gradient or protein-like copolymers that have yet to be studied in silicone blends may guide future compatibilizer design.[44-46]

C.2.2. Reactive Blending

While copolymer modifiers have been shown to be an efficient means to lower the interfacial tension of blends, there are limitations related to cost, micelle formation and limited interfacial diffusion. Reactive compatibilization, the *in-situ* formation of block or graft copolymers at the interface by coupling reactive polymers and that are miscible with at least one component of an immiscible polymer blend (Figure C.5), is an approach that circumvents some of these issues.[4] Moreover, reactive polymers avoid the potentially costly and complicated synthesis of block copolymers.

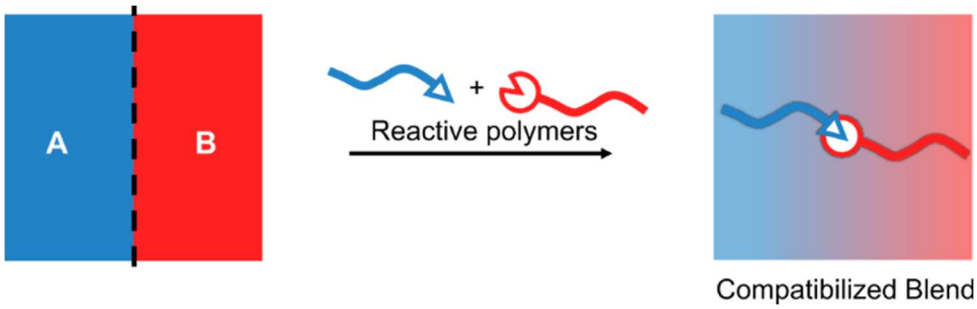

Figure C.5. Compatibilization of an immiscible A/B homopolymer blend by reactive compatibilization. Homopolymers containing reactive groups and/or reactive small molecules undergo *in-situ* coupling to form a block copolymer at the interface, which reduces interfacial tension.

Polymers with reactive comonomers or chain-ends can be mixed or added to unreactive homopolymers they are miscible with to generate polymer blends with block copolymers at their interfaces. Coupling reactions between the reactive homopolymers must be rapid due to the short processing times (often < 5 minutes) and enough copolymer must be formed to sufficiently compatibilize the final blend.[2,47] Thus, it is important to understand the yield of copolymer generated under specific processing conditions to design blends with specific

material properties. Multiple factors controlling copolymer generation at the interface have been investigated, including reaction kinetics, fluid dynamics during processing, and thermodynamic interactions between immiscible polymers.[48-50] A key constraint of reactive compatibilization is reaction efficiency and kinetics. For efficient coupling, reactive species must be able to access phase boundaries and react in the melt during the short processing times associated with blending. The resulting covalent bond must also be sufficiently stable under the processing conditions, further limiting the range of potential functional groups. Additionally, unreacted functional groups left within the final blend can be prone to long term side reactions, causing significant material degradation and drifts in their properties. Despite these challenges, reactive blending has been widely successful for the compatibilization of immiscible polymers and is used in a variety of commercial materials.[51,52]

Maric and coworkers studied the *in-situ* formation of block copolymers with functionalized PDMS and PS bearing various amine (NH_2)/anhydride (Anh), NH_2/epoxy (Ep), and carboxylic acid (COOH)/Ep coupling partners using size exclusion chromatography (SEC) to probe copolymer formation and electron microscopy to determine the morphology.[53] Electron microscopy of the resulting blends showed a clear particle size dependence on the reactive functional groups (Figure C.6). As expected, non-functional PDMS/PS blends produced large PDMS droplets that coarsened rapidly after annealing. The PDMS-Ep/PS-NH_2 and PDMS-Ep/PS-COOH blends were also coarse and unstable at elevated temperatures. In contrast, after only 5 minutes of mixing, PDMS-Anh/PS-NH_2 blends produced stable sub-micron droplets (< 0.5 μm) of PDMS in PS. SEC revealed that the final PDMS-Anh/PS-NH_2 blend contained 3 wt.% block copolymer, which is sufficient to saturate the interface, whereas the non-stable blends did not show evidence of copolymer formation. Maric and coworkers

also noted that *in-situ* block copolymer formation was slower for the PDMS-Anh/PS-NH_2 blends compared to other Anh/NH_2 systems in the literature. They speculated that this lower reactivity may be due to the sharper PDMS/PS interface caused by their poor miscibility leading to decreased chain mixing.

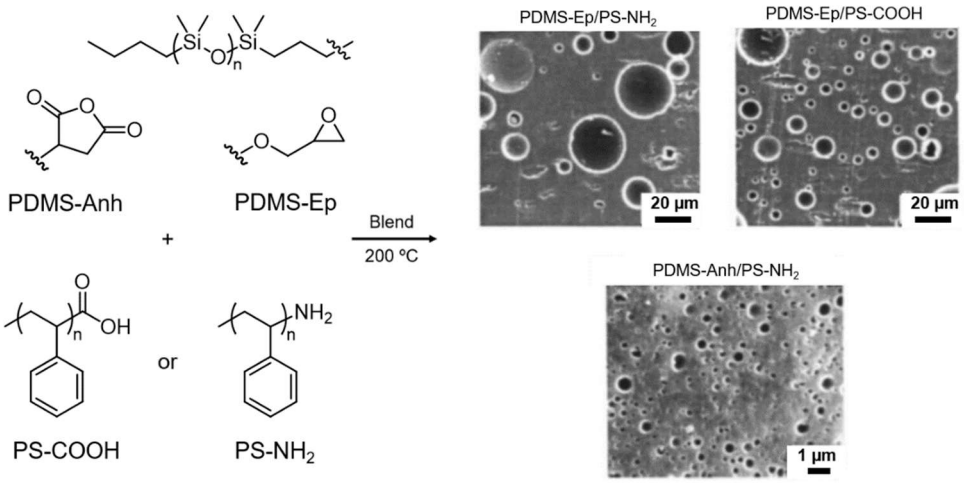

Figure C.6. Compatibilization of PDMS and PS through reactive blending with functional end groups. Adapted with permission.[53] 2004, John Wiley and Sons.

Expanding on this concept, Jones and coworkers examined the impact of the polymer backbone chemistry on Anh/NH_2 reactions at the polymer–polymer interface to elucidate how χ impacts the reactivity.[50] (Figure C.7) The extent of interfacial reaction of anthracene labeled Anh-terminated poly(methyl methacrylate) (PMMA-Anh) or PS-Anh with a range of amine functional polymers was determined by annealing bilayer thin films and measuring the resulting copolymer concentration using SEC with ultraviolet light (UV), fluorescence and refractive index (RI) detectors . In addition, the interfacial roughness was characterized by atomic force microscopy. Two principal effects were observed with decreasing χ: an increase

in the rate and extent of reaction at long times, as well as greater interfacial roughening. PDMS/PS and PDMS/PMMA reactive films were found to have the lowest conversion due to a decreased interfacial volume in which reactions can occur. Furthermore, the maximum interfacial conversion was found to decrease for blends prepared with higher molecular weight PMMA components, likely due the lower concentration of functional groups limiting the amount of chains that react at the PDMS/PMMA interface. In addition, the stronger segregation, suppressed internal fluctuations and increased block copolymer asymmetry at higher PMMA molecular weights may be important.

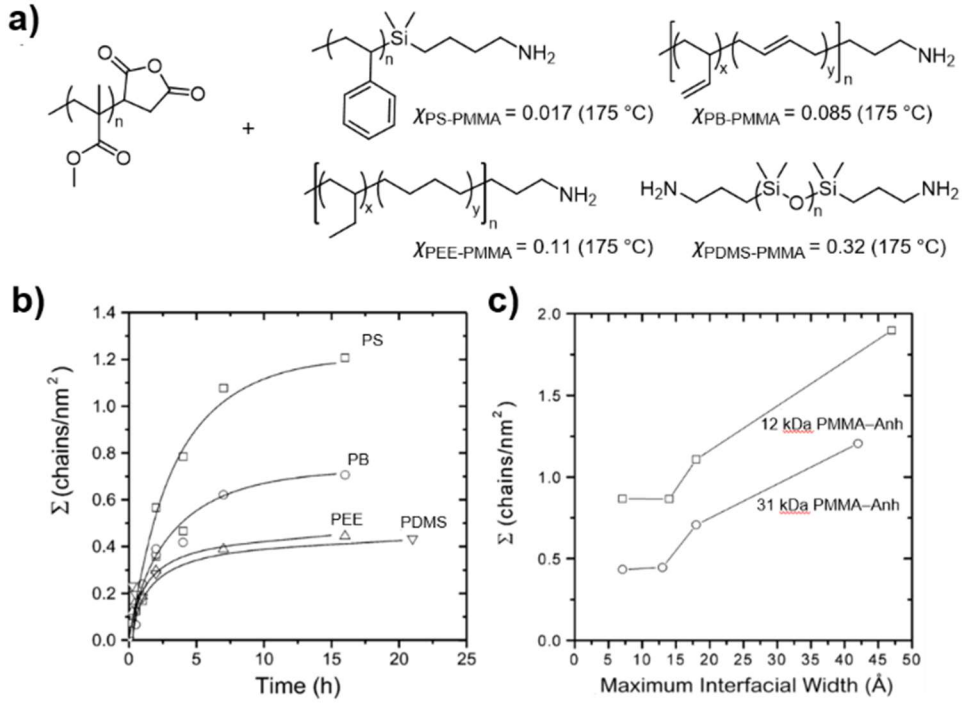

Figure C.7. a) Structure and χ values (at 175 °C) of PMMA-Anh with different amine-terminated polymers. b) Interfacial conversion vs. time for reactive blends (at 200 °C) containing PMMA-Anh. c) Interfacial width for 12 and 31 kDa PMMA-Anh with a range of amine functional polymers. Adapted with permission.[50] 2003, American Chemical Society.

In addition to the Anh/NH_2 reaction, there are a wide variety of other potential reactive blending chemistries for the modification of silicone-based materials based on commercially-available polysiloxanes, including hydrosilylation, thiol–ene, and polycondensation.[54] Of these reactions, only a subset has been reported for the *in-situ* formation of compatibilizers, primarily in the form of graft copolymers. Although graft compatibilizers allow for more "crossings" at the polymer–polymer interface, the location of functional groups impacts the coupling kinetics for reactive polymers due to potential steric hindrance from the polymer backbone.[55] Significantly, the effect of compatibilizer architecture, i.e., block vs. graft compatibilizers, remains an open question for reactive polymer blends and warrants further investigation.

The promise of these studies is illustrated by the improved flow and impact toughness reported by Zhou and Osby for the modification of polycarbonate (PC) with a small amount of ultra-high molecular weight PDMS.[56] By promoting transesterification between the polycarbonate backbone and hydroxyl-terminated PDMS, a novel PC/PDMS/PC-*co*-PDMS polymer blend was prepared with superior flow and excellent performance at low temperatures (Figure C.8). By carefully tuning the molecular weight of the base PC, the blend retained its impact toughness from room temperature down to as low as −40 °C. This change was attributed to the formation of a graft copolymer architecture through the incorporation of low-T_g PDMS chains, which reduced the ductile-to-brittle transition temperature of the final material. Analysis of the blend morphologies by electron microscopy revealed stable, sub-micron PDMS droplets dispersed within a polycarbonate matrix, with near optimum particle sizes between 0.2 – 0.9 μm for good impact toughening. This observation is in stark contrast to nearly identical blends prepared with non-reactive PDMS, where coalescence and macroscopic phase separation resulted in large PDMS domains and poor mechanical performance.

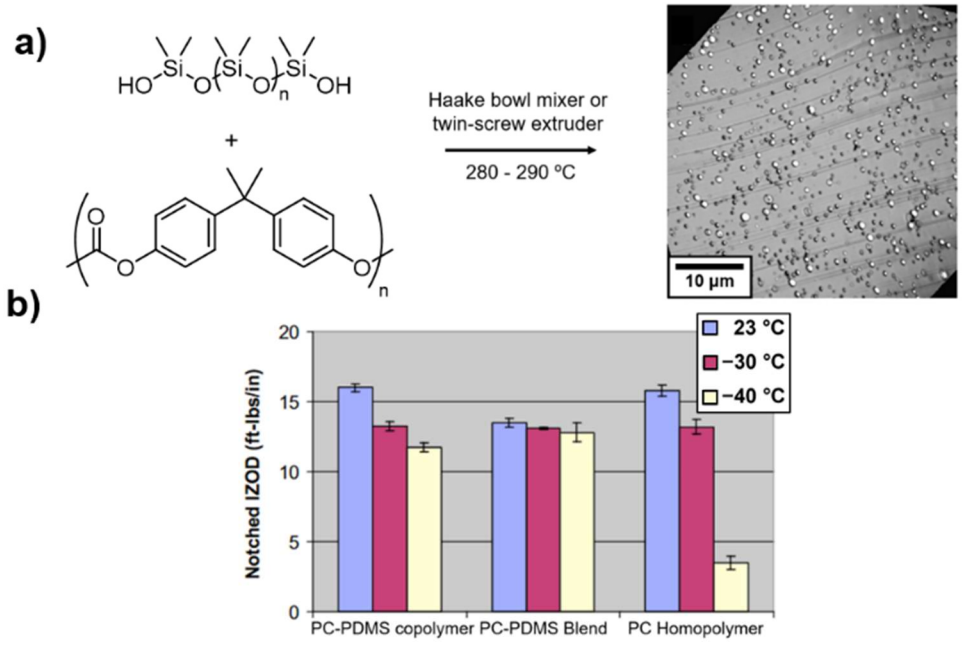

Figure C.8. a) Reactive blending and morphology of PC with PDMS. b) Notched Izod impact toughness for a PC-PDMS copolymer, PC-PDMS reactive blend, and PC homopolymer at various temperatures. Adapted with permission.[56] 2010, Elsevier.

In principle, many functionalization reactions are available to prepare polysiloxanes with an array of architectures and well-defined chain ends, including hydrosilylation, thiol–ene, halogen substitution, and esterification.[7] Although a variety of methods to modify polysiloxanes exist,[50,53,54,56-60] the hydrosilylation of Si–H-containing PDMS is by far the most versatile, allowing for efficient coupling to olefins, carbonyl groups, and other functionalities.[57] Indeed, this highly effective toolbox has enabled the development of various vulcanization strategies for the industrial production of silicone networks.[51] Nevertheless, only a few papers have explored the reactive compatibilization of silicone–organic blends via

hydrosilylation chemistry. In 2012, Bonnet and coworkers reported the reactive blending of Si–H-terminated PDMS and poly(ethylene-*co*-vinyl acetate) (EVA) via metal-catalyzed carbonyl hydrosilylation (Figure C.9).[58] The properties and morphology of the reactive EVA/PDMS blends could be tuned depending on the viscosity and stoichiometry of the homopolymer components. Specifically, a crosslinked material was obtained for low-viscosity PDMS with a high molar ratio of Si–H groups to vinyl acetate (VA) residues along the backbone of the EVA (Si-H/VA = 0.5). In contrast, a compatibilized blend was generated by increasing the PDMS/EVA viscosity ratio and decreasing the Si–H/VA ratio to 3.5×10^{-3}, allowing for the *in-situ* formation of EVA-*g*-PDMS copolymers at the interface between immiscible homopolymers. In the absence of the Ru catalyst, no graft formation was observed, resulting in a coarse morphology with PDMS droplet sizes between 3–5 μm, compared to 0.5 μm in reactive blends. This approach was later expanded to the reactive compatibilization of polyamide/PDMS blends through amide hydrosilylation, which showed similar trends.[59]

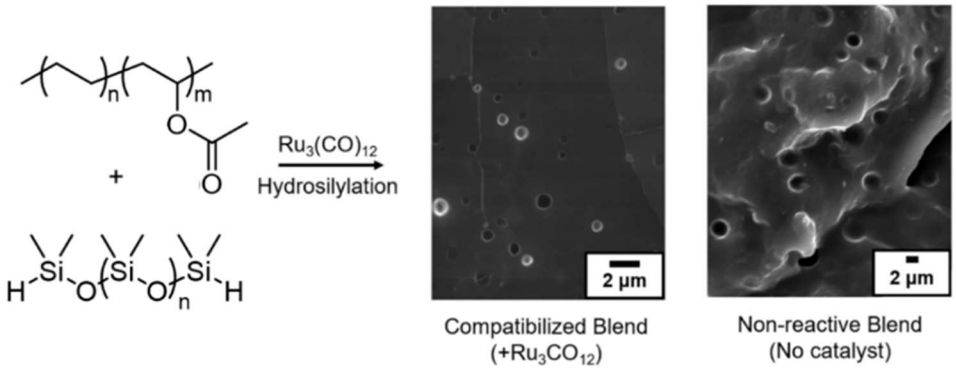

Figure C.9. Morphology of reactive and non-reactive PDMS/EVA blends compatibilized through a metal-catalyzed carbonyl hydrosilylation reaction. Adapted with permission.[58] 2012, Elsevier.

The reactive compatibilization of silicones was also probed by Sun and coworkers by blending linear poly(dimethyl siloxane-*co*-vinylmethyl siloxane) chains, i.e. silicone rubber (SiR), and soluble styrene–butadiene rubber (SSBR) compatibilized by thiol–ene click chemistry (Figure C.10).[60] A trifunctional thiol trimethylolpropane (TMPMP) was chosen to compatibilize SiR and SSBR via an *in-situ* interfacial coupling during the mixing process. Although SiR and SSBR are both vinyl functionalized and can undergo a thiol–ene click reaction with TMPMP, SSBR contains a significantly higher vinyl content and has a tendency to self-crosslink, inhibiting its coupling to SiR. Thus, a two-step process, where TMPMP was first reacted with SiR and then compounded with SSBR, was investigated to address the different reactivities. Blends prepared by a one-step process without TMPMP (referred to as blank) were also prepared for comparison. Both the one-step and two-step blends showed an increased tensile stiffness compared to the control. However, the tensile strength and elongation at break of the one-step blend decreased, indicating an increasing stress concentration from the tendency of TMPMP to internally crosslink the SSBR domains rather than coupling SSBR with SiR to form grafted/hyperbranched architectures. In contrast, the two-step process led to improved tensile strength and tensile modulus stemming from enhanced interfacial SiR and SSBR interactions. These results were supported by increased transparency and decreased SiR domain sizes within the two-step blends, characteristic of improved compatibilization.

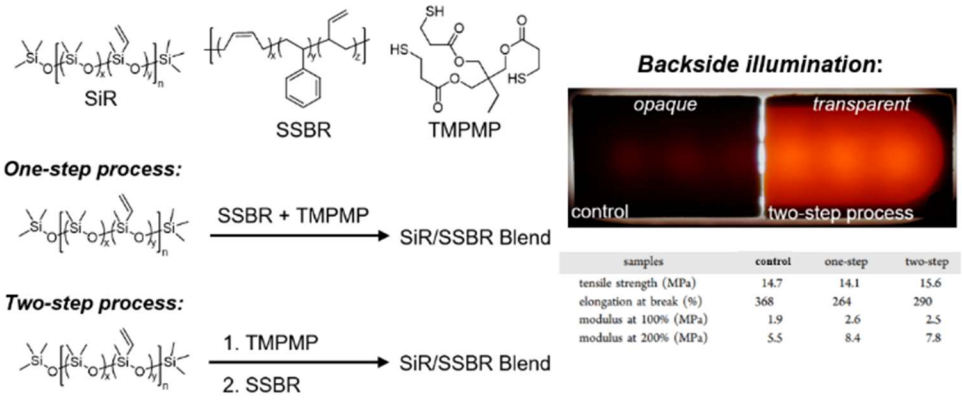

samples	control	one-step	two-step
tensile strength (MPa)	14.7	14.1	15.6
elongation at break (%)	368	264	290
modulus at 100% (MPa)	1.9	2.6	2.5
modulus at 200% (MPa)	5.5	8.4	7.8

Figure C.10. One-step and two-step process for forming SSBR/SiR reactive blends. Backside illuminated images of a control blend (without TMPMP) and a two-step SSBR/SiR blend. Mechanical properties are summarized in the table. Adapted with permission.[60] 2017, American Chemical Society.

C.2.3. Interpenetrating Polymer Networks

Unlike compatibilized blends that are thermodynamically stabilized using block copolymers, interpenetrating polymer networks (IPNs) are kinetically trapped structures containing two or more independently crosslinked networks.[61] Miscible lower molecular weight components (oligomers or monomers) are combined and crosslinked and/or polymerized. This strategy forces the compatibilization of two immiscible polymers by rapidly crosslinking the growing chains, limiting phase separation to produce materials with enhanced properties.[62,63] The domain size and degree of interpenetration are tunable depending on the blending process and the nature of the monomers/oligomers. For example, a simultaneous IPN can be prepared using orthogonal crosslinking reactions where the polymer components are crosslinked simultaneously to form both networks in a single step (Figure C.11a).[64] Alternatively, the formation of the first polymer network can be followed by swelling with an

additional reactive component and subsequent polymerization or crosslinking of the second network in a process typically referred to as sequential IPN formation (Figure C.11b).

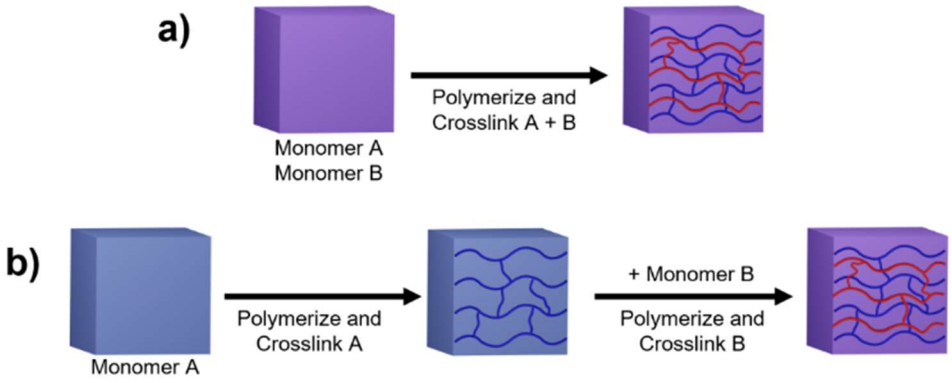

Figure C.11. a) Formation of an interpenetrating network by the simultaneous method starting from homopolymer A swollen with monomer B. The polymerization of polymer B is followed by orthogonally crosslinking both polymers. b) Formation of an interpenetrating network by a sequential strategy starting from a matrix of polymer A. Homopolymer A is initially crosslinked, followed by the addition of monomer B and its subsequent polymerization and crosslinking.

The formation of silicone-containing IPNs is attractive for silicone blends due to the wide variety of available crosslinking methods including alcoholysis, vulcanization, radiation, and hydrosilylation.[54] Careful control over the polymerization, crosslinking, and mixing during preparation prevents macroscopic phase separation, producing small domain sizes in otherwise incompatible polymer mixtures. In particular, the morphology and domain size of an IPN depends on the rate of phase separation and the crosslinking chemistry.[64] Phase separation can

either occur by nucleation and growth, generating polymer droplets within a larger matrix, or by spinodal decomposition, which generally yields a bicontinuous structure with two interconnected domains.

Turner and Cheng prepared PDMS–poly(methacrylic acid) (PMAA) IPN membranes using sequential monomer immersion. Pre-IPN films were first produced by mixing vinyl-terminated PDMS with a multifunctional Si–H crosslinker, which was cured via hydrosilylation (Figure C.12).[65] The crosslinked PDMS resin was then swollen in a methacrylic acid monomer solution containing triethylene glycol dimethacrylate as crosslinker and the IPN formed via free-radical polymerization upon exposure to UV radiation. Fluorescent labeling of the resulting PMAA domains by swelling in fluorescein enabled the direct visualization of the IPN morphology by laser scanning confocal microscopy. The morphology of these PDMS–PMAA sequential IPNs transitioned from a relatively homogeneous hydrogel near the glass surface to coarse phase separation and finally to a bicontinuous structure, indicative of spinodal decomposition, in the interior of the films. This change in film morphology was attributed to a concentration gradient created by monomer evaporation and substrate–surface thermodynamic effects. In contrast, the total immersion of pre-IPN films in a MAA solution ensured an even monomer concentration profile and produced a uniform bicontinuous morphology throughout the IPN. Interestingly, these homogeneous membranes were much more permeable to water-soluble compounds, with the dispersed hydrogels forming an impermeable layer at the air or glass–IPN interfaces.

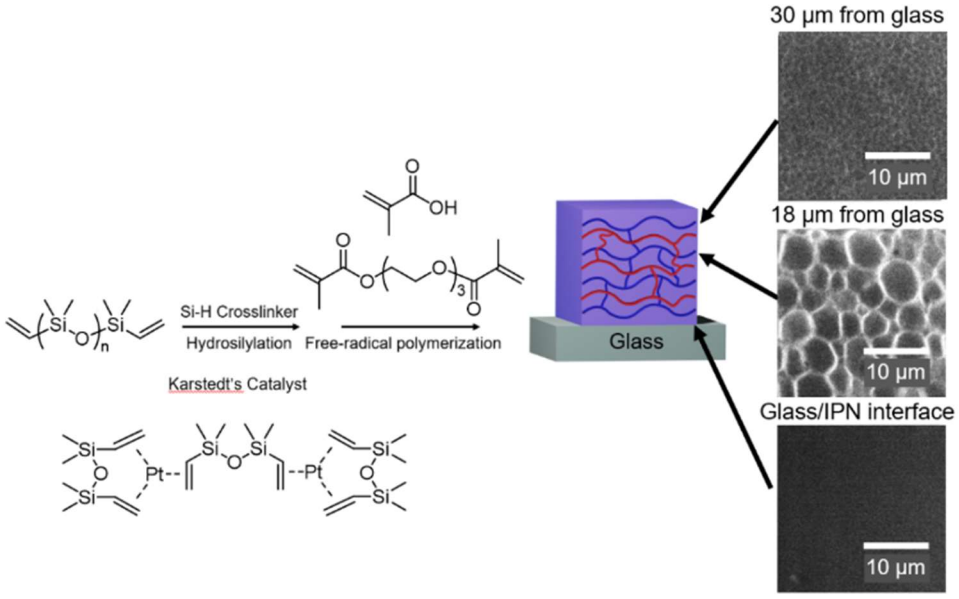

Figure C.12. Sequential formation of a PDMS/MAA IPN and laser scanning confocal microscopy depth profile images of an IPN prepared on a glass substrate. Adapted with permission.[65] 2000, American Chemical Society.

Although sequential strategies provide well-disperse IPNs with unique morphologies, they are often not very practical for industrial applications. An interesting alternative to the sequential approach is IPN formation via simultaneous polymerization processes.[66] In these systems, the morphology depends on homopolymer incompatibility and the polymerization conditions, including mixing and the kinetics of each reaction.[9] Issues such as co-solubility and relative hydrophobicity between the polymers are major constraints in IPN formation and are particularly evident when both hydrophobic and hydrophilic monomers are polymerized simultaneously. To circumvent these issues, Castellino and coworkers formed polydimethylsiloxane–poly(methacrylic acid-*stat*-hydroxyethyl methacrylate) (PDMS-P(MAA-HEMA)) IPNs simultaneously from bicontinuous emulsion templates that were

stabilized with polymerizable silicone/ethylene-glycol-acrylate-functionalized surfactants (**Figure C.13**).[67] This process provides a simpler one-step approach to form silicone IPNs with interpenetration at the nanoscale level. The phase behavior of these pre-IPN silicone microemulsions was evaluated using pseudo-ternary phase diagrams at different temperatures to identify compositional ranges for potential polymerization templates. Compositions with the desired morphology were then polymerized and crosslinked simultaneously to produce the final IPN. Confocal microscopy on samples swollen in aqueous sodium fluorescein confirmed that both phases were well distributed with domain sizes < 1 μm, although for systems with non-reactive surfactants the morphology was not uniform throughout the material. This non-uniformity may be a result of changes in the template microemulsion phase behavior and domain size during polymerization. In contrast, the bulk microstructure of IPNs produced from reactive surfactants was more uniform with reduced domain size down to < 200 nm.

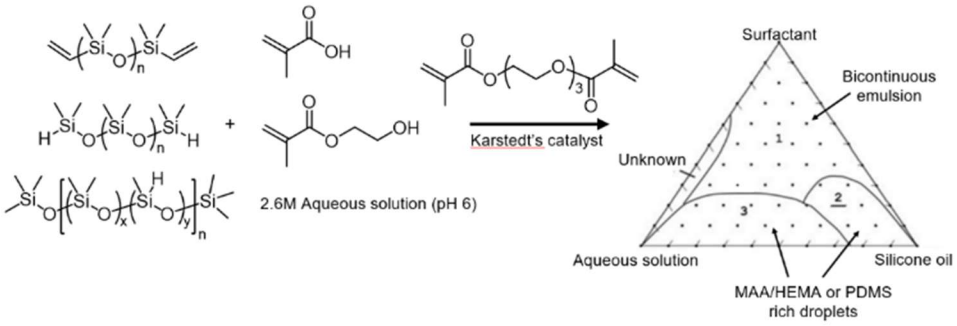

Figure C.13. Simultaneous formation of a PDMS/MAA/HEMA IPN and phase behavior of pre-IPN microemulsion templates with reactive surfactants. Adapted with permission.[67] 2012, Springer Nature.

Although orthogonal chemistries are typically used to crosslink each domain during IPN formation, additional chemical grafts between the two immiscible polymers can increase

the compatibility of the overall material. Meyer and coworkers explored this concept by synthesizing grafted and non-grafted IPNs based on PDMS and PMMA (Figure C.14).[68] The IPNs were synthesized through an *in-situ* sequential strategy involving mixing dihydroxy-terminated PDMS, MMA, azobisisobutyronitrile (AIBN), 1,1,1-trimethylol-propane trimethacrylate (TRIM) and either tetraethyl orthosilicate (TEOS) or trimethoxysilylpropyl methacrylate (TMSPM) as a crosslinker for the PDMS domains. The PDMS network was initially formed by adding tin(II) octanoate to catalyze the polycondensation crosslinking, followed by heating to 60 °C to initiate the copolymerization of the vinyl network. Interestingly, the grafted PDMS/PMMA IPNs (crosslinked by TMSPM) were more transparent when compared to their non-grafted analogs, indicative of a decreased PDMS domain size within the composite material. In addition, differential scanning calorimetry (DSC) showed little change in the glass transition temperatures of the PDMS and PMMA networks, supporting phase separation in the graft IPNs. The stress–strain behavior of full and graft IPNs demonstrated that grafting and crosslinking significantly improved the tensile modulus E while reducing elongation at break ε_u.

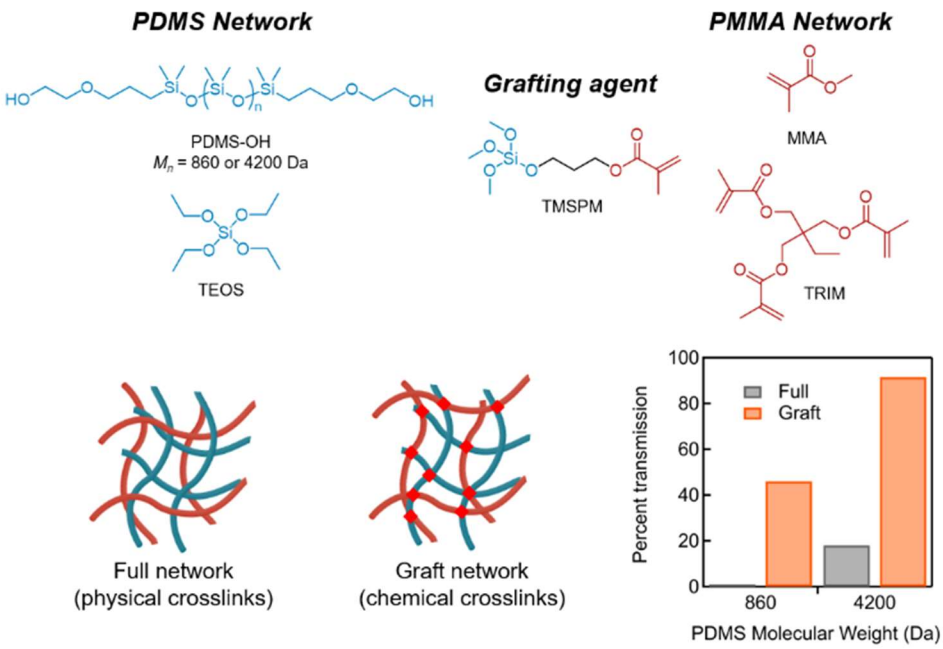

Figure C.14. *In-situ* sequential synthesis and light transmission percentage for full and grafted PDMS/MAA IPNs. Adapted with permission.[68] 1992, Elsevier.

C.2.4 End-group Interaction

Although the formation of stable polymer blends has primarily focused on the design of novel compatibilizers, several publications have demonstrated that interactions between chain ends can significantly impact interfacial properties.[69,70] This approach can lead to increased miscibility by incorporating end groups that have repulsive interactions with both blend homopolymers (Figure C.15). This phenomenon is primarily observed with low molecular weight polymers as end-group effects are diluted with increasing degrees of polymerization.[71]

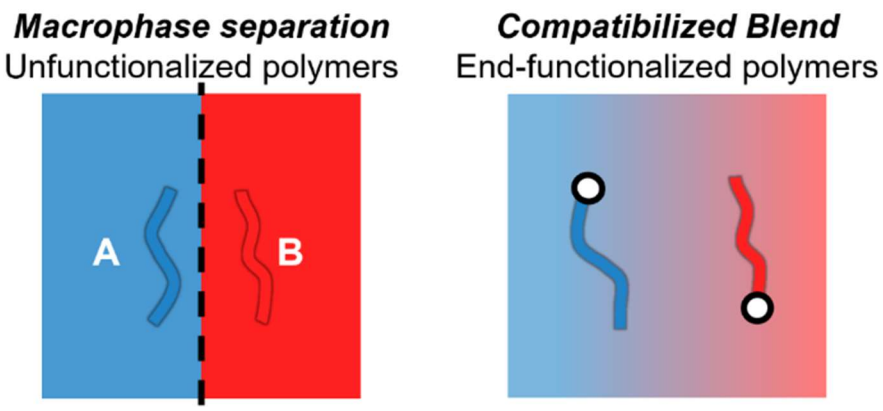

Figure C.15. Compatibilization of immiscible homopolymer A and B through end-group effects.

While underexplored, a limited number of studies have shown significant end group effects on the miscibility of polysiloxanes with organic polymers.[69-73] In one example, the Koberstein group measured the interfacial tension of end-functionalized PDMS blended with polybutadiene (PBD).[69] For this study, the authors measured the interfacial tension between PBD blended with amine-terminated PDMS (PDMS-NH_2) or methyl-terminated PDMS (PDMS-CH_3). At molecular weights around 1300 Da, the interfacial tension of the PDMS-NH_2 blend was 20% lower than that of the PDMS-CH_3 blend. However, at molecular weights around 19 kDa, the change in interfacial tension was only ~5%. Unexpectedly, PDMS-NH_2 did not exhibit significant interfacial activity, indicating the reduction in interfacial tension cannot be attributed to a surfactant effect, but instead to changes in bulk thermodynamic interactions.

To understand this phenomenon, Qian *et al*. used a Flory–Huggins lattice model and molecular simulations to account for end group effects and their impact on the χ interaction parameter.[72] χ values of PDMS and poly(methylphenylsiloxane) (PMPS) blends were

calculated for trimethylsilyl- or silanol-terminated polymers. The results indicate end groups in low molecular weight blends (particularly for oligomers with less than 20 repeat units) significantly impact χ and microphase separation, whereas end-group effects are inconsequential at higher molecular weights. Expanding on this study, Lee and coworkers measured the cloud point of low molecular weight blends of polyisoprene with PDMS-CH_3, PDMS-COOH, and PDMS-NH_2 (Figure C.16).[73] For equivalent molecular weights, the cloud points of PI/PDMS-CH_3, PI/PDMS-COOH, and PI/PDMS-NH_2 dropped dramatically from 250 °C for the methyl-terminated polymer to 190 °C for PDMS-COOH and 85 °C for PDMS-NH_2, scaling inversely with the polarity of the PDMS end group. In particular, the polymer chain end had profound effects on χ, with the largest decrease associated with terminal amine groups on PDMS. Chain ends having repulsive interactions with both homopolymers force the functionalized polymers to interact, leading to increased miscibility as evidenced by lower cloud points. The phase diagrams of these end-functional blends can be modeled by a modified Flory–Huggins–Staverman lattice approach that includes binary interaction theory and group additivity concepts that capture the effect of end groups on the enthalpy of mixing.

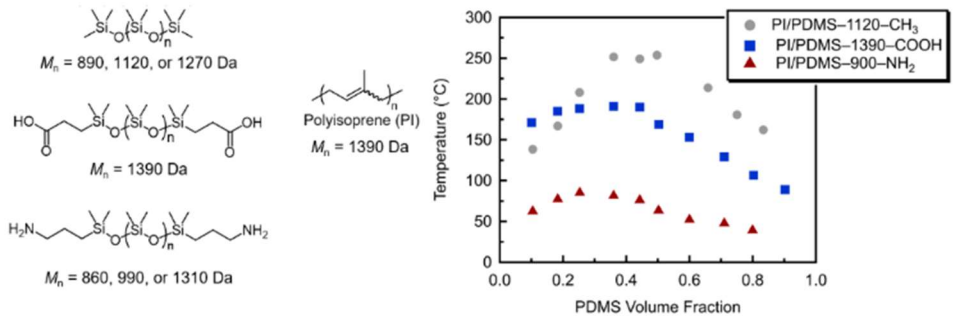

Figure C.16. Experimental cloud point curves of non-reactive PI/PDMS blends with various chain ends. Adapted with permission.[73] 2001, Elsevier.

C.3. Conclusions and Future Work

Advances in silicone chemistry have forged a remarkable toolbox for the preparation of novel block copolymers, reactive coupling systems, and functionalized materials. This increased availability and versatility has allowed researchers the opportunity to design and tune the stability, morphology, and mechanical properties of immiscible polymer blends. The compatibilization of these materials has been achieved through four well-established approaches, namely the addition of silicone–organic block copolymers, reactive blending, highly crosslinked interpenetrating polymer networks, and end-group effects in low molecular weight materials. With precise structural and functional group control, a wide array of silicone–organic blends can now be achieved from previously immiscible polymers despite their strong phase separation.

Although much progress has been made in the compatibilization of immiscible silicone–organic blends, several key areas are still poorly understood and would benefit from further theoretical and experimental studies. Most importantly, the impact of copolymer architecture on silicone-containing BCP additives needs more research despite noted architectural effects on the compatibilization and interfacial structure of immiscible polymer blends. Further studies are also required on reactive blending as it does only form copolymers at the interface. There is a caveat in that a large portion of the added reactive groups on the siloxane and organic polymers are left unreacted and will be prone to degradation, further material drift (potential long term side reactions) and potential hazards as would be in the case of residual SiH containing PDMS (hydrogen formation). The block copolymer approach, on the other hand, could be classified as a more inert approach but also will have its issues since reaching the same level of silicone/organic polymer dispersion will require more (mixing)

energy. Further fundamental studies exploring the effects of silicone-containing BCP architecture on the morphology and mechanical properties of blended polysiloxanes may allow these architecture effects to be more comprehensively evaluated. In addition, the impact of other block copolymer design concepts that are known to strongly influence the phase behavior of neat, non-blended materials—for example, conformational asymmetry—would provide an increased understanding of opportunities in blend compatibilization. Finally, the development of scalable, efficient, and cost-effective reactive systems that generate compatibilizers *in situ* will drastically aid in the commercialization of immiscible silicone–organic polymeric blends. We anticipate that polymeric silicone blends will continue to play a significant role in many areas of materials science with well-dispersed silicone–organic polymer blends being central to an increasing range of academic and industrial applications.

C.4 References

(1) K. Binder, in *Theories and Mechanism of Phase Transitions, Heterophase Polymerizations, Homopolymerization, Addition Polymerization,* Springer-Verlag, Berlin, Germany **1994**, Ch. 4.

(2) C. Koning, M. van Duin, C. Pagnoulle, R. Jerome, *Prog. Polym. Sci.* **1998,** *23,* 707.

(3) D. R. Paul, J. W. Barlow, H. Keskkula, in *Encyclopedia of Polymer Science and Engineering 2nd ed*, Vol. 12, Wiley-Interscience, New York, USA **1988**.

(4) A. A. R., S. Thomas, *Compatibilization of Polymer Blends*, Elsevier, Amsterdam, Netherlands **2020**.

(5) We use silicone and polysiloxane interchangeably and use siloxane to refer to the Si–O functional group.

(6) M. G. Voronkov, V. P. Mileshkevich, Y. A. Yuzhelevskii, *Studies in Soviet Science. The Siloxane Bond: Physical Properties and Chemical Transformations*, Plenum Publishing Corporation, New York, USA **1978.**

(7) E. Pouget, J. Tonnar, P. Lucan, P. Lacroix-Desmazes, F. Ganachaud, B. Boutevin, *Chem. Rev.* **2010,** *110*. 1233.

(8) Centre Européen des Silicones, http://www.silicones.eu, accessed: December, **2020**.

(9) P. Lucas, JJ. Robin, in *Functional Materials and Biomaterials*, Springer, Berlin, Heidelberg **2007**, Ch. 3.

(10) U. Sundararaj, C. W. Macosko, *Macromolecules* **1995**, *28*, 2647.

(11) C. W. Macosko, P. Guégan, A. K. Khandpur, *Macromolecules* **1996**, *29*, 5590.

(12) J. Noolandi, K. M. Hong, *Macromolecules* **1982**, *15*, 482.

(13) AV. Ruzette, L. Leibler, *Nat. Mater.* **2005**, *4*, 19.

(14) C. Creton, E. J. Kramer, H. R. Brown, CY. Hui, *Adv. Polym. Sci.* **2002**, *156*, 53.

(15) D. Schwahn, *Adv. Polym. Sci.* **2005**, *183*, 1.

(16) P. J. Flory, *Principles of Polymer Chemistry.* Cornell University Press, New York, USA **1971**.

(17) P. G. deGennes, *Scaling Concepts in Polymer Physics.* Cornell University Press, New York, USA **1979**.

(18) D. Schwann, K. Mortensen, *Thermal Composition Fluctuations in Polymer Blends studied with Small Angle Neutron Scattering*, Gordon & Breach Science Publishers, Amsterdam, Netherlands **2000**.

(19) F. W. Bates, W. W. Maurer, P. M. Lipic, M. A. Hillmyer, K. Almdal, K. Mortensen, G. H. Fredrickson, T.P. Lodge, *Phys. Rev. Lett.* **1997**, *79*, 849.

(20) F. M. Bates, M. A. Hillmyer, T. P. Lodge, C. M. Bates, K. T. Delaney, G. H. Fredrickson, *Science* **2012**, *336,* 434.

(21) P. C. Hiemenz, T. P. Lodge, *Polymer Chemistry*, CRC Press, Boca Raton, Florida, USA **2007**.

(22) H. B. Eitouni, N. P. Balsara, In *Physical Properties of Polymer Handbook,* (Eds: J. E. Mark) Springer, New York, USA **2007**. Ch. 19.

(23) L. M. Pitet, S. F. Wuister, E. Peeters, E. J. Kramer, C. J. Hawker, E. W. Meijer, *Macromolecules* **2013**, *46*, 8289.

(24) A. Tavakkoli, K. W. Gotrik, A. F. Hannon, A. Alexander-Katz, C. A. Ross, K. K. Berggren, *Science* **2012**, *336*, 1294.

(25) W. J. Durand, G. Blachut, M. J. Maher, S. Sirard, S. Tein, M. C. Carlson, Y. Asano, S. X. Zhou, A. P. Lane, C. M. Bates, C. J. Ellison, C. G. Willson, *J. Polym. Sci. A1.* **2014**, 53, 344.

(26) M. J. Maher, C. M. Bates, G. Blachut, S. Sirard, J. L. Self, M. C. Carlson, L. M. Dean, J. D. Cushen, W. J. Durand, C. O. Hayes, C. J. Ellison, C. G. Willson, *Chem. Mater.* **2014,** *26*, *3*, 1471.

(27) W. W. Maurer, F. S. Bates, T. P. Lodge, *J. Chem. Phys.* **1998**, *108*, 2989.

(28) M. D. Rodwogin, C. S. Spanjers, C. Leighton, M. C. Hillmyer, *ACS Nano* **2010**, *4*, 725.

(29) K. Azuma, J. Sun, Y. Choo, Y. Rokhlenko, J. H. Dwyer, B. Schweitzer, T. Hayakawa, C. O. Osuji, P. Gopalan, *Macromolecules* **2018**, *51*, 6460.

(30) Y. H. Hur, S. W. Song, J. M. Kim, W. I. Park, K. H. Kim, Y. Kim, Y. S. Jung, *Adv. Funct. Mater.* **2018**, *28*, 1800765.

(31) Y. Luo, D. Montarnal, S. Kim, W. Shi, K. P. Barteau, C. W. Pester, P. D. Hustad, M. D. Christianson, G. H. Fredrickson, E. J. Kramer, C. J. Hawker, *Macromolecules* **2015**, *48*, 3422.

(32) Y. Luo, B. Kim, D. Montarnal, Z. Mester, C. W. Pester, A. J. McGrath, G. Hill, E. J. Kramer, G. H. Fredrickson, C. J. Hawker, *J. Polym. Sci. A. Polym. Chem.* **2016**, *54*, 2200.

(33) K. Almdal, M. A. Hillmyer, F. S. Bates, *Macromolecules* **2002**, *35*, 7685.

(34) E. W. Cochran, D. C. Morse, F. S. Bates, *Macromolecules* **2003**, *36*, 782.

(35) K. Chang, C. W. Macosko, D. C. Morse, *Macromolecules* **2007**, *40*, 3819.

(36) K. Chang, C. W. Macosko, D. C. Morse, *Macromolecules* **2015**, *48*, 8154.

(37) L. Leibler, *Makromol. Chem. Macromol. Symp.* **1988**, *16*, 1.

(38) W. Hu, J. T. Koberstein, J. P. Lingelser, Y. Gallot, *Macromolecules* **1995**, *28*, 5209.

(39) K. Chang, C. D. Morse, *Macromolecules* **2006**, *39*, 7746.

(40) M. D. Dadmun, *Macromolecules* **1996**, *29*, 3868.

(41) M. D. Dadmun, *Mater. Res. Soc. Symp. Proc.* **1997**, *461*, 123.

(42) E. A. Eastwood, M. D. Dadmun, *Macromolecules* **2002**, *35*, 5069.

(43) U. Jorzik, B. A. Wolf, *Macromolecules* **1997**, *30*, 4173.

(44) R. Malik, C. K. Hall, J. Genzer, *Macromolecules* **2011**, *44*, 8284.

(45) J. Kim, M. K. Gray, H. Zhou, S. T. Nguyen, J. M. Torkelson, *Macromolecules* **2005**, *38*, 1037.

(46) C. Harrats, R. Fayt, R. Jérôme, S. Blacher, *J. Polym. Sci. Pol. Phys.* **2003**, *41*, 202.

(47) C. W. Macosko, H. K. Jeon, T. R. Hoye, *Prog. Polym. Sci.* **2005**, *30*, 939.

(48) C. A. Orr, J. J. Cernohous, P. Guegan, A. Hirao, H. K. Jeon, C. W. Macosko, *Polymer* **2001**, *42*, 8171.

(49) J. Zhang, J. Shengxiang, J. Song, T. P. Lodge, C. W. Macosko, *Macromolecules* **2010**, *43*, 7617.

(50) T. D. Jones, J. S. Schulze, C. W. Macosko, T. P. Lodge, *Macromolecules* **2003**, *36*, 7212.

(51) S. Y. Hobbs, M. E. J. Dekkers, V. H. Watkins, *J. Mater. Sci.* **1989**, *24*, 2025.

(52) B. N. Epstein, *U.S. 4174358*, **1979**.

(53) M. Maric, N. Ahurov, C. W. Macosko, *Polym. Eng. and Sci.* **2001**, *41*, 631.

(54) M. A. Brook, *Silicon in Organic, Organometallic and Polymer Chemistry*; Wiley, New York, USA **2000**.

(55) K. J. Hyun, C. W. Macosko, B. Moon, T. R. Hoye, Z. Yin, *Macromolecules* **2004**, *37*, 2563.

(56) W. Zhou, J. Osby, *Polymer* **2010**, *51*, 1990.

(57) C. S. Sample, SH. Lee, S. Li, M. W. Bates, V. Lensch, B. A. Versaw, C. M Bates, C. J. Hawker, *Macromolecules* **2019**, *52*, 7244.

(58) J. Bonnet, V. Bounor-Legaré, P. Alcouffe, P. Cassagnau, *Mater. Chem. Phys.* **2012**, *136*, 954.

(59) J. P. Li, P. Passagnau, F. Da Cruz-Boisson, F. Mélis, P. Alcouffe, V. Bounor-Legaré, Polymer **2017**, *112*, 10.

(60) Z. Sun, Q. Huang, Y. Wang, L. Zhang, Y. Wu, *Ind. Eng. Chem. Res.* **2017**, *56*, 1471.

(61) L. H. Sperling, V. Mishra, *IPNs Around the World*; Wiley, New York, USA **1997**.

(62) S. Murayama, S. Kuroda, Z. Osawa, *Polymer* **1993**, *34*, 2845.

(63) L. H. Sperling, V. Mishra, *Polym. Adv. Technol.* **1996**, *7*, 197.

(64) X. Xie, Y. Chen, Z. Zhang, A. Tanioka, M. Matsuoka, K. Takemura, *Macromolecules* **1999**, *32*, 4424.

(65) J. S. Turner, Y. L. Cheng, *Macromolecules* **2000**, *33*, 3714.

(66) A. J. Silvaroli, T. R. Heyl, Z. Qiang, J. M. Beebe, D. Ahn, S. Mangold, K. R. Shull, M. Wang, *ACS Appl Mater Inter* **2020**, *12*, 44125.

(67) V. Castellino, E. Acosta, YL. Cheng, *Colloid. Polym. Sci.* **2013**, *291*, 527.

(68) X. W. He, J. M. Widmaier, J. E. Herz, G. C. Meyer, *Polymer* **1992**, *33*, 866.

(69) C. A. Fleischer, J. T. Koberstein, V. Krukonis, P. Wetmore, *Macromolecules* **1993**, *26*, 4172.

(70) C. A. Fleischer, A. R. Morales, J. T. Koberstein, *Macromolecules* **1994**, *27*, 379.

(71) T. G. Fox, P. J. Flory, *J. Polym. Sci.* **1954**, *14*, 315.

(72) C, Qian, S. Grigoras, L. D. Kennan, *Macromolecules* **1996**, *29*, 1260.

(73) M. H. Lee, C. A. Fleischer, A. R. Morales, J. T. Koberstein, R. Koningsveld, *Polymer* **2001**, *42*, 9163.